



heritage

Optical Technologies Applied to Cultural Heritage

Edited by

Antonio Alvarez Fernandez-Balbuena and Daniel Vazquez-Molini

Printed Edition of the Special Issue Published in *Heritage*

Optical Technologies Applied to Cultural Heritage

Optical Technologies Applied to Cultural Heritage

Editors

Antonio Alvarez Fernandez-Balbuena

Daniel Vazquez-Molini

MDPI • Basel • Beijing • Wuhan • Barcelona • Belgrade • Manchester • Tokyo • Cluj • Tianjin



Editors

Antonio Alvarez Fernandez-Balbuena Optics Universidad Complutense de Madrid Madrid Spain	Daniel Vazquez-Molini Optics Universidad Complutense de Madrid Madrid Spain
--	--

Editorial Office

MDPI
St. Alban-Anlage 66
4052 Basel, Switzerland

This is a reprint of articles from the Special Issue published online in the open access journal *Heritage* (ISSN 2571-9408) (available at: www.mdpi.com/journal/heritage/special_issues/Optical.Heritage).

For citation purposes, cite each article independently as indicated on the article page online and as indicated below:

LastName, A.A.; LastName, B.B.; LastName, C.C. Article Title. <i>Journal Name</i> Year , <i>Volume Number</i> , Page Range.
--

ISBN 978-3-0365-4636-0 (Hbk)

ISBN 978-3-0365-4635-3 (PDF)

Cover image courtesy of Antonio Alvarez Fernandez-Balbuena

© 2022 by the authors. Articles in this book are Open Access and distributed under the Creative Commons Attribution (CC BY) license, which allows users to download, copy and build upon published articles, as long as the author and publisher are properly credited, which ensures maximum dissemination and a wider impact of our publications.

The book as a whole is distributed by MDPI under the terms and conditions of the Creative Commons license CC BY-NC-ND.

Contents

About the Editors	vii
Preface to “Optical Technologies Applied to Cultural Heritage”	ix
Antonio A. Fernandez-Balbuena and Daniel Vazquez-Molini Optical Technologies Applied to Cultural Heritage Reprinted from: <i>Heritage</i> 2022 , 5, 359-361, doi:10.3390/heritage5010020	1
Ángela Gómez Manzanares, Anto J. Benítez and Juan Carlos Martínez Antón Virtual Restoration and Visualization Changes through Light: A Review Reprinted from: <i>Heritage</i> 2020 , 3, 1373-1384, doi:10.3390/heritage3040076	5
Dorukalp Durmus Characterizing Color Quality, Damage to Artwork, and Light Intensity of Multi-Primary LEDs for Museums Reprinted from: <i>Heritage</i> 2021 , 4, 188-197, doi:10.3390/heritage4010011	17
Anto J. Benítez, Xose Prieto Souto, Manuel Armenteros, Esteban M. Stepanian, Rubén Cantos and Miguel García-Villaraco et al. Multi-Camera Workflow Applied to a Cultural Heritage Building: Alhambra’s Torre de la Cautiva from the Inside Reprinted from: <i>Heritage</i> 2021 , 5, 21-41, doi:10.3390/heritage5010002	27
Miguel Pérez, Nathael Cano, José Luis Ruvalcaba-Sil, Alejandro Mitrani and Oscar G. de Lucio Technical Non-Invasive Study of an 18th Century Novo-Hispanic Panel Painting Reprinted from: <i>Heritage</i> 2021 , 4, 3676-3696, doi:10.3390/heritage4040202	49
Manuela Vagnini, Chiara Anselmi, Michela Azzarelli and Antonio Sgamellotti Things Always Come in Three: Non-Invasive Investigations of Alexander and Roxane’s Wedding Room in Villa Farnesina Reprinted from: <i>Heritage</i> 2021 , 4, 2792-2809, doi:10.3390/heritage4040157	71
Alison Stark, Fraser Filice, James J. Noël, Ronald R. Martin, Tsun-Kong Sham and Yanhui Zou Finfrook et al. Retrieving Tarnished Daguerreotype Content Using X-ray Fluorescence Imaging—Recent Observations on the Effect of Chemical and Electrochemical Cleaning Methods Reprinted from: <i>Heritage</i> 2021 , 4, 1605-1615, doi:10.3390/heritage4030089	89
Roberto Padoan, Marvin E. Klein, Roger M. Groves, Gerrit de Bruin, Ted A. G. Steemers and Matija Strlič Quantitative Assessment of Impact and Sensitivity of Imaging Spectroscopy for Monitoring of Ageing of Archival Documents Reprinted from: <i>Heritage</i> 2021 , 4, 105-124, doi:10.3390/heritage4010006	101
Georgios P. Mastrotheodoros, Marios Theodosios, Eleni Filippaki and Konstantinos G. Beltsios By the Hand of Angelos? Analytical Investigation of a Remarkable 15th Century Cretan Icon Reprinted from: <i>Heritage</i> 2020 , 3, 1360-1372, doi:10.3390/heritage3040075	121

Maria Sole Zalaffi, Ines Agostinelli, Najmeh Karimian and Paolo Ugo Ag-Nanostars for the Sensitive SERS Detection of Dyes in Artistic Cross-Sections— <i>Madonna della Misericordia</i> of the National Gallery of Parma: A Case Study Reprinted from: <i>Heritage</i> 2020 , 3, 1344-1359, doi:10.3390/heritage3040074	135
Averie Reinhardt, Renfei Feng, Qunfeng Xiao, Yongfeng Hu and Tsun-Kong Sham Exploring the Dzi Bead with Synchrotron Light: XRD, XRF Imaging and -XANES Analysis Reprinted from: <i>Heritage</i> 2020 , 3, 1035-1045, doi:10.3390/heritage3030056	151
Philippe Colomban, Burcu Kırmızı, Bing Zhao, Jean-Baptiste Clais, Yong Yang and Vincent Droguet Investigation of the Pigments and Glassy Matrix of Painted Enamelled Qing Dynasty Chinese Porcelains by Noninvasive On-Site Raman Microspectrometry Reprinted from: <i>Heritage</i> 2020 , 3, 915-940, doi:10.3390/heritage3030050	163
Vincent Haburaj, Moritz Nykamp, Jens May, Philipp Hoelzmann and Brigitta Schütt On-Site VIS-NIR Spectral Reflectance and Colour Measurements—A Fast and Inexpensive Alternative for Delineating Sediment Layers Quantitatively? A Case Study from a Monumental Bronze Age Burial Mound (Seddin, Germany) Reprinted from: <i>Heritage</i> 2020 , 3, 528-548, doi:10.3390/heritage3020031	189
Ricardo Bernárdez-Vilaboa The Implication of Vision and Colour in Cultural Heritage Reprinted from: <i>Heritage</i> 2020 , 3, 1063-1068, doi:10.3390/heritage3040058	211

About the Editors

Antonio Alvarez Fernandez-Balbuena

Dr. Antonio Alvarez Fernandez-Balbuena, in 2011 earned a PhD degree with a thesis about optical systems for natural lighting entitled “Optical systems for concentration, caption and guiding of solar radiation”. Since 2000, he has been working in the UCM Faculty of Optics in the Lighting & Color laboratory in the area of applied optics, natural lighting, LED signalization and computer-aided lighting design. During his research, he has been working in national and international projects (Eureka, Cénit). In several projects, he has acted as the principal researcher publishing books, more than 20 indexed papers contributing in the field with 15 patents and more than 50 Congress. Additionally, he is professor at the UCM Optics Department.

Daniel Vazquez-Molini

Daniel Vázquez is Professor in the Optics department of Universidad Complutense of Madrid since 1988. He received a PhD in architecture by Universidad Politecnica de Madrid. He works in developing lighting systems applied to several fields: natural lighting devices, signalling, LED panels, LED lighting devices and solar energy. His areas of interest include color perception and lighting systems applied to cultural heritage. His latest works include Portico de la Gloria gate in Santiago de Compostela, Guernica picture in Reina Sofía museum and Altamira cave in Cantabria. He is manager of the color and lighting team of the Applied Optics Complutense Group. This group has worked in lighting technology topics with many industrial companies as Philips, Telvent, Sainco, Abengoa, LLEDO, and Valeo lighting among others.

Preface to "Optical Technologies Applied to Cultural Heritage"

Art and optics have in common one of the most difficult materials to work with: light. Optics and art cannot be understood without light. Light has accompanied humans from the beginning of time. Light allowed human beings to create habitable spaces in places not reached by sunlight. Family, culture, magic, all of them were possible thanks to light. Fire (heat and light) let those early societies be heated, cook food, and have better relationships among individuals. This essential role is shown in many legends from the early stages of human history. For example, Gilgamesh's trip is a metaphoric journey from darkness to light, or even in the Genesis God said:

"Let there be light," and there was light. God saw that the light was good, and he separated the light from the darkness.

Nowadays, light has the same magical power as in those old times: it allows us to know what is beyond our eyes' reach. Scientists from all around the world are changing the way we see nature and cultural heritage. They push the cutting edge of optics further, and this permits us to deepen our knowledge and understanding of artistic goods, apply better preservation technologies and open a window to a wide range of unknown possibilities where imagination is the limit. Light technology makes it possible to obtain extraordinary information about our universe, travel in time and read information that was hidden in the stars, which the history of cultural heritage is and how to restore and preserve this heritage. Like the lighthouse of Alexandria, a mythical construction whose creation was ordered by Ptolemy II (II BC) and was used to guide sailors to find the right way into the harbour with a beacon light, the latest optical technologies enlighten us to make the best decisions regarding how to preserve, restore and make it possible for people to access and enjoy cultural heritage. At the same time as science and technology are changing more and more quickly, cultural heritage is increasing its significance and importance in society. It is a paradox how the oldest and most constant agent gets a progressively more important role in societies where everything changes very fast. Simultaneously, new technologies are developed every year, which enable us to know better and deeper our cultural heritage. The changing world generates a strong need for a sense of belonging and cultural stability in all human beings around the world, but this sense can be more easily obtained by means of these new technologies due to their impact in cultural heritage preservation and exhibition. When we talk about cultural heritage, we refer to very different artefacts and relics with different conditions, shapes, forms, status, etc. It must be considered that cultural heritage includes artefacts, monuments, buildings, sites, museums, industries, and even intangible goods, and they have a diversity of values like symbolic, historic or aesthetic. With such a casuistry, the appropriate technology for each one cannot be the same. Restorers now have many technologies at their disposal, and more of them coming from optical technologies, but this was a chimera only 20 years ago.

All these new actors that appear around the restoration work require a close relationship among experts from both worlds: science and arts. It is necessary to find new spaces where these two sides of cultural heritage can meet and work together. It is not an easy task, and it requires spaces to share relevant information of both worlds, optics and cultural heritage. This is mainly the scope of this book, which contains important contributions that we hope will be useful to improve the knowledge, understanding and valuation of this area.

Antonio Alvarez Fernandez-Balbuena and Daniel Vazquez-Molini

Editors

Optical Technologies Applied to Cultural Heritage

Antonio A. Fernandez-Balbuena *  and Daniel Vazquez-Molini

Departamento de Óptica, Universidad Complutense de Madrid, 28016 Madrid, Spain; dvazquez@ucm.es

* Correspondence: antonioa@ucm.es

Who knows about light? Who knows about art? These are difficult questions to answer. Optical technologies, which can be applied to cultural heritage, are very diverse and can be used for many purposes. Nowadays, new developments in optical technologies have made it possible to apply these technologies in areas where we did not know it was possible and to obtain data that seemed unreachable. We have a higher instrument accuracy, a higher acquisition velocity, smaller devices, and relatively lower-cost systems. All these factors have opened doors that were once thought to be beyond scientific limits. Today, we have new horizons and possibilities. On the other hand, from a cultural, economic, and social point of view, cultural heritage plays a key role in advanced societies every day. It is very difficult to summarize all the fields in which optical technologies are helpful and non-destructive tools can be used for restoration and analysis. We think that proposals such as this Special Issue are very important for improving our knowledge of various scientific areas. Let us here quote the motto of our university, the Complutense University of Madrid, *Libertas Perfundet Omnia Luce* (liberty lights everything), which we can apply to our field as “the light will make free”.

When we issued the call for papers for the Special Issue “Optical Technologies Applied to Cultural Heritage”, our primary objective was to put together a variety of articles that could explain or at least shed some light on these two questions. To achieve this, we invited several authors to contribute papers from their field in relation to the topics of photonic restoration, spectroscopy analysis, light and damage, hyperspectral image acquisition and processing, light-based technique characterization (optical microscopy, FTIR, Raman, X-ray. . .), and color and visual implications. Additionally, we received some other papers from scientists all around the world. This Special Issue has reached a total of 14 papers, including reviews, research articles, and others that will help us to explain the complexity of working in the field of cultural heritage.

The 14 contributions give special focus to the following items:

- Non-invasive technologies;
- Cleaning methods;
- Characterization of color, damage, LED lighting;
- Monitoring ageing;
- Analytical investigation;
- Image analysis;
- Virtual restoration;
- Vision and color;
- Technical and case studies.

In this Special Issue, we present papers on a mix of optical technologies related to different restoration needs, as well as a specific paper related to a digital representation of the Tower of the Captive located in the Alhambra palace in Granada [1]. It is clear that humankind needs light to see in the dark—for example, the behavior of Paleolithic groups was determined by how long the light of their torches lasted, since deeper parts of the Paleolithic caves required light not only to access them but also to carry out artistic activities [2].

Citation: Fernandez-Balbuena, A.A.; Vazquez-Molini, D. Optical Technologies Applied to Cultural Heritage. *Heritage* **2022**, *5*, 359–361. <https://doi.org/10.3390/heritage5010020>

Received: 26 January 2022

Accepted: 7 February 2022

Published: 9 February 2022

Publisher’s Note: MDPI stays neutral with regard to jurisdictional claims in published maps and institutional affiliations.



Copyright: © 2022 by the authors. Licensee MDPI, Basel, Switzerland. This article is an open access article distributed under the terms and conditions of the Creative Commons Attribution (CC BY) license (<https://creativecommons.org/licenses/by/4.0/>).

At present, cultural heritage lighting has been studied quite extensively. The International Commission on Illumination (CIE) provides several guides for the use of lighting. For instance, there is an exhaustive guide on the need to prevent damage caused by lighting in museums [3]. However, this guide has some limitations that should be overcome through further research. The damage function illustrates one of these relevant areas that should be studied. This is related to wavelength and five material categories—namely, low-quality paper, cotton paper, oil paint over canvas, textiles, and watercolors on fabric paper; however, the number of relevant materials that need to be studied is considerable. As can be seen, there is still much work to do. Artwork damage has been studied in the literature, sometimes in relation to museum objects [4] and usually in relation to particular materials such as Japanese lacquer [5].

Scientific studies on cultural heritage conservation have been carried out using non-invasive techniques. Optical technologies are therefore a great ally in this area. As an example, we present two detailed papers on the issue of non-invasive measurements: one of them deals with a combination of imaging and spectroscopic techniques with principal component analysis (PCA) and describes the pigment spatial distribution over the large-format picture of Purísima Concepción located in México [6].

Dr. Dorukalp conducted an interesting study regarding the dilemma concerning light, damage, and visibility when using LED light sources in museums. The author obtained the color quality function related to energy efficiency for a multi-primary LED light source; this is one of the greatest challenges when lighting artworks. Finally, he presents a 3D representation of conflicting parameters (color quality vs. damage) that should be studied carefully to improve lighting conditions and reduce damage. With a tunable RGB light source, optimal spectral combination can reduce damage while maintaining a good level of lighting [7].

Benítez et al. published an interesting article about the digital representation of an historical building. In their case, they explain the workflow followed to reach the digital representation of the whole interior of the Tower of the Captive located in the Alhambra palace in Granada. The objective was to create a photorealistic 3D model to contribute to the dissemination of cultural heritage. Virtual reality (VR) environments are potential systems that can be used to visualize 3D models [1]. The photorealistic 3D projection of this scene could contribute to reducing the damage caused to this fragile building due to high amount of people wanting to visit it. Additionally, this is an example of a new form of experiencing art through virtual reality or augmented reality. For this projection, the authors studied different natural lighting conditions so that the interior of the building could be virtually observed in any desired condition.

Ángela Gómez proposes a review of different virtual restoration techniques and presents projection mapping as a necessary process to obtain a good calibration for future projection lighting for restoration applications. Projected lighting can be useful for restoration and lighting by employing algorithms to reduce damage while improving the appearance of color. There are some artworks, such as Dalí's 1926 picture "Dos Figuras", that cannot be traditionally restored due to the canvas and pigment status; therefore, new technologies such as light projection techniques should be applied.

Finally, the Guest Editors would like to reflect on the issue of lighting and cultural heritage. Cultural heritage is a treasure that humankind has received, so we are responsible for maintaining it for future research and contemplation. This may be difficult to achieve, but non-invasive scientific techniques have been proven to be of great importance in permitting curators to make good decisions about the conservation process. Therefore, curators and scientists must work together to make this work possible.

Author Contributions: Writing—original draft preparation, A.A.F.-B. and D.V.-M. All authors have read and agreed to the published version of the manuscript.

Funding: This research has been funded by project number RTI2018-097633-A-100 of the Ministry of Science and Innovation of Spain.

Conflicts of Interest: The authors declare no conflict of interest.

References

1. Benítez, A.J.; Prieto Souto, X.; Armenteros, M.; Stepanian, E.M.; Cantos, R.; García-Villaraco, M.; Solano, J.; Gómez Manzanares, Á. Multi-Camera Workflow Applied to a Cultural Heritage Building: Alhambra's Torre de la Cautiva from the Inside. *Heritage* **2022**, *5*, 21–41. [CrossRef]
2. Medina-Alcaide, M.Á.; Garate, D.; Intxaurbe, I.; Sanchidrián, J.L.; Rivero, O.; Ferrier, C.; Mesa, M.D.; Pereña, J.; Libano, I. The conquest of the dark spaces: An experimental approach to lighting systems in Paleolithic caves. *PLoS ONE* **2021**, *16*, e0250497. [CrossRef] [PubMed]
3. CIE. *Control of Damage to Museum Objects by Optical Radiation*; CIE 157-2004: Vienna Austria, 2004.
4. Cuttle, C. Damage to museum objects due to light exposure. *Int. J. Light. Res. Technol.* **1996**, *28*, 1–9. [CrossRef]
5. Nakagoshi, K.; Yoshizumi, K. Degradation of Japanese Lacquer under Wavelength Sensitivity of Light Radiation. *Mater. Sci. Appl.* **2011**, *2*, 1507–1515. [CrossRef]
6. Pérez, M.; Cano, N.; Ruvalcaba-Sil, J.L.; Mitrani, A.; de Lucio, O.G. Technical Non-Invasive Study of an 18th Century Novo-Hispanic Panel Painting. *Heritage* **2021**, *4*, 3676–3696. [CrossRef]
7. Durmus, D. Characterizing Color Quality, Damage to Artwork, and Light Intensity of Multi-Primary LEDs for Museums. *Heritage* **2021**, *4*, 188–197. [CrossRef]

Review

Virtual Restoration and Visualization Changes through Light: A Review

Ángela Gómez Manzanares ^{1,*}, Anto J. Benítez ²  and Juan Carlos Martínez Antón ¹

¹ Department of Optics, University Complutense of Madrid, 28040 Madrid, Spain; jcmartin@ucm.es

² Department of Communication. University Carlos III of Madrid, 28903 Madrid, Spain; abenitez@hum.uc3m.es

* Correspondence: anggomez@ucm.es

Received: 15 October 2020; Accepted: 13 November 2020; Published: 17 November 2020

Abstract: The virtual modification of the appearance of an object using lighting technologies has become very important in recent years, since the projection of light on an object allows us to alter its appearance in a virtual and reversible way. Considering the limitation of non-contact when analysing a work of art, these optical techniques have been used in fields of restoration of cultural heritage, allowing us to visualize the work as it was conceived by its author, after a process of acquisition and treatment of the image. Furthermore, the technique of altering the appearance of objects through the projection of light has been used in projects with artistic or even educational purposes. This review has treated the main studies of light projection as a technique to alter the appearance of objects, emphasizing the calibration methods used in each study, taking into account the importance of a correct calibration between devices to carry out this technology. In addition, since the described technique consists of projecting light, and one of the applications is related to cultural heritage, those studies that carry out the design and optimization of lighting systems will be described for a correct appreciation of the works of art, without altering its state of conservation.

Keywords: projection mapping; calibration; lighting; cultural heritage

1. Introduction

The colour and appearance of an object depend on the physical and chemical properties of the object itself, the source of visible electromagnetic energy that illuminates it, and the observer who detects the energy reflected by the object [1]. Taking into account these three factors, it is possible to think that by projecting adequate lighting on an object, its appearance could be altered.

From this idea, the term Mixed Reality arises, in order to alter the perception of reality including virtual content. Milgram and Kishino defined the concept of mixed reality as a subset of the technologies related to virtual reality, which includes Augmented Reality (AR) and Augmented Virtuality (AV). Thus, they defined Milgram's Reality–Virtuality Continuum (Figure 1), which is a line on which the virtual space is located at one end, real space at the other, and AR and AV in the center. AR was defined by Milgram and Kishino as the technology that improves the visualization of a real environment through virtual objects and AV was defined as the opposite of AR. Therefore, in Figure 1, AR is closer to reality and AV closer to virtuality [2].

Taking these factors into account, it is possible to think that by projecting adequate lighting on an object, its appearance could be altered in a virtual and therefore reversible way. Thereby, the technique of Spatial Augmented Reality (SAR) or projection mapping arises, which uses optical elements and video projectors, holograms, radio frequency labels and other tracking technologies to display virtual information directly on an object altering their appearance [3–5].

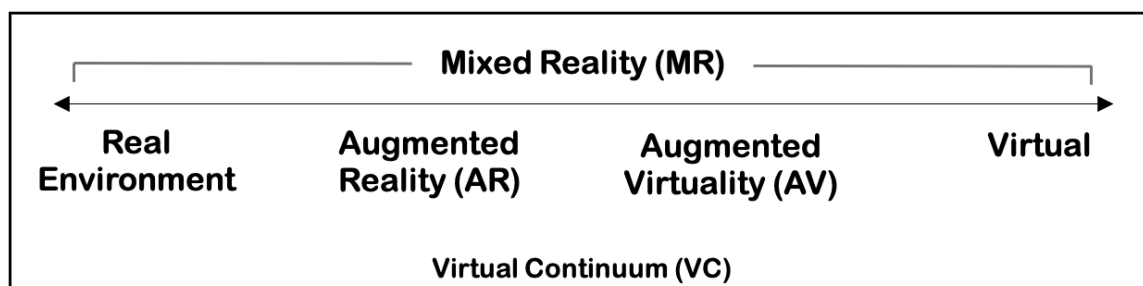


Figure 1. Milgram's Reality–Virtuality Continuum [2].

Azuma, in 1997, completed the definition of Milgram and Kishino, defining AR as 'a technology that allows the user to see the real world, with virtual objects superimposed or compounded with the real world' [6].

In recent years, AR has become more important in fields such as education, entertainment, conservation, restoration and adequate exhibition of cultural heritage, among others [3,7].

The projection mapping technique uses cameras to capture the object to be illuminated and projectors to project the desired image onto the object. It has the advantage over other AR techniques that it doesn't require viewers to use any type of glasses or instrument to appreciate the effect, allowing multiple users to appreciate the effects of projection mapping technology at the same time [5].

Section 2 of this article collects those studies which use the projection mapping technique in order to alter the appearance of an object, with special emphasis on those studies that use the technique as a method of displaying cultural heritage.

For the development of the projection mapping technique, a meticulous calibration method is required that allows adequate synchronization between the instruments used. Then, it is necessary that the image be correctly located on the object, avoiding unwanted effects. Section 3 of this article lists the main calibration techniques used in projection mapping in recent years.

The complexity of implementing this technique in the field of conservation of cultural heritage objects consists in the development of a lighting system that allows a safe display of the artwork without producing alterations in its appearance with respect to when it was made by the artist. This is due to the photochemical and thermal effect of light, causing degradation of the materials it illuminates. Section 4 of this article collects the most significant techniques to address this difficulty.

2. Projection Mapping Applications

The ability of the projection mapping technique to alter the appearance of an object by projecting light on it has made its applications more and more common every day, as shown in Figure 2. Under the name of Shader Lamps, Raskar in 2001 introduced the idea of animating white objects without texture by projecting different graphic images on them, altering the appearance of these objects by varying their perception of colour and texture [8].

Amano, by means of superimposed projection, altered the appearance of contrast in real objects that already had their own colourimetric and texture properties [9].

In Wang et al. (2010), the concept of context-aware light source was introduced, defined by them as 'a light source that can modify its lighting depending on the sensor information obtained from the scene'. It is a projection mapping application, which works by means of the previous acquisition of the information of the scene by a camera, so that after the appropriate image treatment, the improvements are shown on the object through a projector. In this way, it allows improving the appearance of an object in real time, even if the user manipulates it. From a context-aware light source, they developed the concept of proxy light, designing a portable instrument which, as if it were a common flashlight, allows the user to illuminate the areas of the object they want, appreciating parts of the object that are not perceptible to the naked eye by humans. This instrument is a very valuable tool for museumgoers, archaeologists, and art restorers [10].

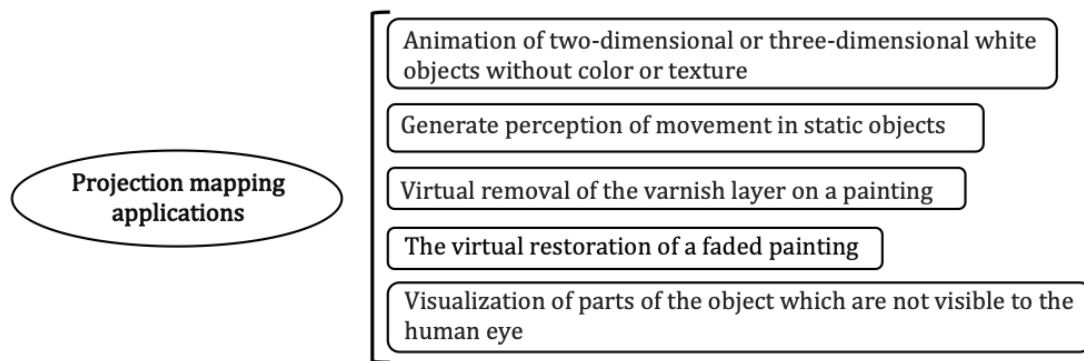


Figure 2. Outstanding applications of the projection mapping technique.

Later, in 2014, Revealing Flashlight emerged. It is an instrument that, like the one described by Wang et al., allows users to visualize hidden parts of an object. Wang et al.'s instrument works in real time, so it is limited by the camera resolution and 2D image processing, Revealing Flashlight performs 3D object pre-analysis, then the displayed images are not limited by the camera resolution or by analysis time, thus allowing a more detailed visualization of the object, obtaining the results shown in Figure 3 [11].

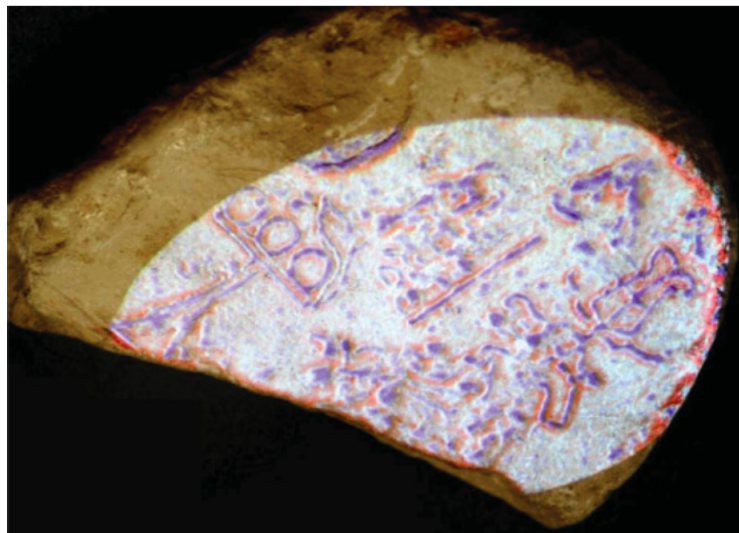


Figure 3. Image proposed by Ridet et al. [11] where the result is shown after illuminating a cultural artifact with the Revealing Flashlight technique.

Both Punpongsanon et al. and Kawabe et al. used the projection mapping technique in combination with psychophysical studies to alter the perception of movement through lighting [12,13]. Kawabe et al. developed a technique called Deformation Lamps to achieve the perception of the movement of objects while maintaining their original colour and texture [12]. Punpongsanon et al. used the mapping projection technique to alter the perception of bending stiffness of a fabric [13].

Among the applications mentioned above, the application related to the conservation and exhibition of cultural heritage objects will be described in more depth.

Some artworks have had their appearance affected due to the action of external agents, such as non-optimal humidity/temperature conditions or the incidence of electromagnetic radiation from the sun or different sources of artificial light over their years of exposure [14–16]. A restoration by a classical method can then be complicated. However, by means of the projection mapping technique, a restored vision of the artwork can be obtained by projecting an image on it, called in many studies the compensation image.

Lafontaine presented the precursor of this technique in 1986: he developed a projection technique by which an artwork can be visualized without affecting the yellowing that occurs in its varnish with the incidence of electromagnetic radiation on it [17].

The projection mapping technique was used in 2005 by Peral to virtually restore the appearance of the portico of Saint Mary's Cathedral in Vitoria (Spain) [18].

Aliaga et al. (2008) presented a technique to restore deteriorated objects by projecting light with multiple overlapping projectors. They proposed an interactive restoration algorithm, in which users could select those points they want to restore in a captured image. Then, using a restoration algorithm, one could obtain the compensation image and thus project it onto the object [19].

Aleksić and Jovanović used the virtual restoration technique through projection mapping to obtain a restored view of Lazar Vozarević's *Untitled* from 1961. To do this, they were inspired by the technique developed by Stenger in restoring Mark Rothko's murals, since both artists used very similar chemical compositions for the development of their work. But unlike Stenger's work, Vozarević's work has a three-dimensional geometry, requiring a different restoration technique [20].

Recently, Vázquez et al. (2020) presented a method of restoring artworks by projecting light point by point, characterized by the previously acquired spectral reflectance of the artwork. For their procedure, they used a photograph of Sorolla's *Walk on the Beach* that was previously artificially aged using a Matlab algorithm, as shown in Figure 4 [21].

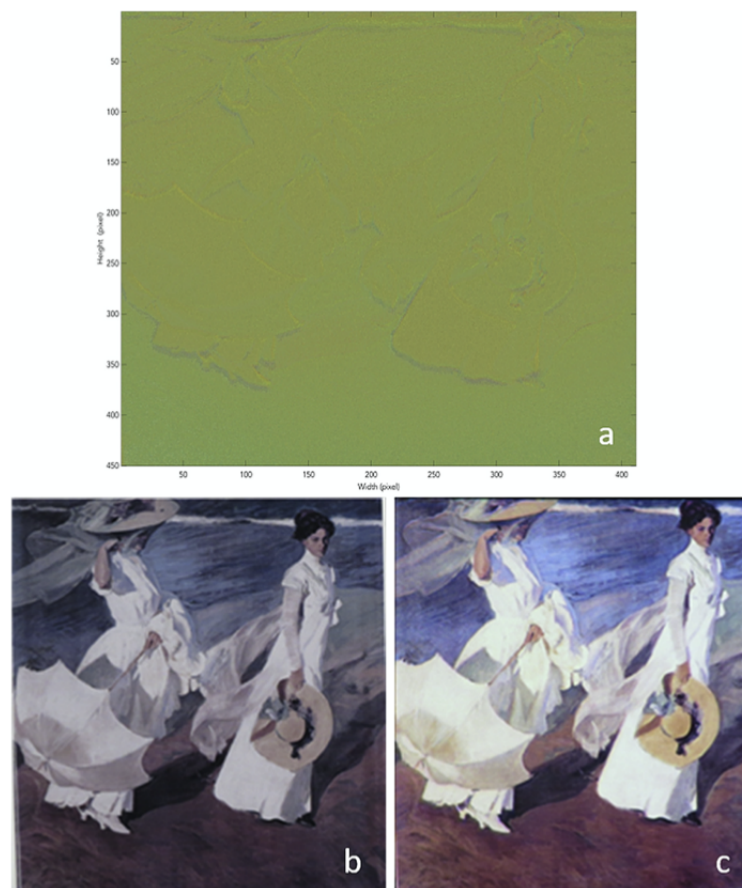


Figure 4. Images proposed by Vázquez et al. [21] where it is shown: (a) RGB color matrix that will be projected onto the aged image to compensate for the aged appearance of the artwork. (b) Photograph of Sorolla's *Walk on the Beach* artificially aged. (c) Photograph of Sorolla's *Walk on the Beach* after virtual restoration process.

3. Calibration

Projection mapping systems use at least one camera and one projector, so that the camera can detect and adjust the image from the projector [5]. In order for an image projected onto the real object to be properly visualized, a series of geometric and photometric calibration algorithms are required [5]. This section shows the evolution of the calibration algorithms designed for projection mapping projects (Figure 5).

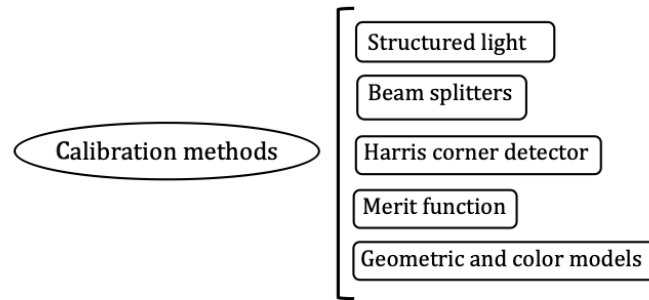


Figure 5. Calibration methods used in the studies shown in this review article.

The technique of Aliaga et al. initially consisted of acquiring a geometric model of the object to be restored and the proper calibration of the projectors based on the self-calibration method they described in [19,22]. Subsequently, the image of the object was captured and restored using an interactive energy minimization algorithm. Finally, the projection image that would be projected onto the object was calculated [19].

They obtained a self-calibrated structured light method allowing data processing from multiple points of view, being able to obtain a 3D object reconstruction. For the correspondence between the pixels they exploited the duality of cameras and projectors [22].

For the development of Revealing Flashlight, Ridet et al. used the calibration method that Audet et al. had proposed in 2010 [11,23]. Audet et al. had developed an alignment algorithm between camera, object and projector [23]. In their method, they described two models, a geometric model and a colour model, through which the necessary information can be obtained to predict how the image projected on the camera sensor is formed. They were based on the pinhole camera model to obtain Equations (1) and (2), which define the projection in the image plane of a camera placed at the origin and a calibrated projector, respectively, for a point x_3 located in the plane of the surface [23].

$$x_c = K_c(Ix_3 + 0), \quad (1)$$

$$x_p = K_p(R_px_3 + t_p), \quad (2)$$

where K is the camera matrix, which contains the internal or intrinsic projective parameters, and where R and t are parameters that shape the orientation and position of the devices [23].

They developed a colour model so that the system could be easily calibrated without camera control with a single projector and flat surface (Figure 6). For this, they formulated Equation (3), which allows predicting the colour information that the camera will observe (p_c) knowing the colour emitted by the projector (p_p) and the reflectance emitted on the surface (p_s).

$$p_c = p_s[gX_{3 \times 3}p_p + a] + b, \quad (3)$$

where g is the gain of the projector light; X is the colour mixing matrix; a , the ambient light; and b , the noise bias of the camera. All vectors are three-vectors in the RGB colour space [23].

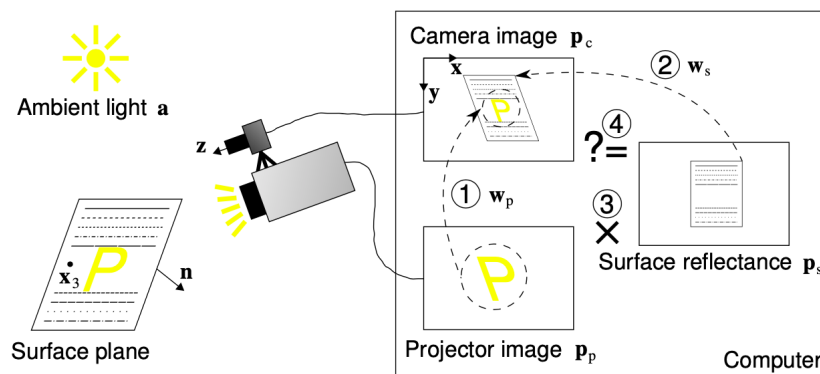


Figure 6. Sketch proposed by Audet et al. [23] where the calibration method used is shown.

In order to use the models correctly, they developed a calibration algorithm to obtain the geometric parameters (K_c , K_p , R_p and t_p) and the colour parameters (X and b). To do this, through Equations (1) and (2) that define the geometric model and a homography (H), they developed the warping functions, which relate a point of the image in the camera with a point of the projector and a point from the camera image x_c with the point x_s of the surface plane image [23].

$$w_p(x_c) = H_{pc}x_c, \quad (4)$$

$$w_s(x_c) = H_{sc}x_c. \quad (5)$$

Finally, the equations are entered into the Equation (3) to obtain the colour of the pixels at the camera point x_c , as shown in Equation (6).

$$p_c(x_c) = p_s(w_s(x_c))x[gXp_p(w_p(x_c)) + a] + b. \quad (6)$$

Once the calibration that provides us with the necessary parameters of the colour and geometric models was developed, they developed a cost function and its minimization function to optimize the system towards correct alignment [23].

Wang et al. (2010) established the alignment between the camera and the projector through a beam splitter, which allowed the light signal to be divided so that the same signal was perceived by the projector and the camera regardless of the detection distance. By performing this synchronization between the camera and the projector, a feedback effect was produced since the projected signal was part of the scene to be detected by the camera sensor. To avoid this phenomenon, the projector emitted in the visible range and the camera detector only detected IR wavelengths, thus preventing the virtual image from interfering with the projection of the following table [10].

Stenger et al. needed to develop a calibration system whereby the compensation image projected onto Mark Rothko's murals was displayed correctly. To do this, they first used the Matlab's control point selection tool to generate a geometric transformation and thus adjust the resolution of the target image and the current image of the artwork. Then, a lighting matrix with the levels of the three equal RGB channels was projected onto the work, in order to create a calibration curve for each channel. These calibration curves together with the colour mixing matrix, created to compensate the dependence of the channels on each other, created a suitable compensation image. In order for the compensation image to be positioned in the correct position relative to the illustration, a very irregular calibration image was projected onto the illustration and an image was captured. Then a Harris corner detector related corresponding points on the captured image and the calibration image. Using these points, a pattern was created in order to make the corresponding geometric transformation. Finally, by means of a RANSAC algorithm, outliers were eliminated, through an iterative non-linear fitting procedure [24].

Deformation Lamps tries to achieve the illusion of the perception of movements in objects by projecting an optimized light pattern on them. To do this, Kawabe et al. (2016) described an algorithm that consisted of defining a dynamic image sequence in order to project it onto a static object, thus achieving the perception of movement on the object.

To obtain this sequence of colour images, it was assumed that an image sequence, I_{movie} , can be calculated as a linear combination of a static colour picture I_{static} and a dynamic grayscale image sequence $I_{luminancedynamic}$ [12].

$$I_{movie}(x, y, t) \approx I_{static}(x, y) + I_{luminancedynamic}(x, y, t), \quad (7)$$

Finally, by means of Equation (8), the dynamic luminance is calculated, which by means of Equation (9) is projected onto the image, w being the factor that modulates the contrast of the dynamic component of the image and B is an arbitrary gray background so as not to take values below 0.

$$I_{luminancedynamic}(x, y, t) = I_{luminancedynamic}(x, y, t) - I_{luminancedynamic}(x, y) \quad (8)$$

$$P(x, y, t) = wI_{luminancedynamic}(x, y, t) + B \quad (9)$$

For the deformation lamps method, Kawabe et al. used a manual alignment between the projector and the object, since for this method on 2D objects, no specific calibration is needed to obtain the visual effect they were looking for [12].

In Aleksić and Jovanović (2018), instead of using an algorithm yielding a real-time compensation image, a meticulous analysis of the artwork was carried out in order to be able to restore it digitally. This procedure was performed at the discretion of restoration professionals and then projected onto the work under controlled lighting conditions. For the alignment between the projected image and the actual artwork, the curvature of the image projection (curvilinear projection) as well as the perspective distortion were determined. The compensation images were projected at an angle and this perspective generated certain distortions of the image. In order for the compensation image to geometrically match the painting surface, the projection image curvature and perspective-generated distortion were determined so that the resulting image geometrically coincided with the surface of the artwork [20].

Vázquez et al. (2020) calibrated the projector to emit the corresponding lighting onto the work through a calibration algorithm and a merit function. Since the spectral power distribution of the projector (SPD) calculated is not the same as the real spectral emission of the projector (D_{PK}), an algorithm was developed that relates both distributions through the Z factor. The purpose of the merit function is to minimize the colour difference (ΔE_{00}^*) between the original and the restored artwork. The ΔE_{00}^* was calculated with CIEDE200. To eliminate distortions between the camera, the projector and the printed image, a T transformation is developed through the Matlab image processing toolbox [21]. Finally, the method of correspondence between pairs of images of Vincent and Laganier (2005) was used for the alignment between the projected image and the printed image [21,25].

4. Lighting

Cultural heritage objects must be exhibited for their appreciation, but inadequate temperature and lighting conditions can cause their deterioration [14,15,26]. Generating yellowing, discoloration or colour variation, corrosion, alteration and corruption, increase in surface temperature, and acceleration of deterioration on works of art [16]. This section reviews the main studies related to the lighting of artworks.

The damage caused by the emission of UV and IR radiation is controlled by filters or LED sources, but the radiation emitted by the visible range of the electromagnetic spectrum is necessary for the appreciation of the artwork and at the same time could produce irreparable damage to it [15]. The International Commission on Illumination (CIE) differentiates between the damage caused by the photochemical effect on different pigments and the damage due to the thermal action of light [26].

Photochemical damage is produced when a photon is absorbed by a pigment, causing the chemical properties of this pigment to change, manifested in artworks as changes in the mechanical properties of the pigments or in their colour [14]. The damage caused by thermal action, according to the CIE, has been more ignored in museums, since the damage has not been as visible as in the case of damage by photochemical action. Elena Lucchi (2016) evaluated the energy and environmental quality of museums, based on 50 European institutions. The result was that light is the most important environmental parameter in museums because it is directly related to the preventive conservation of works of art and to the comfort of viewers [27]. As the control of photochemical damage in museums has gained importance, so has the control of damage by the thermal action of light, taking into account that an increase in temperature favours chemical action at the molecular level in the different pigments [26,28–30]. Recently, a process to minimize the risk of deterioration in multifunctional historic buildings has been developed. It puts forward the profitability associated with the lighting parameters optimization in order to avoid damage to the cultural heritage shown in the exhibition [31].

The CIE made recommendation 157: 2004 to regulate the damage caused by photochemical action and the effects of thermal radiation of light on the different artworks exhibited in museums. Knowing that not all materials respond in the same way to the harmful effects of visible radiation, the CIE established, in its regulations, maximum irradiance limits and a defined exposure time to illuminate artworks, depending on the sensitivity to light radiation of the materials that constitute the artwork [26,28]. Mayorga et al. (2015) introduced the concept of Global Risk Factor (GRF), presenting a system for quantifying the damage produced by natural light, so that it could be used as the main or secondary source, minimizing the intrinsic risks it carries and using its advantages in lighting such as its ability to save energy, non-polluting, renewable source, psychological comfort, circadian cycle, and colour reproduction [32].

In addition to taking into account the damage due to radiation in museum exposures, it is important that the source used does not produce distortions in the perception of the artwork. For this, the colour rendering index (CRI) is usually used, which defines the colour reproduction capacity of a light source [26].

Even so, not all pigments used in an artwork respond in the same way to the effects of radiation, and not in a linear way [15]. This section reviews the main techniques developed for lighting in museums, which, in addition to protecting artworks from the effects of light, allow us to correctly appreciate them.

Historically, incandescent or fluorescent lighting was responsible for lighting in museums [15,33], however, in recent years, LED lighting has become very important for this application. LEDs offer great advantages, such as compactness, long useful life, adjustable intensity [33] and absence of radiation in the ultraviolet range and infrared range [33,34]. In addition, the radiation in the visible spectrum is reduced compared to continuous spectrum emission [34], their surface temperature rarely exceeds 50 °C, allowing them to be placed near wooden objects [14]. In recent years, LED technology has gained higher luminous efficiency, and by combining it with phosphors, it is easy to optimize the spectrum for the desired application [33].

Delgado et al. (2010) presented an optimization strategy applied to improve the luminous efficiency of a light source to illuminate artworks, excluding the part of the visible spectrum that does not contribute to the adequate perception of the illuminated object [35].

Berns et al. (2011) optimized a simulated triband light source made up of three LEDs with the fundamental objective of illuminating without causing damage to the artwork and producing the same colour rendering as the D65 illuminant, which is usually used as a reference in simulations due to its similarity to daylight. To this end, they performed four simulations using the emission of LEDs with bandwidths of 25 nm, 50 nm, 75 nm and 100 nm. The LEDs with bandwidths of 50, 75 and 100 nm provided emissions almost identical to D65, and the LED with a bandwidth of 25 nm had its efficiency improved by combining it with LEDs of greater bandwidth, obtaining very favourable results of ΔE , colour reproduction and luminous efficacy, these being 1.2 ΔE_{94}^* , 92 CRI, and 325 lm/W,

respectively. The $1.2 \Delta E_{94}^*$ is imperceptible to the human eye in lighting conditions between 50 and 200 lux [34].

Furthermore, Berns (2011) developed an optimization algorithm capable of increasing or decreasing chroma depending on the demands of the artwork. On the one hand, an increase in chroma would make it possible to compensate for the lack of colour, respecting in any case the artist's intention. On the other hand, works exhibited in caves or churches must maintain their low chroma status since they were conceived that way [34].

Using an optimized white LED illumination obtained through the combination of different LEDs, Vienot et al. (2011) recreated the appearance of a bird specimen. They were able to intensify the saturation of faded colours by taking advantage of the distortions caused by narrow-band LED lighting [33].

Durmus and Davis (2015a) developed a lighting system with an optimized emission spectrum in order to produce energy savings without altering the appearance of the illuminated object. To do this, they started from the idea of dispensing with the emissions at those wavelengths absorbed by the object, designing a lighting system tuned by detectors with the reflectance of the objects, emitting fundamentally at the wavelengths reflected by the object and perceptible by the human eye. In this way, they managed to develop a lighting system through which an energy savings of 44% can be obtained and without appreciable changes for the human eye in the appearance of the object, with low values of ΔE_{ab}^* calculated in the CIE 1976 colour space $L^* a^* b^*$ [36].

Durmus and Davis (2015b) further perfected that technique by implementing added bandwidths of the order of 10 nm to the peaks of the selected emission spectrum, obtaining energy savings of between 55% and 71% maintaining low values of ΔE_{ab}^* [37].

Mayorga et al. (2016) analysed how lighting affects 23 different pigments in order to develop a system to measure the spectral response of exposed materials. This system allowed estimating the time and the maximum irradiance with which a artwork can be illuminated without noticeable changes in its colour [38].

Stenger (2015) based the lighting of Mark Rothko's murals on the limitation established by the CIE of an illuminance of less than 50 lux, restricting UV and IR radiation [26], since, in addition, one of the artist's requirements was that the artwork not be too illuminated [24].

Taking into account the need to develop a lighting system capable of displaying artworks without causing damage to them, the Zeus project emerged. It has been mainly promoted by scientists from the Complutense University of Madrid. This project also includes institutions involved in the conservation and dissemination of cultural heritage objects and researchers in Communication and Audiovisual Technology. Among other strategies related to the analysis of artworks for their correct conservation and visualization, the Zeus project developed a selective lighting system that calculates the appropriate light distribution point by point based on the characteristics of the artwork [30].

Durmus et al. (2018) designed an optimized lighting system by which the reflectance of the artworks was obtained in order to be able to project onto them an illumination capable of reducing photochemical damage due to spectral absorption of radiation in the pigments used based on the reflectance spectrum of the pigments. In this development, it was essential not to affect the appearance of the objects so as not to alter the intention of the artist. To this end, they used multi-objective genetic optimization algorithms (MOGA). Genetic algorithms (GAs) are based on the theory of evolution, where, starting from a wide range of species, only those suitable survive, the rest facing extinction. The MOGAs, unlike the GA, allow a greater number of solutions by defining an aptitude function that evaluates the solutions at each step, thus generating more precise solutions. Considering that when using a visible spectrum light source, visibility and damage conflict, they used MOGA optimization algorithms since by themselves they can produce more than one result that does not allow the optimal solution. Therefore, it was essential to use Pareto's optimal solution technique, which was responsible for selecting alternatives when there is no single optimal solution, allowing obtaining an optimized lighting source to minimize absorption damage without causing a notable damage to the colour of the artwork [29].

Carla Balocco and Giulia Volante set out a methodology for sustainable cultural heritage lighting that not only complied with the regulations for the correct conservation and protection of works of art, but also provided visual and perception comfort from the point of view of observer reducing the power consumption of the light source. Thus, they carried out a study to illuminate those areas of interest of the work of art by analyzing the eye movements of a series of subjects when viewing it [39].

Muñoz De Luna, in his doctoral thesis published in 2017, developed a point-by-point spectral reflectance measurement system using non-contact spectrophotometers in order to subsequently carry out a colourmetric analysis of the artworks that allows a temporal monitoring of these in an objective. This system was applied to study the following works of Pablo Picasso: *Guernica* and *Woman in Blue*. Using Michiel Sweert's *Boy with a Turban and Corsage*, he carried out a comparative study of the colourimetric values of the artwork, illuminating it using the illuminants that the CIE defines as standard illuminant, finding in certain areas of the work, appreciable colour differences for human perception. Finally, using the reflectance measurement technique previously described and the knowledge of how the different illuminants affect the conservation and appreciation of an artwork, there was studied the lighting used for the cave paintings of the cave of *El Castillo* in Puente Viesgo (Cantabria). To this end, an LED lighting system was developed using a minimum optimization algorithm that allowed the emission of an optimal spectral distribution in terms of minimal deterioration, maximum contrast between the colour stimulus and the background, and minimum chromatic difference between the observed painting under the light used by the artist and observed with the developed illuminant [28].

The lighting system developed by Vázquez et al. (2020) for projecting onto artworks was optimized to minimize radiation damage, while also producing a restored appearance of the art [21]. With the information from the CIE Lab coordinates and reflectance information, they developed a merit function based on Fernandez-Balbuena et al. [40] to optimize the ΔE_{00}^* between the D65 reference and test illuminant. A second merit function was developed in order to minimize the radiation damage through the concept of GRF, developed by Mayorga et al. [32,38]. Using the optimization algorithm, based on Durmus and Davis [36,37] and Muñoz De Luna [28] described above, and the lighting system described by the Zeus Project [30], they calculated the optimal SPD and the intensity of each point in the image [21].

Rui Dang et al. proposed a method of quantifying damage taking the type of paint, the level of illuminance and the exposure time as three variable units, thus allowing to optimize lighting systems in a much more precise way. They found that some works of art allow higher levels of illuminance than those set by the regulations, thus achieving an improved visualization by the viewer [41].

5. Conclusions

This review article has treated the main studies that have been carried out in recent years that use the projection mapping technique. Its purpose has been to provide the necessary help related to the calibration and lighting processes that may be required in future applications.

In the section on calibration techniques, different viable methods have been described to achieve the alignment between camera and projector, such as the structured light method [10,22], the beam splitter method [10], and the use of the Harris corner detector [24]. Furthermore, in many of the studies, different limitations have been taken into account, such as feedback, or the minimization of ΔE in virtual restoration applications, proposing in both cases suitable solutions.

When using the projection mapping technique, attention must be paid to adequate lighting conditions, especially in those applications related to the exhibition and conservation of cultural heritage objects. For this reason, in the fourth section of this article, there have been reviewed the main lighting optimization studies whose aim is to minimize the change in appearance of the illuminated surface while reducing the harmful effects of radiation.

Author Contributions: Conceptualization, Á.G.M; Methodology, Á.G.M. and J.C.M.A.; Validation, Á.G.M, J.C.M.A. and A.J.B., Formal Analysis, Á.G.M; Investigation, Á.G.M; Data Curation, Á.G.M; Writing—Original Draft Preparation, Á.G.M; Writing—Review & Editing, J.C.M.A. and A.J.B.; Visualization, Á.G.M; Supervision,

Á.G.M.; Project Administration, Á.G.M.; Funding Acquisition, Á.G.M. All authors have read and agreed to the published version of the manuscript.

Funding: This work has been funded by project number RTI2018-097633-A-I00 of the Ministry of Science and Innovation of Spain, entitled 'Photonic restoration applied to cultural heritage: Application to Dali's painting: *Two Figures*.'

Conflicts of Interest: The authors declare no conflict of interest. The funders had no role in the design of the study; in the collection, analyses, or interpretation of data; in the writing of the manuscript, or in the decision to publish the results.

References

1. Fairchild, M.D. *Color Appearance Models*; John Wiley & Sons: Hoboken, NJ, USA, 2013.
2. Milgram, P.; Kishino, F. A taxonomy of mixed reality visual displays. *IEICE Trans. Inf. Syst.* **1994**, *77*, 1321–1329.
3. Bimber, O.; Raskar, R. *Spatial Augmented Reality: Merging Real and Virtual Worlds*; CRC Press: Boca Raton, FL, USA, 2005.
4. Carmigniani, J.; Furht, B.; Anisetti, M.; Ceravolo, P.; Damiani, E.; Ivkovic, M. Augmented reality technologies, systems and applications. *Multimed. Tools Appl.* **2011**, *51*, 341–377. [CrossRef]
5. Grundhöfer, A.; Iwai, D. Recent advances in projection mapping algorithms, hardware and applications. *Comput. Graph. Forum* **2018**, *37*, 653–675. [CrossRef]
6. Azuma, R.T. A survey of augmented reality. *Presence Teleoperators Virtual Environ.* **1997**, *6*, 355–385. [CrossRef]
7. Bekele, M.K.; Pierdicca, R.; Frontoni, E.; Malinverni, E.S.; Gain, J. A survey of augmented, virtual, and mixed reality for cultural heritage. *J. Comput. Cult. Herit. (JOCCH)* **2018**, *11*, 1–36. [CrossRef]
8. Raskar, R.; Welch, G.; Low, K.L.; Bandyopadhyay, D. Shader lamps: Animating real objects with image-based illumination. In *Rendering Techniques 2001*; Springer: Vienna, Austria, 2001; pp. 89–102.
9. Amano, T. Projection based real-time material appearance manipulation. In Proceedings of the IEEE Conference on Computer Vision and Pattern Recognition Workshops, Portland, OR, USA, 23–28 June 2013; pp. 918–923.
10. Wang, O.; Fuchs, M.; Fuchs, C.; Lensch, H.P.; Davis, J.; Seidel, H.P. A context-aware light source. In Proceedings of the 2010 IEEE international conference on computational photography (ICCP), Cambridge, MA, USA, 29–30 March 2010; pp. 1–8.
11. Ridet, B.; Reuter, P.; Laviolle, J.; Mellado, N.; Couture, N.; Granier, X. The Revealing Flashlight: Interactive Spatial Augmented Reality for Detail Exploration of Cultural Heritage Artifacts. *J. Comput. Cult. Herit.* **2014**, *7*, 1–18. [CrossRef]
12. Kawabe, T.; Fukiage, T.; Sawayama, M.; Nishida, S. Deformation lamps: A projection technique to make static objects perceptually dynamic. *ACM Trans. Appl. Percept. (TAP)* **2016**, *13*, 1–17. [CrossRef]
13. Punpongsonan, P.; Iwai, D.; Sato, K. Flexeen: Visually manipulating perceived fabric bending stiffness in spatial augmented reality. *IEEE Trans. Vis. Comput. Graph.* **2018**. [CrossRef]
14. Camuffo, D. *Microclimate for Cultural Heritage: Measurement, Risk Assessment, Conservation, Restoration, and Maintenance of Indoor and Outdoor Monuments*; Elsevier: Amsterdam, The Netherlands, 2019.
15. Thomson, G. *The Museum Environment*; Elsevier: Amsterdam, The Netherlands, 2013.
16. Lucchi, E. Review of preventive conservation in museum buildings. *J. Cult. Herit.* **2018**, *29*, 180–193. [CrossRef]
17. Lafontaine, R.H. Seeing through a Yellow Varnish: A Compensating Illumination System. *Stud. Conserv.* **1986**, *31*, 97. [CrossRef]
18. Peral, R.; Sagasti, D.; Sillaurren, S. Virtual restoration of cultural heritage through real-time 3d models projection. In Proceedings of the VAST 2005: The 6th International Symposium on Virtual Reality, Archaeology and Intelligent Cultural Heritage, Pisa, Italy, 8–11 November 2005.
19. Aliaga, D.G.; Law, A.J.; Yeung, Y.H. A virtual restoration stage for real-world objects. *ACM Siggraph Asia* **2008**, *27*, 1–10. [CrossRef]
20. Aleksić, M.; Jovanović, V. Non-physical Painting Restoration in Improved Reality. In *International Conference on VR Technologies in Cultural Heritage*; Springer: Brasov, Romania, 2018; pp. 206–214.
21. Vázquez, D.; Fernández-Balbuena, A.Á.; Canabal, H.; Muro, C.; Durmus, D.; Davis, W.; Benítez, A.; Mayorga, S. Energy optimization of a light projection system for buildings that virtually restores artworks. *Digit. Appl. Archaeol. Cult. Herit.* **2020**, *16*, e00128. [CrossRef]

22. Aliaga, D.G.; Xu, Y. Photogeometric structured light: A self-calibrating and multi-viewpoint framework for accurate 3d modeling. In Proceedings of the 2008 IEEE Conference on Computer Vision and Pattern Recognition, Anchorage, AK, USA, 23–28 June 2008; pp. 1–8.
23. Audet, S.; Okutomi, M.; Tanaka, M. Direct image alignment of projector-camera systems with planar surfaces. In Proceedings of the 2010 IEEE Computer Society Conference on Computer Vision and Pattern Recognition, San Francisco, CA, USA, 13–18 June 2010; pp. 303–310.
24. Stenger, J.; Khandekar, N.; Raskar, R.; Cuellar, S.; Mohan, A.; Gschwind, R. Conservation of a room: A treatment proposal for Mark Rothko’s Harvard Murals. *Stud. Conserv.* **2016**, *61*, 348–361. [CrossRef]
25. Vincent, E.; Laganière, R. Detecting and matching feature points. *J. Vis. Commun. Image Represent.* **2005**, *16*, 38–54. [CrossRef]
26. CIE 157: 2004. *Control of Damage to Museum Objects by Optical Radiation*; Commission Internationale de l’Éclairage: Vienna, Austria, 2004.
27. Lucchi, E. Simplified assessment method for environmental and energy quality in museum buildings. *Energy Build.* **2016**, *117*, 216–229. [CrossRef]
28. Muñoz de Luna Clemente, J. *Sistemas de Iluminación de Altas Prestaciones Aplicados a Bienes de Interés Cultural*. Ph.D. Thesis, Universidad Complutense de Madrid, Madrid, Spain, 2016.
29. Durmus, D.; Abdalla, D.; Duis, A.; Davis, W. Spectral Optimization to Minimize Light Absorbed by Artwork. *Leukos* **2018**, *16*, 45–54. [CrossRef]
30. Benítez, A.J.; Vázquez, D.; Fernández-Balbuena, A.Á. Iluminar obras de arte mejorando la conservación. Proyecto Zeus. *Opción* **2016**, *32*, 196–214.
31. Lucchi, E. Environmental Risk Management for Museums in Historic Buildings through an Innovative Approach: A Case Study of the Pinacoteca di Brera in Milan (Italy). *Sustainability* **2020**, *12*, 5155. [CrossRef]
32. Mayorga, S.; Vázquez, D.; Fernández-Balbuena, A.Á.; Raboso, G.H.; Herráez, J.A.; Azcutia, M.; Botella, Á.G. Advanced daylighting evaluation applied to cultural heritage buildings and museums: Application to the cloister of Santa Maria El Paular. *Renew. Energy* **2016**, *85*, 1362–1370. [CrossRef]
33. Viénot, F.; Coron, G.; Lavédrine, B. LEDs as a tool to enhance faded colours of museums artefacts. *J. Cult. Herit.* **2011**, *12*, 431–440. [CrossRef]
34. Berns, R.S. Designing white-light LED lighting for the display of art: A feasibility study. *Color Res. Appl.* **2011**, *36*, 324–334. [CrossRef]
35. Delgado, M.F.; Dirk, C.W.; Druzik, J.; WestFall, N. Lighting the world’s treasures: Approaches to safer museum lighting. *Color Res. Appl.* **2011**, *36*, 238–254. [CrossRef]
36. Durmus, D.; Davis, W. Optimising light source spectrum for object reflectance. *Opt. Express* **2015**, *23*, A456. [CrossRef] [PubMed]
37. Durmus, D.; Davis, W. Absorption-minimizing spectral power distributions. In *Light, Energy and the Environment*; Optical Society of America: Sydney, Australia, 2015; p. JTU5A.2. [CrossRef]
38. Mayorga, S.; Vázquez, D.; Fernández-Balbuena, A.Á.; Muro, C.; Muñoz, J. Spectral damage model for lighted museum paintings: Oil, acrylic and gouache. *J. Cult. Herit.* **2016**, *22*, 931–939. [CrossRef]
39. Balocco, C.; Volante, G. Lighting design for energy sustainability, information, and perception. A museum environment as a case study. *Sustainability* **2018**, *10*, 1671. [CrossRef]
40. Fernández-Balbuena, A.Á.; Montes, M.G.; Botella, Á.G.; Vázquez, D. Application of dynamic merit function to nonimaging systems optimization. *Opt. Eng.* **2015**, *54*, 025107. [CrossRef]
41. Dang, R.; Liu, R.; Luo, T. Lighting quantity indexes for lighting paintings in museums. *Build. Environ.* **2020**, *182*, 107142. [CrossRef]

Publisher’s Note: MDPI stays neutral with regard to jurisdictional claims in published maps and institutional affiliations.



© 2020 by the authors. Licensee MDPI, Basel, Switzerland. This article is an open access article distributed under the terms and conditions of the Creative Commons Attribution (CC BY) license (<http://creativecommons.org/licenses/by/4.0/>).

Article

Characterizing Color Quality, Damage to Artwork, and Light Intensity of Multi-Primary LEDs for Museums

Dorukalp Durmus 

Department of Architectural Engineering, Pennsylvania State University, University Park, PA 16802, USA; alp@psu.edu

Abstract: Light causes damage when it is absorbed by sensitive artwork, such as oil paintings. However, light is needed to initiate vision and display artwork. The dilemma between visibility and damage, coupled with the inverse relationship between color quality and energy efficiency, poses a challenge for curators, conservators, and lighting designers in identifying optimal light sources. Multi-primary LEDs can provide great flexibility in terms of color quality, damage reduction, and energy efficiency for artwork illumination. However, there are no established metrics that quantify the output variability or highlight the trade-offs between different metrics. Here, various metrics related to museum lighting (damage, the color quality of paintings, illuminance, luminous efficacy of radiation) are analyzed using a voxelated 3-D volume. The continuous data in each dimension of the 3-D volume are converted to discrete data by identifying a significant minimum value (unit voxel). Resulting discretized 3-D volumes display the trade-offs between selected measures. It is possible to quantify the volume of the graph by summing unique voxels, which enables comparison of the performance of different light sources. The proposed representation model can be used for individual pigments or paintings with numerous pigments. The proposed method can be the foundation of a damage appearance model (DAM).

Keywords: art conservation; cultural heritage; spectral optimization; color quality; LEDs; light intensity; illuminance; exposure; energy efficiency; damage

Citation: Durmus, D. Characterizing Color Quality, Damage to Artwork, and Light Intensity of Multi-Primary LEDs for Museums. *Heritage* **2021**, *4*, 188–197. <https://doi.org/10.3390/heritage4010011>

Received: 30 December 2020

Accepted: 15 January 2021

Published: 17 January 2021

Publisher's Note: MDPI stays neutral with regard to jurisdictional claims in published maps and institutional affiliations.



Copyright: © 2021 by the author. Licensee MDPI, Basel, Switzerland. This article is an open access article distributed under the terms and conditions of the Creative Commons Attribution (CC BY) license (<https://creativecommons.org/licenses/by/4.0/>).

1. Introduction

Optical radiation is electromagnetic energy that dissipates through space. Light, the visible part of optical radiation, upon reaching the surface of an object is either reflected, transmitted (if the object is transparent or translucent), or absorbed. Reflected light initiates vision when it is detected by the human visual system. Light absorbed by the object turns into heat and is considered wasted for illumination purposes. The absorbed light (energy) may cause a chemical change in the molecules due to photochemical reactions, and if the object is light-sensitive, such as a painting, it may cause irreversible damage (e.g., color fading) [1,2]. The dilemma between visibility and damage is a crucial aspect of lighting design for museums and galleries.

Characterizing the properties of the absorbed light can enable estimating and preventing further damage to sensitive works of art. Past studies suggest that there are four primary parameters that influence the optical damage to artwork: light intensity, exposure duration, spectral power distribution (SPD) of the light source, and spectral sensitivity of light sources [2,3]. An increase in light intensity and exposure duration increases damage to artwork, although the relationship is likely not linear. The spectral power distribution and spectral sensitivity of the pigments interact in a more complex manner.

Early models of damage were based on the Einstein–Planck law, which states that energy in lower wavelengths (i.e., ultraviolet radiation) may cause more damage than energy in longer wavelengths [4]. However, several research studies showed that energy in long wavelengths, such as infrared radiation, and energy in the visible spectrum could

also cause damage to artwork [5–8]. Another important factor is the selective influence of light source SPD on the magnitude of damage. Studies suggest that the spectral absorption of pigments may dictate the amount of damage to an artwork since only the light absorbed by a pigment causes photochemical action [9–12]. This understanding, coupled with the overall effect of lighting intensity, encouraged researchers to use spectral optimization algorithms to reduce damage caused by lighting [13–19]. Some of these optimization studies even considered the energy consumed by lighting to balance the end-users’ different needs [14,16,18,19]. Despite the increase in computational power and knowledge of materials’ response to light, there is still no universal damage model that can account for different types of pigments. Another unresolved issue is the holistic presentation of the trade-offs and complex relationships between the parameters, such as damage to artwork, the color appearance of the painting, illumination levels (both for damage and visibility), and energy consumption.

Although multi-primary LED (mpLED) systems can be optimized to generate tailor-made solutions for light-sensitive artwork, quantifying the complex relationships between target parameters using a single-dimensional model is not possible. Fortunately, the complex relationships between different aspects can be presented using a 3-D graph, and discretizing each continuous dimension of the graph (voxelating) can result in a discrete, measurable volume. The voxelization method has been previously applied to color rendition variability in mpLEDs [20]. Here, the voxelization method is applied to display the trade-offs between damage, the color appearance of artwork, illumination levels, and energy efficiency. The voxelization method is based on the idea that a large distribution of data points can be grouped into discrete packages or cubes called voxels, as shown in Figure 1. Converting a large dataset to voxels results in increased interpretability of the data, reduces visual cluster, and enables creating predictive models. The data points within each voxel are considered the “same” for classification purposes, and the “sameness” (uniqueness) of the data points within a voxel can be defined by identifying the borders of the voxel in each dimension. The voxelization in the context of museum lighting should contain the primary goals of illuminating artwork, such as preventing damage caused by lighting, optimizing the appearance of artwork (brightness and color), and improving the efficiency of the light sources.

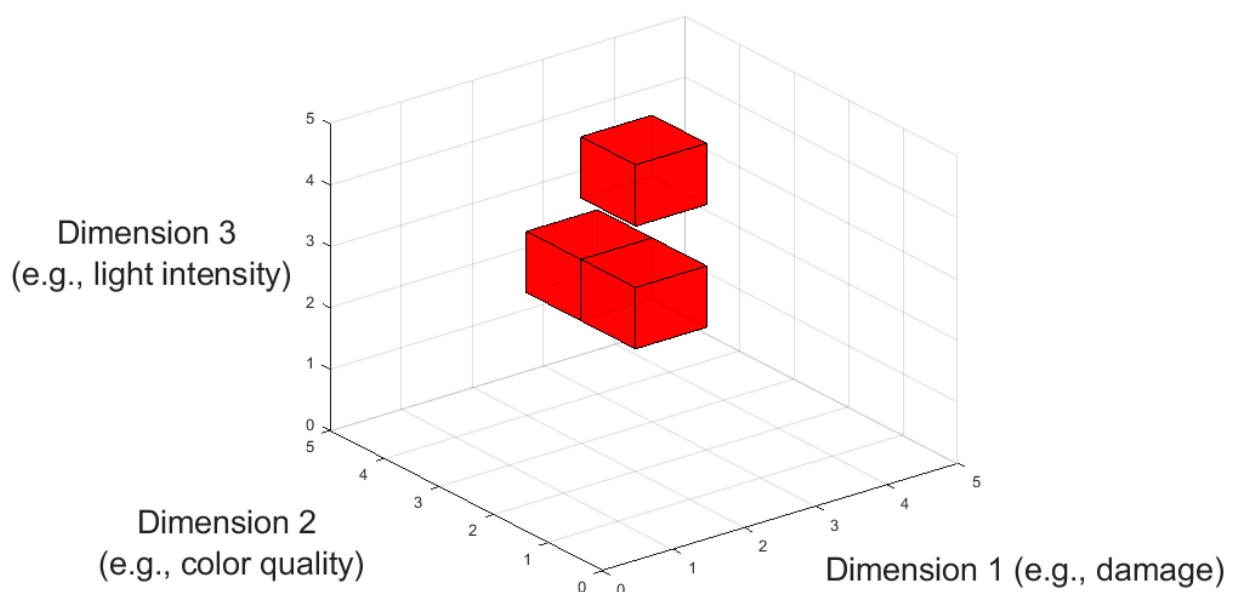


Figure 1. Converting continuous measures to discrete data enables the counting of unique voxels (red cubes), summing them to quantify the volume for a multi-primary LED lighting system. In this example, the size of each unit voxel is 1 for each dimension, and the magnitude of the voxelated volume is 3.

2. Methods

Three-dimensional graphs are widely used in science communication to demonstrate the relationship between conflicting parameters. The proposed voxelization method goes a step further by discretizing the continuous data of each dimension to create unit voxels (analogous to pixels in 3-D shapes). The size of a voxel can be defined by identifying the acceptability or detectability of the minimum value for each dimension. The minimum identifiable value is often characterized as a just-noticeable difference (JND) in psychophysical studies. It is also possible to convert continuous data to discrete data by selecting arbitrary unit sizes when a JND cannot be identified. Once the dimensions of a unit voxel are identified, they can be plotted in a 3-D graph, as shown in Figure 1.

Key dimensions of the proposed demonstration method for museum studies are damage, light intensity, color quality, and energy efficiency. Damage to artwork can be quantified using the Berlin model [3] or the amount of light absorbed by the painting [19]. In the Berlin model, the damage caused by optical radiation is calculated as a function of effective radiant irradiance.

$$E_{dm} = \int_{\lambda} E_{e,\lambda} \times s(\lambda)_{dm,rel} \times d\lambda \quad (1)$$

where E_{dm} (unit: W/m^2) is the effective irradiance that causes damage, $E_{e,\lambda}$ is the spectral irradiance (unit: W/m^2), $s(\lambda)_{dm,rel}$ is the relative spectral responsivity of a material normalized at 300 nm, so that $s(\lambda)_{dm,rel} = 1.0$ for $\lambda = 300$ nm, and λ is wavelength (unit: nm) [3]. The alternative damage calculation method is the ratio of the light absorbed by the surfaces under a test light source to the light absorbed by the surfaces under a reference illuminant

$$A = \frac{\int_{\lambda} E_{e,\lambda,test}(\lambda) \times (1 - R(\lambda)) \times d\lambda}{\int_{\lambda} E_{e,\lambda,ref}(\lambda) \times (1 - R(\lambda)) \times d\lambda} \quad (2)$$

where A is a unitless relative absorption value reported as a percentage, $E_{e,\lambda,test}(\lambda)$ is the test light source irradiance, $E_{e,\lambda,ref}(\lambda)$ is the reference source irradiance, and $R(\lambda)$ is the reflectance factor of a pigment. The test light source $E_{e,\lambda,test}(\lambda)$ should be rescaled so that the light reflected from the painting under the test and reference light sources are equal. Equalizing the reflected light from the painting under the test and reference light source ensures the luminance is the same in both conditions so that the comparison is not affected by luminance related color appearance phenomena, such as the Hunt Effect [21] and Bezold–Brücke hue shift [22].

Both the Berlin Model and relative absorption calculation method account for the Grotthuss–Draper law, which states that only light that is absorbed can cause photochemical activation. The difference between the two methods is that the relative absorption A offers an easy-to-interpret measure for damage, but it does not account for the Planck–Einstein relation (lower wavelength radiation has higher energy potential). On the other hand, the Berlin Model uses a damage curve (action spectra) normalized to 300 nm, which may undermine the Grotthuss–Draper law and can be hard to interpret.

In the proposed voxelization method, the light intensity can also be quantified by using appropriate metrics, such as illuminance (unit: lx) or irradiance (unit: W/m^2). Although illuminance is relevant for the human visual system, irradiance can be used to account for the difference between spectral sensitivity of the materials and the spectral luminous efficiency function (visual system's response to light). The color quality of the painting can be quantified using colorimetric tools, such as color rendition metrics, or more precise tools, such as color difference, chroma, and hue shift formulae. Color shift formulae can provide detailed and specific information about the magnitude and direction of color shifts between two lighting conditions. In the following voxelization example, the two lighting conditions will be a reference white illuminant (i.e., daylight and incandescent lamps are

considered ideal in museums for color quality purposes) and a test light source (SPDs generated by a mpLED).

Test SPDs were generated by the linear optimization of a seven-channel mpLED lighting system. The spectrum of each channel, shown in Figure 2, were combined by iteratively mixing each channel at 20% dimming intervals, resulting in 279,936 (6^7) test SPD combinations. The color differences in the appearance of 24 Macbeth ColorChecker test samples [23] between each test SPD combination and reference incandescent halogen light source were calculated using CAM02-UCS [24]. The root mean square (RMS) of the 24 color difference values ($\Delta E'_{\text{RMS}}$) were calculated to get an average score of the color shifts.

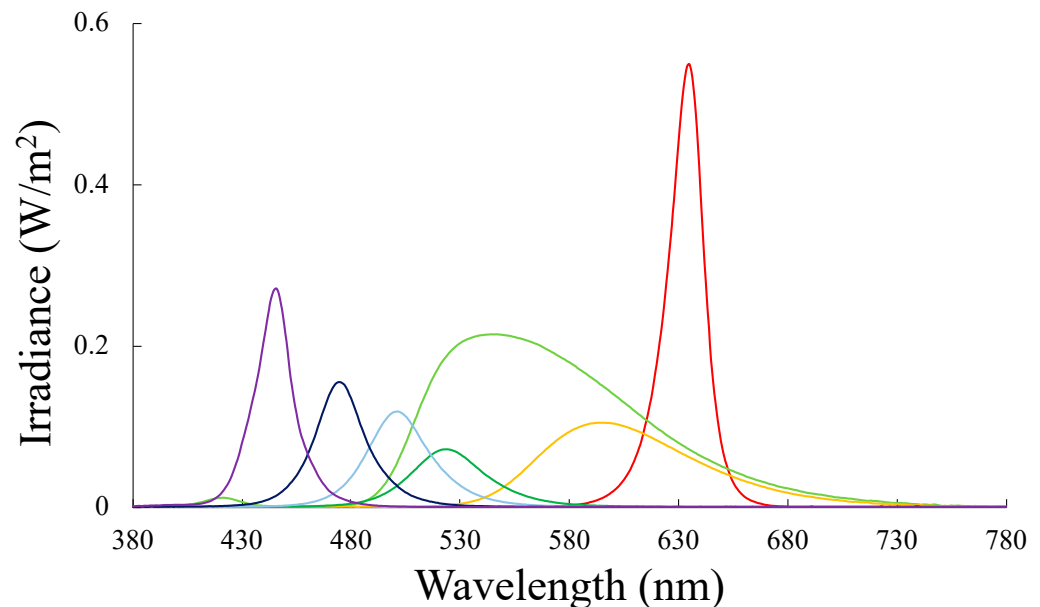


Figure 2. The spectral power distribution of the seven-channel multi-primary LED system is used in the linear optimization to generate data that are analyzed for the proposed 3-D representation of metric trade-offs.

An incandescent halogen light source spectrum was used as a reference since they are still widely used in museums [25]. Macbeth ColorChecker samples include a range of saturated, desaturated, chromatic, and achromatic samples, which can be representative of a wide range of artwork, and it is widely used in color and museum lighting research [26,27]. The color quality of every nominal white light was quantified using an ANSI/IES TM-30 fidelity index R_f , a gamut index R_g , and a local chroma shift in hue bin 1 ($R_{\text{cs,h1}}$) [28]. In addition, relative absorption A (light absorbed by a pigment under the test light source divided by the light absorbed by a pigment under the reference halogen light source), illuminance (E_v), irradiance (E_e), the luminous efficacy of radiation (LER), correlation color temperature (CCT), and the distance from the Planckian locus (D_{uv}) [29] were calculated for each test SPD.

3. Results

The data generated by the linear optimization method have been sorted and analyzed for metric correlation. Since most of the LED combinations (236,502 out of 279,936) were not nominally white, color quality metrics that require a test light source to be close to the Planckian locus (i.e., R_f , R_g , CCT, D_{uv}) were not used in the analysis. However, it is possible to filter out the non-white SPD combinations to utilize color quality metrics that are developed for white lights, with a caveat of reduced damage reduction for individual pigments.

The data generated by the optimization method were voxelated using the most important measures for museum lighting: damage to artwork, color appearance, and

energy efficiency. For example, a 3-D voxelated volume ($VV1$) was calculated using the relative absorption for a test color sample (Macbeth ColorChecker sample #24), the RMS color difference of 24 Macbeth ColorChecker samples $\Delta E'_{RMS}$, and the LER, as shown in Figure 3. Measures in each dimension were discretized by rounding values to a unit size of 1 (e.g., LER of 200.3 lm/W and 200.7 lm/W were rounded to 200 lm/W and 201 lm/W, respectively, and they fell into two different voxels). All the test SPD combinations that fell into the same voxel were considered identical. Therefore, the number of unique voxels ($VV1 = 45,813$) represents the number of unique SPD combinations that can be generated within the seven-channel mpLEDs. It is important to note that the uniqueness of each voxel depends on the voxel size criteria. For example, if the LER was voxelated using 5 lm/W as the unit voxel size, the number of voxels would drastically decrease. Therefore, the absolute magnitude of the volume does not have an inherent meaning.

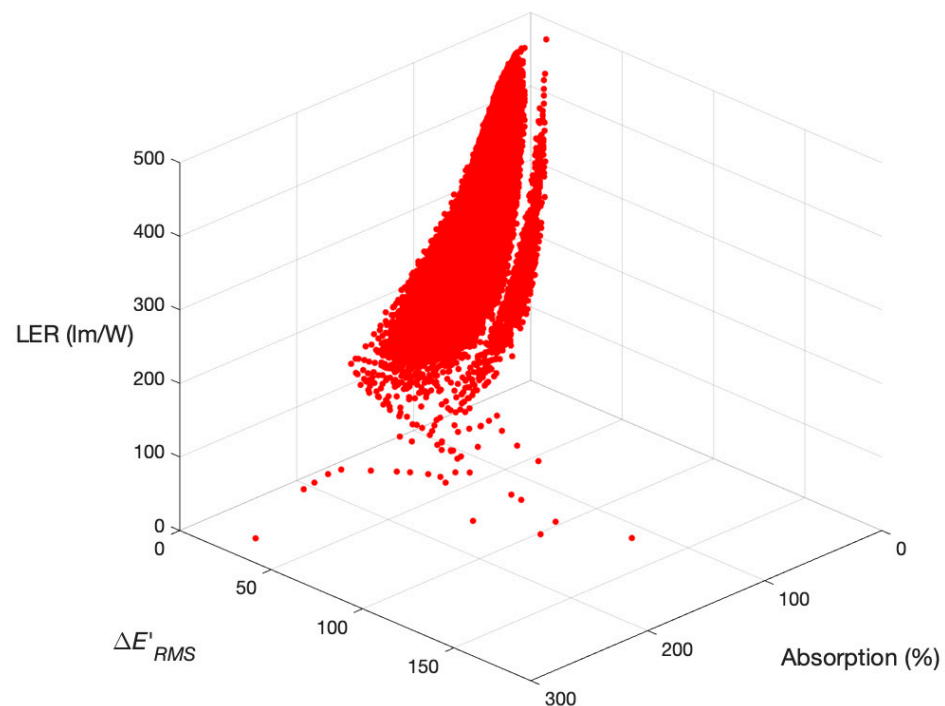


Figure 3. The 3-D voxelated volume $VV1$ shows the trade-offs between damage to artwork (light absorption ratio of test light source to reference), color quality (shifts in the appearance of 24 Macbeth ColorChecker samples between test SPDs and the reference light source), and energy efficiency of the light source (luminous efficacy of radiation; unit: lm/W). Voxels are shown as circles for representation purposes only.

The data departed from normality at the 0.05 significance level as tested by the Shapiro–Wilk test, and a non-parametric test (Spearman’s rank correlation coefficient) was used to analyze the correlation between the dimensions of the voxelated $VV1$ volume. While the correlation between absorption A and $\Delta E'_{RMS}$ were low ($\rho = 0.111$), the LER was inversely correlated to absorption ($\rho = -0.757$) and $\Delta E'_{RMS}$ ($\rho = -0.427$).

Figure 3 illustrates the relationship between color quality, damage, and energy efficiency, where the top far corner is the ideal condition (low absorption, small color shifts, and high efficacy). The visual illustration makes it clear that the ideal SPDs are increasingly scarce compared to other SPDs that perform worse in terms of either damage, color shifts, or energy efficiency. Since the relative absorption $A > 100$ denotes additional damage, and the large color differences are not desired, it is possible to zoom into the graph by limiting the x and y axes (relative absorption ($A < 100$) and color difference ($\Delta E'_{RMS} < 20$), respectively), as shown in Figure 4.

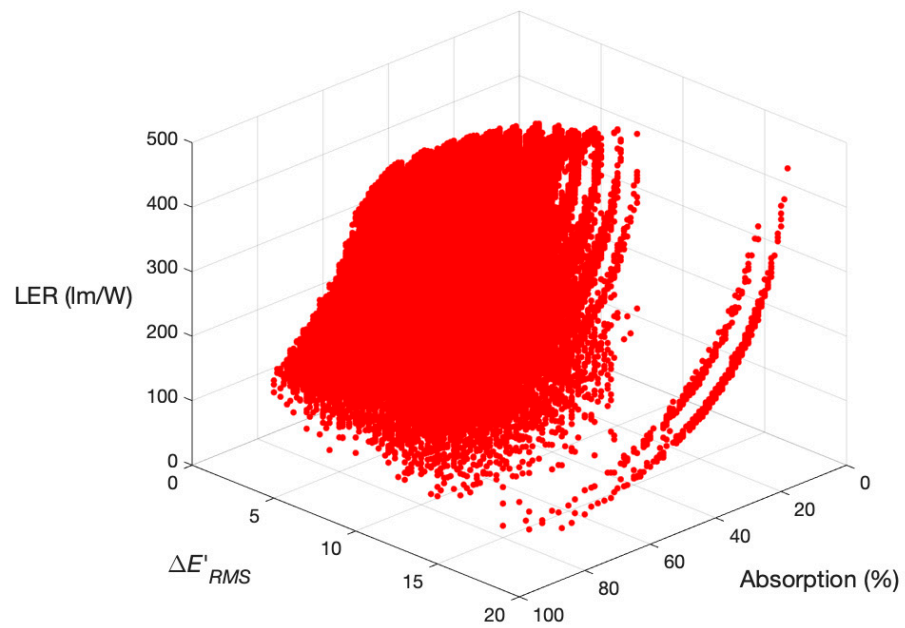


Figure 4. Limiting the x and y axes of the voxelated 3-D volume $VV1$ can highlight areas of interest, such as low relative absorption ($A < 100$) and color difference ($\Delta E'_{RMS} < 20$). Voxels are shown as circles for representation purposes only.

A second example ($VV2$) was calculated using relative absorption A for a test color sample (Machbeth ColorChecker sample #24), the TM-30 fidelity index R_f , and the irradiance E_e , as shown in Figure 5. In the second volume, which is the graphical representation of the same data, there were $VV2 = 2,265$ unique voxels. While the absolute volume size does not have an inherent meaning, comparing two or more light sources—using identical voxel dimension metrics—can provide more information about the performance of the light sources for a specific set of pigments (or the overall color quality of a painting).

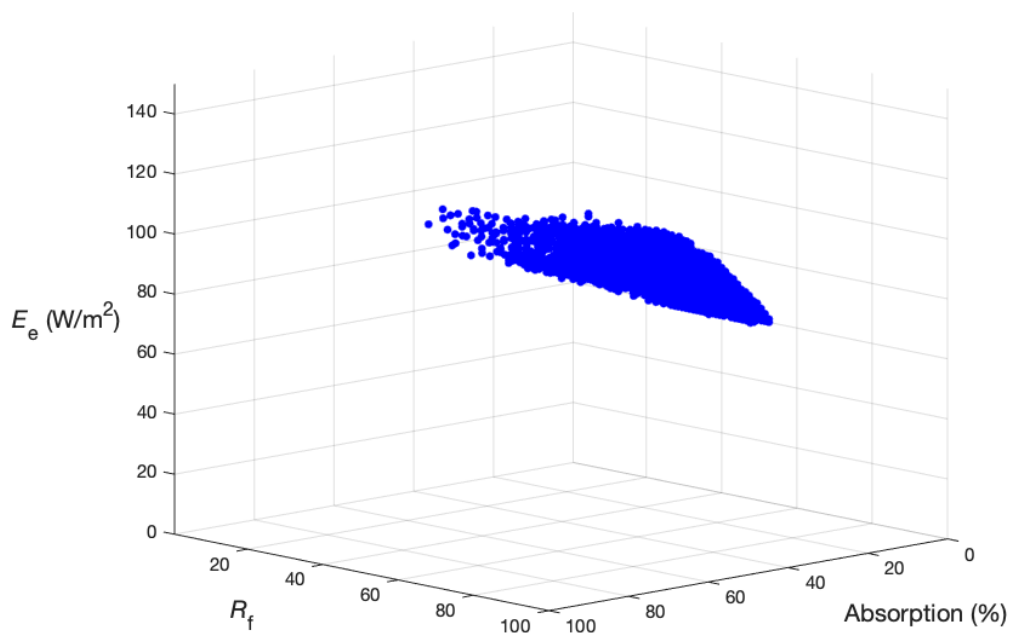


Figure 5. Another 3-D voxelated volume $VV2$ shows the trade-offs between damage to artwork (light absorption ratio of test light source to reference), color quality (ANSI/IES TM-30 fidelity index R_f), and illumination intensity (irradiance E_e). Voxels are shown as circles for representation purposes only.

Voxelated 3-D volume $VV2$ also shows the relationship between competing target parameters. The fidelity index R_f was not correlated with either relative absorption A ($\rho = 0.010$) or irradiance E_e ($\rho = 0.017$). However, irradiance E_e and relative absorption A were highly correlated ($\rho = 0.996$), which is not surprising since absorption increases with light intensity.

It should be noted that the graphical distributions were applied to a single pigment using relative absorption and to multi-pigments (e.g., a painting with numerous colors) using color quality metrics to demonstrate the different use cases of the proposed method. The proposed model can provide a more analogous analysis if all the dimensions are chosen at the individual pigment scale (e.g., absorption for a single color and color difference in the pigment under reference and test light sources). On the other hand, the proposed model can also be used to gain a holistic understanding of a painting by using a high-level approach (e.g., average absorption ratio by the pigments used in a painting, the average color difference of pigments in the painting under reference and test light sources). While the provided examples do not include the exposure time—an important dimension of damage to artwork—it is possible to incorporate the total radiant exposure as a metric to the voxelization method. The total exposure can be calculated by multiplying exposure time t (unit: hr) with irradiance ($E_e \times t$, unit: $W\ h/m^2$) or illuminance ($E_v \times t$, unit: lx h). Alternatively, the radiant exposure can be quantified using the Berlin model (H_{dm} , unit: $W\ h/m^2$) [3].

4. Discussion

The proposed voxelization method can help analyze and compare the performance of multi-primary LED systems. Since each SPD is represented as a single dot in a 3-D graph, the proposed method cannot be used to analyze a single static SPD light source. However, it is possible to analyze large datasets that include commercially available light sources in the proposed 3-D volume. Such large datasets can provide museum curators, conservators, and lighting designers with an opportunity to compare the performance of different lighting technologies. Large datasets of different lighting technologies can also be used to analyze a set of reference test samples collected in a museum or a painting (similar to the color rendition approach) to attain an approximate idea of the performance in a given space. The caveat in such an approach would be the consideration of object surface reflectance characteristics since it may be challenging to identify the action spectra of the pigments and dyes in every painting in a museum or a gallery.

Non-invasive scanning techniques, such as Fourier-transform infrared spectroscopy (FTIR), X-ray fluorescence (XRF), Raman imaging, hyperspectral imaging, scanning electron microscopy (SEM), and energy-dispersive X-ray spectroscopy (EDS) [30–32] are often used to obtain absorption spectra from materials. The analysis of organic and inorganic pigments can also lead to new horizons in tailor-made museum lighting. In the future, it may be possible to build a library of pigment and dye characteristics and their response to light spectra, which may ultimately lead to a universal damage calculation model.

Despite the challenges of facing a universal damage model today, studies investigating the sensitivity of different materials [33–40] can converge into a complex damage appearance model (DAM), similar to color appearance models (CAMs). Although the CIE 1976 $L^*a^*b^*$ (CIELAB) is the most widely used color space in conservation science, the proposed damage model is based on the CAM concept due to the multi-layered nature and better performance of CAMs. The CIELAB has well-documented limitations, such as abnormal hue angle shifts [41,42], poor performance in the [43], and blue regions (negative b^* axis) [44]. Research suggests that color appearance models, such as CAM02-UCS [24], can outperform CIELAB, especially when color differences are small—which are crucial for conservation science [45,46]. In addition, conservation scientists often perform visual observations of the artwork under controlled environmental conditions (e.g., laboratory). Therefore, the additional input parameters required by CAMs (i.e., background and surround conditions, adapting luminance) can be accurately determined by the users. In short,

the CAM provides a better basis both conceptually and mathematically for the proposed damage calculation models compared to a color space, such as CIELAB.

A DAM can have several inputs, such as light source spectrum, light intensity, exposure duration, pigment spectral reflectance/absorption, artwork type (e.g., oil, gauche, acrylic paint), and choice of a reference illuminant (i.e., daylight, incandescent). DAM would provide an output of damage caused by lighting and the color appearance of the resulting pigment under a specific light source, as shown in Figure 6. It should also be noted that color difference formulae are often used in conservation science as a proxy for damage, as illustrated by fading. However, not all types of chemical and structural damage are caused by lighting [47]. For example, viscometry and chromatography are used to measure the brittle effect (the breakdown of paper fibers) [48].



Figure 6. A damage appearance model (DAM) can be developed based on the research studies investigating the impact of different aspects of light on pigments. A computational model such as this can have inputs including spectral power distribution, intensity, exposure duration of the light source, action spectra of the light-receiving material, material (binder, pigment, dye) type, and choice of a reference illuminant (i.e., daylight, incandescent). The DAM outputs can be the color difference to quantify damage and the color appearance of the light-receiving material.

Although a rudimentary DAM can provide an estimation of damage to a single material at a given time, more advanced models can be built by integrating the results across different pigments and dyes (e.g., providing averages with standard deviation and error estimates, using multi-dimensional data analysis or machine learning algorithms). More complex DAMs can be used in adaptive lighting systems, where a sensor detects the spectral reflectance function of paintings, and a projection system emits spectrally and spatially optimized lighting to each colored part of the painting to reduce damage while maintaining the overall color quality of the painting, or even visually restore the faded colors of the artwork [18,49–51].

5. Conclusions

Museum conservators and curators often face the multi-faceted problem of identifying the optimal lighting conditions in museums. While light is needed to display art, it may also damage sensitive artwork over time. Museum conservators, curators, and lighting designers can use the properties of light sources (spectral distribution, intensity, and exposure duration) and materials (spectral absorption characteristics) to estimate the damage caused by optical radiation. Here, a three-dimensional representation of the conflicting parameters (e.g., color quality vs. damage) is provided to display the trade-offs between several measures. The continuous scale of each dimension of the 3-D graph is converted to discrete data using unit voxels. The discretization of continuous data can enable the quantification of the performance of multi-primary LEDs in the context of art conservation. Sample calculations demonstrated the use of the proposed method to highlight the most common trade-offs in museum lighting design: conflicts between the color quality of paintings (average color difference), damage caused by lighting (absorption percentage), illuminance, and luminous efficacy of the radiation. However, it is possible to adopt different metrics for each dimension, such as color discrimination or other color rendition metrics for color quality, the Berlin model [3] and irradiance for damage quantification, and CCT and Duv

for color quality of the light source. In addition, new metrics that are relevant for museum lighting and perception of artwork (e.g., visual clarity [52,53] and visual complexity [54]) can be utilized in the proposed 3-D volume. Future work will investigate the quantification of the trade-offs between various damage, color quality, and visual perception metrics and validate their accuracy through visual evaluations.

Funding: This research received no external funding.

Institutional Review Board Statement: Not applicable.

Informed Consent Statement: Not applicable.

Data Availability Statement: The data that support the findings of this study are available from the corresponding author upon reasonable request.

Conflicts of Interest: The author declares no conflict of interest.

References

- Schaeffer, T.T. *Effects of Light on Materials in Collections: Data on Photoflash and Related Sources*; Getty Publications: Los Angeles, CA, USA, 2001.
- Cuttle, C. Damage to museum objects due to light exposure. *Light. Res. Technol.* **1996**, *28*, 1–9. [CrossRef]
- CIE. *157:2004 Control of Damage to Museum Objects by Optical Radiation*; CIE: Vienna, Austria, 2004.
- Harrison, L.S. *Report on the Deteriorating Effects of Modern Light Sources*; Metropolitan Museum of Art: New York, NY, USA, 1953.
- Feller, R.L. Control of deteriorating effects of light on museum objects: Heating effects of illumination by incandescent lamps. *Mus. News* **1968**, *46*, 39–47.
- Beek, H.V.; Heertjes, P.M. Fading by light of organic dyes on textiles and other materials. *Stud. Conserv.* **1966**, *11*, 123–132. [CrossRef]
- Michalski, S. Time's Effects on Paintings. In *Shared Responsibility*; National Gallery of Canada: Ottawa, ON, Canada, 1990; pp. 39–52.
- Gupta, D.; Gulrajani, M.L.; Kumari, S. Light fastness of naturally occurring anthraquinone dyes on nylon. *Color Technol.* **2004**, *120*, 205–212. [CrossRef]
- Saunders, D.; Kirby, J. Wavelength-dependent fading of artists' pigments. *Stud. Conserv.* **1994**, *39*, 190–194. [CrossRef]
- Nakagoshi, K.; Yoshizumi, K. Degradation of Japanese Lacquer under Wavelength Sensitivity of Light Radiation. *Mater. Sci. Appl.* **2011**, *2*, 1507–1515. [CrossRef]
- Lerwill, A.; Brookes, A.; Townsend, J.H.; Hackney, S.; Liang, H. Micro-fading spectrometry: Investigating the wavelength specificity of fading. *Appl. Phys. A* **2014**, *118*, 457–463. [CrossRef]
- Villmann, B.; Weickhardt, C. Wavelength Dependence of Light Induced Changes in Reflectance Spectra of Selected Dyes and Pigments. *Stud. Conserv.* **2017**, *63*, 104–112. [CrossRef]
- Scuello, M.; Abramov, I.; Gordon, J.; Weintraub, S. Museum lighting: Optimizing the illuminant. *Color Res. Appl.* **2004**, *29*, 121–127. [CrossRef]
- Abdalla, D.; Duis, A.; Durmus, D.; Davis, W. Customisation of light source spectrum to minimise light absorbed by artwork. In Proceedings of the CIE Lighting Quality Energy Efficiency, Melbourne, Australia, 7–9 March 2016; pp. 22–31.
- Lunz, M.; Talgorn, E.; Baken, J.; Wagemans, W.; Veldman, D. Can LEDs help with art conservation? Impact of different light spectra on paint pigment degradation. *Stud. Conserv.* **2016**, *62*, 294–303. [CrossRef]
- Delgado, M.F.; Dirk, C.W.; Druzik, J.; WestFall, N. Lighting the world's treasures: Approaches to safer museum lighting. *Color Res. Appl.* **2011**, *36*, 238–254. [CrossRef]
- Dang, R.; Wang, N.; Liu, G.; Yuan, Y.; Liu, J.; Tan, H. Illumination in Museums: Four-Primary White LEDs to Optimize the Protective Effect and Color Quality. *IEEE Photon J.* **2019**, *11*, 1–15. [CrossRef]
- Vázquez, D.; Fernández-Balbuena, A.; Canabal, H.; Muro, C.; Durmus, D.; Davis, W.; Benítez, A.J.; Mayorga, S. Energy optimization of a light projection system for buildings that virtually restores artworks. *Digit. Appl. Archaeol. Cult. Herit.* **2020**, *16*, e00128. [CrossRef]
- Durmus, D.; Abdalla, D.; Duis, A.; Davis, W. Spectral Optimization to Minimize Light Absorbed by Artwork. *LEUKOS* **2018**, *16*, 45–54. [CrossRef]
- Royer, M.P.; Durmus, D.; Baxter, D.J. Characterizing the color rendition performance of multi-primary LED lighting systems. In Proceedings of the IES Annual Conference, New Orleans, LA, USA, 6–8 August 2020.
- Hunt, R.W.G. Light and dark adaptation and the perception of color. *JOSA* **1952**, *42*, 190–199. [CrossRef]
- Smith, V.C.; Pokorný, J.; Cohen, J.; Perera, T. Luminance thresholds for the Bezold-Brücke hue shift. *Percept. Psychophys.* **1968**, *3*, 306–310. [CrossRef]
- Useful Color Data. Available online: https://www.rit.edu/cos/colorscience/rc_useful_data.php (accessed on 20 November 2020).
- Luo, M.R.; Li, C. CIECAM02 and Its Recent Developments. In *Advanced Color Image Processing and Analysis*; Springer Science and Business Media LLC: Berlin/Heidelberg, Germany, 2013; pp. 19–58.

25. Perrin, T.E.; Druzik, J.R.; Miller, N.J. *SSL Adoption by Museums: Survey Results, Analysis, and Recommendations*; Office of Scientific and Technical Information (OSTI), Pacific Northwest National Laboratory: Richland, WA, USA, 2014.
26. Durmus, D.; Davis, W. Appearance of Achromatic Colors under Optimized Light Source Spectrum. *IEEE Photon J.* **2018**, *10*, 1–11. [CrossRef]
27. Liang, H.; Saunders, D.; Cupitt, J. A new multispectral imaging system for examining paintings. *J. Imaging Sci. Technol.* **2005**, *49*, 551–562.
28. IES. *ANSI/IES TM-30-20, IES Method for Evaluating Light Source Color Rendition*; Illuminating Engineering Society: New York, NY, USA, 2020.
29. Ohno, Y. Practical Use and Calculation of CCT and Duv. *LEUKOS* **2014**, *10*, 47–55. [CrossRef]
30. Antunes, V.; Serrão, V.; Valadas, S.; Candeias, A.; Mirão, J.; Cardoso, A.; Manso, M.; Carvalho, M.L. A Painter in the Shadow: Unveiling Conservation, Materials and Techniques of the Unknown Luso-Flemish Master of Lourinhã. *Heritage* **2019**, *2*, 2725–2744. [CrossRef]
31. Zalaffi, M.S.; Agostinelli, I.; Karimian, N.; Ugo, P. Ag-Nanostars for the Sensitive SERS Detection of Dyes in Artistic Cross-Sections—*Madonna della Misericordia* of the National Gallery of Parma: A Case Study. *Heritage* **2020**, *3*, 1344–1359. [CrossRef]
32. Buse, J.; Otero, V.; Melo, M.J. New Insights into Synthetic Copper Greens: The Search for Specific Signatures by Raman and Infrared Spectroscopy for Their Characterization in Medieval Artworks. *Heritage* **2019**, *2*, 1614–1629. [CrossRef]
33. Druzik, J.R. Evaluating the light sensitivity of paints in selected wall paintings at the Mogao Grottoes: Caves 217, 98, and 85. In *Conservation of Ancient Sites on the Silk Road*; Getty Conservation Institute: Los Angeles, CA, USA, 2010; pp. 457–463.
34. Piccablotto, G.; Aghemo, C.; Pellegrino, A.; Iacomussi, P.; Radis, M. Study on Conservation Aspects Using LED Technology for Museum Lighting. *Energy Procedia* **2015**, *78*, 1347–1352. [CrossRef]
35. Mayorga, S.; Vázquez, D.; Fernandez-Balbuena, A.A.; Muro, C.; Muñoz, J. Spectral damage model for lighted museum paintings: Oil, acrylic and gouache. *J. Cult. Herit.* **2016**, *22*, 931–939. [CrossRef]
36. Farke, M.; Binetti, M.; Hahn, O. Light damage to selected organic materials in display cases: A study of different light sources. *Stud. Conserv.* **2016**, *61*, 83–93. [CrossRef]
37. Degani, L.; Gulmini, M.; Piccablotto, G.; Iacomussi, P.; Gastaldi, D.; Bello, F.D.; Chiantore, O. Stability of natural dyes under light emitting diode lamps. *J. Cult. Herit.* **2017**, *26*, 12–21. [CrossRef]
38. Luo, H.-W.; Chou, C.-J.; Chen, H.-S.; Luo, M.R. Museum lighting with LEDs: Evaluation of lighting damage to contemporary photographic materials. *Light. Res. Technol.* **2018**, *51*, 417–431. [CrossRef]
39. Jo, S.; Ryu, S.R.; Jang, W.; Kwon, O.-S.; Rhee, B.; Lee, Y.E.; Kim, D.; Kim, J.; Shin, K. LED illumination-induced fading of traditional Korean pigments. *J. Cult. Herit.* **2019**, *37*, 129–136. [CrossRef]
40. Dang, R.; Tan, H.; Wang, N.; Liu, G.; Zhang, F.; Song, X. Raman spectroscopy-based method for evaluating LED illumination-induced damage to pigments in high-light-sensitivity art. *Appl. Opt.* **2020**, *59*, 4599–4605. [CrossRef]
41. Liu, Y.; Shigley, J.; Fritsch, E.; Hemphill, S. Abnormal Hue-Angle change of the gemstone tanzanite between CIE illuminants d65 and a in CIELAB color space. *Color Res. Appl.* **1995**, *20*, 245–250. [CrossRef]
42. Durmus, D.; Davis, W. Evaluation OF Hue Shift Formulae in CIELAB and CAM02. In Proceedings of the 29th Quadrennial Session of the CIE, Washington, DC, USA, 14–22 June 2019; International Commission on Illumination: Vienna, Austria, 2019; pp. 888–895.
43. Sharma, G.; Rodríguez-Pardo, C.E. The dark side of CIELAB. In *Color Imaging XVII: Displaying, Processing, Hardcopy, and Applications*; International Society for Optics and Photonics; International Society for Optics and Photonics: Burlingame, CA, USA, 2012; Volume 8292, p. 82920D.
44. Moroney, N. A hypothesis regarding the poor blue constancy of CIELAB. *Color Res. Appl.* **2003**, *28*, 371–378. [CrossRef]
45. Lian, Y.; Liao, N.; Wang, J.; Tan, B.; Liu, Z. Evaluating the uniformity of color spaces and performance of color difference formulae. *LED Disp. Technol.* **2010**, *7852*, 785205. [CrossRef]
46. Shamey, R.; Cao, R.; Sawatwarakul, W.; Lin, J. Performance of various color difference models in challenging regions of CIELAB color space. In *22nd Color and Imaging Conference*; Society for Imaging Science and Technology: Springfield, VA, USA, 2014; Volume 2014, pp. 200–206.
47. Saunders, D. *Museum Lighting: A Guide for Conservators and Curators*; Getty Publications: Los Angeles, CA, USA, 2020.
48. Area, M.C.; Ceradame, H. Paper aging and degradation: Recent findings and research methods. *BioResources* **2011**, *6*, 5307–5337.
49. Durmus, D.; Davis, W. Optimising Light Source Spectrum for Object Reflectance. *Light Energy Environ.* **2014**, *23*, 456. [CrossRef]
50. Vázquez, D.; Alvarez, A.; Canabal, H.; Garcia, A.; Mayorga, S.; Muro, C.; Galan, T. Point to point multispectral light projection applied to cultural heritage. In *Nonimaging Optics: Efficient Design for Illumination and Solar Concentration XIV. Int. Soc. Opt. Photonics* **2017**, *10379*, 103790K.
51. Gómez Manzanares, Á.; Benítez, A.J.; Martínez Antón, J.C. Virtual Restoration and Visualization Changes through Light: A Review. *Heritage* **2020**, *3*, 1373–1384. [CrossRef]
52. Durmus, D.; Davis, W. Blur perception and visual clarity in light projection systems. *Opt. Express* **2019**, *27*, A216–A223. [CrossRef]
53. Khanh, T.; Bodrogi, P.; Guo, X.; Phan, Q.A. Towards a user preference model for interior lighting. Part 2: Experimental results and modelling. *Light. Res. Technol.* **2018**, *51*, 1030–1043. [CrossRef]
54. Durmus, D. Spatial Frequency and the Performance of Image-Based Visual Complexity Metrics. *IEEE Access* **2020**, *8*, 100111–100119. [CrossRef]

Article

Multi-Camera Workflow Applied to a Cultural Heritage Building: Alhambra's Torre de la Cautiva from the Inside

Anto J. Benítez ^{1,2} , Xose Prieto Souto ^{1,2,*}, Manuel Armenteros ^{1,3}, Esteban M. Stepanian ¹, Rubén Cantos ¹, Miguel García-Villaraco ³, Jaime Solano ² and Ángela Gómez Manzanares ⁴

¹ Department of Communication, Universidad Carlos III of Madrid, 28903 Madrid, Spain; abenitez@hum.uc3m.es (A.J.B.); marmonte@hum.uc3m.es (M.A.); estepani@hum.uc3m.es (E.M.S.); rcantos@hum.uc3m.es (R.C.)

² Tecmerin Research Group, Universidad Carlos III of Madrid, 28903 Madrid, Spain; jsolano@hum.uc3m.es

³ Miopía FX, 28006 Madrid, Spain; mike@miopiafx.es

⁴ Department of Optics, University Complutense of Madrid, 28040 Madrid, Spain; angomez@ucm.es

* Correspondence: japsouto@hum.uc3m.es

Abstract: It is increasingly necessary to generate accessible and navigable digital representations of historical or heritage buildings. This article explains the workflow that was applied to create such a digital component for one of the least accessible areas of the Alhambra palace in Granada, the so-called Torre de la Cautiva (Tower of the Captive). The main goal of this process was to create affordable, photorealistic 3D models that contribute to the dissemination of cultural heritage, the decision making for its conservation and restoration, and public engagement and entertainment. With enough preparation, the time spent gathering data following a Structure from Motion (SfM) approach can be significantly reduced by using a multi-camera (low cost DSLR) photogrammetric strategy. Without the possibility of artificial lighting, it was essential to use RAW images and calibrate the color in the scene for material and texture characterization. Through processing, the amount of data was reduced by optimizing the model's topology. Thus, a photorealistic result was obtained that could be managed and visualized in immersive Visual Reality (VR) environments, simulating different historical periods and environmental and lighting conditions. The potential of this method allows, with slight modifications, the creation of HBIMs and the adaptation to VR systems development, whose current visualization quality is below the resolution of actionable models in rendering engines.

Keywords: cultural heritage; photogrammetry; workflow; Alhambra's Tower of the Captive

Citation: Benítez, A.J.; Prieto Souto, X.; Armenteros, M.; Stepanian, E.M.; Cantos, R.; García-Villaraco, M.; Solano, J.; Gómez Manzanares, Á. Multi-Camera Workflow Applied to a Cultural Heritage Building: Alhambra's Torre de la Cautiva from the Inside. *Heritage* **2022**, *5*, 21–41. <https://doi.org/10.3390/heritage5010002>

Academic Editors:

Daniel Vázquez-Molini and Antonio Álvarez Fernández-Balbuena

Received: 28 October 2021

Accepted: 18 December 2021

Published: 22 December 2021

Publisher's Note: MDPI stays neutral with regard to jurisdictional claims in published maps and institutional affiliations.



Copyright: © 2021 by the authors. Licensee MDPI, Basel, Switzerland. This article is an open access article distributed under the terms and conditions of the Creative Commons Attribution (CC BY) license (<https://creativecommons.org/licenses/by/4.0/>).

1. Introduction

A fundamental concern in the field of Cultural Heritage (CH) is the need to document historical monuments as accurately as possible. Before the advent and popularization of digital culture, it was proposed to carry out extensive suitable inventories of each site [1] with photographs and drawings used to capture the nature of these environments, and to guide conservation, restoration, or excavation activities [2,3]. Technological advances have expanded the possibilities of documenting these CH sites, using not only natural light, but also monochromatic light, ultraviolet light, and infrared rays [4]. Subsequently, photogrammetry was specifically mentioned as a standard procedure to document the properties of cultural interest in the 1987 Charter for the Conservation of Historic Towns and Urban Areas [5].

From the time atoms began to be converted into bits [6], digitization has become increasingly widespread, allowing not only for assets to be documented for their conservation, preservation [7] or restoration [8], but also for digital versions to be created. With these, which constitute the Digital Cultural Heritage (DCH), dissemination actions are promoted, play is proposed [9] and access is allowed [7] through virtual tours even in complicated circumstances such as those experienced in recent times, marked by the COVID-19 pandemic [10].

Some arguments have been presented against the creation of DCH models. For example, their cost, the complexity of the processes or the specialization required to obtain them [11,12]. These are arguments that have been losing strength with the simplification of software platforms, the increase in the power of hardware equipment and the lowering of the cost of both elements [9,13].

At the same time, the need for a multidisciplinary approach has been recognized (The Norms of Quito, 1967). New approaches have emerged that make it possible to produce more complete documentation and expand the possible uses of the 3D models that were obtained. An increasing number of heritage buildings have an informative model that was obtained through Historic Building Information Modeling (HBIM) procedures [9,14]. Such models are based on a complex and precise methodology [15,16] originating from architectural functionalities. These approaches encourage the construction of parametric models with the integration of many disciplines [16].

Irrespective of their origin, 3D models have been employed in the interest of the conservation and restoration of CH sites, but also for other objectives. Education [12] or entertainment in the form of video game scenarios or Virtual Reality (VR) experiences [17] are examples. Their use with the holistic intention of gathering as much knowledge as possible about a building and reaching their recipients in the form of 'edutainment' is also remarkable [9]. Moreover, the data collected as a part of these processes can help in the restoration of irreplaceable sites after unexpected catastrophes, as recently highlighted by the fire at the Notre Dame cathedral in Paris [18].

Thus, this article is part of the exploration of the possibilities of digital modeling for historical heritage. Workflows (or pipelines) that are applicable to photogrammetry are being simplified, although they are still not fully standardized. Some of them are becoming clearer and simpler, making them accessible to the uninitiated, but they coexist with others that do require specialization. Some of the possible results can still be achieved in very different ways, sometimes by retracing routes that have already been experienced and commented on. The case that is discussed in this article has tried to avoid this as much as possible by using audiovisual procedures and using only digital photography cameras in the capture, with the aim of obtaining a useful model that works as a video game scenario as well as in a conservation and restoration environment. It was launched before some initiatives were published, several of whose elements we agree with [17], and with which we share the view that it will be necessary to continue looking for procedures that are easy to implement, effective, efficient, cheap, and that can be standardized or become universal.

In an attempt to gain a wider picture by drawing on a multidisciplinary environment, more than a few cinematography techniques are also suitable for projects of this type [19]. Minimum standards of precision and accuracy or fidelity must be achieved in the multi-spectral characterization of the surfaces in order to obtain the right data for HBIM [3,20]. During shooting, cinematographic photography is similarly concerned with the on-screen results, which are achieved through adequate attention to exposure and color calibration. As such, in both cases there is a need to take extreme care in the preparation procedures for shooting.

DHCs can and should be used for dissemination as they are part of a collective heritage [7,9,21]. The main goal of the audiovisual sector is that the stories engage the audience. Since the same is true for the dissemination of DCH, it would be logical to use the methods and procedures adopted by the former, i.e., defining and following a script prepared for that purpose [17]. Indeed, some of the processes that will be discussed in this text are specific to the audiovisual industry, such as: pre-production, multi-camera shooting in rigs, care in exposure, the use of RAW files, re-topology and the integration of lighting and environment.

In this case, the aim was to achieve immersion and presence, with full awareness of having discarded the real environment, in the sense attributed to it by [22]. The aim was to provide a simple viewing in VR with a level of quality that allows the user to experience photorealistic sensations [23].

There are ever more platforms available for this type of experience, although the systems still suffer from many limitations, as their manufacturers warn [17]. It is important to emphasize that at the time of starting this project, the most widespread VR devices were still unable to correctly reproduce the resolution and quality of the models that are being obtained through photogrammetry. However, given the vertiginous advances of the last few years, this team has no doubt that within a short time the performance of the systems that allow VR to be experienced will surpass that of most existing scenes and models.

The objective should be independent of the platform used. Rather, it will have to refer to the appearance of real materiality of the content, not to the predisposition to which the technology subjects the viewer. It will have more to do with contemplation, with the amazement of being in the middle of a story that leaves a feeling of photorealism. It will have to take advantage of the immersive capacity of the narrative device in order to overcome the resistance that the spectator may oppose to letting him or herself be carried away by the story, in the sense that whoever experiences it may reach a state of pathos such as that described by Sergei M. Eisenstein, whereby one is taken out of oneself and immersed in the reality presented on the screen [24]. To achieve this immersion, it was essential to work with lighting and the setting of scenarios with techniques that achieve an optimal degree of integration [12,17].

This article describes all of the processes that were carried out in order to obtain the model of the interior of the Torre de la Cautiva (The Tower of the Captive) of the Alhambra in Granada, to achieve a stereoscopic piece that can be experienced in VR 360°, according to a script that was set in simulations throughout different epochs. For a proper analysis of the experience, we will first present a brief approach to the selected case study and the challenges it posed. Subsequently, the methodology and workflows will be explained in greater detail. Finally, the conclusions of this study will be presented and a series of future lines of research will be proposed.

1.1. *La Torre de la Cautiva (The Tower of the Captive)*

The Alhambra-Generalife complex in Granada, Spain, figures on the World Heritage List since 1984, according to UNESCO records.

The Alhambra has been the ideal setting for artists and writers of Romanticism, inspired on numerous occasions by folklore and medieval historical plots. According to legend, Doña Isabel de Solís, an Andalusian noblewoman, was kidnapped and fell in love with the king of Granada, Muley Hacén. She converted to Islam and adopted the name Zoraya. The outlines of this story were part of Washington Irving's book 'A Chronicle of the conquest of Granada' [25]. A few years later, Francisco Martínez de la Rosa published the historical novel 'Doña Isabel de Solís, Reina de Granada' [26], which delves into this story and is the one that justifies the name of the tower.

The tower is part of the north-northeast walled enclosure and is located between the Torre del Cadí (Tower of the Judge) and the Torre de las Infantas (Tower of the Princesses). It was built in the mid-fourteenth century, in the time of Yusuf I. Its exterior has a sober defensive aspect and a very simple geometry, but inside it is richly decorated. The main hall measures about 5 m × 5 m and its walls contain a good number of epigraphic poems composed by Ibn al-Yayyab (1274–1349).

In addition to the plans drawn up by architects or draftsmen, which are preserved in the Archives of The Alhambra and Generalife Trust, there is also a physical model of part of the interior of the tower, which was made by Enrique Linares in the last quarter of the 19th century, in the Victoria and Albert Museum in London [27]. It weighs 100 kg and is almost one meter high.

1.2. *Case Study*

The Torre de la Cautiva is one of the parts of the Alhambra that is not usually open to the public. In the summer of 2018, the challenge was posed to produce a pilot piece of the interior of the tower. Its goal was to explore the possibilities of 3D models obtained through

affordable passive-sensor data-acquisition techniques, not only as a simulation platform for conservation and restoration, but also as a vehicle for dissemination and engagement. Two rooms were to be covered: the main room, with profuse decoration and ambient light, and the secondary room or courtyard, with simpler decoration and little natural light (see Figure 1b). The result would be used in stereoscopic 3D in the Head Mount Display (HMD). In Milgram and Kishino's Reproduction Fidelity dimension, the aim was to achieve what they call the "ultimate graphic rendering", referred to as "real-time, high-fidelity 3D animation" [28].

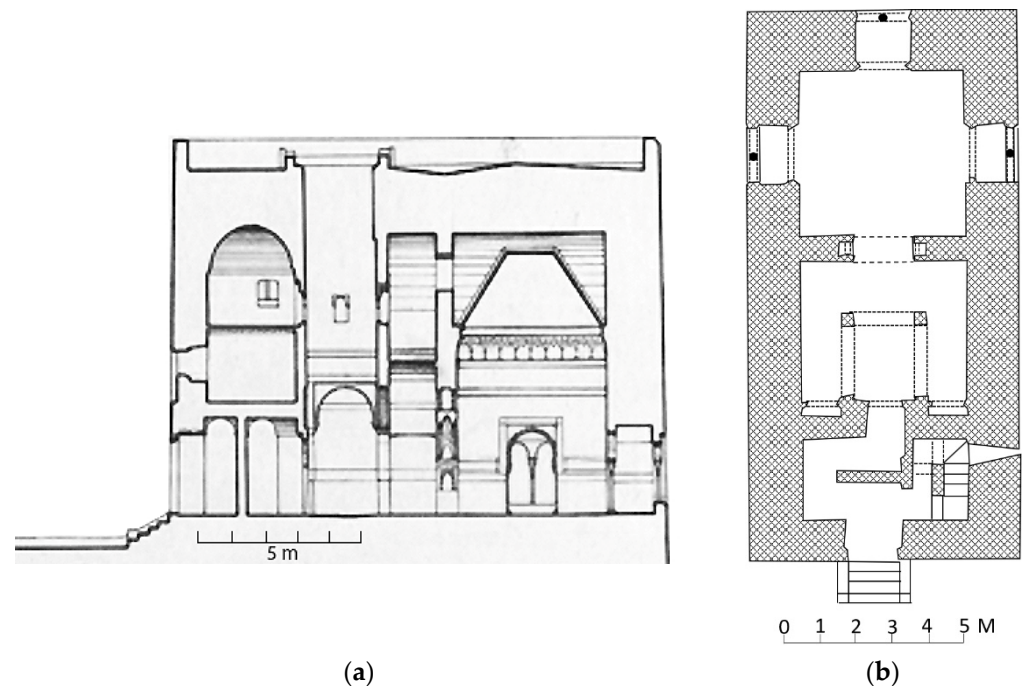


Figure 1. (a,b) Surveys with delineation techniques of the profile and floor plans of the Torre de la Cautiva. The main room has balconies on the walls, while the courtyard or secondary room has no direct lateral exits to the exterior. Compiled by the authors based on documents and plans maintained in the collection of the Patronato de la Alhambra y El Generalife (The Alhambra and Generalife Trust): P-1158_2 and P-4615.

A script was drafted to create a dramatic scene that would take place in different epochs and, therefore, different architectural and decorative moments would be shown in the same piece. The action was meant to observe a certain historical consistency. Some characters inhabited the stage, but they were not overly prominent. In this case, it was not so important to obtain data that were faultless from the architectural point of view, that is to say, the result did not have to consist of an informative HBIM model.

After becoming familiar with the first draft of the script (handling and division into temporal sequences), three strategies were combined, one for each line of work. The first consisted of the application of multi-camera photogrammetry using a vertical rig (see Figure 2) for interiors and walls in their current state of preservation. The second consisted of photogrammetry with a *giratutto* [29] to obtain the characters. Finally, in the third, conventional 3D modeling was used for the setting and assets.

Another of the project's goals, which was aimed at distinguishing this work from those that used similar approaches, was to achieve a look of veracity, or photorealism, by capturing images with low-cost DSLR cameras. The result would be experienced by the audience on a platform that allowed interaction with a freedom of observation on all three axes (pan, tilt, roll), but on principle, without the freedom of displacement. These interaction conditions are known as three degrees of freedom (3DoF) on the scale of

freedom of use [30]. It would also have a sound program to guide and complement what the viewer discovers.



Figure 2. Diagram of the vertical rig with three cameras. Image by the authors.

An additional challenge was the time that was available for data capture, only ten hours spread over one afternoon and the following morning, which was a key factor in choosing the method with which to carry out this task. To complicate matters further, surveying methods to secure control points could not be used, nor lighting supports for photography.

1.3. Choice of Strategy

A wide repertoire of methods is available with which to obtain digital models [12,21], yet the unique nature of each project implies that the solutions employed in earlier strategies are not always the best approaches to adopt, and that the advances in hardware or software are not the only factors to consider [31]. Likely the only generalization that can be made for digital-model-acquisition projects is that there is not yet a methodology that is applicable to the majority of cases.

Among the known strategies, Structure from Motion (SfM) [7,11,13,29,32,33] using only digital camera photography is best adapted to the circumstances associated with the data collection in this study, and it has been used without a set order of shooting [7] or even without checkpoints. This feature constituted a good point of support, since we could not count on having active sensors or Total Stations in our work. Moreover, it was known that stereoscopically configured work reduces the need for a high number of shots [11,34].

Although positive results had been reported with mobile devices [35,36] (which is later than our data collection), much of the success of the work depended on the flexibility and reliability of the cameras in capturing, and therefore the cell-phone option was ruled out. We considered cell phones as offering insufficient and unreliable control over exposure in the conditions in which we had to work, which we would still argue today [36]. The aim was to interfere as little as possible with the physical environment, so the motto was “get in, do it and get out”, just as in photogrammetry projects that involve the police or forensics, which cannot alter the environment in any way whatsoever [37]. With this remit it was clear that the background preparation for the data capture had to be as thorough as possible.

1.4. Photorealism

The great cinematographer Néstor Almendros used to argue that “we must learn to transcend the model, while respecting it” and that “the stylization of an image can sometimes be more important than history and logic” [38]. Obviously, this philosophy cannot be applied to obtaining data for HBIM, yet it is valid to immerse the public in the illusion of photorealism within an environment defined by a script. Similarly, it is not valid to simply confront the user with a 3D graphic model [23] via an HDM that fails to provide the user with any other immediate references to reality. Rather, it is necessary to go further, to create an impression of authenticity and accuracy in the user [20,39], but in this case one that is diachronic. It must be borne in mind that to do so implies moving with the imagination to the past, and the capacity to compare the result of a photograph of that time [40,41] with what is being experienced at that moment.

2. Methodology

This project was approached in three phases that are not necessarily sequential or consecutive: pre-production, production, and post-production. Based on approaches used in the audiovisual industry, these phases were applied to a script and focused on different aspects: inside the tower, obtaining the characters, and the creation of assets. While it is clear that careful preparation is required, as reflected elsewhere in the literature [42,43], phases such as *Data Capture*, *Data Processing* and *Output Presentation* can sometimes be found, which either do not consider shot preparation as a relevant step or do not include it in their first stage [17,29–31,33]. Due to the importance of the decisions that had to be taken in the preparation of the workflow, it is established here as a singular phase, while the presentation of the final result is included in post-production as one of the processes that usually make it up [44].

The general outline of the procedures (Figure 3) will be broken down below, with special attention to the fact that one of the objectives was specifically the development of the workflow.

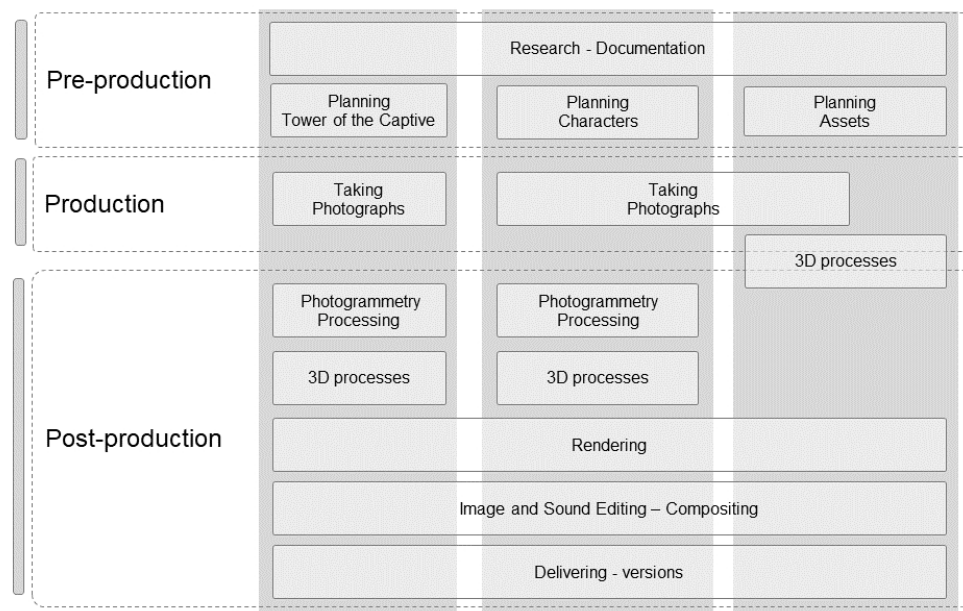


Figure 3. Scheme of the processes employed in the tower project. All the preparative decisions are grouped together in the pre-production phase. Compiled by the authors.

2.1. Pre-Production Stage

The pre-production phase of the pipeline had to ensure that the restrictions that were imposed on the shooting inside the tower were not insurmountable, since the rest of the

lines of work could be readily controlled. After a process of documentation and deliberation about the different possibilities, it was concluded that the only certain method of covering the surfaces in such a short time and without lighting aids was to use a vertical rig of cameras shooting simultaneously (See Figure 2). The preparation of each shot would take more time, but if properly synchronized, the total time required could be divided by the number of cameras used. Initially, calculations were made for a vertical rig consisting of four mid-range DSLR cameras anchored to a rigid, telescoping pole on a tripod. The path of the rig would be parallel to the walls in different passes at different distances, and the relative position of the cameras on the rig would be changed to obtain segments at different heights. According to the specialist literature, this approach has rarely been used for photogrammetry projects and it is much more common to find stereoscopic approaches using two cameras [3,32].

The cameras that were used were four Canon EOS 1200D with 25–80 mm lenses for the main room, and one additional Canon EOS 60D with a 24–70 mm lens for the second room, bringing the total to five simultaneous cameras. The cameras were set to a resolution of 5184×3456 pixels, about 18 MP (megapixels). The sensor of both rooms was identical, and according to the manufacturer had a total of 18.7 MP, but 18 effective MP and a size of $22.3 \text{ mm} \times 14.9 \text{ mm}$ with an aspect ratio of 3:2. This means that the sensor captured 232.47 pixels per mm in width and 231.95 in height (dividing the number of pixels by the number of millimeters). In area: $53,919.7 \text{ pixels}^2/\text{mm}^2$. If photographs were taken at 80 cm from the walls, at a focal length of 25 mm, one would be working with just over three pixels/mm.

The problems of color characterization and exposure could be aggravated by the need to use natural light. The fact that the spaces were either diaphanous or almost diaphanous worked in our favor. The reference for our work was a color chart, such as Color Checker [45], which is often used in film shoots. In order to reduce the possibility of occlusions caused by over- or under-exposures, a fixed aperture was used to ensure a sufficient depth of field and low sensitivity in order to avoid problems with noise reading, and RAW files were also used in order to have the possibility of correcting the exposure values later [29,39,45].

Regarding the characters, the script conceived them as static figures, establishing situations and suggesting activities, but keeping them static so that the scenery would be the most prominent feature. The animation was applied to environmental or weather conditions, so that it would have an impact on the appearance of the surfaces. Research was done on the clothing, styling, and tools with which to dress the models, and they were asked to pose continuously in order to be captured by with photogrammetry methods, but on a *giratutto* and in controlled and constant lighting conditions.

In this phase, research was carried out on the assets that would be used to decorate the main hall. The initial documentation was collected precisely in the Alhambra's own museum, but a number of paintings set in the Nasrid period were also used.

2.2. Production Phase. Shooting Inside the Torre de la Cautiva

Due to the prevailing weather conditions on the days of shooting, i.e., cloudy with clear spells, it was decided to use a vertical rig of three cameras for the main room and four cameras in the courtyard, given the more complicated geometry but simpler decoration of the latter (see Figure 1b). A route was established that ran parallel to the walls, with stops to take shots every 15 cm. At each height, four passes were made in both rooms, starting almost four meters from the parament that was being portrayed and moving closer. To compose the first horizontal band, the cameras were placed on a vertical pole on a tripod, with the camera axis parallel to the ground and perpendicular to the wall at approximately 80, 130 and 170 cm. In the second band, the cameras were settled at approximately two meters, 2.35 m and 2.70 m. Another band was not established due to the risk of excessive camera shaking causing a blurring of the pictures at the exposure speeds that were used. Furthermore, the user experience with 3DoF VR indicates that

the starting point for observation should be at the height of the person experiencing the room, which enables emphasis to be placed on the strong areas in the final result. This way of working requires coordination between the teams that are in charge of the script and photogrammetry, as demanded by some authors [17].

The courtyard needed more time to adjust the exposures and shots, and a Canon 5D camera was used to take cover photographs in hand-held mode at the brightest times of the day. These photographs focused on the most awkward details and the most difficult angles, considering that the main hall had arches with muqarnas and other filigree decorations. This camera was also used to take photographs of the coffered ceiling, which was particularly difficult due to its inverted boat hull shape, making it very difficult to achieve a sufficient depth of field. This situation was aggravated by the minimal relief and the homogeneity of the surface.

The shots of the main room were taken with a focal length of 25mm, at 100 ISO, an aperture of f/8, a manual exposure at 1/6 of a second, and were corrected according to the lighting conditions; manual white balance with presets for dense and light clouds and Color Checker images were taken in both situations (Figure 4).

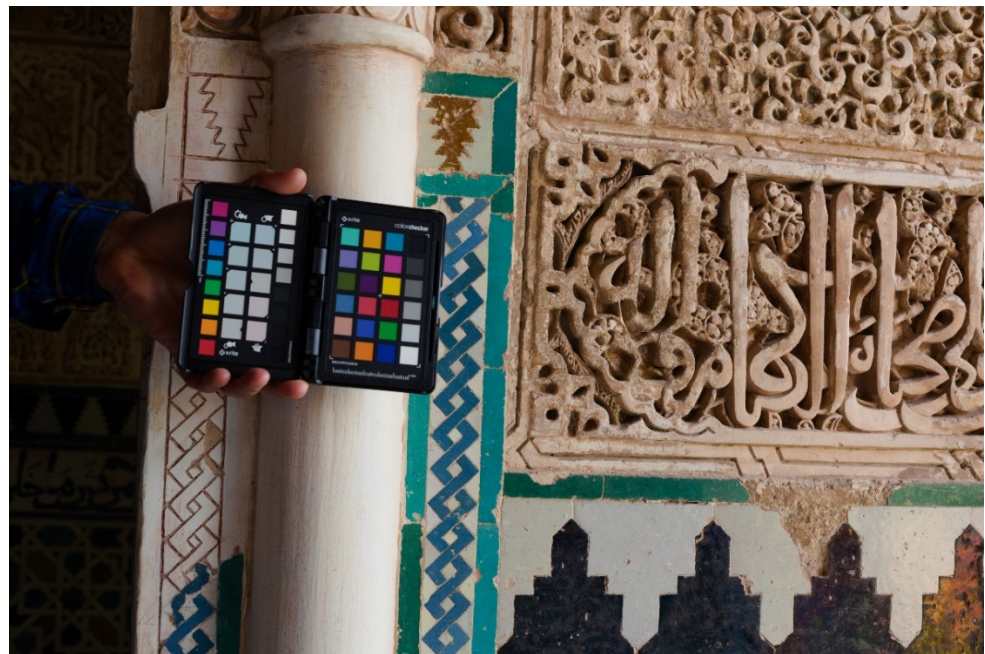


Figure 4. A Color Checker shot near the epigraphic poems on the wall was used to quickly and automatically adjust the color, and to ensure fidelity of the textures and models.

In the inner room, being less accessible to natural light, 20 s exposures were taken. A fourth Canon 60D camera with a 25 mm focal length was attached. The material was simultaneously saved as 30 Mb RAW files and 8 Mb JPEGs.

To obtain the images of the characters, a setup was made with a turntable with tickers to mark control points, a lighting installation with four flash-type fixtures (4 Linkstar DL-500D) and three vertical rigs of five Canon EOS 1200D cameras each [29]. Once characterized with period costumes and styling, the models were asked to pose as still as possible while the *giratutto* was set in motion. After photographing the Color Checker, a shot was taken every 30 degrees (Figure 5a), synchronized to the photographic flash lights through an Arduino ad hoc setup (Figure 5b) and triggering the 15 cameras simultaneously. This was done with two poses of the six different models, sometimes changing the characterization. Finally, the shots of three characters were used, one of them in duplicate.

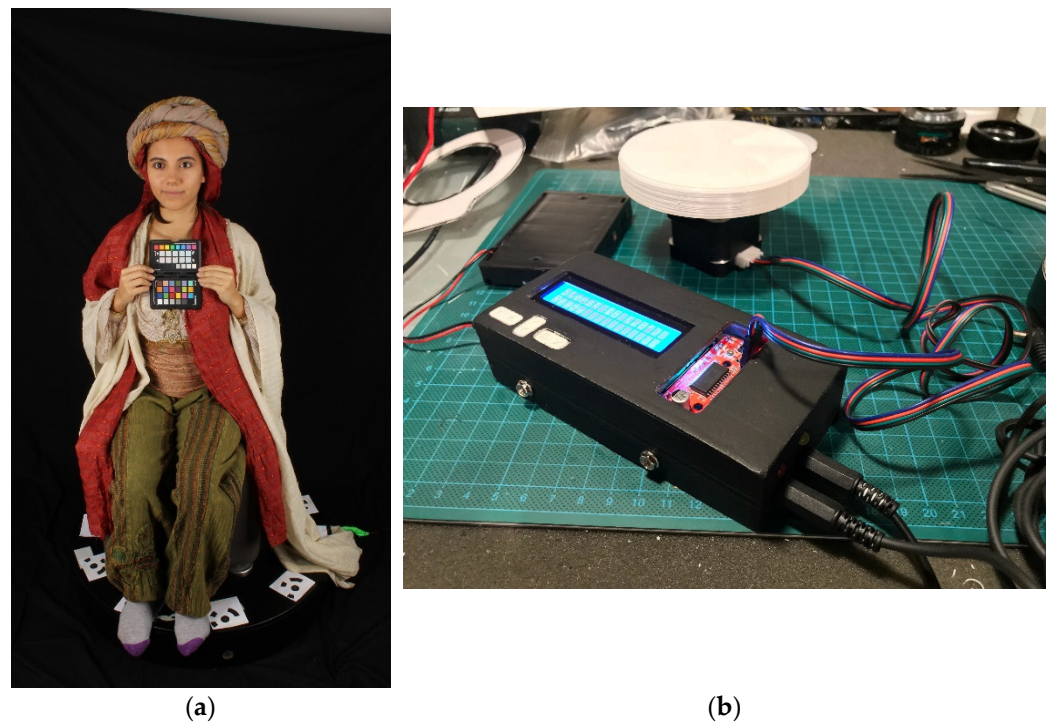


Figure 5. (a,b). Image of one of the models (a) on the giratutto with the control points and the color checker. In (b), the Arduino device used that is connected to a small turntable is shown.

2.3. Post-Production Phase

The first part of the processing (Figure 6), photogrammetry, required an initial step to prepare the photographs, using the RAW files [29], with two objectives: to adjust the color from the images that had been taken from the chart and to try to avoid occlusions due to incorrect exposures (Figure 7a,b).

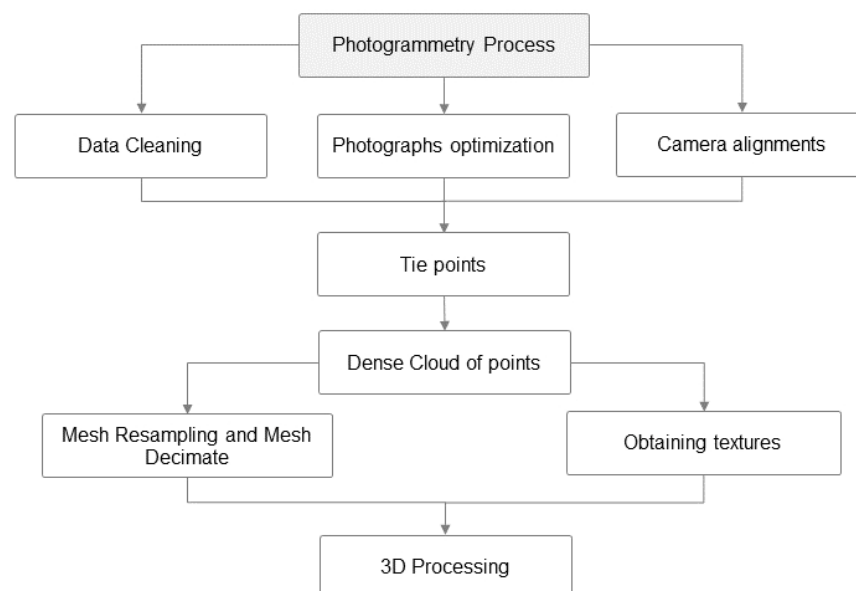


Figure 6. Pipeline for the photogrammetry phase. Compiled by the authors.

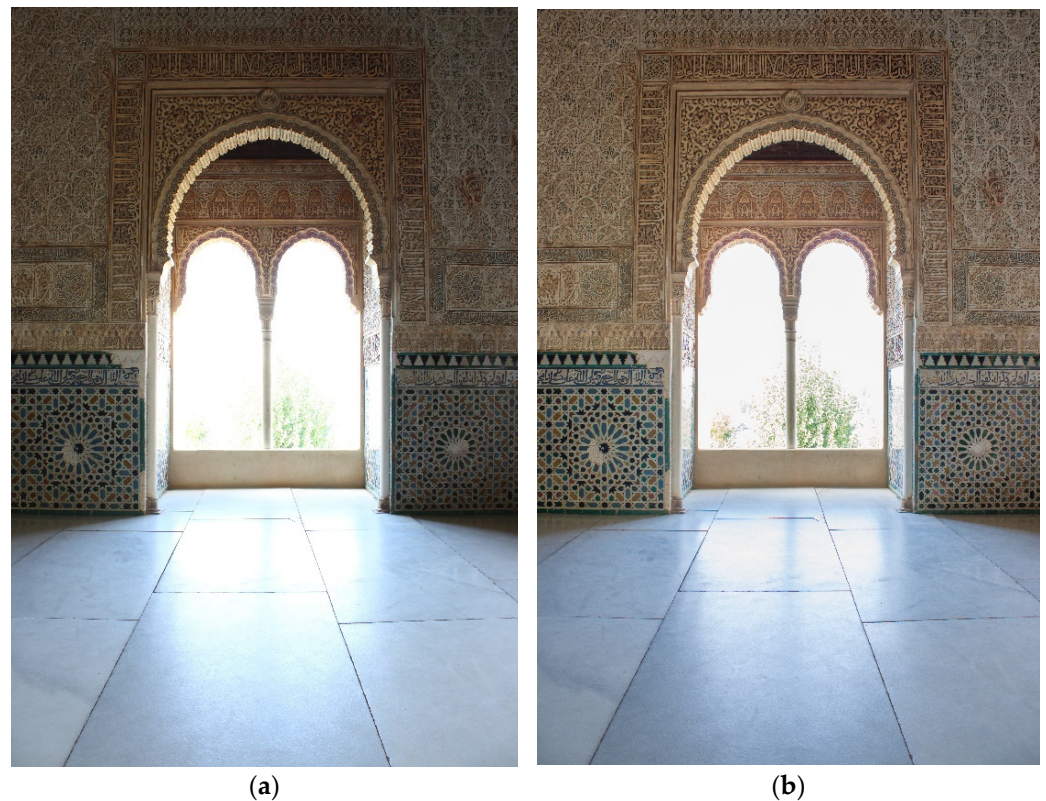


Figure 7. (a,b). Image before and after color correction from the RAW file. Note how the walls are much darker in the image on the left ((a), before applying corrections) owing to the contrast and how the edges of the column on the balcony are barely visible. When using a RAW file, the EVs can be modified to optimize the image before (b) copying it to the photogrammetry software.

Meanwhile, camera alignment tests were carried out to check if the software, Reality Capture 1.3, recognized the camera positions well and provided enough homologous points, which in this case was a number close to 22 million. Through adjustments and corrections, a corrected data set was obtained and redundant points were eliminated from the dense point cloud in order to achieve one that was as faithful as possible to the shots. This was necessary because the software is asked to propose a geometric model that is built with triangles, and this model is usually disproportionately large with a huge number of triangles and is very difficult to handle. In this case, about 50 million triangles were counted in the first version of the mesh.

With careful planning of the photographic sessions, the photogrammetry software can produce a geometry with sufficient detail and with textures that are true to the original surfaces. Once the cloud of points was obtained through photogrammetry, simplifying the mesh proved to be useful for the subsequent tasks, as recently noted elsewhere [17,29]. However, there are programs available that specialize in this type of task, such as Zbrush, which recreates the mesh in a much simpler form through a process known as re-topology. As a result, the mesh was eventually reduced to about 200,000 polygons. This process was necessary for two reasons: first to restore areas that have been left with little or no detail [17], which in our case affected the corners of the floor and some small interior sectors of the balcony arches; second, it offers the possibility of creating clean UVs in order to obtain masks that extend the resolution of the textures using multi-UDIM. If the program originally generated an 8K texture for each room, through this procedure it was possible to have that resolution for each of the maps that were generated, 27 in total (see Figure 8a).

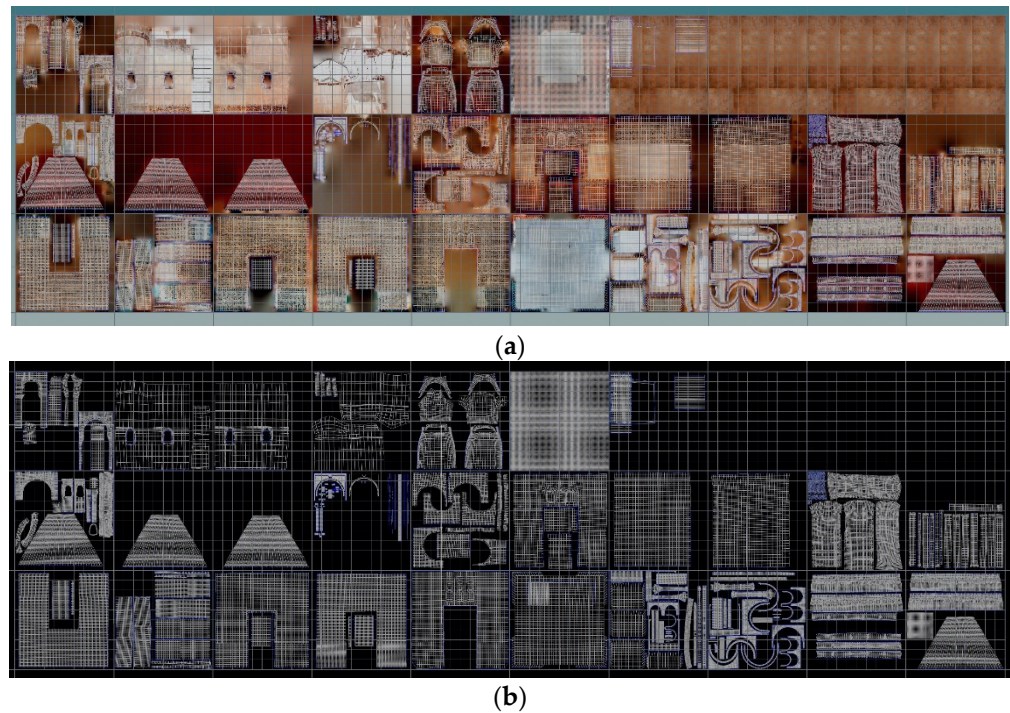


Figure 8. (a,b). UDIMs with textures (a) and masks (b) prepared for back-projection on the optimized model once the re-topology process had been completed.

The textures that were obtained in this way were albedo (from photogrammetry with color and shadow or exposure correction), tile mask, wooden coffered ceiling mask, stone surfaces mask, floor mask, albedo for the artisan scene (because this scene is conceptualized at the time before the room decoration and therefore needs to be colorless), a displacement map, a normal map, a roughness map and a specular map [17,30].

A few days after the capture, the photogrammetry-generated 3D model visualization tests were carried out with the Clarisse iFX 3.5 program. Re-topology was a complex and laborious task, especially the geometry of the arches, in which there were many small details that required significant precision. It was also necessary to intervene in the wooden coffered ceiling, which was difficult to capture due to the lack of light and the lack of detail, which prevented the software from differentiating between sectors and locating the homologous points. Nowadays, in the same programs, there are new algorithms that perform very accurate automatic re-topology, especially for static models, but at the time of this project they did not exist, so everything was done by hand.

The shading and look-dev processes (Figure 9), which are common in the work of 3D artists in audiovisuals or video games, for example [17], were directly responsible for the desired photorealism in this study, since they controlled the perception of the surface of the objects and considered their reaction to the light illuminating the scene and the atmosphere.

The modeling and look-dev of the assets were also performed using Maya and Zbrush. In total about thirty were worked on, although not all of them were included in the final scenes. Carpets, curtains, cushions and pillows, the brazier, the jamuga (a type of medieval chair), the latticework, vases, the rebec, scaffolding, masonry objects and painter's tools, lamps, etc., were all inspired or taken directly from originals that were kept in the Alhambra Museum or the National Archaeological Museum of Madrid.

As mentioned above, these phases do not have to be carried out consecutively and thus, to save time, the integration of the characters and assets in the scenery can be done gradually, starting by obtaining a geometry of materials that are not yet fully worked on or are in wireframe. Positions, sizes, scales and points of view can be harmonized with enough experience to handle scene overlays in this way (see Figure 10a,b).

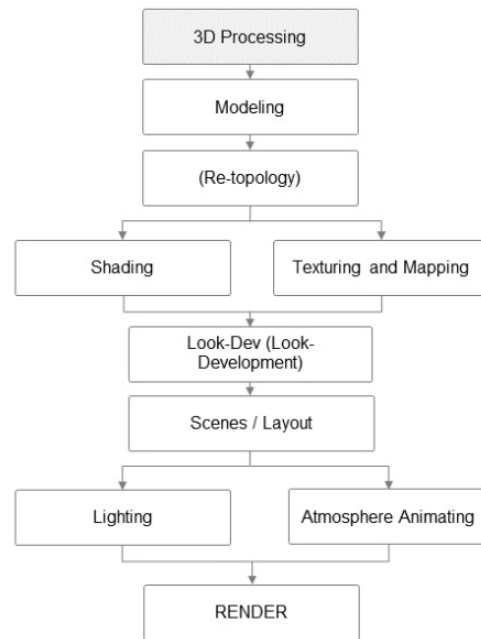


Figure 9. Diagram of the workflow of the last phases of post-production, just before obtaining the final artwork. Own elaboration.

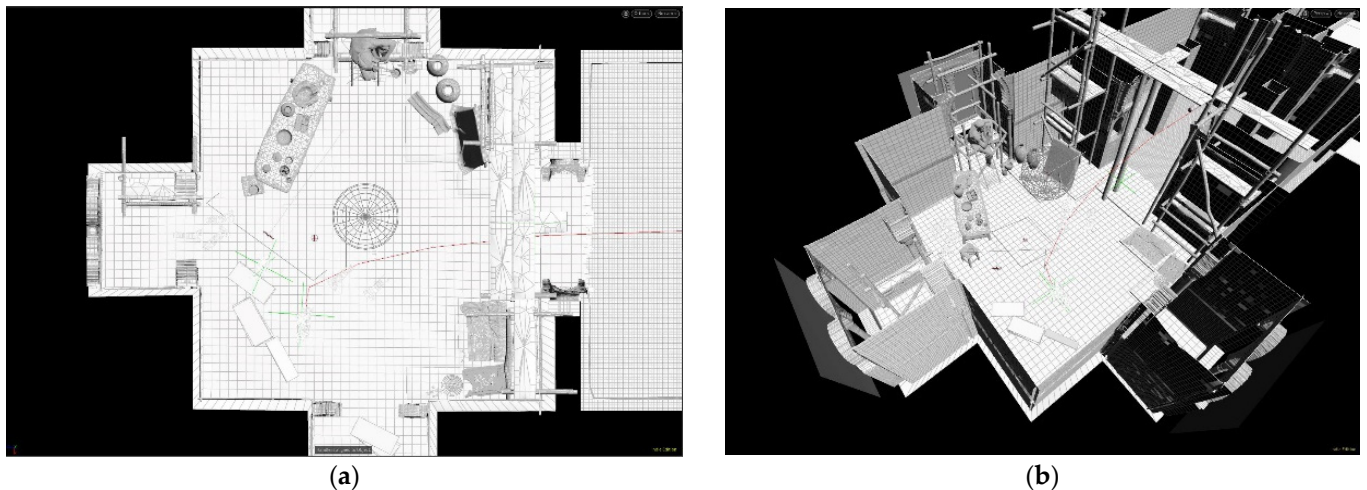


Figure 10. (a,b). Craftsman scene in plan (a) and perspective (b) views in wireframe render. It is crucial to arrange the elements to be able to work interactively with quick previews within the layout of the scenes.

However, in order to check if the scene works, it is necessary to test with more or less the final textures and a setting that brings the scene together properly, after ensuring that the chosen light interacts correctly with the surfaces and the camera positions and animations are well chosen. In addition to other qualities, the view of the integrated scene must not be disjointed. To achieve this, the first rendering tests were performed with Arnold. However, each image took between three and four hours to process at 4K with its optimal parameters (Figure 11), which was unacceptable, especially to observe the result of the animation of lights and cameras and make final decisions about its placement on screen. It was possible to reduce the time for each image at 4K to 25 min using Houdini 17.5 with Octane render 2019 1.2.0, which is a GPU-based engine, and a computer equipped with two NVIDIA 2080 TI GPUs.

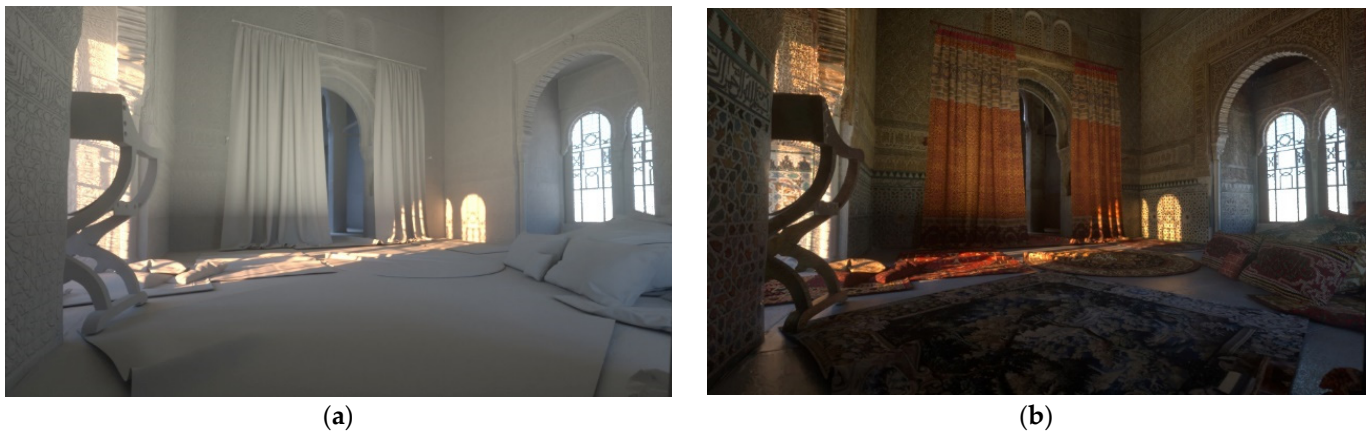


Figure 11. (a,b) Light tests are essential to observe the integration of surfaces and environmental elements in the scene, as well as the suitability of the arrangement of elements and camera positions. For this, it is necessary to launch renders, which in conventional form can take up to four hours using powerful computers for processing.

Following the script, the scenes of the present day, the night storm, the artisan and the captive were composed, while fine-tuning the light and camera animations and creating transitions between them. With a previous low-quality rendering, the sound program was created, and the voiceover, music, effects and Foley were adjusted. This task, together with the sound synchronization, was performed using DaVinci Resolve 16. This program was also used to perform the final rendering at a resolution of 4096×4096 , with Quick Time output format without YUV 4:2:2 compression. A conversion to the 360° 3D stereoscopic format of the BT (Bottom-Top) type was performed so that it could be experienced with Oculus Rift glasses, with an appearance similar to that shown in Figure 12a–c.

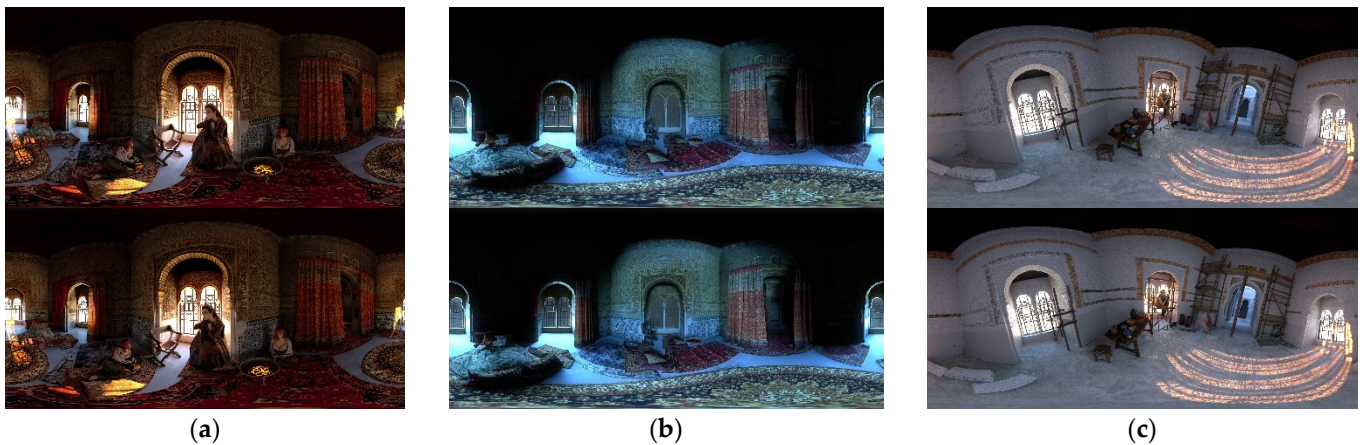


Figure 12. (a–c) Scenes of the captive (a), the night storm (b) and the craftsman (c) in 360 3D Stereoscopic BT format.

3. Results and Discussion

3.1. Multi-Camera Techniques with Rigs

Using a multi-camera data-capture setup ensures the overlapping of images so that each point appears in more than one, which is known since stereoscopy has been used for the same processes [3,11,32,46]. But it allows us to go a step further, covering a larger area in the same amount of time, relative to the number of cameras at each shooting position. A simple technique to prepare the multi-camera shot is to imagine the space in slices (which would be equivalent to the geographical longitude, the vertical sector to be covered), which are represented by each shooting position of a vertical rig, and segments (the geographical

latitude, the horizontal sector to be covered), which are represented by each camera anchor on the tripod.

There is concern about the minimum cost that needs to be addressed for a photogrammetry project [7,11,29,33,45]. While increasing the number of cameras clearly increases the budget, at current prices, it is still much less than covering the costs of using more photographers, a laser scanner or a Total Station [36]. In this project, mid-range DSLR cameras with about 18 Mpix resolutions and conventional optics were used, but mirrorless, medium-format cameras with higher resolution (thus providing more detail from the same number of shots) and faster speeds, because each shot does not involve mechanical displacement, are becoming more affordable. When a large number of shots is involved, time savings are multiplied, especially if bracketing is used to ensure correct exposure, which reduces the possibility of occlusion due to under- or over-exposure. In addition, access to better optics also reduces the exposure time, but raises the budget. Nevertheless, this project was less expensive overall as the costs associated with the number of cameras used were much lower than those that would have been imposed by increasing the number of photographers [45].

Another important issue to foresee is the shooting path. It is often necessary to resort to complex algorithms, such as those of the Traveling Salesman Problem for active sensors [47]. In this case, the chosen route was more or less simple and always parallel to the walls with sufficient shots. To generalize the optimization of the route, one should perhaps resort to artificial intelligence (AI), which considers factors such as the geometry of the object, the available equipment, the environmental conditions and the demands of the script [17]. Any software used must be able to interpret camera positions and locate sufficient homologous points, thereby avoiding occlusions. In our case, it was important to cover all possible angulations in order to obtain a sufficient number of overlapping points, but equal care must be taken not to oversize the shots, as it makes the project unmanageable. On the other hand, when using a multi-camera setup, coordination errors that may exist are multiplied, so extreme care must be taken in this regard. Other factors are focus and exposure, which are explained below.

Some 1900 photographs were taken in the tower (7 cameras \times 4 passes \times 2 heights \times 29–35 rig positions), and some 800 without a tripod. Among them, about 2500 were used for the photogrammetric models. For the characters, about 2150 pictures were taken (6 models \times 2 poses \times 12 shots \times 15 cameras) and about 720 were used.

The time required to make adjustments before each shot increases when using the multi-camera technique. The exposure and focus must be set manually, even if some parameters are automatic. Again, affordable technology facilitates the operation, as nowadays it is common to control camera viewfinders remotely (both the image displayed and the overlays) as they are the main operations for exposure, focus and shooting.

Another problem was camera shaking; in order to gain height and ensure angles that might otherwise cause occlusions, the cameras had to be raised as high as the pole would allow without swaying. Maintaining stability with light equipment three meters off the ground was difficult, but essential when the shots exceeded 1/30th of a second. This circumstance arose in virtually all of the cases in our work. However, the results were equally dramatic, enabling views from the coffered ceiling with the viewer positioned four meters above the floor to be included in the final experience.

There is no doubt that a robotic system that incorporates AI, which is capable of making some decisions regarding settings and routes and also of detecting and solving possible occlusions, would ultimately simplify and reduce the cost of projects, leading to optimal results.

3.2. The Importance of Preparation in Pre-Production

Audiovisual projects such as film animation or video games are exceptionally complex, and the procedures they have been developing and turning into knowledge with their experience can certainly be beneficial to apply to a photogrammetry challenge that should

have a photorealistic final look. With this conviction, this project has assumed some of their techniques.

A key factor for the success of the project, given the restrictions that were to be experienced during data collection, was to be aware of the relevance of the pre-production-style decision-making process. What had been studied and agreed upon during this phase significantly determined the subsequent capacity for action, since it contained an element that was lacking in both the filming and post-production stages, i.e., time [48]. In the specialized literature, significant relevance is always given to the duration and intensity of this phase [49,50].

The first decision was to work on a draft script with a fixed number of sequences. It was prepared according to the capabilities that the project wanted to demonstrate: the creation of environments, the simulation of past scenarios with naturalness, and mastery over the scenery. This mastery was especially directed towards the fidelity of the geometry, the variety in the application of textures, and the animation of light sources.

Foresight and the careful preparation of the capture allows for decisions to be made ahead of time in terms of overcoming the main challenges, which allows more time to be dedicated to study and optimization of the workflow, thereby avoiding confusion. This factor will also help to define the areas where authenticity and accuracy are more or less important, so that the script does not conflict with the pre-production workflow of time optimization. On the contrary, storytelling should be another criterion by which to define technical parameters such as the number of polygons and their layout [17]. It is important to establish fluid communication between those who develop the script and the members of the team responsible for taking the shots and processing the digital models in order to optimize work times and effort.

3.3. Exposure and Color Correction

In cinema, a scientific approach to questions concerning the control of color and exposure when shooting has long been employed. It is common for all image- and video-editing programs to implement procedures with externally calibrated measurements [45], using very accurate meters and different procedures to control EVs, as well as employing Color Checker. These procedures, which are also described in the literature specialized in photogrammetry [29,45] were used in this project to solve the color-characterization problem and to avoid occlusions due to exposure problems. By obtaining RAW and compressed JPEG files simultaneously, a safety margin was established in the acquisition that neutralized the risks associated with working with natural light. In fact, during the days of data capture, the sky was very cloudy in Granada and at times quite dark. The use of RAW files allowed us to vary the exposure values and, to some extent, to correct the fluctuations and prevent over- or under-exposure.

In terms of focus, there is always a moment when the image is zoomed in when the circle of confusion is no longer small enough and, therefore, when further scaling up means losing sharpness. Obtaining the correct focus in the shot is very important both for the subsequent definition of the textures and for the photogrammetry program to determine where the points of interest are, and to be able to identify the homologous points. In this project, according to the previsions made in pre-production, we wanted to ensure a minimum aperture of $f/8$ in order to obtain a sufficient depth of field. In this way, the details of the decorations (4 cm fretwork or longer muqarnas) could be captured without the need to correct the focus at each rig position. Such a decision implied a trade-off that increased the exposure time, which ran the risk of blurring the edges and consequently of increasing the time needed for stabilization and exposure. This time can be carefully calculated so that it is less than the time that would be invested in an eventual focus correction. An alternative solution would be to increase the sensitivity, which was kept at 100 ASA, but such an operation would have the consequence of increasing the noise in the images, which is detrimental to the unequivocal obtention of homologous points. Finally,

thanks to this set of decisions, it was ensured that the results surpassed what the playback or viewing platforms are currently capable of resolving in terms of fluidity and sharpness.

3.4. Photorealism

Shading and look-dev processes are crucial for making the scenery, assets and characters appear photorealistic on screen, but lighting and environmental effects are also equally important. In this project, a detailed study of each character in the environment, light and optics was carried out (see Figure 13a–c), and such a challenge requires a lot of time with conventional methods, so it is recommended, after the experience, to use a rendering engine for testing.



Figure 13. (a–c). Some of the lighting, framing and environment tests that were carried out with the captive character. Note the variations in the depth of field due to the use of different optics in the simulation.

Sometimes a large number of possibilities for configuration or modification can be counterproductive in achieving clarity in the final results, even making them less convincing. Nevertheless, such tools make it possible to obtain well-integrated scenes that give the illusion of coming close to what historical reality must have been like, or what could now be interpreted as such. In this sense, the audiovisual industry’s way of proceeding consists of trying to make the integration of the different elements invisible, so that even experts find it difficult to reverse engineer and extract the method that was used to achieve this result.

Photorealism aims to provide the audience with a product that seems natural, such that studies of user experience and acceptance should be considered in order to determine if this is achieved. Strictly speaking, by definition, no image can be photorealistic if it is intended to portray a past era, as it will resemble, at best, what other previous artists have imagined those realities to be. If 3D artists are given the opportunity to work closely with those in charge of the care of monuments and with specialists such as archeologists and architects, many possibilities open up for their conservation, or at least for the simulation of interventions and recreations.

In this project, the starting point was a narrative script that placed the story in the realm of fiction. However, under certain conditions and scales, the use of photorealism is not incompatible with the possibility of obtaining the necessary and sufficient data to make the HBIM of the heritage sites usable by conservators and restorers, from a data-collection method that is more or less accessible and rigorous with the color parameters and with elements of anchorage or location. For the objective of photorealism, accuracy and fidelity are not as important as the feeling of naturalness and coherence with the imagination of the audience.

It is true that the desire for photorealism pushes a project towards obtaining an excessive amount of data, thereby generating problems of manageability. For now, not all systems and formats can handle all of these models and sometimes the rendering capacity is insufficient. However, if the scenes have been set up with consistency and are ambitious, the renderings can be improved and adapted to systems with better performance in the near future.

3.5. Re-Topology

Coinciding in time with the work presented in this article, but more diligent in publishing their results, the text 'New realities for Canada's Parliament: A workflow for preparing Heritage BIM for game engines and Virtual Reality' [17] already explains clearly and sufficiently the importance of re-topology in the processes of building 3D models and, therefore, in photogrammetry projects. It does not deny that it could always have been photographed better and more effectively and, as is proposed in the mentioned research, that it would have been helpful to have a previous understanding of the script with respect to the points of most interest to the viewers, in order to make decisions during the data capture and processing that would have helped in the composition and the rendering.

Without going into the depths of the analysis, the 3D models that were directly produced by the data from photogrammetry platforms far exceeded the dimensions that were manageable by graphics cards and processors, however powerful they may have been, and yet such a profusion of data does not result in improved accuracy or fidelity, nor photorealism, as we have seen. An intermediate process, re-topology, is necessary to simplify the models, retouch possible occlusions or imperfections and produce textures that, once back-projected onto the new model, allow greater detail that is more similar to the real scenarios, and much greater fluidity in the interaction with the scenes.

The specific issue of viewer interaction with the scene also needs to be addressed, as there are specific methods that can improve the performance of the platforms. At the end of 2015, Nick Kraaman explained in his Headjack blog [51] the progress made by different professionals to develop scenes in which viewers would be immersed and equipped with HMD. One of the points made was the possibility of covering up areas of inactivity with static images instead of video, which would make interaction in the other areas much smoother and take up far fewer system resources.

There is no doubt that platforms will continue to improve, as will hardware devices, and it is clear that, by knowing the geography of the scene well and foreseeing the points of greatest interest, it will be possible to make better use of resources.

3.6. Integration and the Problem of Previsualization

Logic or common sense establishes an order when it comes to the integration of all the elements of the scenes. Once the geometries have been created, the textures made available, the look-dev has been worked on and the lighting, camera positions and eventual environmental effects and animations have been thought of, it is time to see what the scenes will look like.

But working according to a script has advantages: the challenges are already established, the range of possible decisions is narrower, a narrative structure that makes sense can be followed and the dimension of the result is more or less clear from the beginning. It is also possible to fit the pieces together without all the elements being finished, so that processes can be followed. For example, in this project it was possible to work in sequences, fitting elements into the layout and studying camera trajectories before the textures were applied.

As the time will ultimately arrive to check what the final result will look like, rendering must be performed. The usual and most sensible thing to do is to choose some frames first and process them, and then do the same with small sequences, using definitive textures (much more laborious for the machines) or materials depending on what you want to test.

Scenes with large amounts of information require a lot of calculation time and, therefore, necessary decisions must be postponed until the end of the computer processes. The experience of this project before and after using render engines for these tasks is clear: the entire scene must be passed to an engine of these characteristics in order to speed up the decision-making process as much as possible before the final calculations. The time required for pre-testing is drastically reduced in this way. This assertion is all the more valid when the final layout of the scenes is less studied, i.e., if there is no script, it is more essential to carry out tests with immediate visualizations.

4. Conclusions

The Torre de la Cautiva is located in one of the walls of the Alhambra in Granada, a complex named a World Heritage Site in 1984, and is one of its enclaves to which the general public does not usually have access.

Bearing in mind its historic value and the fact that it can rarely be enjoyed in person, the challenge of creating a photorealistic 3D model of its interior was posed. This initiative was intended to serve both conservators and restorers, and as a DCH site for public dissemination and entertainment. Throughout this article we have explained the workflow that achieves this.

Regarding the execution of the project, it should be noted that the data collection was carried out with important restrictions: only ten hours to shoot, using only natural light, and with no cables or control points. The model was built with low-cost photogrammetry techniques, using conventional DSLR cameras as passive sensors. The display was planned on 360° Stereoscopic VR platforms with interactivity and 3DoF on the scale of freedom of action.

The script contemplated several scenes that predominantly focused on the past, although one of them was set in the present day. The others recreated a night storm, a typical scene of the period in which the interior of the tower was decorated, and a third evoking the routine atmosphere of the captive princess's lodging. In addition, three lines of work were defined for the script: that of the stage, which should be given maximum prominence, that of the characters with a narrative sense and that of the assets, fulfilling the function of ambience and decoration. A specific procedure was used to obtain data for each of these lines.

Without reaching the demands that HBIM informative models may have, a certain historical and traditional coherence with the period scenes was attempted, as well as a certain level of detail and fidelity to the original decoration.

Although in agreement with the academic literature in many points and starting from a script and a desire for photorealism, this project also adopted some procedures commonly employed in the audiovisual industry, which is accustomed to this type of complexity. The pre-production process is therefore analyzed in more detail within its workflow.

Since it is difficult to reach an agreement on the meaning of photorealism, especially if the past is to be shown, it was established as a principle of the project that it could be perceived naturally and coherently by the viewer. In this case, moreover, being accurate with geometry and color characterization was assumed as being of the utmost importance.

Another common process in the audiovisual industry that was an important part of the project workflow was the multi-camera work, which was carried out with vertical rigs and careful planning.

In the post-shooting processes, the importance of re-topology to obtain simpler meshes and of UDIM textures to retain great definition of detail was clear, as was the importance of the script to be able to work separately on the integration of the elements in the scenes, their lighting, environmental effects, and animation.

Two key ideas for future work stem from the experience of this project: the convenience of using robotic devices coupled to AI algorithms to optimize decisions during the data acquisition process, and the adaptation of rendering engines, not only for final viewing or creation of VR environments, but also for previsualization and tests, since they radically reduce the time required to perform different procedures.

Author Contributions: Conceptualization, A.J.B., X.P.S., M.A.; methodology, A.J.B., X.P.S., M.A.; validation, A.J.B., X.P.S., M.A., E.M.S., J.S., Á.G.M.; investigation, A.J.B., X.P.S., M.A., Á.G.M.; resources, M.A., M.G.-V.; data curation, M.G.-V., J.S., R.C.; writing—original draft preparation, A.J.B.; writing—review and editing, A.J.B., X.P.S., E.M.S.; visualization, A.J.B., M.A., M.G.-V., R.C.; supervision, A.J.B., X.P.S., M.A., E.M.S., J.S., Á.G.M.; funding acquisition, Á.G.M. All authors have read and agreed to the published version of the manuscript.

Funding: This work was funded by of the Ministry of Science and Innovation of Spain, project number RTI2018-097633-A-I00, ‘Photonic restoration applied to cultural heritage: Application to Dalí’s painting: Two Figures’.

Institutional Review Board Statement: Not applicable.

Informed Consent Statement: Not applicable.

Acknowledgments: The authors wish to thank Miopía FX, GVAM SL, Voxel School of Digital Arts and its students, as well as the Patronato de la Alhambra y El Generalife de Granada (Alhambra and Generalife Trust).

Conflicts of Interest: The authors have no conflict of interest to declare. The funders had no role in the design of the study; in the collection, analyses, or interpretation of data; in the writing of the manuscript, or in the decision to publish the results.

References

1. The Athens Charter for the Restoration of Historic Monuments—1931—International Council on Monuments and Sites. Available online: <https://www.icomos.org/en/resources/charters-and-texts/179-articles-en-francais/ressources/charters-and-standards/167-the-athens-charter-for-the-restoration-of-historic-monuments> (accessed on 6 December 2021).
2. Icomos. The Venice Charter. 1964. Available online: <https://www.icomos.org/venicecharter2004/> (accessed on 12 December 2021).
3. Buill, F.; Jordana, J.J.R.; Andrés, M.A.N. *Fotogrametría Arquitectónica*; Universitat Politècnica de Catalunya: Barcelona, Spain, 2008.
4. Declaration of Rome (1983)—International Council on Monuments and Sites. Available online: <https://www.icomos.org/en/resources/charters-and-texts/179-articles-en-francais/ressources/charters-and-standards/185-declaration-of-rome> (accessed on 6 December 2021).
5. Icomos. Charter for the Conservation of Historic Towns and Urban Areas (The Washington Charter). 1987. Available online: https://www.icomos.org/charters/towns_e.pdf (accessed on 12 December 2021).
6. Negro Ponte, N. *El Mundo Digital*; Ediciones B: Barcelona, Spain, 1997.
7. Santagati, C.; Lo Turco, M.; Bocconcino, M.M.; Donato, V.; Galizia, M. 3D Models for All: Low-Cost Acquisition through Mobile Devices in Comparison with Image Based Techniques. Potentialities and Weaknesses in Cultural Heritage Domain. *Int. Arch. Photogramm. Remote Sens. Spat. Inf. Sci.* **2017**, *XLII-2/W8*, 221. [CrossRef]
8. Remondino, F.; Rizzi, A. Reality-based 3D documentation of natural and cultural heritage sites—Techniques, problems, and examples. *Appl. Geomat.* **2010**, *2*, 85. [CrossRef]
9. Banfi, F.; Brumana, R.; Stanga, C. A Content-Based Immersive Experience of Basilica of Sant’ambrogio in Milan: From 3d Survey to Virtual Reality. *Int. Arch. Photogramm. Remote Sens. Spat. Inf. Sci.* **2019**, *XLII-2/W11*, 159. [CrossRef]
10. El-Said, O.; Aziz, H. Virtual Tours a Means to an End: An Analysis of Virtual Tours’ Role in Tourism Recovery Post COVID-19. *J. Travel Res.* **2021**, 0047287521997567. [CrossRef]
11. Westoby, M.J.; Brasington, J.; Glasser, N.F.; Hambrey, M.J.; Reynolds, J.M. ‘Structure-from-Motion’ photogrammetry: A low-cost, effective tool for geoscience applications. *Geomorphology* **2012**, *179*, 300. [CrossRef]
12. Bustillo, A.; Alaguero, M.; Miguel, I.; Saiz, J.M.; Iglesias, L.S. A flexible platform for the creation of 3D semi-immersive environments to teach Cultural Heritage. *Digit. Appl. Archaeol. Cult. Herit.* **2015**, *2*, 248. [CrossRef]
13. Inzerillo, L. smart SfM: Salinas Archaeological Museum. *Int. Arch. Photogramm. Remote Sens. Spat. Inf. Sci.* **2017**, *XLII-2/W5*, 369. [CrossRef]
14. Zita Sampaio, A.; Gomes, A.M.; Sánchez-Lite, A.; Zulueta, P.; González-Gaya, C. Analysis of BIM Methodology Applied to Practical Cases in the Preservation of Heritage Buildings. *Sustainability* **2021**, *13*, 3129. [CrossRef]
15. Angulo-Fornos, R.; Castellano-Román, M. HBIM as Support of Preventive Conservation Actions in Heritage Architecture. Experience of the Renaissance Quadrant Façade of the Cathedral of Seville. *Appl. Sci.* **2020**, *10*, 2428. [CrossRef]
16. Murphy, M.; McGovern, E.; Pavia, S. Historic Building Information Modelling—Adding intelligence to laser and image based surveys of European classical architecture. *J. Photogramm. Remote Sens.* **2013**, *76*, 89. [CrossRef]
17. Pybus, C.; Graham, K.; Doherty, J.; Arellano, N.; Fai, S. New Realities for Canada’S Parliament: a Workflow for Preparing Heritage Bim for Game Engines and Virtual Reality. *Int. Arch. Photogramm. Remote Sens. Spat. Inf. Sci.* **2019**, *XLII-2/W15*, 945. [CrossRef]
18. Al-Muqdad, F. Assessing the Potentials of Heritage Building Information Modelling (Hbim) in Damaged Heritage Reconstruction. In Proceedings of the 36th Annual ARCOM Conference, Leeds, UK, 7–8 September 2020; Scott, L., Neilson, C.J., Eds.; ARCOM: Leeds, UK, 2020; pp. 25–35.
19. Benitez, A.J.; Sánchez Cid, M.; Armenteros, M. Fotogrametría en el audiovisual. Perspectivas de evolución. In *Los Nuevos Retos en Ciencias Sociales, Artes y Humanidades*; Gedisa: Barcelona, Spain, 2018; pp. 31–45.
20. Roussou, M.; Drettakis, G. Photorealism and Non-Photorealism in Virtual Heritage Representation. In Proceedings of the 4th International Symposium on Virtual Reality, Archaeology and Intelligent Cultural Heritage, Brighton, UK, 5–7 November 2003. [CrossRef]
21. Pavlidis, G.; Tsiafakis, D.; Koutsoudis, A.; Arnaoutoglou, F.; Tsioukas, V.; Chamzas, C. Preservation of Architectural Heritage through 3D Digitization. *Int. J. Archit. Comput.* **2007**, *5*, 221. [CrossRef]

22. Slater, M.; Wilbur, S. A Framework for Immersive Virtual Environments (FIVE): Speculations on the Role of Presence in Virtual Environments. *Presence Teleoperators Virtual Environ.* **1997**, *6*, 603. [CrossRef]
23. Shashi, M.; Jain, K. Use of Photogrammetry in 3D Modeling and Visualization of Buildings. *ARPN J. Eng. Appl. Sci.* **2007**, *2*, 37.
24. Eisenstein, S.M. *Teoría y Técnica Cinematográficas*; Ediciones Rialp: Madrid, Spain, 1989.
25. Irving, W. Manuscript of The Chronicle of the Conquest of Granada: Isabella Stewart Gardner Museum. Available online: <https://www.gardnermuseum.org/experience/collection/28622> (accessed on 4 December 2021).
26. Martínez de la Rosa, F. Doña Isabel de Solís, Reina de Granada. 1837. Available online: <http://www.cervantesvirtual.com/obra-visor/dona-isabel-de-solis-reyna-de-granada-novela-historica--0/html/> (accessed on 5 November 2021).
27. Marques, S. Mixed media object: Large and fragile structure—Victoria and Albert Museum. Available online: <http://www.vam.ac.uk/content/journals/conservation-journal/issue-48/mixed-media-object-large-and-fragile-structure/> (accessed on 6 December 2021).
28. Milgram, P.; Kishino, F. A Taxonomy of Mixed Reality Visual Displays. *IEICE Trans. Inf. Syst.* **1994**, *E77-D*, 1–15.
29. Apollonio, F.I.; Fantini, F.; Garagnani, S.; Gaiani, M. A Photogrammetry-Based Workflow for the Accurate 3D Construction and Visualization of Museums Assets. *Remote Sens.* **2021**, *13*, 486. [CrossRef]
30. Dhanda, A.; Reina Ortiz, M.; Weigert, A.; Paladini, A.; Min, A.; Gyi, M.; Su, S.; Fai, S.; Santana Quintero, M. Recreating Cultural Heritage Environments for Vr Using Photogrammetry. *Int. Arch. Photogramm. Remote Sens. Spat. Inf. Sci.* **2019**, *XLII-2/W9*, 305. [CrossRef]
31. Tucci, G.; Bonora, V.; Conti, A.; Fiorini, L. Digital Workflow for the Acquisition and Elaboration of 3D Data in a Monumental Complex: The Fortress of Saint John the Baptist in Florence. In Proceedings of the 26th International CIPA Symposium 2017, Ottawa, ON, Canada; 2017; pp. 679–686.
32. Moyano, J.; Nieto-Julián, J.E.; Bienvenido-Huertas, D.; Marín-García, D. Validation of Close-Range Photogrammetry for Architectural and Archaeological Heritage: Analysis of Point Density and 3D Mesh Geometry. *Remote Sens.* **2020**, *12*, 3571. [CrossRef]
33. Rahaman, H.; Champion, E. To 3D or Not 3D: Choosing a Photogrammetry Workflow for Cultural Heritage Groups. *Heritage* **2019**, *2*, 112. [CrossRef]
34. Furukawa, Y.; Ponce, J. Accurate, Dense, and Robust Multiview Stereopsis. *IEEE Trans. Pattern Anal. Mach. Intell.* **2010**, *32*, 1362. [CrossRef]
35. Rehany, N.; Barsi, A.; Lovas, T. Capturing Fine Details Involving Low-Cost Sensors –a Comparative Study. *Int. Arch. Photogramm. Remote Sens. Spat. Inf. Sci.* **2017**, *XLII-2/W8*, 213. [CrossRef]
36. Khalloufi, H.; Azough, A.; Ennahahi, N.; Kaghat, F.Z. Low-Cost Terrestrial Photogrammetry for 3D Modeling of Historic Sites: A Case Study of the Marinids’ Royal Necropolis City of Fez, Morocco. *Mediterr. Archaeol. Archaeom.* **2020**, *2*, 257–272. [CrossRef]
37. Abate, D.; Toschi, I.; Sturdy-Colls, C.; Remondino, F. A Low-Cost Panoramic Camera for the 3D Documentation of Contaminated Crime Scenes. *Int. Arch. Photogramm. Remote Sens. Spat. Inf. Sci.* **2017**, *XLII-2/W8*, 1. [CrossRef]
38. Almendros, N. *Días de Una Cámara*; Seix Barral: Barcelona, Spain, 1990.
39. Mueller, P.; Vereenoghe, T.; Vergauwen, M.; Gool, L.V.; Waelkens, M. Photo-Realistic and Detailed 3D Modeling: The Antonine Nymphaeum at Sagalassos (Turkey). In Proceedings of the 32nd Conference on Computer Applications and Quantitative Methods to Archeology. CAA 2004, Prato, Italy, 13–17 April 2004; pp. 1–10.
40. Ferwerda, J.A. Three varieties of realism in computer graphics. In Proceedings of the Electronic Imaging VIII, 2003, Santa Clara, CA, USA, 17 June 2003. [CrossRef]
41. Tang, R.; Fritsch, D. Correlation Analysis of Camera Self-Calibration in Close Range Photogrammetry. *Photogramm. Rec.* **2013**, *28*, 86. [CrossRef]
42. Fraser, C.S. Network design considerations for non-topographic photogrammetry. *Photogramm. Eng. Remote Sens.* **1984**, *50*, 1115–1126.
43. James, M.R.; Chandler, J.H.; Eltner, A.; Fraser, C.; Miller, P.E.; Mills, J.P.; Noble, T.; Robson, S.; Lane, S.N. Guidelines on the use of structure-from-motion photogrammetry in geomorphic research. *Earth Surf. Processes Landf.* **2019**, *44*, 2081. [CrossRef]
44. Benítez, A.J.; Jiménez, I.; Sánchez Cid, M. Conceptos de Postproducción. In *Una Perspectiva Contemporánea*; Utray Armenteros, M.F., Benítez, A.J., Eds.; Postproducción digital: Madrid, Spain, 2015; p. 13.
45. Gaiani, M.; Apollonio, F.; Ballabeni, A.; Remondino, F. Securing Color Fidelity in 3D Architectural Heritage Scenarios. *Sensors* **2017**, *17*, 2437. [CrossRef] [PubMed]
46. Martínez Rodríguez, S. *Evaluación en Campo de Una Nueva Técnica Fotogramétrica de Rango Cercano y Bajo Coste Basada en la Correlación Automática de Imágenes*; U de Santiago de Compostela Campus de Lugo: Lugo, Spain, 2014. Available online: <https://minerva.usc.es/xmlui/handle/10347/12884> (accessed on 20 November 2021).
47. Díaz-Vilariño, L.; Frías, E.; Balado, J.; González-Jorge, H. Scan Planning and Route Optimization for Control of Execution of as-Designed Bim. *Int. Arch. Photogramm. Remote Sens. Spatial Inf. Sci.* **2018**, *XLII-4*, 143. [CrossRef]
48. Rea, P.W.; Irving, D.K. *Producción y Dirección de Cortometrajes y Vídeos*; Instituto Oficial de Radio y Televisión: Madrid, Spain, 2002.

49. Millerson, G.; Owens, J. *Television Production*, 14th ed.; Focal Press/Elsevier: Amsterdam, The Netherlands; Boston, MA, USA, 2009; p. 399.
50. Rabiger, M. *Dirección Cinematográfica: Técnica y Estética*; Ediciones Omega: Barcelona, Spain, 2009.
51. Kraaman. The Best Encoding Settings for Your 4k 360 3D VR Videos. Available online: <https://headjack.io/blog/best-encoding-settings-resolution-for-4k-360-3d-vr-videos/> (accessed on 20 November 2021).

Article

Technical Non-Invasive Study of an 18th Century Novo-Hispanic Panel Painting

Miguel Pérez^{1,2}, Nathael Cano^{1,3} , José Luis Ruvalcaba-Sil¹, Alejandro Mitrani¹  and Oscar G. de Lucio^{1,*} 

- ¹ Laboratorio Nacional de Ciencias para la Investigación y la Conservación del Patrimonio Cultural, Instituto de Física, Universidad Nacional Autónoma de México, Apartado Postal 20-364, Ciudad de México 01000, Mexico; miguel.pf@ciencias.unam.mx (M.P.); nathcano@comunidad.unam.mx (N.C.); sil@fisica.unam.mx (J.L.R.-S.); mitrani@fisica.unam.mx (A.M.)
- ² Posgrado en Ciencia e Ingeniería de Materiales, Universidad Nacional Autónoma de México, Ciudad de México 04510, Mexico
- ³ Posgrado en Historia del Arte, Universidad Nacional Autónoma de México, Ciudad de México 04510, Mexico
- * Correspondence: olucio@ciencias.unam.mx

Abstract: *Purísima Concepción*, a large-format and unusual panel painting attributed to the 18th century, based on style and the common aspect of the visual tradition of the Virgin Mary found in the Viceroyalty of New Spain, is sheltered at the *Museo Ex-convento San Agustín Acolman-INAH*, México, an institution opened in late 1920, and one of the oldest museums in México. In this work, we present the material characterization of the surface layer of the painting by means of a non-invasive methodology, resulting from the combination of imaging and spectroscopic techniques. Analysis of hyperspectral images employing methods such as spectral angle mapper and principal component analysis allowed us to describe spatial distribution of the pigments and manufacturing methods, while XRF and FORS allowed us to record the complex and diverse color palette employed to achieve effects such as brightness, hue, saturation, and even the covering power of this painting.

Keywords: hyperspectral imaging; 18th century painting; FORS; XRF

Citation: Pérez, M.; Cano, N.; Ruvalcaba-Sil, J.L.; Mitrani, A.; de Lucio, O.G. Technical Non-Invasive Study of an 18th Century Novo-Hispanic Panel Painting. *Heritage* **2021**, *4*, 3676–3696. <https://doi.org/10.3390/heritage4040202>

Academic Editors: Daniel Vazquez-Molini and Antonio Alvarez Fernandez-Balbuena

Received: 31 August 2021
Accepted: 13 October 2021
Published: 19 October 2021

Publisher's Note: MDPI stays neutral with regard to jurisdictional claims in published maps and institutional affiliations.



Copyright: © 2021 by the authors. Licensee MDPI, Basel, Switzerland. This article is an open access article distributed under the terms and conditions of the Creative Commons Attribution (CC BY) license (<https://creativecommons.org/licenses/by/4.0/>).

1. Introduction

The study of painting in México is an important challenge due to the number of preserved artworks over a long period (16th–21st centuries) of time, with different pictorial traditions. In this research area, each technical study provides a piece of the puzzle, and contributes to the understanding of the heritage legacy developed through generations.

Purísima Concepción is an artifact of time and technique, and an artistic document in which different plastic and formal solutions can be studied. Its research strategy, defined by the study of its technology, materiality, and state of conservation through imaging and spectroscopic techniques, can complement the understanding of its temporality and material meaning of its production related to the 16th, 17th, and 18th centuries. By using imaging techniques, underlayer versions representing the Virgin Mary were recently discovered, as shown in [1], and the study of those layers will help understand the changes and formulations of its meaning. Meanwhile, the upper layer composition of Virgin Mary coronated by the angels, related to the 18th century, and the relevance of the *Museo Exconvento San Agustín Acolman-INAH* are discussed in this paper, and should provide a starting point for further and deeper studies of the currently hidden layers. The painting technique from the 18th century Novo-Hispanic period is scarcely studied, and it is unknown if there was a continuity of materials, anonymous painters, and geography. This research also seeks to provide an insight on such subjects.

The study of cultural heritage requires the use of non-invasive techniques and a multidisciplinary approach, in order to generate significant knowledge while preserving

the studied objects. It has been necessary to develop methodologies where complementary techniques provide pieces of information that, when assembled, deliver the *whole picture* on the material properties and historical importance of an object. It is in this fashion that XRF spectroscopy data provides unequivocally elemental information in order to discriminate the material composition of a pigment, and FORS information provides a chemical signature of pigments and binders. Both are known to be powerful techniques, but are limited to analyze a single point, and usually require complex interpretations if a detailed description of the manufacture of an object is required. In contrast, some imaging techniques, such as digital radiography, ultraviolet photography, and even visible photography, can provide global information on a given object, and usually enhance details on the production of the studied object.

Hyperspectral imaging (HSI) combines properties of both spectroscopic and imaging techniques. Therefore, it is not limited to a local analysis (as with spectroscopic techniques), but instead, it can deliver a global description of the studied object. The generated images contain physical or chemical information, describing the distribution maps of certain materials. Therefore, results are not limited to a mere material study, but they can also provide—through an adequate analysis and interpretation—insights on the manufacturing process of the object, information regarding later interventions or modifications, and even its preservation state. HSI analysis has recently proven to be useful for heritage sciences [2–6]. In fact, it has become a well appreciated analysis technique due to its intrinsic characteristics: it is a non-invasive and portable technique which provides results over large areas in a relatively short time.

As recent examples of the use of HSI in heritage science studies, we have: the work by Pérez et al. [7], where different manufacturing stages were identified in the painting *The Pentecost* by Baltasar de Echave Orio (1558–1619); the work by Padoan et al. [8], in which HSI was used to monitor preservation and aging conditions of historical documents; the study by Sun et al. [9], where different degrees of flaking deterioration were evaluated in mural paintings at the *Mogao Grottoes* by using NIR-his; and the work of Hou et al. [10], where a combination of HSI information and multivariable analysis algorithms were employed to create a virtual restoration of ancient Chinese Qing dynasty paintings.

1.1. Description of the Painting

The Purísima Concepción painting (see Figure 1) depicts Mary, expectant, her delicate face and smooth skin are accompanied by wide and flowing hair, a pair of ruby earrings set in fine gold hang from her ears, and a pearl necklace hangs from her neck. The Virgin looks towards the devotee, and the hands are fixed in a prayerful position. These, in turn, frame the golden *christogram* on her womb, announcing her future motherhood. His elongated figure, covered with fine cloth, stands on cherubs and the inverted waning moon. (Genesis 3, 15 and Lk 1, 28). Behind her, the reddish mid-afternoon sun peeks out, and at the top, her head is accompanied by a *stellarium*, two angels hold the great imperial crown, composed of the golden cirlet of jewels, the crimson reddish lining and three arches. The Holy Spirit witnesses the event, and the blazing sunlight opens the clouds of heaven. In the lower plane, a horizon of warm waters, represented by blue hues and white lights, ends in a continental terrain. On this island firm, the palm, the cypress, and a palm tree appear stoically, accompanied by a lily with a recent shoot and a rose bush with soft and rounded brushstrokes. On the periphery, a simulated frame, with a golden appearance, presents pebbles, shells, and black tendrils made with the point of a round brush.

The visual tradition of this painting had been associated with the characteristics of the art of New Spain which shows variants of the iconography of *Tota Pulchra*, which arrived in America in 16th century, and had continuity almost up to the 18th century [1]. The support of this image is a rectangular panel measuring 258 cm × 165 cm, and is made up of five live-joint planks and three crossbars measuring 11 cm × 165 cm wide each. Tangentially cut and brown in color, the plank and crossbar wood are distinguished by a large presence of knots and a rough surface finish due to the roughing of the material with a possible

hatchet. The reinforcement between crossbars and planks also coincides with the insertion of forging nails through the front and an iron ring located in the upper center of the panel, possibly to hold it to the wall.



Figure 1. Visible image of Purísima Concepción. Museo Exconvento de Acolman-INAH, México.

Specially in Spain between the 15th and 17th centuries, the size, format and quality of the wood used to support paintings were directly based on an economy controlled by the regulations stipulated in ordinances. The diptych or triptych panels, with dimensions of up to 300 cm high by 250 cm wide, gave rise to altarpieces that, in some cases, reached great monumentality [11,12]. Due to the magnitude of these altarpieces, their execution depended on the collaboration of several artists. The use of wood as a support for paintings lasted during the three centuries of the viceroyalty of New Spain with basically the same construction technology, but during the eighteenth century, its use declined when compared to canvas [13].

1.2. Analytical Techniques

1.2.1. Visible (VIS) and Ultraviolet (UV) Imaging

The use of VIS and UV fluorescence as complementary imaging techniques provide information regarding the manufacturing process of the artwork. The painting was examined using a lamp UVP mod. B-100AP in long wave (365 nm), and was recorded with a DSLR Nikon D7100, lens NIKKOR 24–120.

1.2.2. Hyperspectral Imaging (HSI)

Hyperspectral images were generated using a Surface Optics 710VP camera, based on a dispersive system and a silicon sensor, providing a 4.5 nm spectral resolution in the 375 nm to 1047 nm range. Image dimensions are 696 × 520 pixels. Two 3200 K halogen lamps illuminate the object, and its intensity is determined right in front of the artwork using a solar power meter H110 series from Anaheim Scientific. Verification of the wavelength calibration is achieved by using yellow, blue, red, and green reflectance standards

CSS-04-020 AS-01178-060. Deconvolution of the light source and detector contributions were calculated with Spectral Radiance Analysis Toolkit v3.5 using a Spectralon certified reflectance standard (model SRT-99-050 AA-00821-000) with a 5 cm × 5 cm reflective area. Classification, image analysis, and generation of hypercubes was performed with Harris Geospatial Solutions ENVI 5.5 software. HSI analysis methods used in this work allowed us to generate different images: pseudo color IR; spectral angle mapper (SAM); UV fluorescence; PCA-RGB composite image; and single PC images, which are described in detail in the work of Perez et al. [7], and references therein. Such images permit a detailed description of the techniques involved in the manufacture of the *Purísima Concepción*.

In brief, the classification workflow was: (i) images were background-subtracted and normalized to rule out contributions from light source and detector efficiency; (ii) endmembers were determined using the *pixel purity index* (PPI) criteria, and resulting pixels were processed following the process described in the work of Veganzones et al. [14] and Kale et al. [15]; (iii) endmembers were mapped by using the ENVI-SAM algorithm, thus resulting in an artificially colored image, where each color corresponds with a material with a characteristic spectrum; (iv) optimization of angle thresholds was achieved by using the ENVI *rule classifier* tool to determine the correct threshold angle for each class, and the results were tuned by examination of the corresponding angle distribution histograms, as in the work of Foglini et al. [16].

Principal component analysis (PCA) was performed to provide a direct classification of regions with spectral information variations, which could not be easily distinguishable in each of the *single-band* images. Resulting images provide a *reduced* set, in which material, spectral, or even manufacturing features are condensed. Most of the data variance is included in the first PC, thus we propose that an RGB-PCA image conformed with the first three PCs will significantly enhance such features. Mathematically, each PC is determined by a linear combination of the wavelengths, thus providing insights on chemical or physical properties linked with the associated spectra. We have shown in a previous work [7] that it is possible to go even further by considering a multidisciplinary approach for PCA image interpretation, allowing the description of manufacturing details on the studied object.

1.2.3. Fiber Optic Reflectance Spectroscopy (FORS)

FORS spectral information was generated and recorded by a FieldSpect-4 ASD system, with spectra in the visible, near infrared (NIR), and short-wave infrared (SWIR) wavelengths. Spectral resolution is 3 nm for the visible and NIR regions (300–1000 nm), and 10 nm for the remaining region of the spectra (1000–2500 nm). The analysis area is about 1 cm², and requires the probe to be in contact with the studied object. The system employs a D65 illuminant, and spectra acquisition time was set at 0.2 s. The system is routinely calibrated by an ASD Inc. certified reflectance standard (AS-02035-000CSTM-SRM-990-362).

1.2.4. X-ray Fluorescence Spectroscopy (XRF)

A *home built* portable X-ray system (SANDRA) was used for recording the elemental composition of the studied object, this system and its applications are described in detail elsewhere [17]. In brief, the system employed a Mo X-ray source collimated to a 1 mm area, and an Amptek SDD detector with detection angle fixed at 45°. Calibration of the system is achieved by using a NIST multicomponent glass standard reference material (SRM 1412). Irradiation parameters were 45 kV, 0.200 mA with a recording time of 90 seconds, and no filters were used during the spectra acquisition. Spectra analysis and deconvolution was performed by means of ESRF-BLISS PyMca software.

Due to the existence of an underlying painting, interpretation of XRF data could be complex, since the range of photons in matter allow them to penetrate hundreds of micrometers, encompassing not only the surface, but most of the layers of the painting. However, the physics ruling the interactions between X-rays and solids, such as the attenuation of photons in matter, provide a testing ground for determining the depth from which the recorded photons arise. We considered the K_{α}/K_{β} (or L_{α}/L_{β} , depending on

the studied element) relative intensity ratio of the representative elements in each pigment, since the attenuation strongly depends on the energy (especially for the energy range involved). When the ratio corresponded (within uncertainties) with predictions from databases, XRF data was then related with the surface layer, otherwise data were associated with deeper layers

2. Results and Discussion

Results of the spectroscopic techniques (FORS, XRF) are grouped by the binding media and the materials associated by the color palette of this painting: golden; blue; red; brown; green; flesh tones. Results from the imaging techniques are grouped by following the main areas of the painting composition: the Virgin's face and hands; the crown; and the right-side angel. These images provided the most relevant information of the upper layer version of Mary. The analysis always considered the underlayer versions registered by the radiographic images, which are described in detail in [1], to achieve a correct interpretation of the results provided by the spectroscopic techniques. Imaging results are presented as mosaics, where the different acquired images of one region are contrasted: visible; UV fluorescence; IR pseudo-color (IRPC); spectral angle mapping (SAM); a pseudo-color image composed by the three main PC (PC-1,2,3); principal component 1(PC-1); and three selected different principal components (PC-n).

2.1. Purísima Concepción: Materials and Painting Technique

Results from the spectroscopic techniques are divided in a description of the binding media and color palette. In a first approximation, the color palette appears to be simple, with predominance of golden, blue, and red hues. However, the interpretation of the studies applied show a great diversity of materials employed to achieve effects such as brightness, hue, saturation, and even covering power of the paint.

2.1.1. Binding Media

FORS SWIR spectra from regions with different colors of the paint are shown in Figure 2, from which it was possible to find common characteristics associated with the binder.

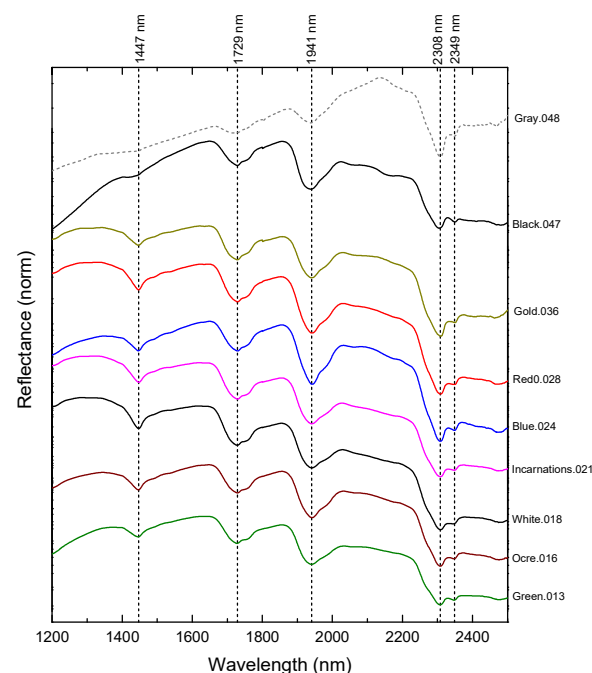


Figure 2. FORS spectra from representative regions corresponding to different colors. Principal features related with binder media are indicated. Spectra corresponding numbers are indicated in Appendix A Figures A1 and A2 general diagram.

In Figure 2, we can observe spectral features related to lipids on 1729 nm, associated with the first overtone of the stretching mode from the methylenic group [$2\nu_a\text{CH}_2$], and combination bands from stretching (ν_a asymmetric and ν_s symmetric) and bending (δ) modes on 2308 nm, [$(\nu_a + \delta)\text{CH}_2$], and 2349 nm [$(\nu_s + \delta)\text{CH}_2$]. Such characteristics have been noticed in the works by Pérez et al. [7], and Dooley et al. [18]. These absorption bands are common all over the paint, and their presence indicates the knowledge of the drying oil to bind the pigments.

2.1.2. Color Palette

Table 1 summarizes the main findings by FORS and XRF spectroscopic techniques of the materials composing the color palette. A detailed description of each pigment is also provided further in this section.

Table 1. Description of the palette by FORS and XRF spectroscopic techniques. ^a = absorption maximum, ^b = inflection point, ^c = reflectance maximum. A correspondence between FORS and XRF measurements as well as a detailed description of XRF results can be found in Appendix B Tables A1–A6.

Palette	Region	Compounds Identified/Inferred	FORS (nm)	XRF
Golden	Virgin Mary: Trimming	Gold Alloy: Au and Cu Ochre (FeO) + Orpiment (AsS)	538 ^b	Pb, Cu, Au, Hg
	Collar		536 ^b	Pb, Au, Cu, Ca
	Christogram		558 ^b	–
	Star Mantle		–	Pb, Cu, Au, Fe
	Imperial crown arche		–	Pb, Cu, Fe, Hg
	Imperial crown circlet		–	Pb, Au, Cu, Fe
	Holy Spirit: Nimbus		535 ^b	Pb, Au, Cu, Fe
	Simulated frame		546 ^b	Pb, Cu, Fe, Au
	Stellarium		–	Pb, Fe, Au, Ca
	Radiance		–	Pb, Fe, Ca, As
Blues	Virgin Mary Mantle Angel Mantle Holy Spirit Celestial Background	Azurite (CuCaCO) Azurite (CuCaCO) Indigo	465 ^c , 646 ^a , 1000 ^b , 1496 ^a , 2289 ^a , 2352 ^a , 483 ^c , 645 ^a , 1003 ^b , 1496 ^a , 2289 ^a , 2352 ^a 784 ^b	Pb, Ca, Cu, As Pb, As, Ca, Cu Pb, Ca, As
	Reds	Virgin Mary: Lips Sleeve Corona	Vermillion (HgS) 594 ^b 596 ^b 594 ^b	Pb, Hg, Ca, Fe Hg, Pb, Fe, Ca Pb, Hg, Cu, Fe
Brownish	Virgin Mary: Hair Crown Angel: Hair Eye	Iron Oxide, Orpiment (AsS) Iron Oxide, Pb-Sn Yellow Iron Oxide Iron Oxide, Pb-Sn Yellow	578 ^b , 718 ^b , 831 ^a – 567 ^b , 720 ^b , 832 ^a –	Pb, Fe, Ca, Cu, As Pb, Cu, Fe, Ca, Hg, Sn – Pb, Fe, Hg, Ca
	Greens	Virgin Mary Emerald Palm Lily	Copper Resinate 704 ^a 708 ^a	Pb, Cu, Au, Fe Pb, As, Ca, Fe Pb, As, Cu, Fe
		Flesh tones	Virgin Mary Angel Cherub	Vermillion (HgS) + Lead White + Azurite –

The gilding strategies: In the *Purísima Concepción*, golden regions are present in Mary's apparel, her jewelry, in the *stellarium*, radiance, and in the *painting's frame*, with different shades and finishes. The interpretation of the XRF spectra (Figure 3) of the golden regions indicate the presence of Pb, Au, Cu, Fe, Ca, Sn, and As. These elements are, in turn, associated with the presence of various pictorial materials. For the gilding, a gold alloy, mainly composed of Au and Cu with a significant presence of Pb, commonly associated with lead white ($2\text{PbCO}_3 \text{Pb}(\text{OH})_2$), e.g., in the trimming, *stellarium*, crown, and frame. The presence of Fe is due to the use of brown layers for shadows. These two elements (Fe and Pb) are present in a higher proportion in the broad golden lights on the upper part of the painting. The spectra also present an associated signal of Sn, probably related to the tin lead yellow present in the jewelry highlights. The As signal and a noticeably intense

enhancement in the region where the S signal is expected provide evidence that orpiment (As_2S_3) could be present in the earrings and radiance of the Virgin Mary.

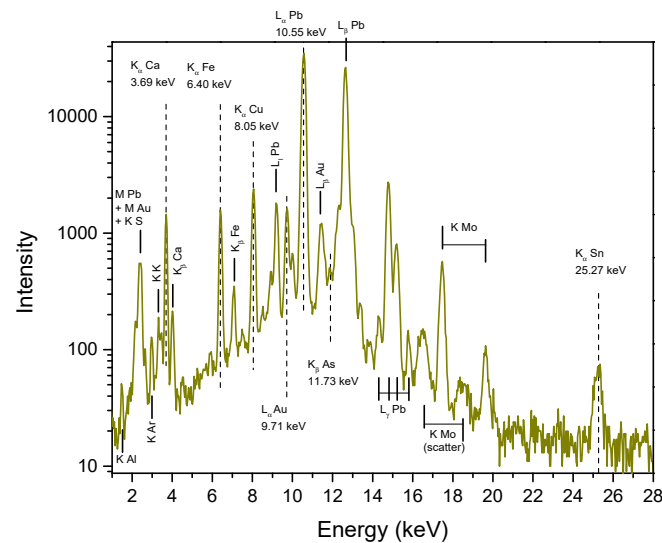


Figure 3. Representative XRF spectrum of a golden region around the crown (XRF.30). See the Appendix A general diagram for details on the acquisition location.

Likewise, representative FORS spectra of the golden regions are presented in Figure 4, where their main characteristics correspond to inflection points between 535 nm and 590 nm. In metals such as gold, radiation absorption in the visible region is mainly due to processes that involve free electrons.

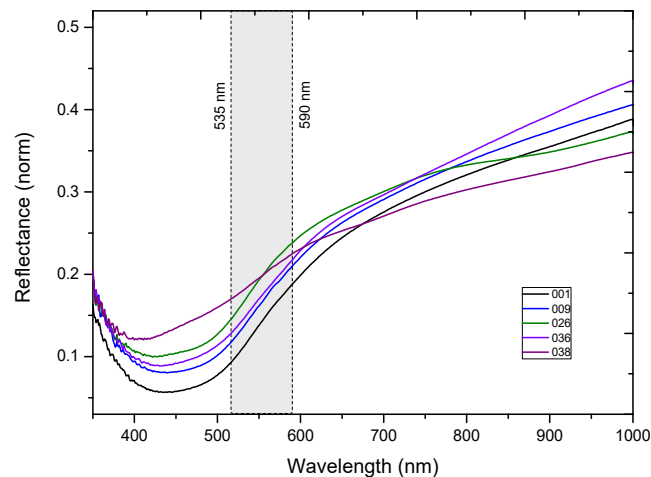


Figure 4. FORS representative spectra from golden regions. Inflection points between 535 nm and 590 nm are indicated. Spectra corresponding numbers are indicated in the Appendix A general diagram.

The gilding technique in this painting consisted of flakes ground to a powder, then mixed in oil. Lead white was used to increase the covering power and density of the pictorial layer. The earrings and radiance were made with orpiment, and due to its characteristic tone, saturation, and brightness which makes it look like a precious metal, as well as its ease of handling, plasticity and economy, it replaced the use of gold in certain areas.

In contrast, the simulated frame was created with a golden and matte surface applied with a flat brush, whereas organic figures such as shells and tendrils are highlighted by a brownish shade applied with a round brush. In Novo-Hispanic works from the second half of the 17th century, simulated frames were recurring resources used by artists [19] due to

an economic limitation, as it was necessary to provide a frame for the works, and bespoke frameworks may have been out of budget, or perhaps the painting of a frame was used to dignify the artistic content.

Gold, an incorruptible and shiny-looking material, has been related to the solar, the igneous, and the divine over time, in addition to its aesthetic and theological metaphors that have added to the notions of prestige and wealth of the precious metal with economic value [20]. The difference between the materials identified to produce the golden effect of the jewels and the Virgin's crown, radiance, and the frame accounts for the knowledge about their properties, their cost, and possibly their existence in the market. The *decorum*, ornament, and splendor as an object for the liturgy, shows in the gold dust applied in the frame and trimmings, a consideration of distinction of power, luxury, and the elite, entrusted to the master workshop.

Shades of blue: Blue tones are in the second hierarchy of this painting. Even though different shades are registered for the mantle of the Virgin, the cloth of the right angel, the celestial background of the Holy Spirit, and the insular sea in the background, our results by imaging techniques, and by XRF and FORS spectroscopic techniques, indicate the use of only two pigments (see Figure 5 for XRF results), and also provide their distribution throughout the painting. Spectroscopic elemental analysis revealed the use of a Cu rich pigment in the blue regions of the Virgin's mantle and the clothing of the right angel, which was identified as azurite- $\text{Cu}_3(\text{CO}_3)_2(\text{OH})_2$ -from its characteristic bands (646 nm, 1496 nm, 2289 nm and 2352 nm, see references [18,21]) in the FORS spectra (see Figure 6). In the region of the Holy Spirit, the absorption peaks in these spectra are between 645 nm and 707 nm, and the shift in absorption peaks could be related to bathochromic effect caused by the mixing of pigments. With precision, the 660 nm peak is reported as the main characteristic of indigo [21]. Regarding the blue hues, the material distinction between a mineral and lake-pigment was researched in paintings of Virgin Mary from the 16th and 17th centuries [22]. The predominant color in the mantles is azurite, and indigo for the backgrounds. In this case, the anonymous painter continues with this knowledge and significance, proposing not only a common solution, but also the knowledge of treatise, and the cost of these materials.

Traces of mercury for red areas: XRF spectra from the red areas revealed the use of a Hg rich pigment (Figure 7). Likewise, FORS reflectance spectra from these red areas show an inflection point around 594 nm as the main characteristic (Figure 8), confirming the presence of vermilion (HgS) as the main pigment to give this hue. Additionally, absorption characteristics were identified at 1198 nm and 1447 nm, associated with the first overtone of the hydroxyl group [$2\nu\text{OH}$] in the lead white pigment, as reported in Picollo et al. [23].

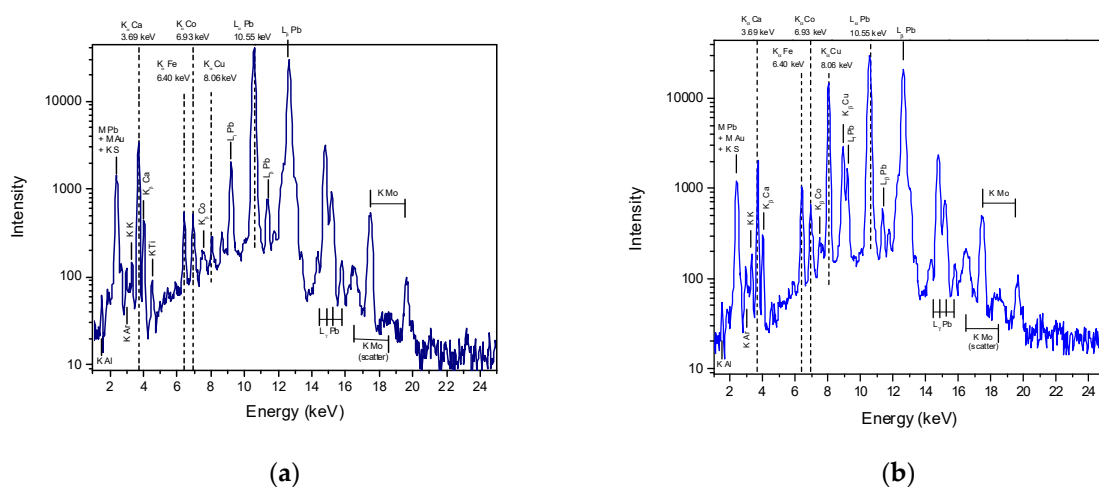


Figure 5. (a) representative spectrum (XRF.24) from Holy Spirit region, (b) representative spectrum (XRF.55) from Virgin's mantle region. Their corresponding locations are detailed in Appendix A general diagram.

Green tones: A single pigment was identified in all the green areas from this painting, found in the representation of emeralds in the imperial crown, and the stems and leaves of the palm and the lily in the lower area. FORS spectra for this pigment have a reflectance maximum between 554 nm and 584 nm, and absorption bands between 696 nm and 717 nm (Figure 9), which together with the IR signature (Figure 10) allowed to identify the pigment as copper resinate [7]. XRF spectra (Figure 11) confirm the presence of Cu in the green areas, but also presents Pb, Hg and Fe, and vermilion or iron earth to change the saturation of the jewel and the volume from the shadows. Finally, the presence of Au in the green emeralds from the crown may indicate that these were painted over the golden region.

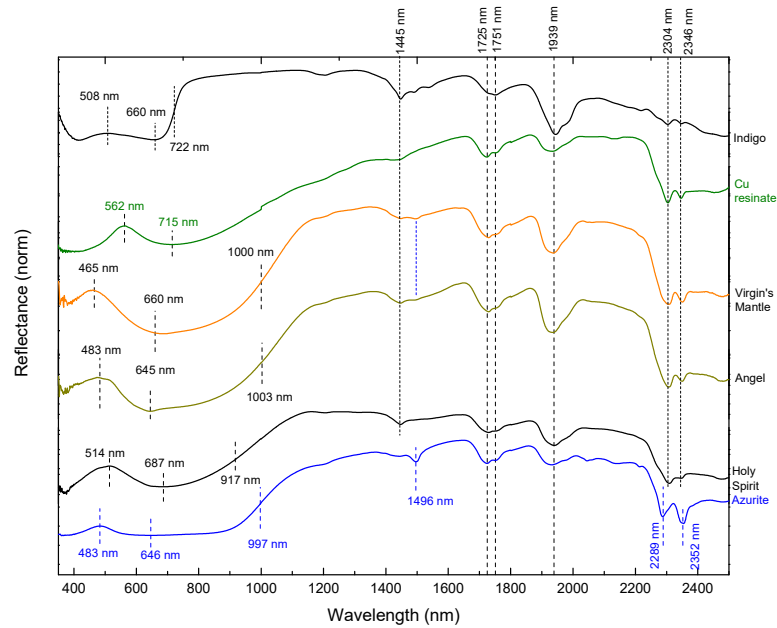


Figure 6. FORS spectra from blue regions: Virgin’s mantle, angel’s mantle, and Holy Spirit blue background. Vis-NIR reflectance features are indicated. Reference materials (indigo, Cu resinate, and azurite) are included for comparison.

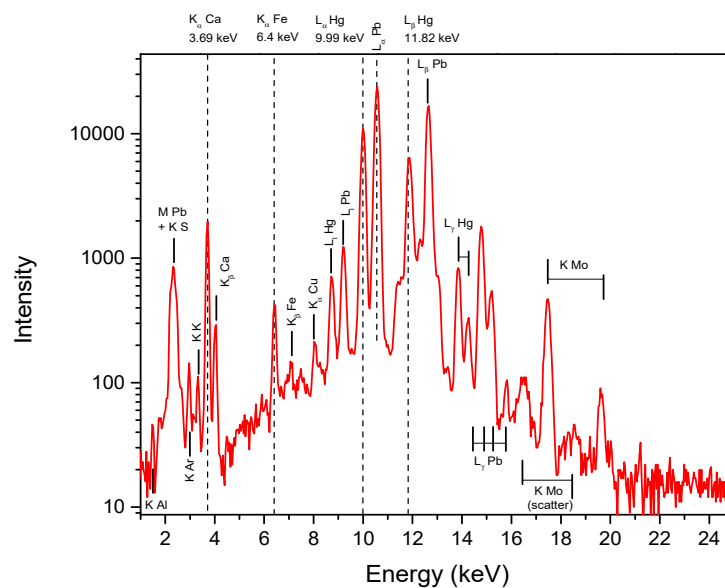


Figure 7. Representative spectrum (XRF.73) from red regions. Features related with Hg are indicated. Spectra detailed location can be seen in Appendix A general diagram.

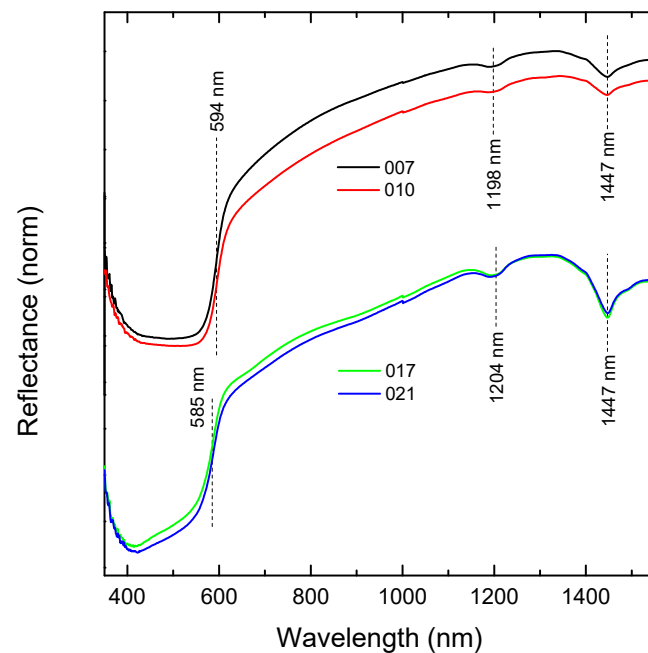


Figure 8. (TOP) FORS representative spectra from red regions (FORS.007 and FORS.010), inflection point near 594 nm related with vermilion (HgS) is indicated. **(BOTTOM)** (FORS representative spectra from incarnation regions (FORS.017 and FORS.021). Features near 1198 nm and 1447 nm, related with lead white are indicated. Spectra corresponding locations are indicated in Appendix A general diagram.

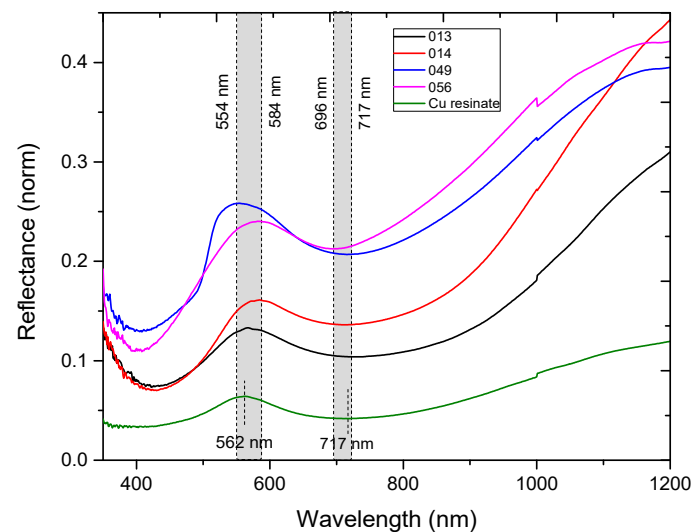


Figure 9. FORS representative spectra from green regions. Reflectance maxima were observed between 554 nm and 584 nm, and absorption bands between 696 nm and 717 nm. Copper resinate reflectance spectrum was included for comparison. Numbers corresponding to spectra are shown in Appendix A general diagram.

Brown: Brown areas in the painting were associated with the presence of Fe, as determined by XRF, possibly related with the use of burnt earth for the shadows, and are of a uniform hue. Its use in the hair and pupils of Mary and the angels were defined by brushstrokes at the tip of a round and fine brush, whereas for the volume of the cloths, the jewelry, or the crown, a flat brush was applied. From the interpretation by XRF spectroscopy, the abundant presence of Pb indicates the incorporation of white lead in this color layer, probably to provide a greater covering power.

Flesh tones: To generate the flesh tones of *Mary* and the angels, XRF identified the incorporation in a higher proportion of white lead (Pb), vermilion (Hg), azurite (Cu), and calcine natural iron oxide (Fe) (Figure 12). This mixture was made on a palette and applied with a fine brush tip. Vermilion was used for the touches of blush on the cheeks, whereas the volume of the face from lights used an abundance of lead white, and the shadows used natural sienna.

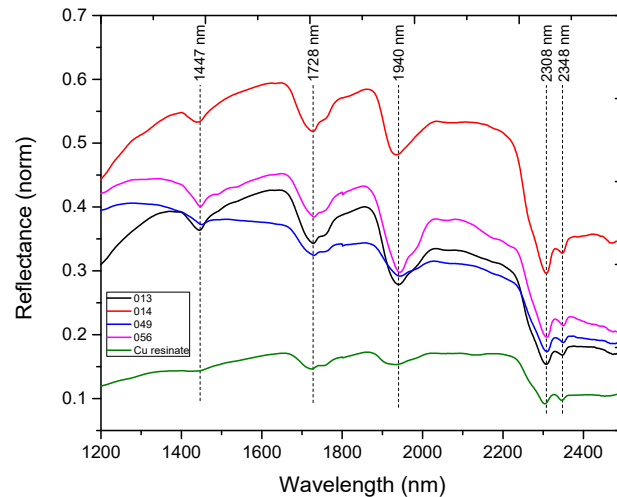


Figure 10. FORS spectra from green regions. Spectral features are indicated and compared with copper resinate reference. Spectra numbers of corresponding regions are shown in Appendix A general diagram.

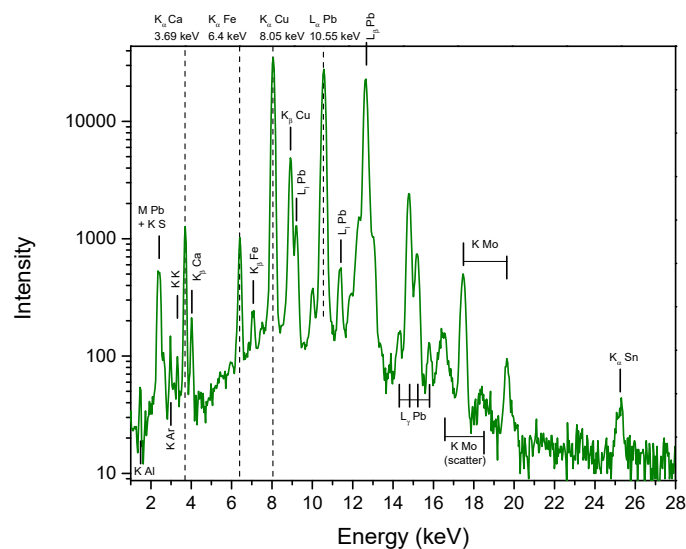


Figure 11. Representative spectrum (XRF.029) from green regions, features related with Ca, Fe, and Cu are indicated. Spectrum corresponding location is indicated in Appendix A general diagram.

2.2. The Virgin Mary: Changes of View and Composition by Imaging Techniques

The comparison of the resulting images from the different techniques allowed the identification of changes in the Virgin Mary, the angels, and the iconographic elements that accompany them, and made it possible to identify restoration areas more easily in the artwork, which were not noticeable due to the yellowish varnish and the absence of documentation on the restoration carried out in the painting. Table 2 gathers the characteristics observed from the different imaging techniques for the three areas analyzed (Figures 13–16), where visible image, IRPC, UV image, and PC stand out.

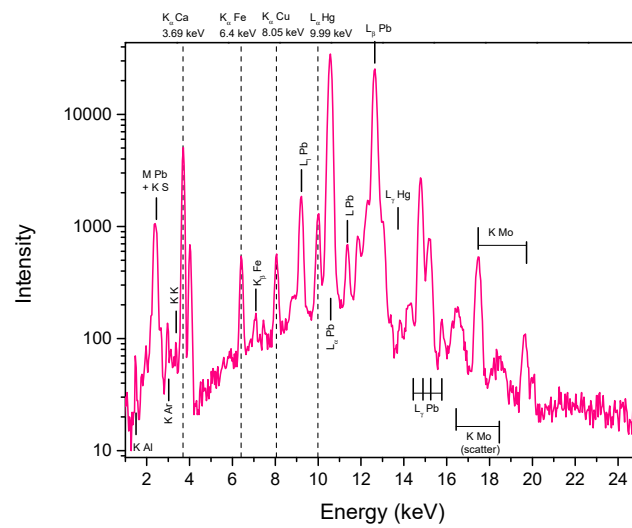


Figure 12. Representative spectrum (XRF.041) from flesh tones, features related with Ca, Fe, Cu, and Hg are indicated, associated with the use of vermilion. Spectrum corresponding location is indicated in Appendix A general diagram.

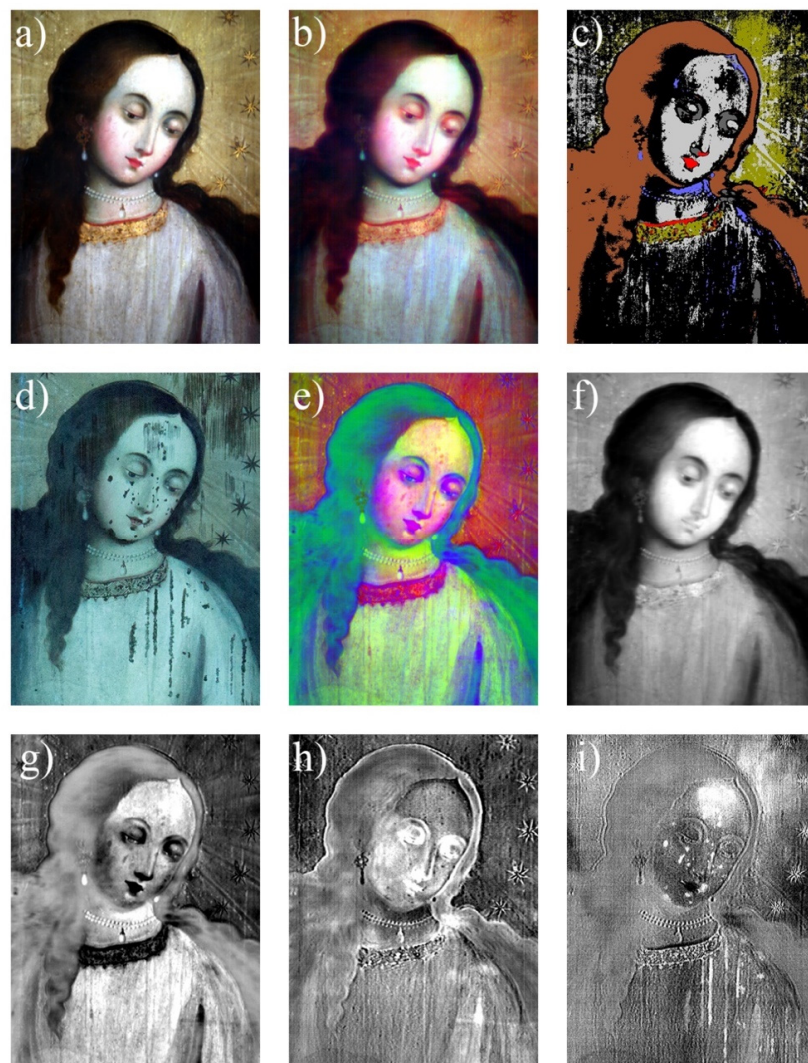


Figure 13. Virgin Mary face region: (a) visible image; (b) pseudo color image; (c) SAM image; (d) UV fluorescence image; (e) RGB-PCA; (f) PC1; (g) PC2; (h) PC3; and (i) PC9.

Table 2. Results from imaging analysis for the three studied regions in the *Purísima Concepción*.

Region	Image	Results
Virgin Mary, Face (Figure 13)	(a), (d)	When comparing the mosaics (a) and (d), we notice the restoration by vertical lines on the face and the white tunic.
	(h)	Mosaic (h) highlights the volume of the layers of color in the golden areas.
	(a), (e)	When comparing (a) and (e), the pseudo color image shows that the reddish tones of the eyelids, cheeks, and tunic present a similar tonality, which indicates a vermilion distribution. This pigment was identified by XRF and FORS.
	(a), (e)	Image (e) allows us to appreciate the distribution of the gilding applied in the jewels, trimmings, and <i>Stellarium</i> .
	(a), (i)	By comparing (a) and (i), we can observe the restoration areas on the face corresponding with white tones. It also highlights the texture of the <i>Stellarium</i> fillings, the pearl necklace, and trimmings for the tunic.
Virgin Mary, Hands (Figure 14)	(a), (b), (e)	Images (a), (b), and (e) make it possible to compare the distribution of the material applied in the gilding of the trimmings, the <i>Christogram</i> , and the stars of the mantle. From XRF, the presence of Au and Cu indicate a gold alloy, such as in the quadrant of Mary's face, whereas the stars of the mantle were made by a pigment with a high content of Pb and Sn.
	(a), (d)	Comparing (a) and (d), we can observe restoration areas.
	(a), (i)	Between (a) and (i), we could see the profile of a version of the Virgin Mary, an underlying composition painted in a previous century.
Imperial Crown (Figure 15)	(a), (b)	Images (a) and (b) exhibit different contributions of the materials used in the golden, reddish, bluish, and green tones. First, the application of gilding in the lower area of the crown and <i>Stellarium</i> present a similar composition of Au and Cu, whereas the upper area presents an opaque tonality due to the use of an earth shade. The reddish bonnet of the crown, in addition to the incarnation of the angels' hands, and the representation of rubies, present the same yellow hue based on vermilion. Blush is distinguished by a reddish hue for the celestial background of the Holy Spirit, compared to FORS spectroscopic techniques, and this material indicates the presence, in greater contribution, of a lacquer pigment, such as indigo. As for the green, the jewels that represent the emeralds indicate the same bluish material, whereas the XRF spectroscopy indicates the presence of Cu, and, in complement with FORS, they help us to confirm the presence of a copper resinate.
	(a), (d), (i)	The comparison of Images (a), (d), and (i) allows us to distinguish the restoration of the background of the painting by means of the <i>Rigatino</i> , which is vertical and fine brushstrokes applied in the regions with material losses.
	(a), (b), (d)	In Figures (a) and (b), the distribution of materials with the same behavior are shown: the reddish tone of vermilion was used in the blush of the cheeks, lips, and wings of the angels, whereas in the blue tone of the cloth, there is azurite.
right-Side Angel (Figure 16)	(a), (d)	The restoration of the background by <i>Rigatino</i> is noticeable when comparing Figures (a) and (d).

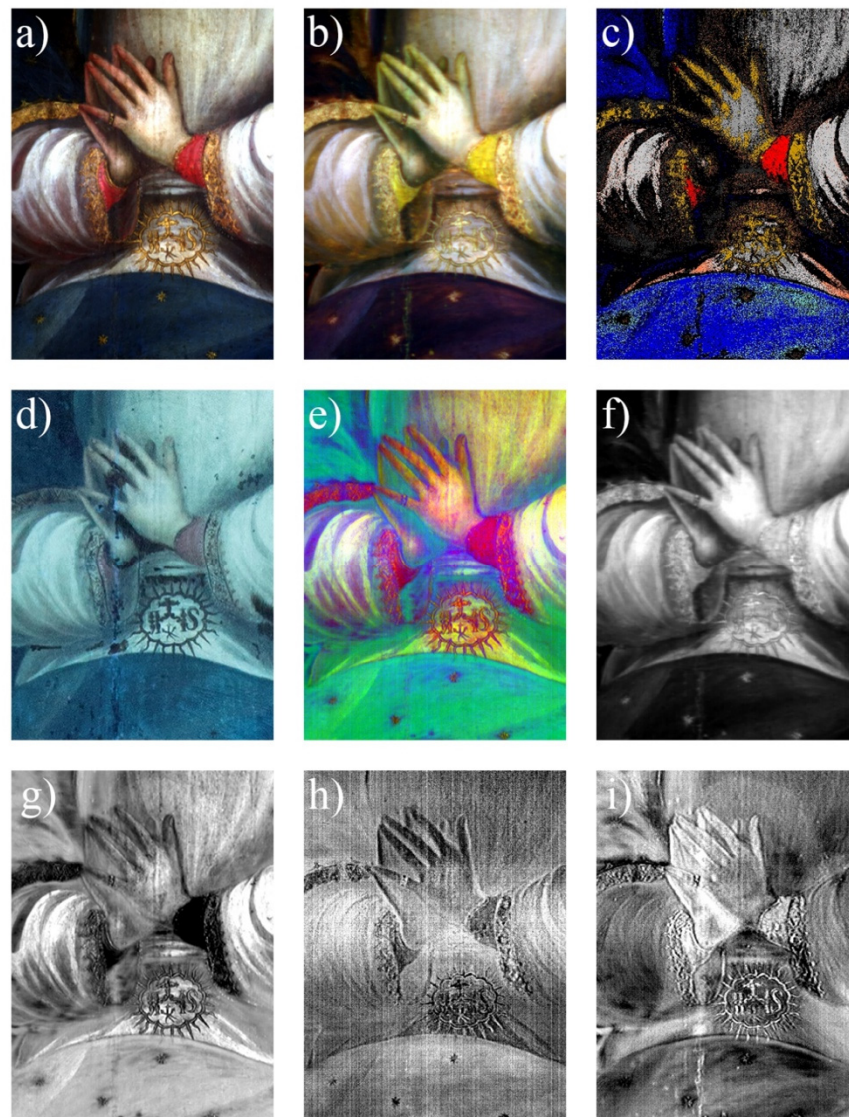


Figure 14. Virgin Mary's hands region: (a) visible image; (b) pseudo color image; (c) SAM image; (d) UV fluorescence image; (e) RGB-PCA; (f) PC1; (g) PC2; (h) PC3; and (i) PC8.

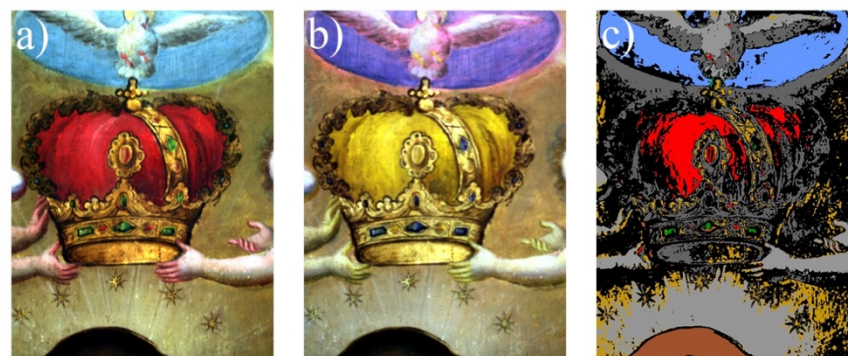


Figure 15. *Cont.*

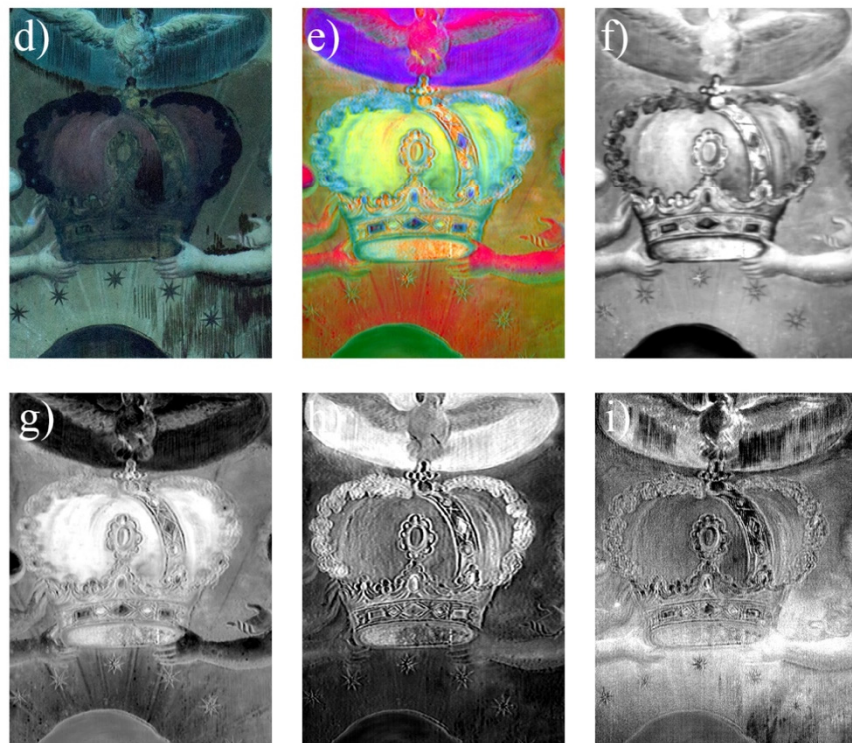


Figure 15. Imperial crown and Holy Spirit region: (a) visible image; (b) pseudo color image; (c) SAM image; (d) UV fluorescence image; (e) RGB-PCA; (f) PC1; (g) PC2; (h) PC3; and (i) PC4.

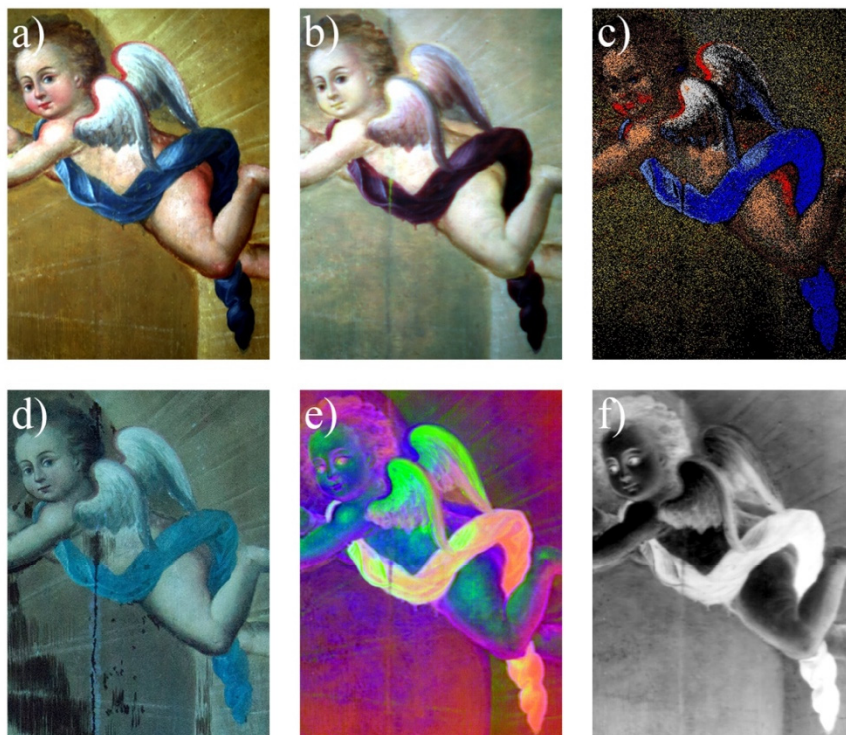


Figure 16. *Cont.*

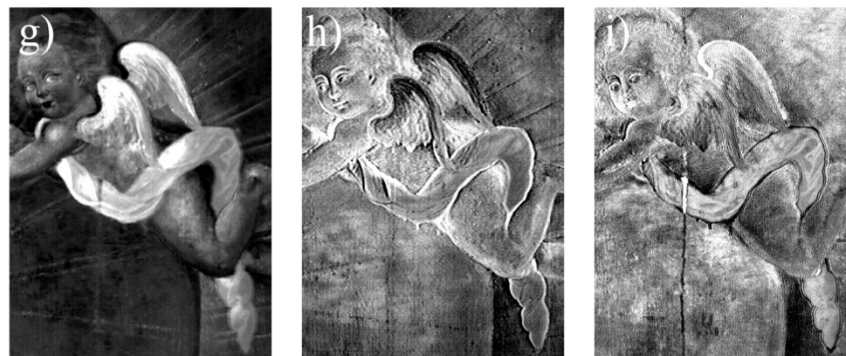


Figure 16. Right-side angel region: (a) visible image; (b) pseudo color image; (c) SAM image; (d) UV fluorescence image; (e) RGB-PCA; (f) PC1; (g) PC2; (h) PC3; and (i) PC8.

3. Conclusions

This work provided detailed information on the material composition of the color palette, by means of a combined imaging and spectroscopy method. HSI analysis has proven to be a powerful tool, and it allowed us to describe details on the distribution of the pigments, as well as a description on the manufacture of the painting. It also provided information on the presence of later repairs (consistent with UV imaging analysis), as well as insights on the existence of a previous painting (as was demonstrated by radiography of the painting).

In this artwork, the selection of materials by the artist considered the importance of the represented objects. Golden regions are present with different shades and finishes, and a gold alloy was used for the trimming, stellarium, crown, and frame. Fe was used for brown layers in the shadows. Tin lead yellow is present in jewelry highlights, orpiment in the earrings, and in radiance of the Virgin Mary. Blue tones characterization indicates the use of only two pigments: azurite for the Virgin's mantle and the clothing of the right angel; and indigo for the Holy Spirit region. A single green pigment was found in the painting, located in the representation of emeralds, and the stems and leaves in the palm and the lily in the lower area, which has been identified as copper resinate. Brown areas exhibit the presence of Fe, which is related with the use of burnt earth, used in the hair and pupils of Mary and the angels. Flesh tones of Mary and the angels contain a mixture of white lead, vermilion, azurite, and calcine natural iron oxide.

Results suggest the knowledge and experience of an oil-on-wood painter who possibly still conformed to the conditions of the ordinances and traditions established in the prior two centuries of colonial establishments. For the wood panel, its cut and construction are due to a process of specialized knowledge of carpentry work. However, it would be worthwhile to carry out studies on the cellular structure of the wood, the ring count to identify the selected genus, its possible extraction region, and when the tree was cut, in order to specify the work production system, in terms of the time and use of material resources.

Regarding the color palette, the system of selection and application of materials possibly considered qualities of stability, accessibility, and cost, which makes us think about the knowledge and versatility on the part of the architect to work with the different materials available.

It is also necessary to mention that the non-invasive studies by imaging techniques complemented with FORS and XRF spectroscopic techniques, although they offer high sensitivity and precision, had limitations in interpreting the areas of analysis, due to the complex layer superposition in the painting. The continuity of this study is suggested through the application of invasive techniques by means of a strategic selection of samples, and their eventual analysis by optical and electron microscopy to identify the sequence of their application and distribution, as well as the underlying pictorial campaign.

Author Contributions: M.P.: Writing—original draft, Methodology, Software, Formal analysis, Investigation. N.C.: Writing—original draft, Project administration, Methodology, Formal analysis, Investigation. J.L.R.-S.: National Laboratory Manager, Funding acquisition, Project administration, Investigation, Writing—review and editing. A.M.: Writing—review and editing, Formal analysis, Investigation. O.G.d.L.: Writing—review and editing, Methodology, Visualization, Investigation. Authors M.P. and N.C. contributed equally to this work and they both should be considered as FIRST AUTHOR. All authors have read and agreed to the published version of the manuscript.

Funding: This research was funded by CONACYT, grants numbers LN315853, LN299076, LN 314846, CB239609 and by DGAPA-PAPIIT grants numbers IN108521 and IT101219.

Institutional Review Board Statement: Not applicable.

Informed Consent Statement: Not applicable.

Data Availability Statement: Not applicable.

Acknowledgments: We express our gratitude to the following individuals and *institutions*: María del Perpetuo Socorro Villarreal Escárrega, *Asuntos Jurídicos INAH*; María del Carmen Castro, Liliana Giorguli, Irlanda Fragoso, Emmanuel Lara, María Eugenia Marín Benito, Cristina Noguera *CNCPC-INAH*; Antonio Huitrón Santoyo, Josué Alcántara, *Centro INAH Estado de México*; Armando Rosas, *Museo Ex Convento San Agustín Acolman*. We acknowledge the technical support of E. Casanova a I. Rangel. M. Pérez and N. Cano acknowledge the support of PNPC scholarship granted by CONACYT.

Conflicts of Interest: The authors declare no conflict of interest. The funders had no role in the design of the study; in the collection, analyses, or interpretation of data; in the writing of the manuscript, or in the decision to publish the results.

Appendix A

A general description of the acquisition regions and points for the different analysis techniques are presented here.

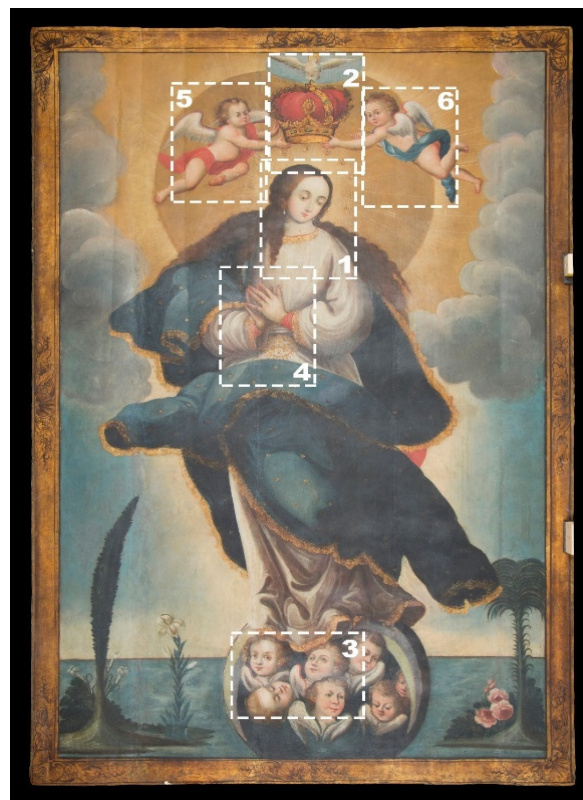


Figure A1. Hyperspectral analysis locations and dimensions. A total of six regions were studied in this research work by HSI technique.

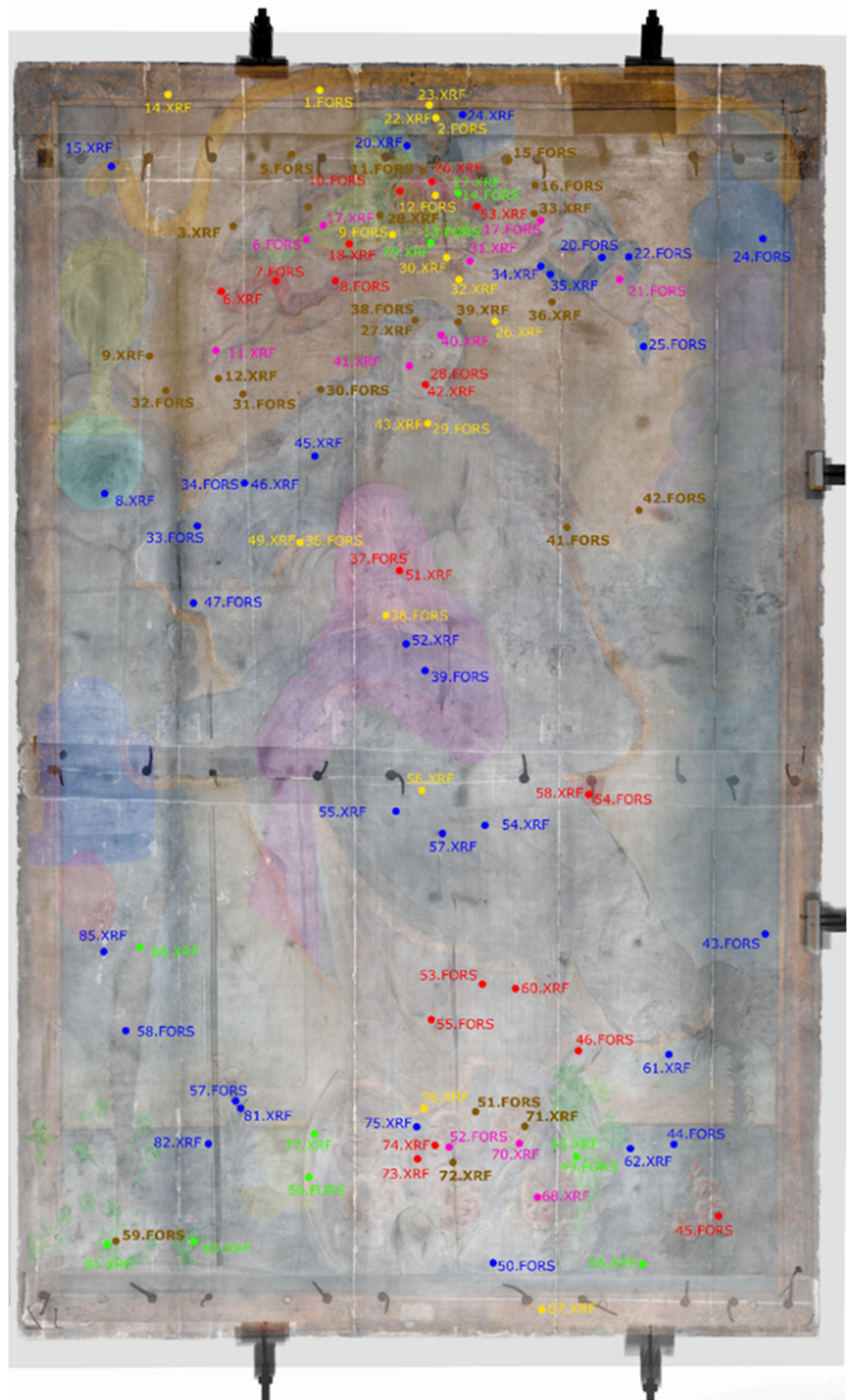


Figure A2. General diagram. Superposition of visible image and radiography image of *Purísima Concepción*, indicating the acquisition points for XRF (nn.XRF) and FORS (nn.FORS) spectroscopic techniques. Underlying features are highlighted with colors to facilitate the reading of the image.

Appendix B

The main findings from spectroscopic techniques are presented in the following tables, grouped by colors. Acquisition region is indicated, as well as ID for XRF and FORS acquisition points. In some cases, both spectroscopic techniques correspond with the same geometric spot, although they have different ID numbers. Elements reported are sorted in descending order by the intensity of their most intense characteristic X-ray line. Each pigment's representative elements are highlighted.

Table A1. Golden.

Region	XRF ID	Elements	FORS ID
<i>Virgin Mary</i>			
Trimming	49	Pb, Cu, Au, Hg, Ca, Fe	36
Collar	43	Pb, Au, Cu, Ca, Hg, Fe	29
Christogram			38
Star Mantle	56	Pb, Cu, Au, Fe, Co, K	
Imperial Crown Arche	28	Pb, Cu, Fe, Hg, Zn, Ca, Au	
Imperial crown Circlet	30	Pb, Au, Cu, Fe, Ca, Hg, Sn	
<i>Stellarium</i>	32	Pb, Fe, Au, Ca, Cu, Hg	
<i>Radiance</i>			
Radiance	1	Pb, Fe, Zn, Ca, Hg, Cu	
Radiance	13	Pb, Fe, Ca, Cu, Hg, As	
Radiance	37	Pb, Ca, Fe, As, Hg, Cu	
<i>Glory Break</i>			
Glory Break	2	Pb, Ca, Fe, Hg, As, Cu, Sn	5
Glory Break	3	Pb, Fe, Ca, As, Cu, Hg	
Glory Break	7	Pb, Zn, Fe, Ca, Hg, As	
Glory Break	9	Pb, Fe, Ca, As, Hg, Cu	
Glory Break	10	Pb, Fe, Ca, Cu, As, Hg	32
Glory Break	12	Pb, Fe, Ca, As, Cu, Hg	31
Glory Break	36	Pb, Fe, Ca, As, Hg, Cu,	
<i>Holy Spirit</i>			
Nimbus Holy Spirit	22	Pb, Au, Cu, Fe, Co, Hg, Ca	2
<i>Simulated Frame</i>			
Simulated Frame	14	Pb, Cu, Fe, Au, Ca, Hg	1
Simulated Frame	23	Pb, Au, Cu, Fe, Hg, Ca, Sn	
Simulated Frame	67	Pb, Fe, Au, Cu, Ca, Hg	

Table A2. Blue.

Region	XRF ID	Elements	FORS ID
<i>Virgin Mary</i>			
Mantle	45	Pb, As, Cu, Fe, Ca, Co, K	
Mantle	46	Pb, Ca, As, Fe, Cu, Co	33, 34
Mantle	47	Pb, Cu, Fe, Ca, Cu, K, Co	
Mantle	52	Pb, Ca, As, Fe, Co, Cu	39
Mantle	54	Pb, Cu, As, Fe, Co, Ca, K	
Mantle	55	Pb, Cu, As, Ca, Fe, Co	
Mantle	57	Ca, Zn, Cr, Sr, Ti, Co, Fe, Pb	
<i>Angel</i>			
Mantle	34	Pb, As, Ca, Cu, Fe, Hg	20, 22
Mantle	35	Pb, As, Ca, Fe, Cu, Hg	25
Holy Spirit celestial background			
	20	Pb, Ca, Zn, As, Fe, Ti, Co	4
	24	Pb, Ca, As, Fe, Co	

Table A3. Red.

Region	XRF ID	Elements	FORS ID
<i>Virgin Mary</i>			
Lips	42	Pb, Hg, Ca, Fe, Cu	28
Sleeve	51	Hg, Pb, Fe, Ca, Cu	37
Mantle	58	Pb, Hg, Ca, Fe, Cu	54
Crown	26	Pb, Hg, Ca, Fe, Cu	10
Crown	53	Pb, Hg, Cu, Fe, Ca	

Table A4. Brown.

Region	XRF ID	Elements	FORS ID
<i>Virgin Mary</i>			
Virgin's Hair	38	Pb, Fe, Ca, Cu, As, Hg	27
<i>Left Angel</i>			
Hair	16	Pb, Fe, Ca, Hg, As, Cu, Au, Sn	
<i>left Angel</i>			
Hair			16
Eye	33	Pb, Fe, Hg, Ca, Cu, K, Au Sn	

Table A5. Green.

Region	XRF ID	Elements	FORS ID
<i>Virgin Mary</i>			
Emerald	27	Pb, Cu, Au, Fe, Ca, Hg, Zn	14
Emerald	29	Pb, Cu, Ca, Fe, Hg, Zn	13
<i>palm</i>			
	86	Pb, As, Ca, Fe, Hg, Cu	58
<i>Lily</i>			
Lily	81	Pb, As, Cu, Fe, Hg, Ca	57

Table A6. Flesh tones.

Region	XRF ID	Elements	FORS ID
<i>Virgin Mary</i>			
Head	40	Pb, Ca, Hg, Fe, Cu	
Cheek	41	Pb, Ca, Hg, Cu, Fe	
<i>Angel</i>			
Foot	11	Pb, Ca, Hg, Fe, Cu	
Cheek	17	Pb, Ca, Hg, Fe, Cu	6
Hand	31	Pb, Ca, Hg, Fe, Cu	17, 21
<i>Querubin</i>			
Head	68	Pb, Ca, Hg, Fe, Cu	
Cheek	70	Pb, Hg, Ca, Cu, Fe	

References

1. Cano, N.; de Lucio, O. *Purísima Concepción. Tiempo y Forma de Una Pintura Novohispana*; Anales del Instituto de Investigaciones Estéticas: Mexico City, Mexico, 2021.
2. Rowlands, A.; Sarris, A. Detection of exposed and subsurface archaeological remains using multi-sensor remote sensing. *J. Archaeol. Sci.* **2007**, *34*, 795–803. [CrossRef]
3. Cavalli, R.M.; Colosi, F.; Palombo, A.; Pignatti, S.; Poscolieri, M. Remote hyperspectral imagery as a support to archaeological prospection. *J. Cult. Herit.* **2007**, *8*, 272–283. [CrossRef]
4. Bassani, C.; Cavalli, R.M.; Goffredo, R.; Palombo, A.; Pascucci, S.; Pignatti, S. Specific spectral bands for different land cover contexts to improve the efficiency of remote sensing archaeological prospection: The Arpi case study. *J. Cult. Herit.* **2009**, *10*, e41–e48. [CrossRef]

5. Fiumi, L. Surveying the roofs of Rome. *J. Cult. Herit.* **2012**, *13*, 304–313. [CrossRef]
6. Hällström, J.; Barup, K.; Grönlund, R.; Johansson, A.; Svanberg, S.; Palombi, L.; Lognoli, D.; Raimondi, V.; Cecchi, G.; Conti, C. Documentation of soiled and biodeteriorated facades: A case study on the Coliseum, Rome, using hyperspectral imaging fluorescence lidars. *J. Cult. Herit.* **2009**, *10*, 106–115. [CrossRef]
7. Pérez, M.; Arroyo-Lemus, E.; Ruvalcaba-Sil, J.; Mitrani, A.; Maynez-Rojas, M.; de Lucio, O. Technical non-invasive study of the novo-hispanic painting the Pentecost by Baltasar de Echave Orio by spectroscopic techniques and hyperspectral imaging: In quest for the painter's hand. *Spectrochim. Acta Part A Mol. Biomol. Spectrosc.* **2021**, *250*, 119225. [CrossRef] [PubMed]
8. Padoan, R.; Klein, M.E.; Groves, R.M.; de Bruin, G.; Steemers, T.A.G.; Strlič, M. Quantitative assessment of impact and sensitivity of imaging spectroscopy for monitoring of ageing of archival documents. *J. Cult. Herit.* **2021**, *4*, 105–124. [CrossRef]
9. Sun, M.; Zhang, N.; Wang, Z.; Ren, J.; Chai, B.; Sun, J. What's wrong with the murals at the Mogao Grottoes: A near-infrared hyperspectral imaging method. *Sci. Rep.* **2015**, *5*, 14371. [CrossRef] [PubMed]
10. Hou, M.; Zhou, P.; Lv, S.; Hu, Y.; Zhao, X.; Wu, W.; He, H.; Li, S.; Tan, L. Virtual restoration of stains on ancient paintings with maximum noise fraction transformation based on the hyperspectral imaging. *J. Cult. Herit.* **2018**, *34*, 136–144. [CrossRef]
11. Verougstraete, H. *Frames and Supports in 15th and 16th Century—Southern Netherlandish Painting*; Royal Institute for Cultural Heritage: Brussels, Belgium, 2015.
12. Moreno, P.S. Fernando Gallego and the altarpiece of Ciudad Rodrigo. In *Fernando Gallego and His Workshop: The Altarpiece from Ciudad Rodrigo*; Dotseth, A.W., Anderson, B.C., Roglán, M.A., Eds.; Philip Wilson Publishers: London, UK, 2008; p. 41.
13. Carrillo, A. *Técnica de La Pintura de Nueva España*; Instituto de Investigaciones Estéticas: Ciudad de México, Mexico, 1983.
14. Veganzones, M.A.; Graña, M. Endmember extraction methods: A short review. *Lect. Notes Comput. Sci.* **2008**, 400–407. [CrossRef]
15. Karbhari, V.K.; Mahesh, M.S.; Dhananjay, B.N. Hyperspectral endmember extraction techniques. In *Processing and Analysis of Hyperspectral Data*; IntechOpen: London, UK, 2020; p. 13.
16. Fogliani, F.; Grande, V.; Marchese, F.; Bracchi, V.A.; Prampolini, M.; Angeletti, L.; Castellan, G.; Chimienti, G.; Hansen, I.M.; Gudmundsen, M.; et al. Application of hyperspectral imaging to underwater habitat mapping, Southern Adriatic Sea. *Sensors* **2019**, *19*, 2261. [CrossRef] [PubMed]
17. Sil, J.L.R.; Miranda, D.R.; Melo, V.A.; Picazo, F. SANDRA: A portable XRF system for the study of Mexican cultural heritage. *X-Ray Spectrom.* **2010**, *39*, 338–345. [CrossRef]
18. Dooley, K.A.; Lomax, S.; Zeibel, J.G.; Miliani, C.; Ricciardi, P.; Hoenigswald, A.; Loew, M.; Delaney, J.K. Mapping of egg yolk and animal skin glue paint binders in Early Renaissance paintings using near infrared reflectance imaging spectroscopy. *Analyst* **2013**, *138*, 4838–4848. [CrossRef] [PubMed]
19. Vargaslugo, E.; Ángeles, J.P.; Gutiérrez, A.C.; Correa, J. *Su Vida y Su Obra*; Instituto de Investigaciones Estéticas: Ciudad de México, Mexico, 2017.
20. Rodríguez Nóbrega, J. Pintura en los reinos: Identidades compartidas. Territorios del mundo hispánico, siglos XVI-XVIII. In *El Oro en la Pintura de los Reinos de la Monarquía Española—Técnica y Simbolismo*; Haces, J.G., Ed.; Fomento Cultural Banamex: Mexico City, Mexico, 2009; pp. 1314–1375.
21. Aceto, M.; Agostino, A.; Fenoglio, G.; Idone, A.; Gulmini, M.; Picollo, M.; Ricciardi, P.; Delaney, J.K. Characterisation of colourants on illuminated manuscripts by portable fibre optic UV-visible-NIR reflectance spectrophotometry. *Anal. Methods* **2014**, *6*, 1488–1500. [CrossRef]
22. Arroyo, E.; Espinosa, M.E.; Falcón, T.; Hernández, E. Variaciones celestes para pintar el manto de la Virgen. *An. Inst. Investig. Estéticas* **2012**, *34*, 85–117. [CrossRef]
23. Picollo, M.; Bacci, M.; Magrini, D.; Radicati, B.; Trumpy, G.; Tsukada, M.; Kunzelman, D. Modern white pigments: Their identification by means of noninvasive ultraviolet, visible, and infrared fiber optic reflectance spectroscopy. In *Modern Paints Uncovered, Proceedings of the Modern Paints Uncovered Symposium, London, UK, 16–19 May 2006*; Getty Conservation Institute: Los Angeles, CA, USA, 2007; pp. 118–128.

Article

Things Always Come in Three: Non-Invasive Investigations of Alexander and Roxane's Wedding Room in Villa Farnesina

Manuela Vagnini ^{1,*}, Chiara Anselmi ^{2,*} , Michela Azzarelli ¹ and Antonio Sgamellotti ^{3,4}

¹ Laboratorio di Diagnostica Per i Beni Culturali, Piazza Campello 2, 06049 Spoleto, Italy; m.azzarelli@diagnosticabeniculturali.it

² Istituto CNR-IRET, Via G. Marconi 2, 05010 Porano, Italy

³ Dipartimento di Chimica, Biologia e Biotecnologie, Università Degli Studi di Perugia, Via Elce di Sotto 8, 06123 Perugia, Italy; sgamellotti.antonio@gmail.com

⁴ Accademia Nazionale dei Lincei, Via della Lungara 10/230, 00165 Rome, Italy

* Correspondence: m.vagnini@diagnosticabeniculturali.it (M.V.); chiara.anselmi@cnr.it (C.A.)

Abstract: Non-invasive optical spectroscopical analyses were conducted on the three main walls of Alexander and Roxane's Wedding Room in Villa Farnesina, Rome. The north and the east walls were frescoed by Sodoma in 1519. The decoration of the third wall was subsequent and neither the author nor the period is known. The north and east walls underwent various restorations, some even very invasive. For these reasons, the supposed remaining original parts of the two walls by Sodoma were studied and compared with the third one, aiming to obtain more information about its author and epoch. The results show the use of the same pigments for the three walls. In particular, the same yellow pigments including lead antimonate, the use of enamel blue with Bi impurities whose use is time-limited, and the use of a certain kind of purple hematite. The commonality in the pictorial technique also emerged, especially in the yellow parts, painted in the same way on each wall. This information, and documentary sources, reinforce the hypothesis that the third wall was decorated shortly after the death of Agostino Chigi by someone who was well-acquainted with the materials and techniques used by Sodoma for the other two walls.

Keywords: non-invasive investigations; portable/reflectance spectroscopy; portable Raman spectroscopy; lead antimonate; enamel blue; caput mortuum

Citation: Vagnini, M.; Anselmi, C.; Azzarelli, M.; Sgamellotti, A. Things Always Come in Three: Non-Invasive Investigations of Alexander and Roxane's Wedding Room in Villa Farnesina. *Heritage* **2021**, *4*, 2792–2809. <https://doi.org/10.3390/heritage4040157>

Academic Editors: Antonio Alvarez Fernandez-Balbuena and Daniel Vazquez-Molini

Received: 30 August 2021

Accepted: 25 September 2021

Published: 29 September 2021

Publisher's Note: MDPI stays neutral with regard to jurisdictional claims in published maps and institutional affiliations.



Copyright: © 2021 by the authors. Licensee MDPI, Basel, Switzerland. This article is an open access article distributed under the terms and conditions of the Creative Commons Attribution (CC BY) license (<https://creativecommons.org/licenses/by/4.0/>).

1. Introduction

Villa Farnesina, the Renaissance Roman villa built in 1506 by the Sienese banker Agostino Chigi, patron and close friend of Raphael, is currently the headquarters of the Accademia Nazionale dei Lincei, which is devoted to promoting and protecting its huge artistic heritage consisting in some of the most famous artworks of the Italian Renaissance Masters—Raphael included—which were summoned by Chigi for adorning his own private, suburban, relaxing place. Among the artists who left their sempiternal mark inside the residence was Giovanni Antonio Bazzi, better known as Sodoma (1477–1549), who frescoed the bridal suite of Agostino Chigi and his beloved Francesca Ordeaschi. The suite was decorated with scenes from the life of Alexander the Great, including his marriage with Roxane, in explicit reference to that of Chigi. Before the new restoration of the room began, some non-invasive analyses were carried out on the two walls painted by Sodoma and his workshop depicting the *Darius family before Alexander* on the east wall (Figure 1) and *Alexander meeting his new bride-to-be Roxane* on the north wall (Figure 2). A third wall, the west one, depicts the *Taming of Bucephalus* by an unknown author (Figure 3). It was frescoed later than the other two walls because it hosted the double bed of Agostino Chigi and Francesca Ordeaschi. After the death of both of them, in 1520, the wall was decorated, but it is still uncertain how much later this work was carried out and by whose hand. Taking advantage of an imminent restoration campaign involving the northern and eastern

walls, the non-invasive analyses were also extended to the *Taming of Bucephalus*, the west wall, which was never investigated before, aiming to collect information about its painting material to be compared with the other two walls of certain authorship in order to establish the epoch of this fresco. It is important to highlight that both the north and the east wall underwent many restorations, three of them documented. The first restoration dates back to 1870, when the Duke of Ripalta, shortly after buying the Villa in emphyteusis [1], had these murals restored, adopting as a programmatic choice to “entrust the restoration of the frescoes by Sodoma, not to an illustrious artist—who no doubt would have hardly resisted the desire to redo as much as possible but, on the contrary, to a modest painter—already elderly—whose action would be limited to the indispensable” [2]. The second one, carried out at the beginning of the 20th century, is documented by an inscription on one of the walls of the room: “Vito Mameli restored in May 1915” whose work remained a “thick dark mixture painted with glue”, which the Istituto Centrale del Restauro (ICR) was called to remedy in the 1970s, as can be seen from the technical report attached to the cost report no. 4 of 1 February 1974 signed by the restorer Paolo Mora, which provided for “consolidation, cleaning and restoration of the frescoes by Sodoma and other 16th century artists” and referred to the “implementation of the work plan prepared for the restoration of the entire pictorial decoration of the Villa” [3].



Figure 1. The *Darius family before Alexander* Fresco by Giovanni Antonio Bazzi, known as Sodoma, 1519. Alexander and Roxane’s wedding room, north wall. Villa Farnesina, Rome. Courtesy of Archivio Villa Farnesina.

For this reason, the non-invasive investigations of the east wall depicting the *Darius family before Alexander* and on the north one depicting *Alexander meeting his new bride-to-be Roxane* were limited to the supposed original parts and were compared with the results emerged from the third wall, the west one, showing the *Taming of Bucephalus* by an unknown artist, trying to chronologically locate such fresco, in order to establish whether it was coeval to the other two.

A set of non-invasive optical spectroscopic analyses, including Visible Reflectance (Vis-R) portable Raman and Reflectance Infrared Spectroscopy (MIR), have been used in a multi-technique approach, widely used and well-established in the last decade [4,5] for the individuation of painting materials by refining and unravelling the information

about chemical elements from X-Ray Fluorescence (XRF), making possible the comparison among the pigments of the three walls and even disclosing some peculiarities of the execution technique.



Figure 2. *Alexander meeting his new bride-to-be Roxane.* Fresco by Giovanni Antonio Bazzi, known as Sodoma, 1519. Alexander and Roxane's wedding room, east wall. Villa Farnesina, Rome. Courtesy of Archivio Villa Farnesina.



Figure 3. *Taming of Bucephalus.* Unknown author and date. Alexander and Roxane's wedding room, west wall. Villa Farnesina, Rome. Courtesy of Archivio Villa Farnesina.

2. Materials and Methods

2.1. X-ray Fluorescence Spectrometer (XRF)

The portable XRF instrument Tracer III-SD (Bruker AXS) consists of an X-ray tube equipped with a Rh target, and a Peltier cooled Si drift XFlash detector having a resolution of 130 eV FWHM at 5.9 keV. The source was operated at 40 kV and 0.030 mA, with a data acquisition time of 30 s. This instrumental setup allows for the analysis of elements with an atomic number (Z) greater than 10. The X-rays emitted by the tube are collimated on the analyzed surface with a spot diameter of 4 mm. The spectra, corrected for the efficiency of the detector, were expressed as counts per second (cps).

2.2. Portable Raman Spectrometer

The BRAVO spectrometer uses a new patented technology called SSETM (Sequentially Shifted Excitation, patent number US8570507B1) in order to mitigate fluorescence [6,7]. The laser is slightly wavelength-shifted during the acquisition three times, and three raw Raman spectra are recorded. A proper algorithm recognizes all the peaks that shift at different laser wavelengths as good Raman peaks, and other peaks, non-shifting, as fluorescence (or absorbance) peaks, removing them. Moreover, the BRAVO use two different lasers (DuoLaserTM), ranging from 700 to 1100 nm, during the acquisition. The use of the second laser is not intended as in usual commercial handheld or portable Raman spectrometer as a tool to try to mitigate the fluorescence, but as a way to collect Raman spectra up to 3200 cm⁻¹ and hence to access the CH stretching region also. The first laser is dedicated to the acquisition of the Raman spectra in the first range (called fingerprint region), and the second one in the second range (called CH region). The BRAVO acquired spectrum is finally a Raman spectrum free from fluorescence on a whole spectral range from 3200 to 300 cm⁻¹. The applied laser power is always less than 100 mW for both lasers. Obviously, using the two BRAVO lasers ranging from 700 to 1100 nm, the sensitivity to inorganic green and blue is very reduced compared to the use of a 532 nm laser. The spectral information from the enhanced spectral range are useful for identification, for example, of resins and waxes. The spectra were acquired with acquisition time ranging from 500 ms to 2 s and accumulation ranging from 5 to 100. For all the measurements, OPUSTM software (Version 7.7) has been used in order to select the appropriate acquisition parameters. We performed at least 4 acquisitions for each point.

2.3. Visible Reflectance

The visible reflectance measurements have been carried out by a portable spectrometer CM-700d produced by Konika Minolta. The spectrometer is equipped with an UV radiation filter Xenon lamp and a silicon photodiodes array detector. The analysis range is 400–700 nm with a slit of 10 nm. Illumination area: 8 mm², Observer: 10, Illuminant: D65, measurement conditions: SCI (SCI/SCE, illumination/acquisition geometry), number of averaged acquisitions: 5. We performed at least 4 acquisitions for each point.

2.4. Reflection Infrared Spectroscopy

The portable infrared spectrophotometer ALPHA-R (Bruker Optik GmbH) is equipped with a Globar IR source, a patented interferometer (RockSolidTM, insensitive to external vibrations and able to work in any spatial orientation), and a DLaTGS room temperature detector. The working optical layout for reflection measurements is 22°/22° (specular optics), with about 15 mm of working distance. The infrared spectra have been acquired in the spectral range 7500–375 cm⁻¹ with a spectral resolution of 4 cm⁻¹ and 200 interferograms. The sampling area was 28 mm². A background correction using a reference spectrum from a gold flat mirror was applied for representing the reflectance profile (R), expressed in the graphs as pseudo-absorbance, log (1/R).

3. Results

Non-invasive analyses were carried out on the supposed unrestored parts of the north and east walls of Alexander and Roxane's wedding room in Villa Farnesina, both attributed to the painter Giovanni Antonio Bazzi, called Sodoma, and his workshop. Further analyses were also carried out on the third wall, the west one, of an unknown period and author in order to compare the results. The Tables 1–3 show the colors investigated and the main results for each employed technique. Not every color of the frescoes has been analyzed because a large part of the walls underwent heavy restorations, whose traces are also still sometimes visible in the investigated areas. Therefore, we limited our investigation to those supposed unrestored parts whose colors are shared by each of the three walls. The XRF analysis indicates Fe and Co as the most abundant elements. Fe, which often characterizes most of the pigments used for the fresco technique because of their stability and coverage, is found in red, orange, yellow, and purple areas. Cobalt is present instead as the main constituent of blue areas, widely used in all the walls studied both alone and in a mixture with other pigments.

3.1. Red

In the red areas, the presence of Fe-based pigments prevails (Table 1). In the darker shades, Raman spectroscopy identified red ochre, with the addition of a few hematite (Figure 4a, right, line 2). The bright red of Dario's daughter's dress at the left edge of the east wall is characterized by Fe (XRF, Figure 4a, left, line 1), but Raman spectroscopy individuates only calcium carbonate with its band at 1085 cm^{-1} due to the symmetric stretching of C-O bonds [8], while hematite results instead in the dark red areas, such as the skirt of Alexander (Figure 4a, line 2). In Figure 4a, the characteristic Raman bands of hematite at 498 and 610 cm^{-1} are highlighted [9].

A similar mixture of generic Fe-based red with hematite can be found in the north wall on the red curtains of Roxane's canopy bed on the north wall and in the dress of the putto on the right edge (Table 2). The first derivative of the reflectance spectrum of the red curtains (Figure 4b, line 3) does not show differences with respect to the bright red ones of the east wall (Figure 4b, lines 1, 2, areas 1, 2), and in each analyzed point, the spectrum follows the trend of a generic iron oxide. It is worth noting that on the curtains (Figure 4b, area 3), traces of cinnabar were also found, confirmed by Raman spectroscopy [17] and by Hg from XRF. Since from the reflectance spectrum it is not possible to individuate the features of cinnabar, it is likely that it was used in a mixture and is not found enough on the surface so as to be revealed. The third wall shows again the use of Fe-based red and hematite in the skirt of the back-turned man running away behind Bucephalus (Table 3). The reflectance spectrum of this area (Figure 4b, line 4/area 4) is similar to those recorded on the other two walls.

Table 1. Main results of non-invasive investigation on the east wall—*The Darius family before Alexander* (Ip: Inflection point, Max: maximum, Min: minimum).

Wall	Colored Area	X-ray Fluorescence (XRF) Main Elements	Vis-Reflectance (Vis-R)	Raman	Medium Infrared (MIR)	Comments
<i>The Darius family before Alexander</i> (east wall)	Red	Ca, Fe, Sr, K (bright red)	Ip:580,640 nm	CaCO ₃ [8]		Generic Fe-based red from Vis-R [9]
	Yellow	Fe, Ca, K, Sr (dark red)	Ip:580,640 nm	Hematite [10]		Generic Fe-based red from Vis-R [9]
		Ca, Fe, Pb, Sr, Sb (bright yellow)	Ip:440,540,630 nm	Yellow ochre [11]		From Vis-R yellow ochre [12] + Naples yellow [12]
	Purple	Ca, Fe, Pb, Sr (dark yellow)	Ip:451,533,640 nm		CaCO ₃ [8], silicates [13] and acrylic resin [14]	Mostly Pb-yellow [12] +yellow ochre from Vis-R
	Purple/greyish	Ca, Fe, K, Sr	Ip:589,640,695 nm	CaCO ₃ [8], hematite [10]		Hematite-based purple, possible caput mortuum [15]
		Ca, Fe, Co, K, Si, As, Bi, Sr	Ip:589,640,690 nm	CaCO ₃ [8], hematite [10]		Hematite-based purple, possible caput mortuum [15]. Small is not visible in Vis-R
Blue	Ca, Co, Fe, Pb, As, K, Bi, Sr, Si	Max:468,561,622 nm; Min:530,590,650 nm; Ip:687 nm	CaCO ₃ [8]		Small [16]	
		Ca, Co, Fe, Pb, As, Ti, K, Bi, Si	Max:468,561,622 nm; Min:530,590,650 nm; Ip:687 nm			Small [16] and traces of restoration materials (Ti)

Table 2. Main results of non-invasive investigation on the north wall—*Alexander meeting his new bride-to-be Roxane* (Ip: Inflection point, Max: maximum, Min: minimum).

Wall	Colored Area	X-ray Fluorescence (XRF) Main Elements	Vis-Reflectance (Vis-R)	Raman	Medium Infrared (MIR)	Comments
<i>Alexander meeting his new bride-to-be Roxane</i> (north wall)	Red	Fe, Ca, K, S, Sr, Pb, Hg	Ip:580, 640 nm	Cinnabar [17]		Generic Fe-based red from Vis-R [9] Cinnabar from XRF and Raman, but not visible by Vis-R.
	Orange	Ca, Fe, Sr, K, S, Pb	Ip:583, 640 nm	CaCO ₃ [8] + yellow ochre [11]		Generic Fe-based red from Vis-R [9] Mixture of red and yellow ochre. Yellow ochre visible from Raman and Vis-R. Pb-yellow not to be excluded due to the inflection at 510 nm from Vis-R [12]
	Yellow	Fe, Ca, K, Sr, Pb	Ip:434,510,579,636 nm	Pb-antimonate [18,19]		Only yellow ochre from Vis-R
		Ca, Fe, K, Sr, Pb	Ip: 440, 544, 640 nm	Pb-antimonate [18,19]		Yellow ochre+Naples yellow from Vis-R
		Fe, Ca, Pb, K, Sr, Sb	Ip: 436,541,631 nm	Pb-antimonate [18,19]		Mostly Pb-yellow from Vis-R [12]
		Ca, Pb, Fe	Ip:450, 519,631 nm	Pb-antimonate [18,19]		Naples yellow+Pb-yellow +yellow ochre from Vis-R [12]
		Pb, Sb, Fe (K)	Ip:443,508,546,640 nm	Hematite [10]		Hematite-based purple, possible caput mortuum [15]
	Purple	Fe, Ca, K, Sr, S,	Ip:589,640,695 nm	CaCO ₃ [8], weak signal of lapislazuli [20], acrylic resin [14]		Lapislazuli from Vis-R [12] and traces of restoration materials
	Blue	Ca, Fe, K, Sr, S	Max:477 nm, Min:603 nm, Ip:683 nm	CaCO ₃ [8]		Lapislazuli and smalt [16] in different superimposed layers. From Vis-R only Lapislazuli [12]
		Ca, Fe, Co, As, K, Si, Sr, Bi	Max:480 nm, Min:595 nm, Ip:680 nm			Lapislazuli [12] and smalt [16] mixed together: Vis-R spectrum has both the features of these pigments
	Ca, Fe, Co, As, K, Sr, Bi	Max:481 nm, Min:541,590,637 nm, Ip:680 nm			Smalt [16]	
	Ca, As, Co, Fe, K, Bi, Sr, Pb, Si	Max:470,574,623 nm, Min:524, 593,652 nm, Ip:685 nm			Lapislazuli-like spectrum in Vis-R [12]; smalt visible only in first derivative of Vis-R	
	Ca, Fe, As, Co, K, Sr, Bi	Max:478 nm, Min:576 nm, Ip:688 nm				

Table 3. Main results of non-invasive investigation on the west wall—*The Taming of Bucephalus* (Ip: Inflection point, Max: maximum, Min: minimum).

Wall	Colored Area	X-ray Fluorescence (XRF) Main Elements	Vis-Reflectance (Vis-R)	Raman	Comments
<i>The Taming of Bucephalus</i> (west wall)	Red	Ca, Fe, K Sr Fe, Ca, Sr, K, S (dark red)	Ip:582,640 nm Ip:580,640 nm	CaCO ₃ [8] Hematite [10]	Generic Fe-based red from Vis-R [9] Generic Fe-based red from Vis-R [9] Mixture of red and yellow ochre; Pb-yellow not to be excluded due to the inflection at 510 nm [12]
	Orange	Fe, Ca, Sr, Pb, K	Ip:435,510,570,635 nm	CaCO ₃ [8]	Pb-yellow and few yellow ochre from Vis-R [12]. Naples yellow from XRF and Raman
	Yellow	Pb, Fe, Sb (K)	Ip:450,521,627 nm	Pb-antimonate [18,19] Pb-antimonate [18,19]	Mostly Pb-yellow from Vis-R [12]
	Purple	Fe, Ca, Sr, K	Ip:590,639,688 nm	CaCO ₃ [8], hematite	Hematite-based purple, possible caput mortuum [15]
	Blue	Ca, Co, Fe, Bi, As, K, Si, Pb	Max:440,549,608 nm; Min:500,580,637 nm; Ip:692 nm	CaCO ₃ [8]	Smalt [16]

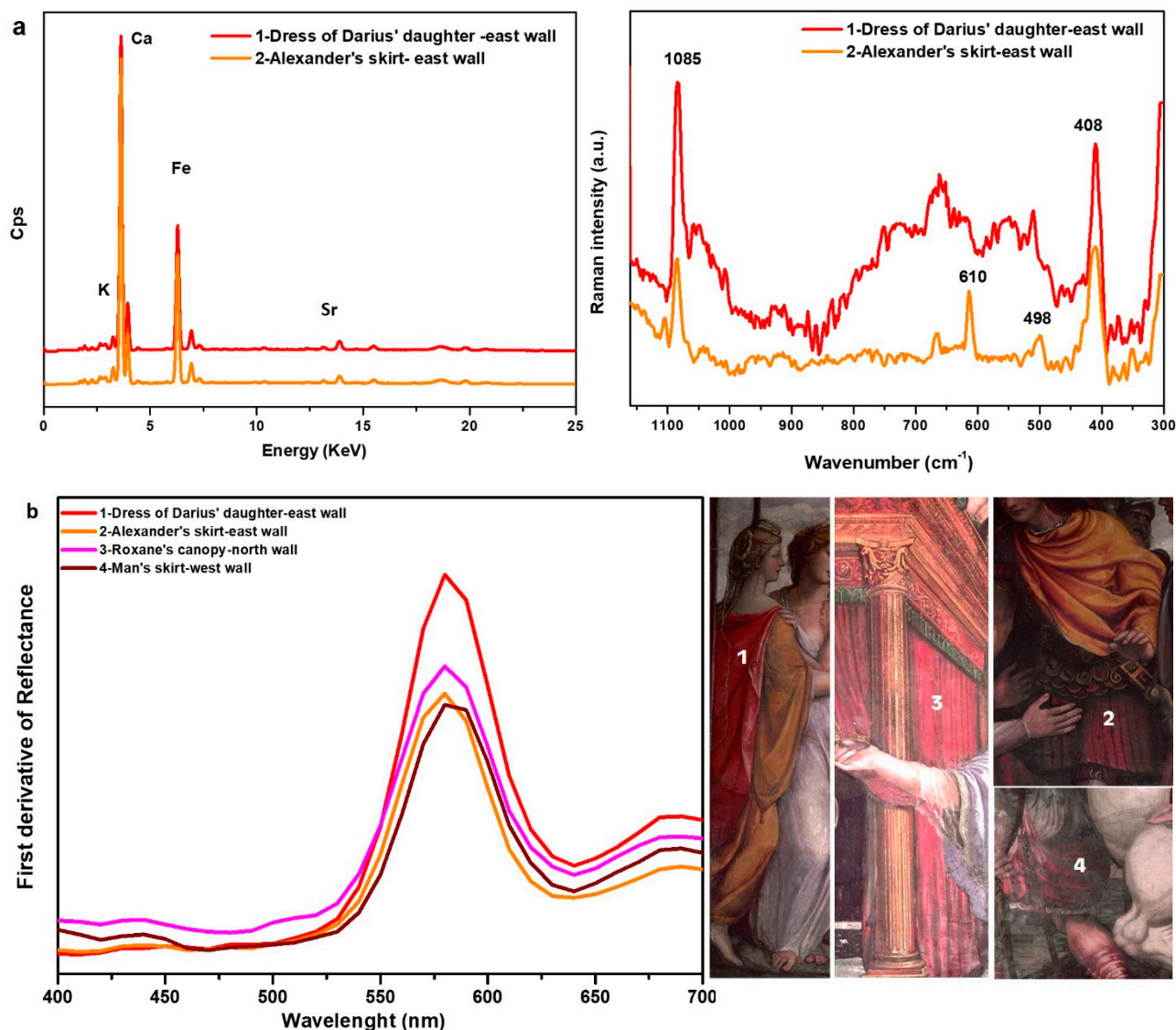


Figure 4. (a) From left to right: XRF and Raman spectra of points 1 and 2 on the east wall. (b) Comparison of the first derivative reflectance spectra measured on selected red areas (lines 1–4).

3.2. Purple

The composition of the purple areas by XRF is the same as the red ones on each of the three walls (see Tables 1–3). Raman spectroscopy instead individuates stronger hematite signals with respect to the red ones in all the purple zones, such as in the dress of Dario's wife on the east wall (Table 1).

The dress of Darius' wife Statira II appears as red/purplish (Figure 5, area 2) and has the same elemental composition as the red dress of Darius' daughter (Figure 5, area 1) depicted next to her (Table 1, bright red), but Raman spectroscopy indicates a strong presence of hematite only in the former (Table 1, dark red).

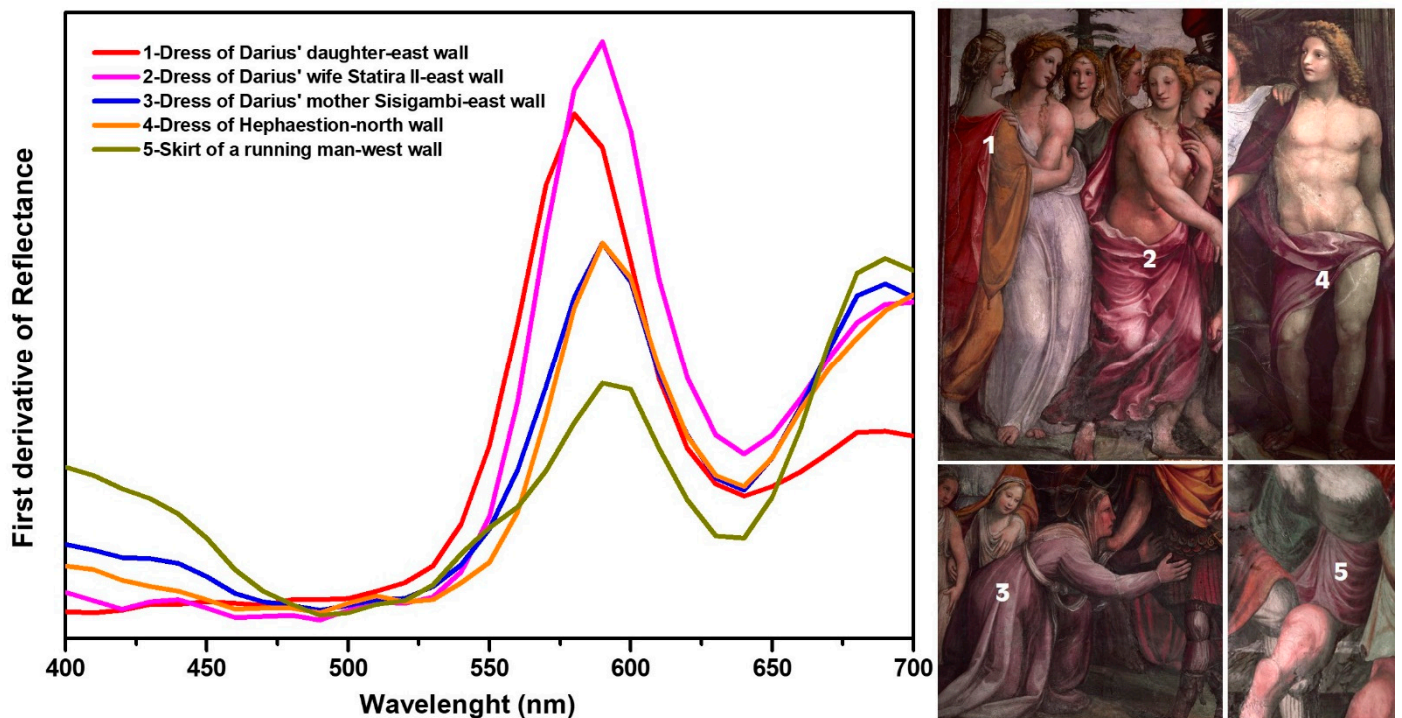


Figure 5. Comparison of first derivative reflectance spectra measured on selected red and purple areas (lines 1–5).

This difference of hue is hardly appreciated in the reflectance spectra but becomes clearer when considering their first derivatives. Indeed, for the dress of Darius' wife Statira II (Figure 5, line 2), there is a shift of the maximum of about 10 nm towards the red, and at the same time, the narrowing of the minimum to 640 nm and the consequent steep climb up to 700 nm with respect to the daughter's red dress (Figure 5, line 1). These features recur in the purple areas of each of the three walls, and more particularly, in the already discussed robe of Statira II on the east wall (Figure 5, line 2), of the half-naked Hephaestion on the north wall (Figure 5, line 4/area 4), and on the skirt of a running, back-turned figure on the third wall, the Taming of Bucephalus (Figure 5, line 5/area 5).

The purple/greyish dress of Darius' mother Sisigambi (Figure 5, area 3) consists of hematite and smalt according to a common technique concerning frescoes [15].

Smalt is indicated by XRF from the Co presence and its associated impurities, such as Bi and As. The presence of smalt is not identifiable in the reflectance spectrum, which follows exactly those of Co-free, hematite-based purples, so this area was probably painted with different superimposed layers, with purple hematite on the surface.

3.3. Yellow

The yellow areas are quite articulated, being a mixture of two or three different yellow pigments. Their composition is mostly of two types: one containing Fe and Pb, and the other Fe, Pb, and Sb. The simultaneous presence of Sb and Pb indicates the use of Pb-antimonate, also known as Naples yellow [21,22], and always coincides with lighter yellow hues. On the east wall, the use of Naples yellow is found on the lighter parts of the dress of Darius' daughter (Figure 6, area 1), where XRF indicates Fe, Pb, and Sb (Table 1). The first derivative of its reflectance spectrum is mostly that of yellow ochre (Figure 6, line 1), but a little broader, according to Naples yellow features [12]. In the yellow skirt of Hephaestion, XRF indicates Fe and Pb but no Sb. Since there is no evidence of lead white in this area, Pb is probably due to litharge, a lead monoxide, as can be inferred in the first derivative of the reflectance spectrum from the maximum at 530 nm [12], mixed with yellow ochre, which can be seen in its weakened maximum at 450 nm (Figure 6, line 2). An abundant use of litharge still accompanied by a background of yellow ochre, as suggested by Fe

presence, is even clearer in the landscape on the north wall (Figure 6, area 4), where XRF indicates only three main elements: Ca, Pb, and Fe (Table 2), and the reflectance shows, in its first derivative, mostly the spectrum of litharge but little modified by yellow ochre, recognizable for the maximum at 450 nm (Figure 6, line 4). The yellow dress of Roxane's maid on the left edge is characterized by Fe and Pb, and the first derivative of its reflectance spectrum essentially shows yellow ochre, so in this case, the source of Pb should be other than litharge (Figure 6, line 3/area 3). All three types of pigments, yellow ochre, litharge, and Naples yellow, can be found in Roxane's dress (Figure 6, area 5), where Naples yellow is used to paint lighter, cold tones. The main elements found from XRF, Fe, Pb, and Sb, suggest the presence of Naples yellow and yellow ochre, but from Vis-reflectance, litharge can also be individuated.

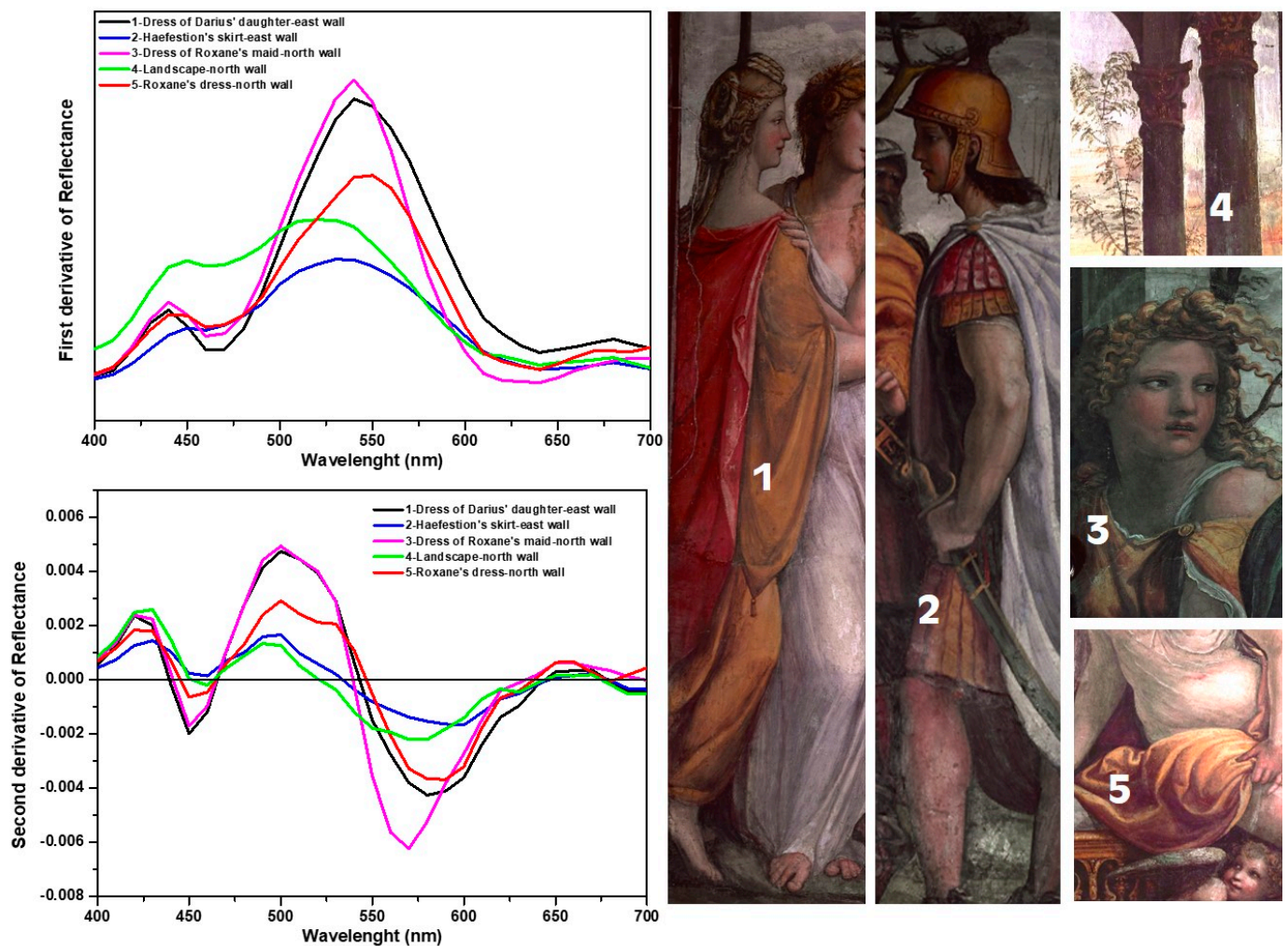


Figure 6. Comparison of first (**top**) and second (**bottom**) derivative reflectance spectra, recorded on selected yellow areas (lines 1–5).

Litharge's presence can be argued by the first derivative (Figure 6, line 5), where Roxane's dress shows the main features of both yellow ochre and Naples yellow: namely, the relative maximum at 445 nm and the broader shape of the main band, respectively. Nevertheless, a further growth at 509 nm (Figure 6, line 5) suggests the presence of litharge, otherwise impossible to establish on the basis of XRF data alone, due to the joint presence of Pb and Sb. Litharge features of Roxane's dress are more evident if the second derivatives are checked, in the maximum at 494 nm when compared with the landscape area, which was the one with the most evident presence of litharge (Figure 6, lines 4, 5). In fact, if we consider the second derivatives, the mixture of yellow ochre and Naples yellow (Figure 6,

line 1) does not account for the trend between 465 and 550 nm of Roxane's dress (Figure 6, line 5), which can be explained by the presence of litharge already seen in the landscape (Figure 6, line 4) with the two relative maximums at 494 and 529 nm, which also appear in this spectrum, facilitating the identification of litharge in a situation difficult to decipher due to the overlapping of common elements. Naples yellow is also easily individuated by its Raman features at 510 and 655 cm^{-1} [11,12], together with calcium carbonate [8] (Figure 7). The 655 cm^{-1} Raman band of Naples yellow is present when there is an excess of lead and it is specific to a non-stoichiometric Pb:Sb molar ratio [11].

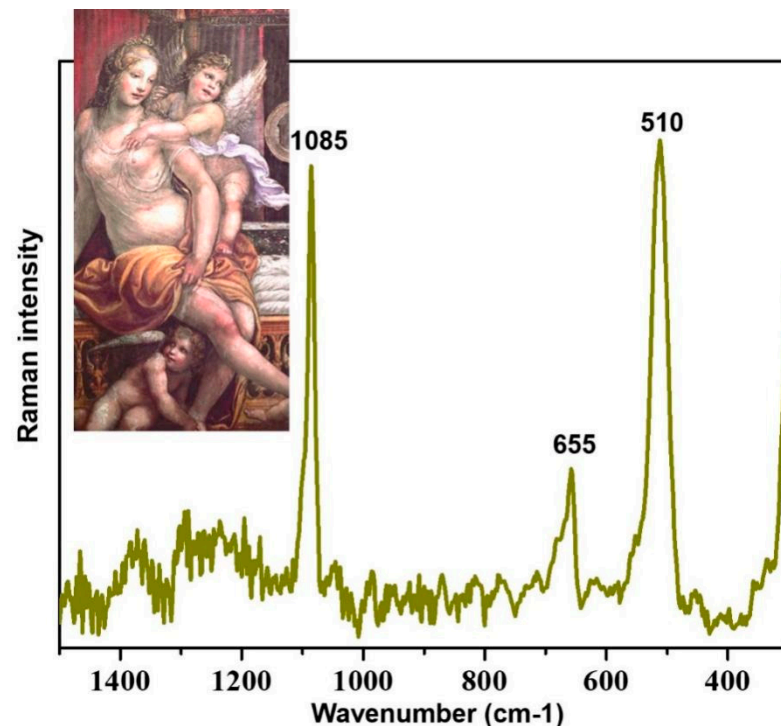


Figure 7. Raman spectrum of Roxane's yellow dress showing the presence of lead antimonate and calcium carbonate.

The presence of Naples yellow is also found on the third wall, as revealed by XRF and Raman spectroscopy (Table 3). However, in these areas, the first derivative of reflectance spectra almost exclusively shows the shape of litharge (Figure 8, lines 3, 4), as can be seen from Figure 8 by comparison with the reflectance spectrum on the landscape of the north wall (mostly litharge and yellow ochre, Figure 8, line 2) and with the dress of Roxane's maid, which in reflectance shows mostly yellow ochre (Figure 8, line 1). The striking presence of litharge allows for its otherwise difficult identification, due to the simultaneous presence of Pb and Sb.

3.4. Orange

In orange areas, the most evident and common feature of the three walls is the disappearance of Sb from the XRF analysis with respect to the corresponding yellow areas (Tables 2 and 3). In Alexander's mantle on the north wall, the use of red ochre added to the yellow ochre was identified. In addition, the presence of Pb was seen by XRF, and the first derivative of reflectance with the hinted maximum at 510 nm (Figure 9, line 1) also suggests, if compared with other litharge-based areas (Figure 9, lines 2, 4), its presence, which is not so strange due to its yellow/orange hue (Figure 9, area 1).

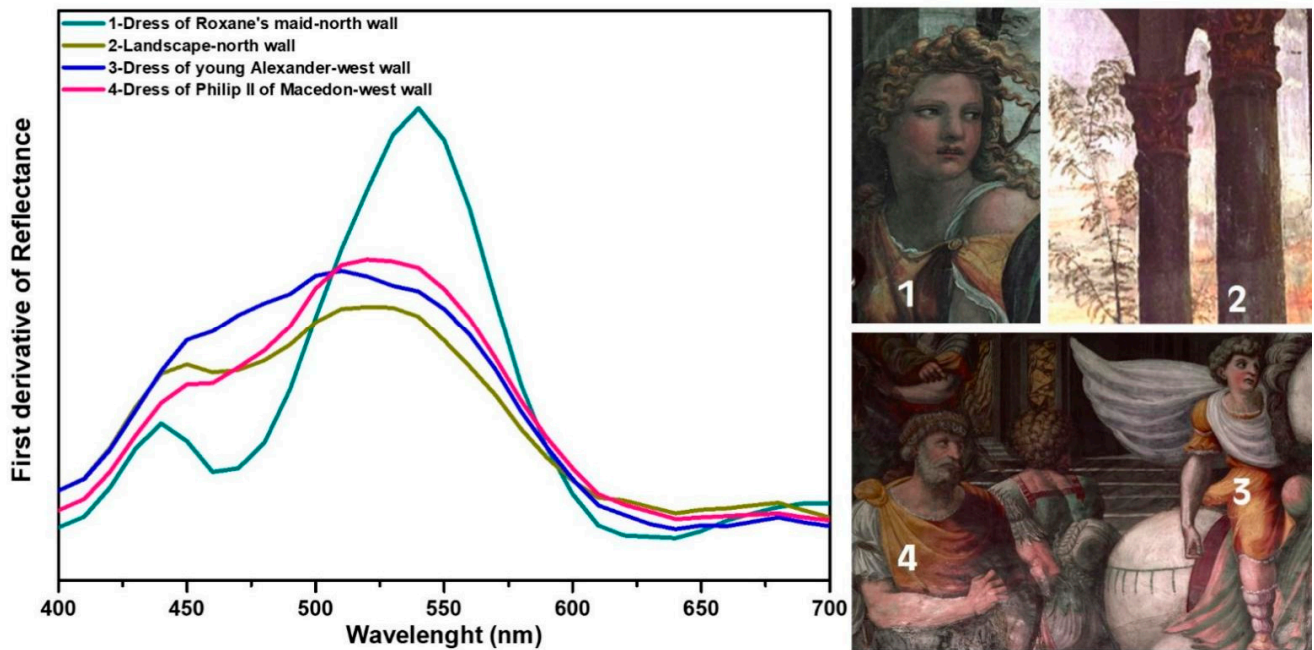


Figure 8. Comparison of first derivative reflectance spectra, recorded on selected yellow areas (lines 1–4).

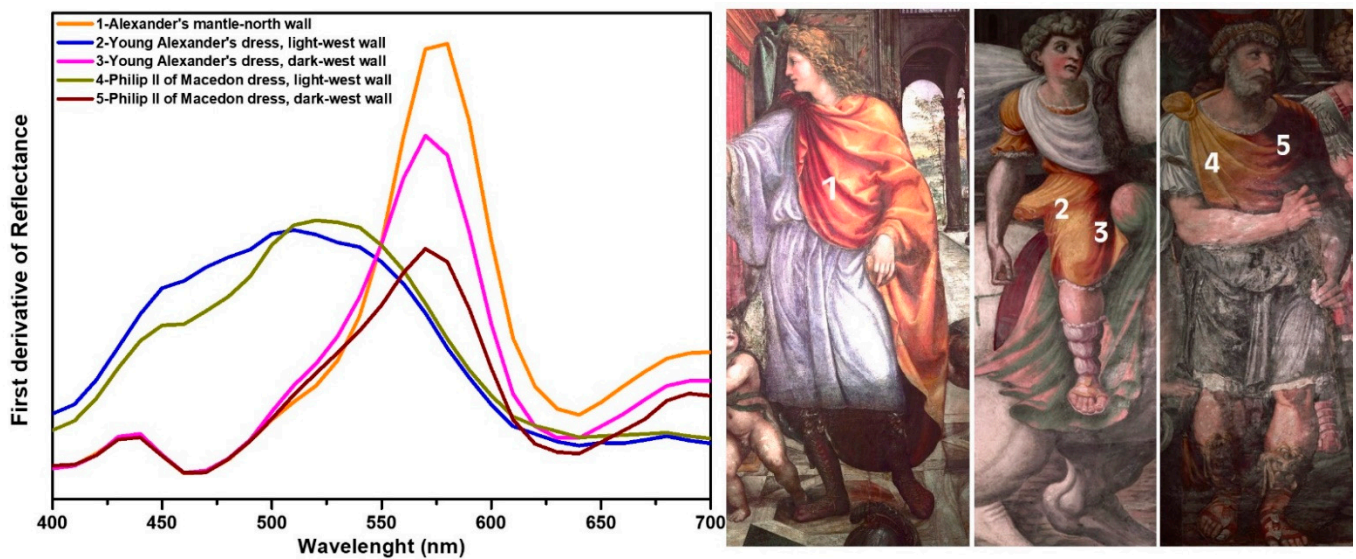


Figure 9. Comparison of first derivative reflectance spectra, recorded on selected orange and yellow areas (lines 1–5).

Additionally, on the third wall, the orange areas are characterized by mixtures of yellow and red ochre, with the presence of Pb seen from XRF (Table 3). The use of litharge is also perceivable in the orange hue of the dress of both young Alexander and his father Philip II of Macedon, when considering in the first derivative of their reflectance the weakened maximum at 510 nm compared to their yellow counterparts (Figure 9, lines 2, 3 and lines 4, 5).

3.5. Blue

The blue areas in each of the three walls studied are characterized by the presence of Co, which corresponds—in most cases—to the reflectance spectrum of smalt. Along with Co, associated impurities such as As and Bi are always found.

On the east wall, smalt is used to create the shades in the white robe of one of Darius' daughters (Figure 10, area 1) and in the white cloak of Hephaestion (Figure 10, area 2). It

is also found mixed with hematite to obtain the gray/purple hue of Sisigambi's dress, as already highlighted above (Figure 5, area 3). On the third wall, the use of smalt returns, as indicated by the presence of Co, Bi, and As, in the dark blue areas of Alexander's father's robe, Philip II of Macedon (Figure 10, area 4), and in the white garment of the young Alexander taming the horse Bucephalus (Figure 10, area 3). The first derivative of the reflectance spectra measured in the same points confirms its presence (Figure 10).

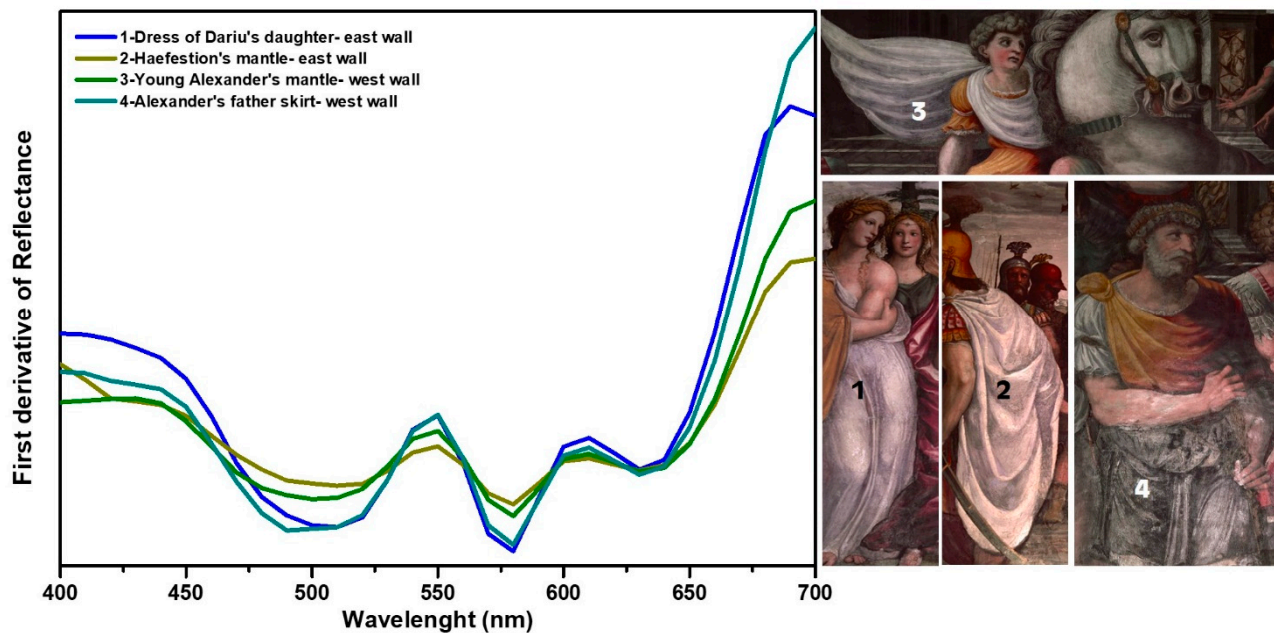


Figure 10. Comparison of first derivative reflectance spectra recorded on selected blue areas (lines 1–4).

On the north wall, two different blue pigments were individuated: smalt and lapis lazuli, with the latter univocally identified by infrared spectroscopy (Figure 11) thanks to its characteristic infrared band at 2340 cm^{-1} [20]. Both these pigments have been used to obtain different shades of blue in different ways, namely:

- (1) The use of lapis lazuli, only on the north wall, for the blue highlights on white draperies, such as on the white dress of the putto that helps Roxane to get ready (Figure 12, line 1).
- (2) The use of smalt. It is found as the only blue for highlighting the white dress of Hymenaeus (Figure 12, area 3): from XRF, the characterizing elements Co, Bi, and As emerged, and the reflectance spectrum corresponds to that of smalt (Figure 12, line 3). It is also found in those areas currently perceived as grey, such as in the helmet in the foreground, on the north wall. XRF indicates the presence of Co, Bi, and As, throughout the whole helmet.
- (3) The use of smalt and lapis lazuli in single superimposed layers, with lapis lazuli on the surface, distinguishable only with the joint use of XRF and reflectance spectroscopy, because the latter individuates only pigments on the surface. This is the case of the upper part of Alexander's dress, where the characteristic elements of the blue enamel emerged from the XRF, but its reflectance is almost entirely attributable to that of lapis lazuli, whose elements cannot be revealed by XRF (Figure 12, line 2).
- (4) The use of smalt and lapis lazuli mixed together, which is evident from the reflectance spectra of the points analyzed, where the characteristics of both pigments are found. This is the case of the lower part of Alexander's dress and that of the putto on the right, intent on playing with Alexander's shield (Figure 12, line 4).

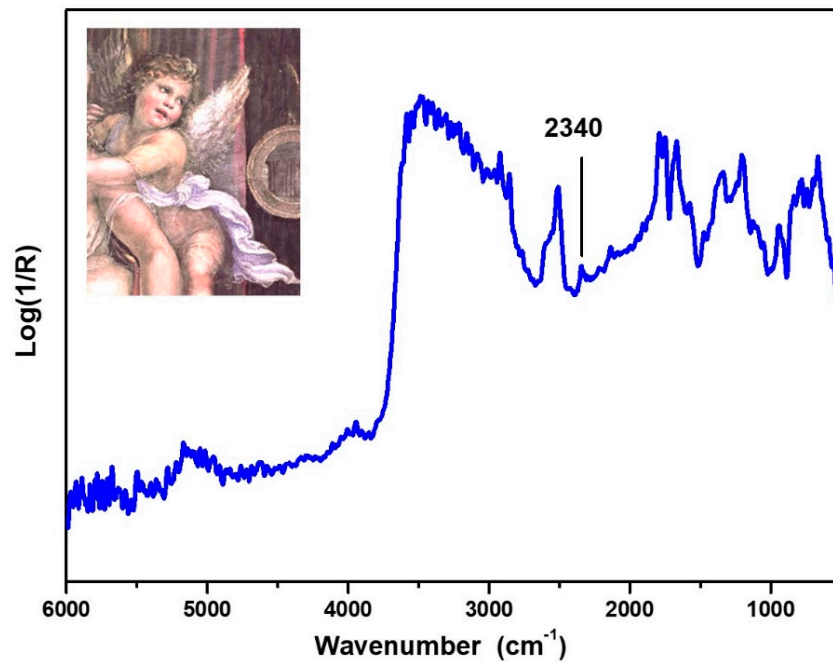


Figure 11. Infrared reflectance spectrum recorded on putto's dress, north wall. The lapis lazuli characteristic infrared band is evidenced in the spectrum.

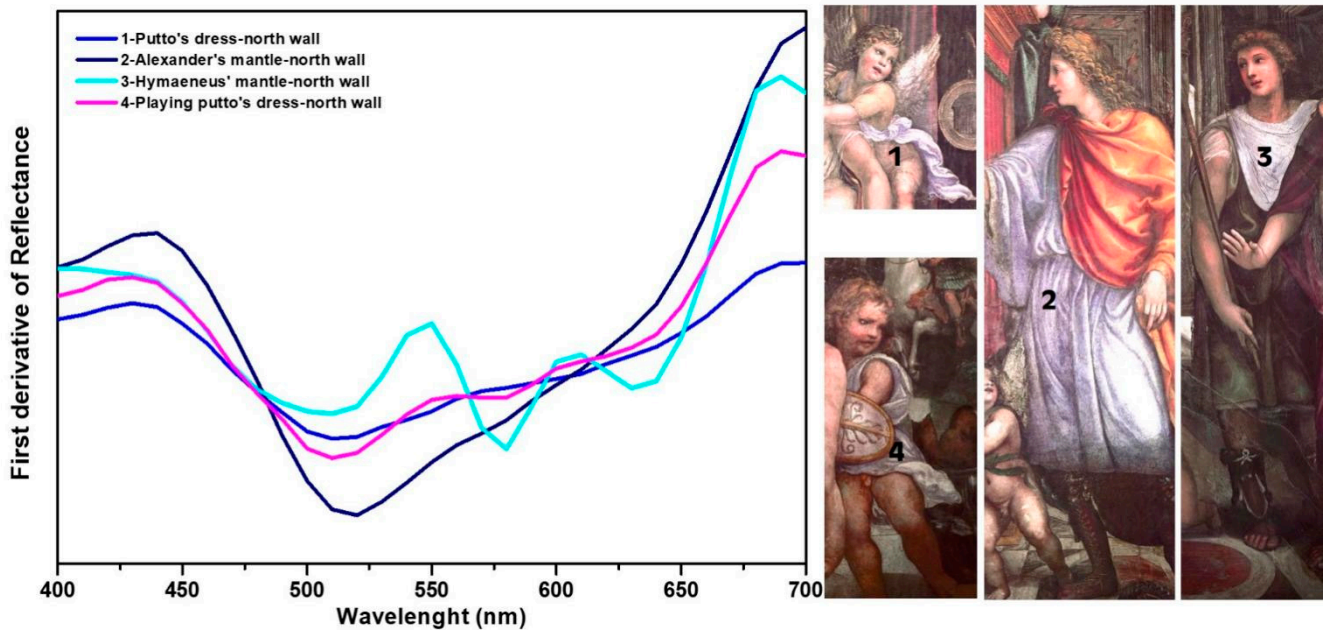


Figure 12. Comparison of first derivative spectra of visible reflectance spectra recorded on selected blue areas (lines 1–4).

Further lapis lazuli finishes would also seem by now lost or seriously compromised, as can be seen from the heavy repainting of some mantles, to restore the outlines that are no longer perceptible, including Alexander's dress, which presents elements attributable to restoration interventions such as Ti and Zn. Moreover, some gold finishes which were revealed by XRF only in the north wall also seem to be very compromised by restoration. They are present in the columns, in the mirror behind Roxane, and as labile traces in the sleeves' edge of Alexander's blue garment.

4. Discussion

Some common features emerged from the non-invasive analyses of the three walls, which are worthy of discussion. The presence of hematite, identified by Raman spectroscopy, seems to always coincide with a purplish hue. In fact, if we exclude the cases in which hematite is added to a Fe-based pigment to obtain a darker red tone, all the other areas rich in hematite are purple. No organic compound ascribable to a dye has been identified in these purple hues, which show the same composition and the same impurities as the red ones without hematite, and compared to these, show a definitely different shade. This chromatic diversity, with the elemental composition being the same and in the absence of organic dyes, suggests the use of hematite as a purple pigment in its own right, perhaps in the form of *caput mortuum* [15]. The use of this hematite-based purple pigment occurs in each of the three walls. The yellow areas show a very articulated composition. They are all characterized by the presence of yellow ochre to which other yellow pigments are added. First, Pb-antimonate, also known as Naples yellow, is easy to individuate from Sb and Pb by XRF. Furthermore, from the joint analysis of XRF and visible reflectance, a Pb-based yellow was also revealed, namely litharge, which would otherwise be impossible to identify by the elemental analysis alone when used together with Pb-antimonate. In fact, the contemporary presence of Pb and Sb from XRF may have distracted from considering other Pb-based yellows, but the Vis-reflectance revealed the spectral shape of litharge also in those areas where Pb-antimonate has been found. The presence of the Pb-antimonate or Naples yellow occurs in the yellow areas in the lighter hues, with a cold tone. Naples yellow is one of the synthetically produced pigments known and lost and rediscovered a number of times throughout history [21]. It comes from the glassmakers' tradition and its use as a pigment at the beginning of the XVI century was very early and unexpected [22]. It is worth noting that Naples yellow has already been individuated in Villa Farnesina, in the Loggia of Cupid and Psyche, both in the figurative part of the scenes and in the fruits of the vegetable festoons [23].

In Alexander and Roxane's Wedding Room, it is used in the walls painted by Sodoma to lighten the yellow tones, affording a lighter and cooler shade.

Additionally, on the third wall, the same three yellow pigments were used, but with an interesting difference. On the walls by Sodoma, the Naples yellow is always detectable by reflectance, and this means that it is on the surface, as a "final touch" in the lighter shades. On the third wall, Naples yellow is present in the yellow areas because it is individuated by XRF, but the reflectance does not always detect it, with litharge or yellow ochre prevailing instead.

Thus, even though we found the same yellow pigments for each of the three walls, it is important to highlight the diversity in the "final touch". Indeed, Sodoma used Naples yellow to refine the light hues, while the painter of the third wall, who used the same materials as Sodoma, indifferently mixed Naples yellow with yellow ochre and litharge, without preferring one particular pigment for finishing. Furthermore, the evidence that Sb disappears in the orange areas in both walls one and two, and in the third wall as well, indirectly confirms the precise choice by both Sodoma and the unknown painter to use Naples yellow only for light yellow shades.

Smalt, which is widely used in each of the three walls studied, has the characteristic of having, associated with the Co, some impurities of As and Bi. In particular, the latter allows the pigment to be placed within a specific processing method that obtained the blue of enamel from the bismuth slag, locating its extraction both geographically, as a German manufacture from the Erzgebirge, and chronologically as well, attesting to it within the XVI century [24,25]. This means that the decoration on the third wall is realistically ascribable within the 16th century. It must be remembered that the third wall was the one that housed the double bed of Agostino Chigi and Francesca Ordeaschi, who both died in 1520, *terminus post quem* from which to start the decoration of the third wall. Documentary sources attest the presence of Sodoma in Rome to settle and open a workshop in 1521 [25], and the same sources exclude any kind of pictorial production from Sodoma in the capital from that

date, apart from a few drawings [25]. This fact does not exclude that he may have passed on his knowledge to the students in the workshop, who could have worked inside Villa Farnesina, as their Master did. This information together with the scientific evidence of the painting material support the hypothesis that the third wall is probably coeval to the other two, and painted by someone who had attended Sodoma's workshop and had learned his painting techniques and his painting materials as well.

Finally, it must also be noted that for the north wall, i.e., that depicting Alexander meeting his new bride-to-be Roxane, some precious painting materials such as gold finishes and lapis lazuli were used, which do not appear on the other two walls. These unique features only present on the north wall tell us something about the relevance of this fresco, other than the authorship. In fact, Sodoma used very precious materials for decorating this wall, which he himself did not use for the east one. This must be ascribed to the painted subject of this wall—the marriage of Alexander and Roxane—which must be the most significant of the room and therefore deserving the most precious painting materials which were circulating at that time.

5. Conclusions

The results obtained show a substantial uniformity in the typology of the pigments used on the east, north, and west walls of Alexander and Roxane's Wedding Room in Villa Farnesina, Rome. Additionally, the execution technique relative to the mixtures of pigments used was found to be the same, in the rendering of yellows and their different shades from colder tones to golden ones, and in the blue hues on a white background. Although it is not known how much time passed between the execution of the two frescoes, it should be noted that the palette of the east and north walls is the same as the third wall, the west one. In particular, those pigments that in the two walls frescoed by Sodoma are a reason of interest because they were still uncommon or because they were available in a limited period of time, such as Naples yellow, caput mortuum, and smalt, are also found, used in the same way, in the third wall. Combining the spectroscopic evidence resulting from the non-invasive analyses of pigments with historical sources, we hypothesized that the decoration of the third wall, which represents the Taming of Bucephalus, was carried out shortly after 1520 and within the sixteenth century, as evidenced by the use of smalt containing Bi impurities. Moreover, the decoration of the third wall was likely accomplished by an artist who surely knew Sodoma's painting technique very well, as evidenced by the same materials used, and the same execution technique for painting particular areas. This work demonstrates how investigations on pictorial materials can reveal very useful details, much like documentary sources, in order to obtain—totally non-invasively—crucial information about some still uncertain artistic productions.

Author Contributions: Conceptualization, C.A. and M.V.; methodology, M.V., M.A. and C.A.; investigation, M.V., M.A., C.A. and A.S.; resources, A.S.; data curation, M.V. and C.A.; writing—original draft preparation, C.A. and M.V.; writing—review and editing, M.V., M.A., C.A. and A.S.; supervision, A.S. All authors have read and agreed to the published version of the manuscript.

Funding: This research received no external funding.

Institutional Review Board Statement: Not applicable.

Informed Consent Statement: Not applicable.

Acknowledgments: Virginia Lapenta is gratefully acknowledged for her kind availability, the interesting case which she invited us to study, and the images supplied.

Conflicts of Interest: The authors declare no conflict of interest.

References

- Lapenta, V. Il Duca di Ripalta (Salvador Bermúdez de Castro) in Villa Farnesina. In *La Saletta Pompeiana e l'Ottocento in Villa Farnesina*; Lapenta, V., Sgamellotti, A., Eds.; Bardi Edizioni: Rome, Italy, 2020.
- Bigot, C. Raphaël et la Farnésine. In *Gazette des Beaux-Arts*; Paris, France. 1884, p. 10. Available online: <http://www.icr.beniculturali.it/pagina.cfm?usz=5&uid=68&rid=93> (accessed on 15 July 2021).
- Invernizzi, C.; Daveri, A.; Rovetta, T.; Vagnini, M.; Licchelli, M.; Cacciatori, F.; Malagodi, M. A multi-analytical non-invasive approach to violin materials: The case of Antonio Stradivari “Hellier” (1679). *Microchem. J.* **2016**, *124*, 743–750. [CrossRef]
- Vagnini, M.; Gabrieli, F.; Daveri, A.; Sali, D. Handheld new technology Raman and portable FT-IR spectrometers as complementary tools for the in situ identification of organic materials in modern art. *Spectrochim. Acta Part A Mol. Biomol. Spectrosc.* **2017**, *176*, 174–182. [CrossRef]
- Cooper, J.B.; Abdelkader, M.; Wise, K.L. Sequentially Shifted Excitation Raman Spectroscopy: Novel Algorithm and Instrumentation for Fluorescence-Free Raman Spectroscopy in Spectral Space. *Appl. Spectrosc.* **2013**, *67*, 973–984. [CrossRef] [PubMed]
- Cooper, J.B.; Marshall, S.; Jones, R.; Abdelkader, M.; Wise, K.L. Spatially compressed dual-wavelength excitation Raman spectrometer. *Appl. Opt.* **2014**, *53*, 3333–3340. [CrossRef] [PubMed]
- DeCarlo, T.M. Characterizing coral skeleton mineralogy with Raman spectroscopy. *Nat. Commun.* **2018**, *9*, 5325–5327. [CrossRef]
- Oltrogge, D. The Use of VIS Spectroscopy in Non Destructive Paint Analysis Research Project Painting Techniques of Impressionism and Postimpressionism. Köln. 2008. Available online: www.museenkoeln.de/impressionismus (accessed on 15 July 2021).
- Jubb, A.M.; Allen, H.C. Vibrational Spectroscopic Characterization of Hematite, Maghemite, and Magnetite Thin Films Produced by Vapor Deposition. *Appl. Mater. Interfaces* **2010**, *2*, 2804–2812. [CrossRef]
- Froment, F.; Tournié, A.; Colomban, P. Raman identification of natural red to yellow pigments: Ochre and iron-containing ores. *J. Raman Spectrosc.* **2008**, *39*, 560–568. [CrossRef]
- Toffoletto, E. Analisi non Invasive per la Caratterizzazione di Dipinti ad Olio su tela, Conservati nel Museo Ca’ Rezzonico di Venezia. Master’s Thesis, Università Ca’ Foscari, Venezia, Italy, 2015.
- Huang, Y.; Jiang, Z.; Schwieger, W. Vibrational Spectroscopic Studies of Layered Silicates. *Chem. Mater.* **1999**, *11*, 1210–1217.
- Manfredi, M.; Barberis, E.; Rava, A.; Robotti, E.; Gosettia, F.; Marengo, E. Portable diffuse reflectance infrared Fourier transform (DRIFT) technique for the non-invasive identification of canvas ground: IR spectra reference collection. *Anal. Methods* **2015**, *7*, 2313–2322. [CrossRef]
- Castagnotto, E.; Locardi, F.; Slimani, S.; Peddis, D.; Gaggero, L.; Ferretti, M. Characterization of the Caput Mortuum purple hematite pigment and synthesis of a modern analogue. *Dyes Pigment.* **2021**, *185*, 108881–108889. [CrossRef]
- Poldi, G. L’individuazione del blu di smalto sano e decolorato in dipinti mediante ED-XRF e spettrometria in riflettanza, conference paper. In Proceedings of the ATIV Conference, Parma, Italy, 9–10 July 2009.
- Moon, D.-H.; Lee, N.-R.; Lee, E.-W. Ancient Pigments in Afrasiab Murals: Characterization by XRD, SEM, and Raman Spectroscopy. *Minerals* **2021**, *11*, 939. [CrossRef]
- Rosi, F.; Manuali, V.; Miliari, C.; Brunetti, B.G.; Sgamellotti, A.; Grygar, T.; Hradil, D. Raman scattering features of lead pyroantimonate compounds. Part I: XRD and Raman characterization of Pb₂Sb₂O₇ doped with tin and zinc. *J. Raman Spectrosc.* **2008**, *40*, 107–111. [CrossRef]
- Simsek, G.; Geckinli, A.E. An assessment study of tiles from Topkapı Palace Museum with energy-dispersive X-ray and Raman spectrometers. *J. Raman Spectrosc.* **2012**, *43*, 917–927. [CrossRef]
- Smith, G.D.; Klinshaw, R.J. The presence of trapped carbon dioxide in lapis lazuli and its potential use in geo-sourcing natural ultramarine pigment. *J. Cult. Herit.* **2009**, *10*, 415–421. [CrossRef]
- Roy, A. *Artists’ Pigments: A Handbook of Their History and Characteristics*; Oxford University Press: Oxford, UK, 1993; Volume 1.
- Seccaroni, C. *Giallorino. Storia dei Pigmenti Gialli di Natura Sintetica*; De Luca Editori d’arte: Rome, Italy, 2005.
- Seccaroni, C.; Aresi, N.; Frizzi, T.; Anselmi, C.; Sgamellotti, A. Raphael’s workshop at Villa Farnesina in Rome: The frescoed vault of Cupid and Psyche investigated by macro-X-ray fluorescence scanning. *Rend. Fis. Acc. Lincei* **2018**, *29*, 499–510. [CrossRef]
- Haldi, J.-P.; Seccaroni, C. *Cobalto, Zaffera, Smalto Dall’Antichità al XVIII Secolo*; ENEA: Rome, Italy, 2016.
- Colomban, P.; Kırmızı, B.; Franci, G.S. Cobalt and Associated Impurities in Blue (and Green) Glass, Glaze and Enamel: Relationships between Raw Materials, Processing, Composition, Phases and International Trade. *Minerals* **2021**, *11*, 633. [CrossRef]
- Bartalini, R. On the Room of Alexander and Roxane at the Farnesina and on the activity of Sodoma in Rome (with reference to Girolamo Genga and his relations with the Chigi family). *Prospettiva* **2014**, *153*, 39–73.

Article

Retrieving Tarnished Daguerreotype Content Using X-ray Fluorescence Imaging—Recent Observations on the Effect of Chemical and Electrochemical Cleaning Methods

Alison Stark¹, Fraser Filice¹, James J. Noël¹ , Ronald R. Martin¹, Tsun-Kong Sham^{1,*} , Yanhui Zou Finfrock^{2,3} and Steve M. Heald³

¹ Department of Chemistry, Western University, London, ON N6A 5B7, Canada; astark9@uwo.ca (A.S.); ffilice@uwo.ca (F.F.); jjnoel@uwo.ca (J.J.N.); rrrhm@uwo.ca (R.R.M.)

² CLS@APS, Science Division, Canadian Light Source, Saskatoon, SK S7N 2V3, Canada; zou.finfrock@lightsource.ca

³ Advance Photon Source, Argonne, National Laboratory, Argonne, Lemont, IL 60439, USA; heald@anl.gov

* Correspondence: tsham@uwo.ca

Abstract: We report a study on the effect of chemical and electrochemical cleaning of tarnished daguerreotypes observed using X-ray fluorescence (XRF) microscopy with a micro-focussed X-ray beam from a synchrotron source. It has been found that, while both techniques result in some success depending on the condition of the plate and the experimental parameters (chemical concentration, voltage, current, etc.) the effect varies, and cleaning is often incomplete. The XRF images using Hg $L_{\alpha,\beta}$ at an excitation energy just above the L_3 edge threshold produce fine images, regardless of the treatment. This finding confirms previous observations that if the bulk of the image particles remains intact, the surface tarnish has little effect on the quality of the original daguerreotype image retrievable from XRF.

Keywords: daguerreotype; tarnish; chemical cleaning; electrocleaning; synchrotron; X-ray fluorescence imaging

Citation: Stark, A.; Filice, F.; Noël, J.J.; Martin, R.R.; Sham, T.-K.; Finfrock, Y.Z.; Heald, S.M. Retrieving Tarnished Daguerreotype Content Using X-ray Fluorescence Imaging—Recent Observations on the Effect of Chemical and Electrochemical Cleaning Methods. *Heritage* **2021**, *4*, 1605–1615. <https://doi.org/10.3390/heritage4030089>

Academic Editors: Antonio Alvarez Fernandez-Balbuena and Daniel Vazquez-Molini

Received: 6 July 2021
Accepted: 31 July 2021
Published: 5 August 2021

Publisher's Note: MDPI stays neutral with regard to jurisdictional claims in published maps and institutional affiliations.



Copyright: © 2021 by the authors. Licensee MDPI, Basel, Switzerland. This article is an open access article distributed under the terms and conditions of the Creative Commons Attribution (CC BY) license (<https://creativecommons.org/licenses/by/4.0/>).

1. Introduction

1.1. The Daguerreotype

Daguerreotypes are the earliest form of photography, produced on a silver-coated copper plate, which was used predominantly in the mid to late 1800s [1,2]. The process of creating a daguerreotype was developed by Louis-Jacques-Mande Daguerre and perfected in 1839. As creating daguerreotypes was a lengthy and costly practice, only people of high status could afford to have their photo taken this way [3,4]. Nevertheless, daguerreotypes offer snapshots, literally, for the very first time, into this era of human activities, and are of artistic, cultural, and historical significance. Efforts to preserve and restore these images have aroused considerable interest in the art preservation community [5].

The production of a daguerreotype image requires several steps. The result is a high contrast, one-of-a-kind photograph [1–4]. The process begins with making a finely polished silver-coated copper plate. This is followed by the exposure of the surface to iodine, making the plate photosensitive upon the formation of silver iodide. Later variations utilized alternative halogens, chlorine, bromine, or a combination of these, in order to increase the sensitivity of the surface to light. The photosensitive plate is mounted in the lightproof interior of a camera. When the photo to be taken is appropriately framed, the lens cap is removed, exposing the plate to light. This step causes the formation of silver image particles that result from the photolysis of the silver halide on the silver surface, creating the image. Areas with dense distributions of image particles of a rather consistent shape and size correspond to a high light intensity, whereas areas exposed to a low light intensity

display thin and nonuniform image particles. Bright regions are the result of the particles scattering light, and where there are few image particles, only light from specular reflection can be seen. This is why the light and dark areas can change if the daguerreotype is tilted [1]. After the image has formed on the surface, the plate is then exposed to mercury vapor, which fixes the image on the silver-coated copper plate. This is the crucial step in the entire process and, as we shall show below, the presence of Hg on the image's particles allows us to retrieve the fine image details from a tarnished daguerreotype. Excess halides are removed with a salt solution, such as sodium thiosulfate. This makes the surface insensitive to light, and halts the creation of additional image particles, which could cloud the image [1,2]. Next, the silver-coated copper plate is washed with distilled water, and a gold chloride solution is poured on the daguerreotype to ensure the longevity and durability of the image [1]. Note, the addition of gold chloride, known as the gilding step, was later introduced into the final stages of the daguerreotype procedure. Finally, the plate is heated to dry the surface. This process produces a completed daguerreotype image of the subject.

1.2. Deterioration of the Daguerreotype

Daguerreotypes are subject to the formation of surface tarnish, which, in the extreme, can completely obscure the image. Surface corrosion will alter the shape and refractivity of the image particles, and hence the direction and intensity of the scattered light. The most frequent tarnishes are silver halides, silver oxides, and sulfur compounds originating from incomplete washing during the original preparation, exposure to atmospheric gases, and deterioration of the cover glass [5,6]. Studies have also focused in great detail on the effects of the daguerreotype storage and exposure conditions. Extreme temperatures and/or humidity can have a negative influence on the integrity of the surface. When a daguerreotype is stored, a glass cover is usually present on the image side of the surface; however, deterioration of the glass cover can be another factor contributing to the degradation of the plate [7]. Many original glass cover plates contained sodium and potassium, which have been shown, over time, to diffuse from the glass and leave deposits on the daguerreotype surface. This leads to highly localized spots of corrosion across the daguerreotype. In addition, the glue that was used to adhere the glass cover to the plate also contributed to corrosion at the perimeter of the daguerreotypes [8,9]. Compounds such as oxides and various sulfides may have been formed because of this practice [10].

1.3. Conservation and Preservation Methods

Daguerreotypes are fragile, and Daguerre himself recommended that the plate be protected with a cover glass. About 20 years after their invention, the commercial production of daguerreotypes ceased; there was little effort to preserve them and they became collectors' items. It was not until the twentieth century that archives and art institutions began to collect and preserve daguerreotypes [1]. Many preservation and restoration processes have been tried with varying success. As a result of the variation in the methods of preparation, as well as diverse storage conditions, many daguerreotypes have unique damage requiring tailored cleaning methods. As a result, there is not a single method guaranteed to restore these images. While progress has been made towards a more universal cleaning procedure, these procedures completely depend on the original quality of the surface [5]. There are two general cleaning techniques: chemical cleaning and electrocleaning [1,2]. There are also two common methods in electrocleaning, sometimes referred to as the Wei method and the Barger method [11,12]. The Wei method simply applies a cathodic polarization to the daguerreotype plate in a cleaning solution [11]. The Barger method applies both oxidizing and reducing polarizations to induce anodic and cathodic currents on the daguerreotype, switching between the two throughout the process. It is hoped that by manipulating the surface chemistry, the tarnish will be removed, while the image particles (nano particles of Ag coated with Hg forming an amalgam) will remain intact. Various studies have proven that both methods can help restore the daguerreotype image to some extent. However, as

each daguerreotype is unique in terms of the elemental composition of the tarnish and how deteriorated it is, the methods are not always effective. In some cases, electrocleaning treatments have further damaged the daguerreotype. To remove the tarnish from the surface with electrocleaning methods, adjustments of the potential are made. This potential is biased on the daguerreotype surface, and monitored by a reference electrode, as described below.

1.4. XRF Imaging Using a Micro Focused X-ray Beam

It was recently reported that using a micro-focused X-ray beam from a synchrotron light source and selecting the excitation energy to just above the L_3 absorption edge of Hg and tracking the intensity of the Hg L_α and L_β lines in a two-dimensional scan across the daguerreotype plate could retrieve the original image from the daguerreotypes tarnished beyond recognition [7]. These results show that it is the integrity of the silver image particles that were formed upon the photochemical reaction of the photosensitizer, silver halide, when exposed to the object, and the subsequent exposure to hot Hg vapor that determines the quality of the daguerreotype [1,2]. Thus, Hg vapor stabilizes the image particles of silver clusters, forming an amalgam that defines the image, and the image particles are preserved by the presence of Hg. If surface reactions or adventitious contaminants such as the organic molecules that tarnish the plate only affect the surface and the near-surface region (on the order of $< \text{nm}$), this would have very little effect on the image retrieved from Hg L_α fluorescence X-rays. This is also why chemical and electrocleaning would work if the bulk of the image particles remained largely undisturbed after cleaning. The objective of this work is to proceed with chemical cleaning and electrocleaning methods under various conditions on a single daguerreotype plate, and to then conduct Hg XRF imaging to further confirm this notion [3,7].

2. Materials and Methods

2.1. The Daguerreotype Plate and Cleaning Solutions

The daguerreotype plate under investigation, “Little Girl, Pretty Purse”, was provided by the Canadian Conservation Institute, National Gallery of Canada (Ottawa, Canada). The reagents used for the chemical cleaning portion included reagent grade ammonium hydroxide (NH_4OH , Caledon Laboratory Chemicals) and reagent grade sodium thiosulfate $\text{Na}_2\text{S}_2\text{O}_3$, 99% assay (Sigma Aldrich). Solutions containing specific reagent concentrations were prepared, including a sodium thiosulfate solution of 3% mass/volume (0.190 M) and 1% and 0.5% mass/volume of ammonium hydroxide (0.294 M and 0.147 M, respectively). Additionally, 0.01 M and 0.1 M reagent grade potassium chloride (KCl BioShop), and 0.01 M reagent grade potassium sulfate (K_2SO_4 , 99% assay, Caledon Laboratory Chemicals) solutions were created for the electrochemical cleaning process. All of the dilution schemes and rinsing processes were done with Type 1 water ($18.2 \text{ M}\Omega \times \text{cm}$ resistivity).

2.2. Chemical and Electrochemical Solution Cell Fabrication

To clean the daguerreotype, two cells were designed using Autodesk Inventor Professional 2020, and were 3D printed from UV-cured resin (ANYCUBIC Photon UV 3D Printer, ANYCUBIC 405 nm Resin Green) for chemical and electrochemical cleaning. These cells were designed to be clamped against the face of the daguerreotype, compressing an O-Ring and creating a tight seal with the surface. Both designs exposed a small surface area of the sample surface to the solution, allowing for multiple reagents and techniques to be tested on localized regions of the same specimen. The chemical cleaning device was composed of three solution wells in proximity, allowing for the simultaneous testing of multiple solutions on a localized area. The electrochemical cell incorporated a much larger solution volume, accommodating a three-electrode electrochemical setup [13]. These arrangements are displayed in Figure S1.

2.3. Chemical Cleaning and Electrocleaning

The chemical cleaning cell was clamped onto the daguerreotype surface, as shown in Figure S1c. Each of the three wells had a different solution pipetted into them and were left for 1 h. After that, the solutions were removed, and each well was gently rinsed with Type 1 water. The daguerreotype was then rinsed and patted dry with Kimwipes. Each site was then inspected at Surface Science Western with a VHX-6000 optical microscope (Keyence), as well as VP-SEM (Hitachi SU3900) and EDX (Oxford Instruments Ultim Max 65).

Electrocleaning and measurements were performed with a Solartron 1287 potentiostat on the daguerreotype plate. A three-electrode setup was used, as shown in Figure S1a,b, where the daguerreotype was the working electrode, Ag/AgCl was the reference electrode, and platinum foil was the counter electrode. The solution cell was clamped onto the daguerreotype, then filled with one of the several electrolytes being studied, and a 5 min open circuit potential (OCP) measurement was performed. The OCP measurement determines the resting potential of the working electrode. This was followed by an electrolytic cleaning step using the Wei method [11] or the Barger method [12], described as follows.

In the Wei method, we applied a constant cathodic polarization (constant negative potential) for 90 s, as seen in the potential versus time graph (Figure 1, top-left). In the corresponding current versus time graph (Figure 1, top-right), a typical current response is shown; the current started at a rather negative value, while reducible species were abundant on the surface, and then gradually approached zero, suggesting that the oxidized surface species were becoming depleted as the cleaning procedure progressed.

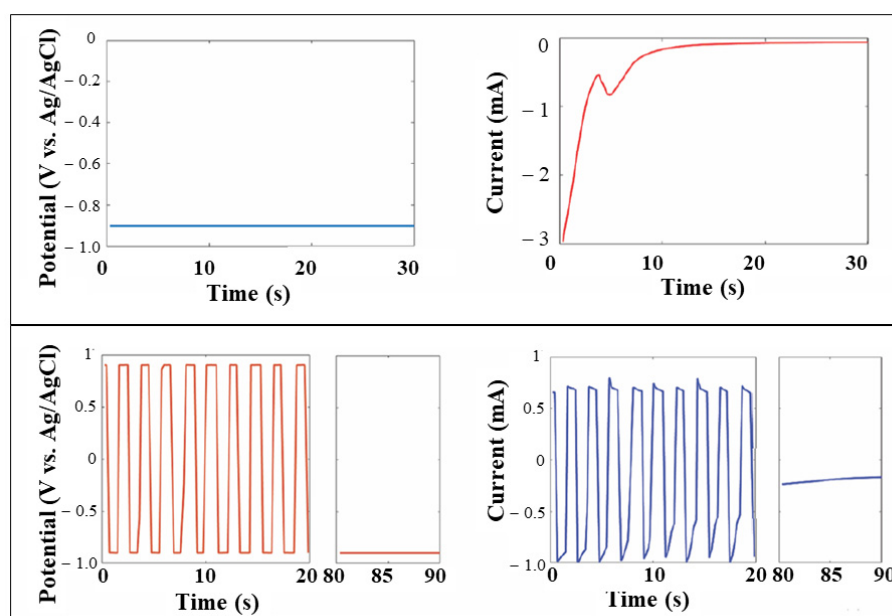


Figure 1. (Top): the potential versus time, and current versus time profiles for the Wei method; only the first 30 s were plotted in a 90-s test. (Bottom): the potential versus time, and current versus time profiles for the Barger method; only the first 20 s were plotted in an 80-s test, including the 10 s of the constant negative potential applied at the end of each test.

In the Barger method, we applied a modified version in which the applied potential was alternated between anodic and cathodic polarizations in 2-s intervals for 80 s, followed by a 10-s cathodic cleaning step, also seen in Figure 1, bottom-left, in the potential versus time graph. The corresponding current versus time graph (Figure 1, bottom-right) does not show the same approach to zero current seen in the Wei method, for several reasons. First, the electrode was not given enough time during any of the cathodic stages to achieve a steady state. Second, the anodic phase preceding each cathodic phase of the oscillation generated more oxidized species [7] for reduction during the subsequent cathodic phase,

and finally, the current during the anodic phase should never be eliminated because it could correspond to the oxidation of the Ag that makes up the bulk of the daguerreotype. Following the application of one of these cleaning profiles, the electrolyte solution was immediately removed, and the daguerreotype surface was gently flushed with Type 1 water. Each site was then analyzed optically, as well as by VP-SEM and EDX.

2.4. SEM and EDX Characterization

The morphology and elemental distribution of the plate before and after the cleaning were examined with SEM and EDX, respectively [14]. A Hitachi SU3900 Large Chamber Variable Pressure SEM combined with an Oxford ULTIM MAX 65 SDD X-ray analyzer was used. High resolution (up to 100 k X magnification) [15] FE-SEM imaging was performed using a Hitachi SU8230 Regulus Ultra High-Resolution Field Emission SEM. Selected areas on the daguerreotype were imaged using FESEM (image resolution of 0.6 nm at 15 kV acceleration or 0.8 nm at 1 kV acceleration).

2.5. XRF Imaging Using Synchrotron Radiation

XRF images of the plate were recorded at the microprobe station at CLS@APS at the ID beamline of sector 20 of the Advanced Photon Source at Argonne National Laboratory [16]. The ID line was equipped with a Si(111) double crystal monochromator and a KB mirror capable of focussing the X-ray beam down to 5 micrometres routinely. We used an excitation energy of 13 keV; this energy is just above the Hg L₃ (12,284 eV) and Au L₃ edge (11,919 eV), producing Hg L $\alpha_{1,2}$ (9989 eV and 9898 eV) and Au L $\alpha_{1,2}$ (9713 eV and 9628 eV) X-ray fluorescence lines, as well as other lines of interest, e.g., K α of first row transition elements [17]. The incident beam was tuned to a spot size of ~ 50 μ m to optimize the data acquisition efficiency. The experiment was conducted when APS was running in a top-up mode, 24 bunches with a total current of 100 mA. This mode, together with the incident focussed beam (I₀) being monitored with an ionization chamber, ensured the beam stability and proper normalization, which is essential as it normally takes several hours to scan the entire plate. In this run, the photon flux was approximately 10¹² photons per second over a spot size of ~50 μ m with a step size of 50 μ m. The illumination time was 50 ms per pixel, number of pixels of the map was 881 X 1061, and the total scan time was 13 h 24 min and 23 s. It should be noted that synchrotron XRF imaging has been widely used and the scope of its application can be found in a recent contribution [18].

The daguerreotype plate was mounted on a three-axis platform and the scanning was done by moving the plate across the beam pixel by pixel. The XRF image was obtained by setting the energy window of interest, e.g., Hg L α and Au L α , in the X-ray fluorescence spectra collected by a four-element Vortex-Me4 solid state detector (~250 eV energy resolution) and stored in a multichannel analyser (MCA). The experimental set-up is shown in Figure S2, and a snapshot of the MCA display is shown in Figure S3, where the fitting of the overlapping fluorescence X-rays with which we could obtain more accurate elemental distribution and better contrast were obtained.

3. Results

The optical images of the “Little Girl, Pretty Purse” daguerreotype before cleaning and after cleaning, as well as the XRF image from collecting Hg L α fluorescence X-rays, are shown in Figure 2. It is apparent from Figure 2 that the chemical and electrochemical cleaning methods are generally effective. We will inspect several selected areas and discuss the effects below.



Figure 2. (a) Optical image of the plate before cleaning, the oval marks are due to some preliminary cleaning test using similar solution cell prior to this experiment. (b) Optical image after a series of local cleaning attempts with chemical (two regions marked by three wells of the solution cell) and electrochemical methods using larger oval shape cells (see text). (c) XRF image obtained with Hg L_{α} fluorescence X-rays.

3.1. Chemical Cleaning

Let us examine the three different sites cleaned using the three-well cell assembly (small oval marks) on the left of Figure 2b, each with its own solution, namely: 3% sodium thiosulfate, 1% ammonium hydroxide, and 0.5% ammonium hydroxide. An ammonium hydroxide solution was chosen as it removes halides from the surface by forming soluble ammonia silver complexes, and sodium thiosulfate was historically used in the production of daguerreotypes to remove silver-halides from the material surface. As the haze on a daguerreotype surface is normally attributed to halide formation, sodium thiosulfate would also be a good chemical cleaning method in addition to ammonium hydroxide [2]. The results of the chemical cleaning are closely examined in Figure 3.

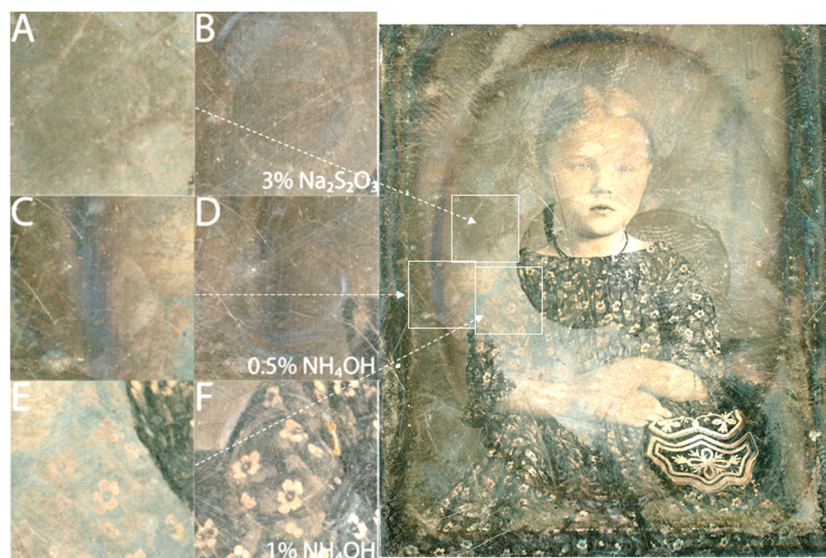


Figure 3. Optical images of the plate before (A,C,E) and after local cleaning (B,D,F) with solutions, as marked. The locations were situated on the optical image of the plate before cleaning.

From the left panel of Figure 3, we see that all cleaning solutions were successful in removing the foggy haze from the surface. The 3% $\text{Na}_2\text{S}_2\text{O}_3$ solution produced a noticeable reduction in surface clouding (Figure 3A,B). A similar increase in sample clarity was observed with the application of 0.5% NH_4OH (Figure 3C,D). The 1% NH_4OH (Figure 3F) uncovered the masked floral print with fine details and good contrast. EDX maps (Figure S4) revealed

the presence of Ag, Au, Hg, S, and Cl, as well as Hg-coated image particles that were slightly less than a micrometre. After cleaning, they remained intact, while the Cl and S signals were reduced.

3.2. Electrochemical Cleaning with Cathodic Method

A preliminary testing with silver-coated copper wires was performed to ensure that the applied potentials would not damage the daguerreotype. Although previous studies employed much higher potentials in their electrochemical cleaning procedures, our initial testing indicated that a potential of -0.9 V would be sufficient to cathodically clean the surface (the Wei method) [11] without causing any noticeable surface damage.

To test the effectiveness of the cathodic electrochemical cleaning methods, we used different electrolytes that were applied to selected sites, as illustrated in Figure 4, where the optical images before and after cleaning are shown. The Wei method involved the application of a constant negative potential (Figure 1) to the daguerreotype plate, therefore constantly reducing the surface. The electrolytes were selected such that they had a negligible chemical cleaning effect. Then, 0.01 M, 0.1 M KCl, and 0.01 M K_2SO_4 solutions were used. All of the electrochemically cleaned sites showed an optically improved image (Figure 4B,D,F, left panel). Most remarkably, the hands (Figure 4E,F, left panel) revealed greater details than before any cleaning attempts.

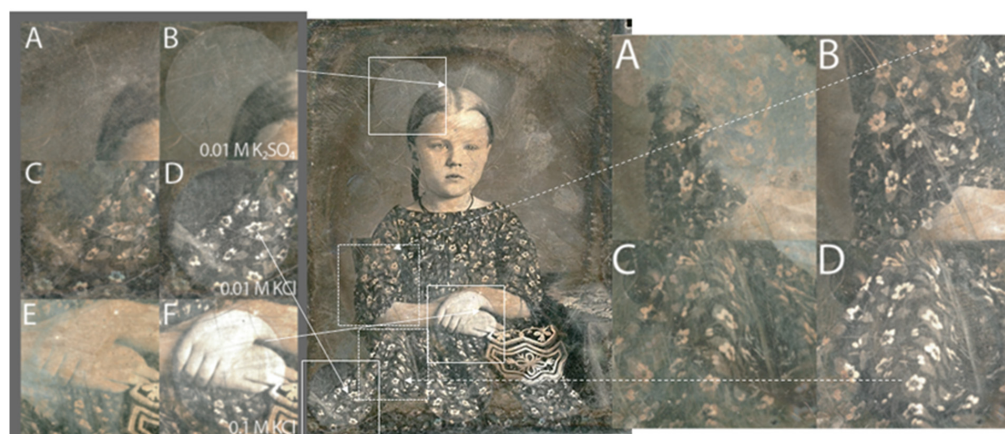


Figure 4. Left panel: Optical images (A,C,E) before and (B,D,F) after electrochemical cleaning using the Wei method with an electrolyte solution: B, 0.1 M KCl; D, 0.01 M KCl; and F, 0.01 M K_2SO_4 . Mid panel: Optical image after all of the cleaning processes. The regions of interest are marked with squares. Right panel: Optical images before (A,C) and after (B,D) electrochemical cleaning with 0.01 M KCl as the electrolyte. Image B, Barger method (-0.9 V to 0.9 V), and image D, Barger method (-1.2 V to 1.2 V).

It should be noted, however, that cleaning with a KCl solution (0.1 M), introduced Cl^- ions into the solution. This site showed a greater amount of residual white haze (formation of AgCl) following cleaning than the site using the lower concentration KCl solution (0.01 M, Figure 4D, left panel). This was the result of the common ion effect reducing the solubility of AgCl. An improved image is observed for Figure 4B, left panel, where 0.01 M K_2SO_4 solution was used. All three sites showed great improvement optically after only 90 s of cleaning. EDX maps were also obtained before and after cleaning, showing results like those obtained from the chemical cleaning experiment noted above.

3.3. Electrochemical Cleaning Using Chemical Cleaning Solutions

We have also explored the effect of using chemical cleaning solutions, such as NH_4OH and $Na_2S_2O_3$, as the electrolytes for the electrochemical cleaning procedures with both the Wei and Barger methods. In Figure 5, the optical images of the daguerreotype before and after the application of the combined electrochemical and chemical cleaning are

shown. The improvement of the overall image quality when cleaning was performed with a solution of 0.15% NH_4OH can clearly be seen. This procedure was applied with a 0.19% $\text{Na}_2\text{S}_2\text{O}_3$ solution with similar results. Figure 5B,D, right panel, correspond to the Barger method with an applied potential range of -0.9 V to 0.9 V , and -1.2 V to 1.2 V versus Ag/AgCl , respectively. Again, all of the images after cleaning showed more detail than before.



Figure 5. Left panel: Optical images (A,C) before and (B,D) after electrochemical cleaning using the Wei method with an electrolyte solution: B, 0.19 M $\text{Na}_2\text{S}_2\text{O}_3$; D, 0.15 M NH_4OH . Middle panel: Optical image after all of the cleaning processes. The regions of interest are marked with squares. Right panel: Optical images before (A,C) and after (B,D) electrochemical cleaning with 0.5 M NH_4OH . Image B, Barger method (-0.9 V to 0.9 V), and image D, Barger method (-1.2 V to 1.2 V).

For example, in Figure 5C, right panel, it is difficult to see what is present, but after cleaning it becomes apparent that there is a very intricate table cloth (Figure 5D, right), where many details within it are now evident. According to the EDX maps, both the Barger and Wei method can remove both the halides and sulfides present on the surface.

3.4. XRF Imaging

A closer look at Figure 2 shows the optical images before and after cleaning, as well as the Hg L_α image. It is apparent from Figure 2C that the XRF image has revealed a finely detailed portrait of the little girl and the pretty purse with a very clean background, as if all the tarnish were removed. The most noticeable difference is that, while the various cleaning methods applied to the plate show nonuniform cleaning in the optical image depending on the cleaning condition and the region of interest, removal of tarnish from the daguerreotype is complete in the XRF image, which reveals fine details everywhere across the portrait.

The XRF image can be fitted using the software package PyMCA [19,20], in which the X-ray fluorescence peaks are fitted and the area under the curve is the intensity contributing to the image. This procedure removes contributions from the overlapping peaks, such as Au L_α in the case of Hg L_α . An XRF image can also be obtained using Hg L_β , Au L_α , and Au L_β . The images from the Hg L PyMCA fit, and Hg L_β and Au L_α without fitting, are shown in Figure 6. It is interesting to note that the image is also finely revealed in the Hg L_β map and is noticeable in the Au map, albeit thinly veiled. The presence of a veiled Au image indicates that a gilding step using a gold chloride solution was applied after the image particles were formed and fixed when the plate was made, so that Au was found all over the plate, tracking how the gliding was done at the time. An image can still be observed from the Au fluorescence, suggesting that Au tracks the density and the distribution of the image particles, as well as the featureless region of the Ag plate.

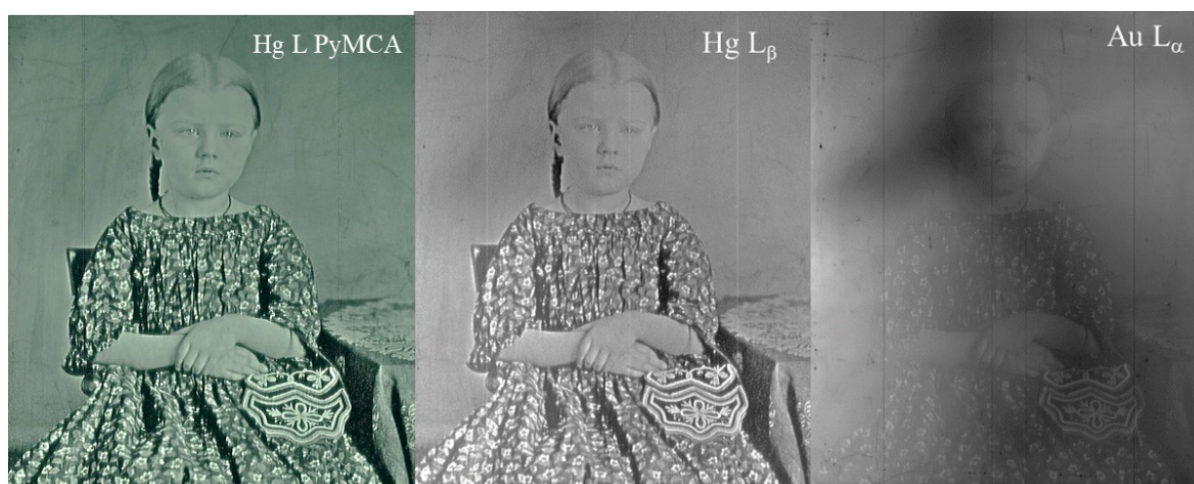


Figure 6. XRF image from left to right using the Hg L PyMCA fit, and Hg L $_{\beta}$ and Au L $_{\alpha}$ without fitting.

When comparing the Hg L $_{\alpha}$ image in Figure 2C with the Hg L PyMCA and L $_{\beta}$ images (Figure 6), it appears that while the L $_{\alpha}$ and L $_{\beta}$ images without fitting were of equally good quality, the PyMCA image showed a slightly better spatial resolution and contrast at closer scrutiny. This is because the Hg and Au L $_{\alpha}$ lines could not be completely resolved with the solid-state detector (SSD) without fitting. We also tracked the Cu K $_{\alpha}$ line, which did not show any image as the signal came from the Cu plate, and Cu was not involved in the formation of image particles. The Ag L emission was too weak at this excitation energy to be detected, and did not reveal any image either. It will be of interest to track Ag with tender X-ray excitation at just above the Ag L $_3$ edge (3351 eV) [3].

4. Conclusions

We conducted chemical and electrochemical cleaning procedures on various sites from a single, partially tarnished daguerreotype. We found that both methods of cleaning were effective at removing the tarnish and restoring the image. While all procedures seemed to improve the image by some degree, the tarnish was never removed uniformly or entirely. The chemical cleaning procedures were sufficient to remove the halides/white haze from the surface. Optical images taken after cleaning still appeared to have areas with a brown/orange tinge on the surface. Electrochemical cleaning was sufficient at removing the sulfides from the surface in addition to the halides, and did it faster. Both the Barger and the Wei electrocleaning methods improved the visual appearance of the image. Again, they did not always remove the orange/brown tarnish colour from the surface. As noted in the introduction, daguerreotypes can vary significantly depending on when they were made, the methods and equipment of the artist who made them, and the conditions under which they were stored. By performing these experiments on small regions of the same daguerreotype, we tried to obtain the most consistent possible initial conditions for comparison. The effectiveness of the treatment will depend entirely on the original integrity of the daguerreotype. They are not uniform. This work confirms previous observations that the only sure way to retrieve the complete contents of the daguerreotype is through synchrotron radiation X-ray fluorescence imaging. This technique will ensure that events of historical significance from a tarnished plate can be retrieved. With the XRF method, even if the daguerreotype is severely tarnished, provided there is still sufficient mercury on the image particles on the surface, the image in its entirety can still be reconstructed through digitizing the XRF images. The cleaning methods have been shown to improve the image optically; nevertheless, this should be undertaken with caution. Once the Hg is gone, the image will be lost forever. To refine the daguerreotype cleaning methods even more, further research would need to be performed to determine the detailed chemical

composition of the substrate plate, the image particles, the tarnish, and its interplay with the environment, such as the daguerreotype housing and the protecting glass.

Supplementary Materials: The following are available online at <https://www.mdpi.com/article/10.3390/heritage4030089/s1>. Figure S1: Experimental setup for electrochemical cleaning and chemical cleaning. (a) Schematic for the three-electrode set up for electrocleaning. (b) Actual set up for electrocleaning; the area of interest is confined by the perimeter of the cell, which leaves an oval mark on the plate after cleaning. The working electrode (daguerreotype), counter electrode (Pt), and reference electrode (Ag/AgCl) are noted. (c) Setup for chemical cleaning with the three-well cell clamped down on the plate. This setup leaves behind three small oval marks on the plate. (see Figure 2, middle panel and text). Figure S2: Experimental arrangement for the XRF imaging. The focussed beam (yellow line from left to right) with a spot size of $30\ \mu\text{m} \times 20\ \mu\text{m}$ is stationary. The plate is mounted on a three-axis stage that moves the plate across the beam with submicrometre precision, pixel by pixel. The fluorescence X-rays are collected with a four element SSD (VotexME4). The data are stored in a multichannel analyzer (MCA). Desired energy windows are set to collect element-sensitive maps (see Figure S4). Figure S3: A snapshot of the MCA display during a scan (top); the abscissa is photon energy and the ordinate axis is intensity in a semi-log plot. The Hg L intensities fit using PyMCA are shown in the bottom panel (both L_{α} and L_{β} are used, black dotted curve). Figure S4: EDX maps of Ag, S, Au, Hg, and Cl, and the backscattered (BSE) SEM image (black and white) for the chemical cleaning solutions discussed in Figure 3A,B. A: before cleaning; B: after 3% Na_2SO_3 .

Author Contributions: Conceptualization, R.R.M., J.J.N., and T.-K.S.; methodology, A.S., F.F., J.J.N., Y.Z.F., and T.-K.S.; lab experiment and analysis, A.S. and F.F.; A.S. is an undergraduate student under the supervision of J.J.N., R.R.M., and T.-K.S.; synchrotron, XRF imaging experiment and analysis, Y.Z.F., S.M.H., and T.-K.S.; writing—original draft, T.-K.S.; writing—review and editing, all of the authors. All of the authors have read and agreed to the published version of the manuscript. All authors have read and agreed to the published version of the manuscript.

Funding: This research was supported by the Natural Science and Engineering Research Council of Canada (NSERC, RGPIN-2019-05926), the Canada Research Chair Program (CRC), the Canada Foundation for Innovation (CFI), and the University of Western Ontario (UWO). This research used resources of the Advanced Photon Source, an Office of Science User Facility operated for the U.S. Department of Energy (DOE) Office of Science by Argonne National Laboratory, and was supported by the U.S. DOE under contract no. DE-AC02-06CH11357.

Institutional Review Board Statement: Not applicable.

Informed Consent Statement: Not applicable.

Data Availability Statement: Data used in this work are available from the authors upon request.

Acknowledgments: CLS@APS where XRF imaging was conducted is an operation of the Canadian Light Source, which is supported by the Canada Foundation for Innovation (CFI), the Natural Sciences and Engineering Research Council (NSERC), the National Research Council (NRC), the Canadian Institutes of Health Research (CIHR), the Government of Saskatchewan, and the University of Saskatchewan.

Conflicts of Interest: The authors declare no conflict of interest.

References

1. Foster, I. The Daguerreotype. *PhotoLife* **2019**, *44*, 46.
2. Kozachuk, M.S. Synchrotron Radiation Analysis of Daguerreotypes: Surface Characterization, Electrocleaning, and Preservation. Ph.D. Thesis, The University of Western Ontario, London, ON, Canada, 2019.
3. Kozachuk, M.S.; Sham, T.K.; Martin, R.R.; Nelson, A.J.; Coulthard, I. Exploring tarnished daguerreotypes with synchrotron light: XRF and μ -XANES analysis. *Herit. Sci.* **2018**, *6*, 12. [CrossRef]
4. Kozachuk, M.S.; Aviles, M.O.; Martin, R.R.; Potts, B.; Sham, T.K.; Lagugne-Labarthe, F. Imaging the Surface of a Hand-Colored 19th Century Daguerreotype. *Appl. Spectrosc.* **2018**, *72*, 1215. [CrossRef] [PubMed]
5. Prieto, C.M. Protecting daguerreotypes: A New Structural Housing System (SHS). *J. Inst. Conserv.* **2017**, *40*, 226. [CrossRef]

6. Grieten, E.; Schalm, O.; Tack, P.; Bauters, S.; Storme, P.; Gauquelin, N.; Caen, J.; Patelli, A.; Vincze, L.; Schryvers, D. Reclaiming the image of daguerreotypes: Characterization of the corroded surface before and after atmospheric plasma treatment. *J. Cult. Herit.* **2017**, *28*, 56–64. [CrossRef]
7. Kozachuk, M.S.; Sham, T.K.; Martin, R.R.; Nelson, A.J.; Coulthard, I.; McElhone, J.P. Recovery of Degraded-Beyond Recognition 19th Century Daguerreotypes with Rapid High Dynamic Range Elemental X-ray Fluorescence Imaging of Mercury L Emission. *Sci. Rep.* **2018**, *8*, 1.
8. Fischer, A.; Eggert, G.; Dinnebier, R.; Runcevski, T. When Glass and Metal Corrode Together, V: Sodium Copper Formate. *Stud. Conserv.* **2018**, *63*, 342. [CrossRef]
9. Barger, M.S.; Barger, D.K.; White, W.B. Characterization of corrosion products on old protective glass, especially daguerreotype cover glasses. *J. Mater. Sci.* **1989**, *24*, 1343. [CrossRef]
10. Marquis, E.A.; Chen, Y.M.; Kohanek, J.; Dong, Y.; Centeno, S.A. Exposing the sub-surface of historical daguerreotypes and the effects of sulfur-induced corrosion. *Corros. Sci.* **2015**, *94*, 438. [CrossRef]
11. Wei, W.; Gerritsen, I.; Waldthausen, C. Re-Examining The (Electro-)Chemical Cleaning of Daguerreotypes: Microscopic Change Vs. Macroscopic Perception. *Top. Photogr. Preserv.* **2011**, *14*, 24.
12. Barger, M.S.; White, W.B. *The Daguerreotype: Nineteenth-Century Technology and Modern Science*; The Smithsonian Institution: Washington, DC, USA, 1991.
13. Polcari, D.; Dauphin-Ducharme, P.; Mauzeroll, J. Scanning Electrochemical Microscopy: A Comprehensive Review of Experimental Parameters from 1989 to 2015. *Chem. Rev.* **2016**, *116*, 22. [CrossRef]
14. SEM/EDX-Surface Science Western Website. Available online: <https://www.surface-science-western.com/analytical-services/scanning-electron-microscopy-coupled-with-energy-dispersive-x-ray-sem-edx-spectroscopy/> (accessed on 1 March 2020).
15. Field Emission Scanning Electron Microscopy (FESEM)-Photometrics, Inc. Available online: <https://photometrics.net/field-emission-scanning-electron-microscopy-feseem/> (accessed on 1 March 2020).
16. Heald, S.M.; Brewster, D.L.; Stern, E.A.; Kim, K.H.; Brown, F.C.; Jiang, D.T.; Crozier, E.D.; Gordon, R.A. XAFS and micro-XAFS at the PNC-CAT beamlines. *J. Synchrotron Radiat.* **1999**, *6*, 347. [CrossRef] [PubMed]
17. Thompson, A.C.; Attwood, D.; Gullikson, E.; Howells, M.; Kim, K.-J.; Kirz, J.; Kottricht, J.; Ingolf, L.; Liu, Y.; Pianetta, P.; et al. *X-ray Data Booklet (the Orange Book)*; Lawrence Berkeley National Laboratory, University of California: Berkeley, CA, USA, 2001.
18. Paterson, D.; Howard, D. Synchrotron Radiation in Art and Archaeology. *Synchrotron. Radiat. News* **2019**, *32*, 2. [CrossRef]
19. Adams, F.; Janssens, K.; Snigirev, A. Microscopic X-ray fluorescence analysis and related methods with laboratory and synchrotron radiation sources. *J. Anal. Atomic Spectrom.* **1998**, *13*, 319–331. [CrossRef]
20. Solé, V.A.; Papillon, E.; Cotte, M.; Walter, P.; Susini, J. A multiplatform code for the analysis of energy-dispersive X-ray fluorescence spectra. *Spectrochim. Acta Part B Atomic Spectrosc.* **2007**, *62*, 63–68. [CrossRef]

Article

Quantitative Assessment of Impact and Sensitivity of Imaging Spectroscopy for Monitoring of Ageing of Archival Documents

Roberto Padoan ^{1,*} , Marvin E. Klein ², Roger M. Groves ³ , Gerrit de Bruin ⁴, Ted A. G. Steemers ⁴ and Matija Strlič ^{5,6} 

¹ Artlab Australia, Department of the Premier and Cabinet—Government of South Australia, 70 Kintore Avenue, Adelaide, SA 5000, Australia

² DEMCON Advanced Mechatronics Enschede BV, Institutenweg 25, 7521 PH Enschede, The Netherlands; marvin.klein@demcon.com

³ Aerospace Non-Destructive Testing Laboratory, Faculty of Aerospace Engineering, Delft University of Technology, Kluyverweg 1, 2629 HS Delft, The Netherlands; r.m.groves@tudelft.nl

⁴ Nationaal Archief (National Archives of The Netherlands), Prins Willem Alexanderhof 20, 2595 BE The Hague, The Netherlands; gerrit.de.bruin@nationaalarchief.nl (G.d.B.); ted.steemers@nationaalarchief.nl (T.A.G.S.)

⁵ Institute for Sustainable Heritage, University College London, 14 Upper Woburn Place, London WC1H 0NN, UK; m.strlic@ucl.ac.uk

⁶ Heritage Science Lab Ljubljana, University of Ljubljana, Vecna Pot 113, 1000 Ljubljana, Slovenia

* Correspondence: roberto.padoan@hotmail.com

Abstract: Ageing of historical documents often results in changes in the optical properties of the constituent materials. Imaging spectroscopy (IS) can be a valuable tool for monitoring of such changes, if the method fulfils two important conditions. Firstly, compared to natural ageing, the accumulated light dose from repeated measurements of the monitored document must not induce any significant degradation. Secondly, the monitoring instrumentation and procedures should be sensitive enough to detect changes in the materials before they become visible. We present experimental methods to evaluate the suitability of IS instrumentation for monitoring purposes. In the first set of experiments, the impact of repeated monitoring measurements was determined using a set of Blue Wool Standard materials. In the second set of experiments, the capability of the instrument to detect spectral changes was tested using ISO standard materials and several documents representative of European archive collections. It is concluded that the tested hyperspectral instrument is suitable for monitoring of the colour change of documents during display. The described experimental approach can be recommended to test the suitability of other imaging spectroscopy instruments for monitoring applications.

Keywords: light damage; colour difference; ageing; monitoring; imaging spectroscopy; spectral imaging; exhibitions; preventive; quantitative; books; paper; conservation; exhibitions; archive; library

Citation: Padoan, R.; Klein, M.E.; Groves, R.M.; de Bruin, G.; Steemers, T.A.G.; Strlič, M. Quantitative Assessment of Impact and Sensitivity of Imaging Spectroscopy for Monitoring of Ageing of Archival Documents. *Heritage* **2021**, *4*, 105–124. <https://doi.org/10.3390/heritage4010006>

Received: 18 December 2020

Accepted: 7 January 2021

Published: 12 January 2021

Publisher's Note: MDPI stays neutral with regard to jurisdictional claims in published maps and institutional affiliations.



Copyright: © 2021 by the authors. Licensee MDPI, Basel, Switzerland. This article is an open access article distributed under the terms and conditions of the Creative Commons Attribution (CC BY) license (<https://creativecommons.org/licenses/by/4.0/>).

1. Introduction

Imaging spectroscopy (IS) is a well-established analytical method in heritage science [1,2]. Based on the literature review done in 2014 [3] and a more recent one in 2020, it was possible to identify a deficiency about standards and experimental studies for the quantification of the impact and monitoring sensitivity of IS on heritage materials. With the intent of partly filling this knowledge gap we have been using the “SEPIA” hyperspectral imager of the *Nationaal Archief* (National Archives of The Netherlands) as a case study instrument. The described method can be transferred to validating other IS instruments and applications.

Assessing the impact of the environment and potential changes on cultural heritage during exhibitions is part of the professional standards of conservators [4] and their code

of ethics [5]. The environmental parameters for long-term preservation of historical documents in storage are recommended to be 16 °C to 20 °C, 35 to 50% RH, and complete darkness [6–8]. When a historical document is not in storage but exhibited or otherwise exposed to light, it could undergo unwanted degradation. In conservation assessment, qualitative methods such as visual examination or photographic documentation are usually employed. More advanced and objective methods for monitoring changes are point-based measurements done with non-destructive methods such as single beam spectrometry or with micro-invasive chemical analysis by micro-sampling the monitored object. Both methods are effective in giving information about the analysed area, but they preclude the assessment of the overall condition of those artefacts that are very inhomogeneous. Moreover, the use of micro-invasive tests is in most of the cases not allowed and it cannot be repeated multiple times on the same spot. IS represents for this reason the most promising method for monitoring the optical properties of heritage materials in a non-invasive way and in the long term [9–11]. The spatial and spectral characteristics of IS instruments can in fact allow for the identification of entire areas on the monitored document where changes occur rather than single spots.

There is a clear distinction between using IS as an analytical tool and as a monitoring instrument. Monitoring involves technical challenges such as the alignment and comparison of images taken of the same area at different times, repositioning of the camera and illumination and choice of calibration standards. A project on the digitization of paintings using multispectral imaging at the National Gallery of London in 1988 was one of the first works in the field of heritage science that addressed these issues [12]. Following to that, the VASARI project was the first attempt to standardize monitoring of paintings [13,14]. This project was then followed by the MARC and the CRISATEL projects [15–17]. In book and paper conservation, only a few research projects have so far addressed the use of IS for monitoring purposes [18–24].

From a conservation point of view, ideally repeated measurements should not damage the monitored objects at all. It is of course essential that the monitored condition indicators are not changed more significantly by the monitoring instrument itself than by the exhibition conditions. The cumulative light dose depends on the measurement frequency, monitoring period (typically years), and the construction of the IS instrument itself. The IS instrument is deemed to be suitable for the intended monitoring applications, if any cumulative colour changes induced by the measurement itself remain well below the threshold of visual perception for even the most light-sensitive material. Note that different criteria and thresholds for the acceptable impact of the instrument may be chosen, depending on the range of materials, the measurement schedule, and the intended monitoring period.

Ideally, the IS instrument has to enable the detection of changes before such changes become visibly detectable so to prevent the occurrence of damages rather than documenting them. The repeatability of measurements, which determines the sensitivity limit for detecting changes in the object, depends on the construction of the instrument and the measurement method, spectral calibration, and methods and software algorithms applied to the comparison of measurements of the same object taken at different times.

2. Materials and Methods

In this case study, the “SEPIA” Hyperspectral Imager (Art Innovation BV, now DEMCON based in Enschede, The Netherlands) was used. The instrument features two identical wavelength-tunable light sources (70 spectral bands in the range 365 nm–1100 nm) and a monochrome CCD camera (4 megapixel) mounted at a 45°/0° geometry with respect to the surface of the recorded document. This is a fully enclosed system, meaning that no external light can enter the recording area. Figure 1 shows a schematic drawing of the setup and an image of the instrument installed at the Nationaal Archief.

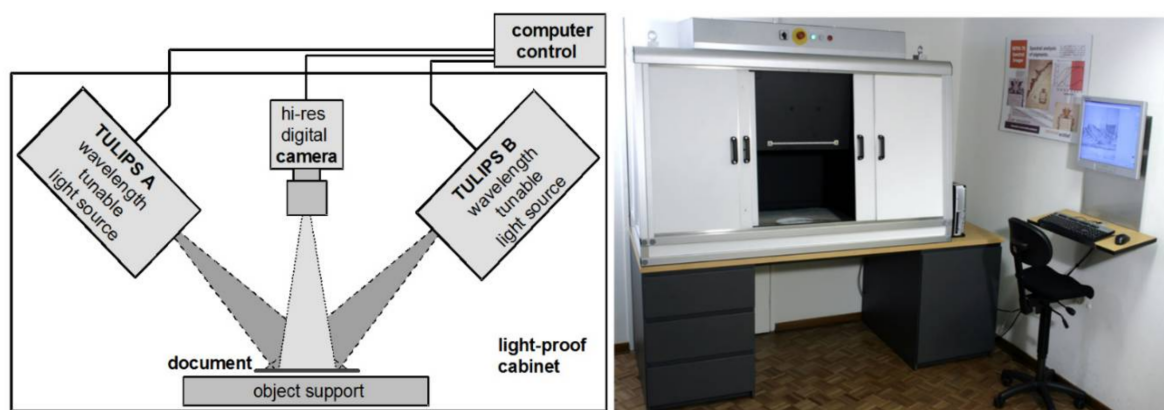


Figure 1. The case study Imaging spectroscopy (IS) instrument installed in the conservation laboratory of the Nationaal Archief [25].

During a measurement, the document is consecutively illuminated for pre-programmed exposure time periods by monochrome light from the light sources at each band. The instrument and the recording parameters are described in more detail in a previous publication [25].

For measuring the monitoring impact of repeated IS recordings, a set of Blue Wool Standard (BWS) acquired from Preservation Equipment Ltd. (based in Norfolk, UK) was used. BWS are dyed textile references with well-defined fading characteristics and they are available in a range of light-fastness grades [26].

These references are very well-known in the field of conservation as they are generally used to assess the impact of illumination during exhibitions in a qualitative way [27] or to calculate the cumulative light dose through calibration [28]. In this study, samples of grades 1 to 8 were mounted on a flat black-painted sample holder. To provide a reference, one half of the area of each sample was shielded with a paper board for most of the measurements, while the other half was exposed to the lights of the instrument at every IS measurement. The samples were exposed to 45 IS measurements, corresponding to a monitoring period of about 20 years. The monitoring period of 20 years was chosen as the best representation for the operational lifetime of such an instrument and because two recordings per year were considered for the exhibited documents at the Nationaal Archief as they follow a rotation schedule every six months. The effect of the IS measurements on the BWS samples was determined by repeated measurements of their reflectance spectra with a spectrophotometer (model Xrite i1pro-1) that provides reflectance values at every 10 nm over the spectral range of 380 to 730 nm, using a measurement spot diameter of 4.5 mm in a 45°/0° illumination/detection geometry. After calibration with the white standard provided with the device (calibration software “i1 Diagnostic v 4.0.0.127”), 10 different spots were measured on each BWS sample. The reproducibility of these spot measurements is shown in Figure 2, with the spectrum of BWS Grade 1 before any exposure to IS as an example. The average spectral reflectance values over the 10 spot measurements are connected by straight lines. The error bars around each average value indicate ± 1 standard deviation (SD) of the spectral reflectance values of the 10 individual measurements. For further analysis, the average spectra of the 10 spots were used.

To enable the assessment of the impact of IS, the reproducibility of the photospectrometer for measuring any spectral changes must be high enough so that the corresponding error on the measured colour change is below the visual detection threshold. This was verified by comparing any two photometer spectra (each averaged over 10 spots) that were measured on the same BWS reference area when it had been exposed to the same number of IS measurements. For each BWS sample, 51 unique pairs of such measurements are available. For each pair, the difference spectrum of the later minus the earlier one of both measurements and their colour difference ΔE_{2000} [29] were calculated. The visual thresh-

old was set at a value of $\Delta E_{2000} = 0.7$, which based on the work of Pretzel [30] corresponds to the 30% probability that a human observer is able to detect a colour difference.

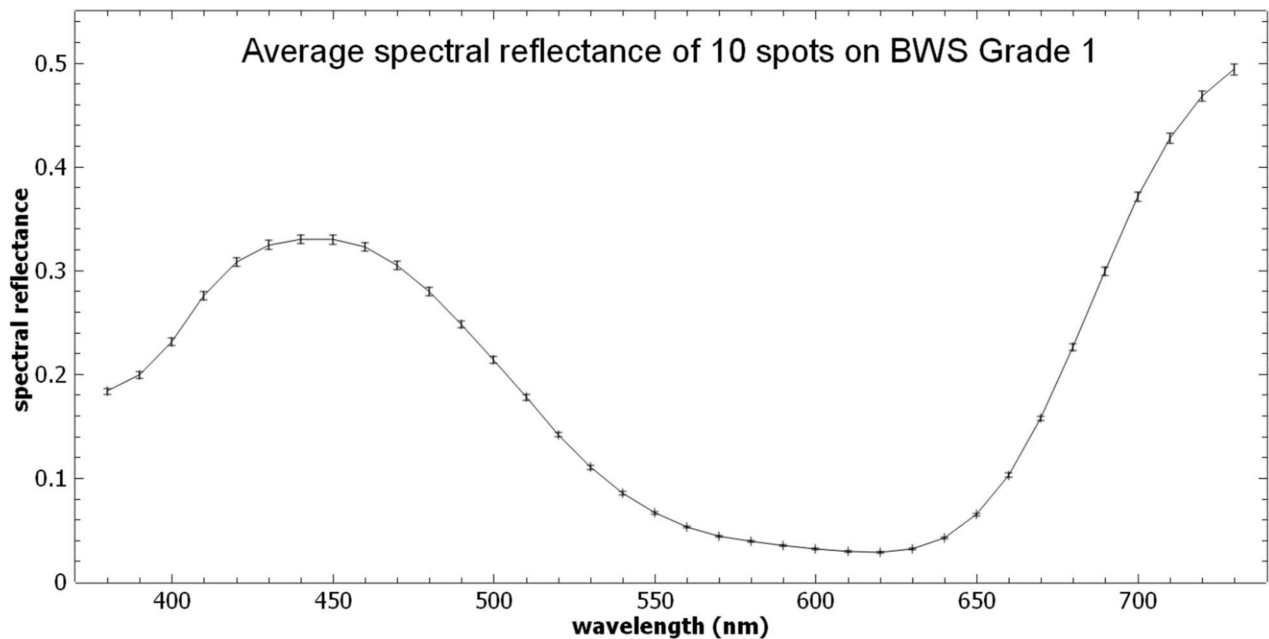


Figure 2. Spot measurement reproducibility of the Xrite spectrophotometer on the Blue Wool Standard (BWS) grade 1.

As seen in Figure 3, the mean value of the differences does not exceed the SD, and for most wavelengths it even remains considerably below the SD. This means that there is no significant bias (drift) of the photospectrometer measurements and no significant change of the spectra of the reference area in the course of the experiment. The SD of the photospectrometer measurements on the reference areas can therefore be used to estimate the measurement error: measured spectral changes on the exposed BWS areas can be assumed to be significant (i.e., real changes) if they exceed ± 2 SD.

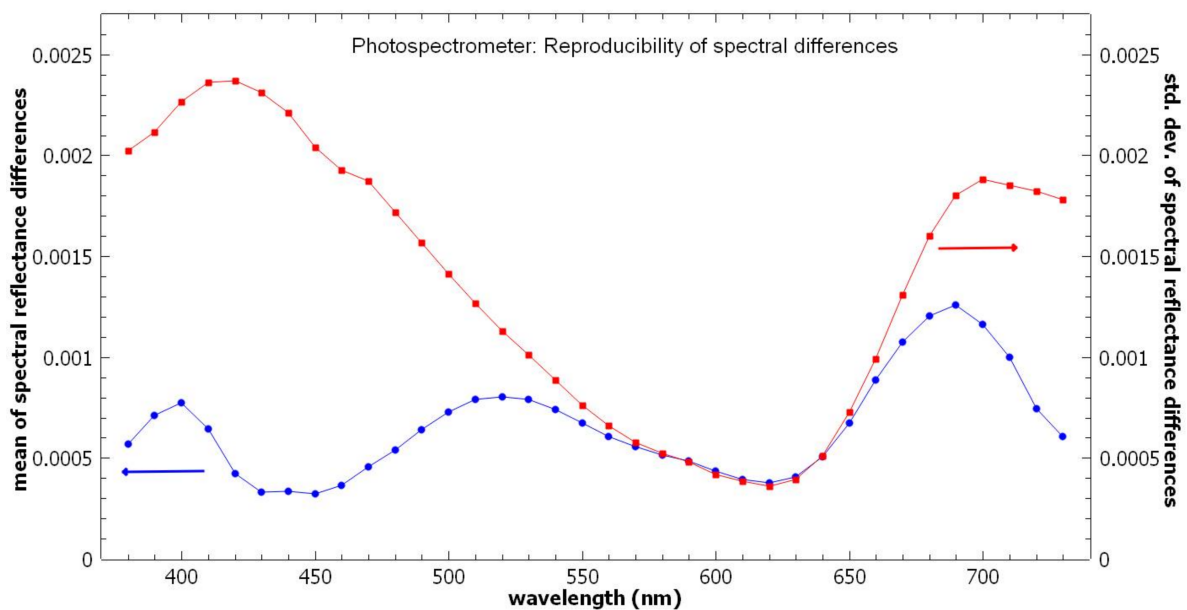


Figure 3. Average and standard deviation of the spectral difference curves based on 51 unique pairs of photospectrometer measurements of the BWS Grade 1 performed without an IS measurement cycle in between.

For each of the 51 pairs of reference area measurements, the colour difference (ΔE_{2000}) was calculated. The average colour difference is 0.14 (SD = 0.08), and for 95% (i.e., for 49 pairs) of the measured colour difference values were less than 0.27. The latter value can be used as a conservative estimate of the measurement error for the colour difference: if a colour difference measured on an exposed area exceeds this value, it very likely indicates a true colour change rather than a measurement error.

Spectrophotometer measurements themselves required irradiation of the BWS samples, and the overall results therefore represent an overestimation of both the measurement error and of the impact of long-term monitoring.

For testing the monitoring sensitivity, a second set of samples containing the BWS as well as common archival materials were exposed to photodegradation using a range of light doses. Table 1 reports the six test materials that were selected.

Table 1. Specifications of the materials used for the accelerated light-ageing tests.

Blue Wool Standard Grade 1	
Source	986–1000 Blue Scale Fading Cards (Preservation Equipment Ltd.)
Characteristics	<ul style="list-style-type: none"> • Light-sensitive: useful to study spectral changes caused by small light doses • Often used in conservation to monitor light quality during exhibitions: it is a valid reference for conservators • ISO standard BS EN ISO 105-B08
Blue Wool Standard Grade 2	
Source	986–1000 Blue Scale Fading Cards (Preservation Equipment Ltd.)
Characteristics	<ul style="list-style-type: none"> • Same as above, only half as sensitive to exposure to light
Iron-gall Ink on Paper	
Source	Discarded original blotting paper found in the Nationaal Archief.
Characteristics	<ul style="list-style-type: none"> • Used to absorb the ink from documents during their redaction. • Dated to 1798 based on a date absorbed on it from unknown document • Uniform ink stain sufficiently large to produce samples of high homogeneity • The most common ink in European historical archives • Well-known for its chemical instability [31]
Lignin-containing Paper	
Source	SurveNIR reference material collection [32] code SUR916
Characteristics	<ul style="list-style-type: none"> • Dated to 1894 • 70% ground-wood, 30% bleached cellulose • pH 4.2 • Lignin content 153 mg/g • Rosin-sized • This paper type is expected to oxidize and rapidly change colour [33]
Contemporary Print Paper	
Source	Fastprint® A4, 80 g/m ²
Characteristics	<ul style="list-style-type: none"> • In use at Nationaal Archief as considered to be highly durable • Expected to be stable during light ageing, thus a good reference to compare other materials with higher sensitivity • ISO 14001
Rag Paper	
Source	Sample JP422, UCL Institute for Sustainable Heritage Reference Material Collection, source: Swedish National Archives
Characteristics	<ul style="list-style-type: none"> • Dated to early 19th century • Gelatine-sized • Rag paper is expected to be more chemically stable than lignin-containing paper [34], useful as a second historical paper sample in this study

The main light sources used in the exhibition *De Verdieping van Nederland* at the Nationaal Archief at the time of the experiments are quartz-tungsten halogen reflector lamps without infrared suppression, which are mounted on the room ceiling for spot illumination of the objects in their glass cases. The dedicated setup that was built for accelerated light ageing [33,34] was designed to approximate the light spectrum of the illumination of the objects in the exhibition. To achieve this, the same type of halogen reflector lamps were used and the light was transmitted through the top glass plate of an exhibition case. As opposed to the situation in the exhibition, a homogeneous distribution of the light intensity on the samples at the intended level was required. Therefore, the light transmitted through the glass was diffused by scattering it from white cardboard in two steps before it reached the sample areas. The homogeneity with each area was verified with a lux meter.

Figure 4 shows the spectral power distribution of the homogenized halogen light with which the samples were irradiated in this research.

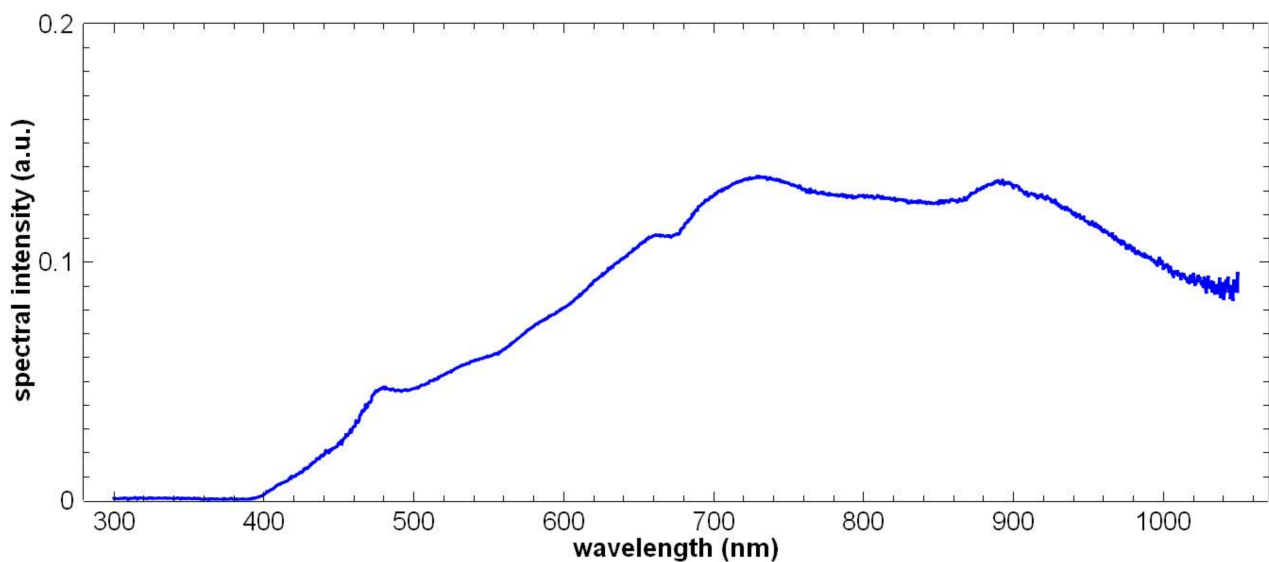


Figure 4. Spectral power distribution of the light sources used during accelerated light ageing.

The setup was used to induce accelerated light ageing at five intensity levels, by placing a set of samples at a suitable distance from the diffused light source. The light intensity to which each sample set was exposed was measured with a lux meter and monitored after each exposition time.

To prevent excessive heating of the samples, which could impact on their ageing behaviour in an uncontrolled way, forced air cooling was applied to the confined space of the sample chamber. The air temperature and relative humidity were monitored inside and just outside of the sample chamber. During the light ageing experiments the temperature ranged from 20 °C to 26 °C and the relative humidity from 35% to 62% RH.

The illumination in the *De Verdieping van Nederland* exhibition at the time of the experiments were 50 lux for 7 h/day over a period of three months.

The samples in this research were exposed to light doses ranging from ca. 1.5 to 500 klx·h, which corresponds to a range of 4–1400 days of exhibition at the above conditions. Table 2 reports the range of light doses obtained using different combinations of irradiation intensities and exposure times. In addition, 5 subsamples of each material underwent the same preparation but remained covered (i.e., 0 lx) during the accelerated light ageing process to serve as reference samples, having experienced only a small light dose during sample preparation.

Table 2. Light doses in klx·h achieved through different combinations of intensity and exposure times, as applied to each of the 6 tested materials. The values in parentheses indicate the number of exhibition days equivalent to the light doses.

Intensity	Exposure Times				
	5 h	10 h	30 h	60 h	100 h
0 lx	0	0	0	0	0
312.5 lx	1.6 (4 d)	3.1 (9 d)	9.4 (27 d)	18.8 (54 d)	31.3 (89 d)
625 lx	3.1 (9 d)	6.3 (18 d)	18.8 (54 d)	37.5 (107 d)	62.5 (179 d)
1250 lx	6.3 (18 d)	12.5 (36 d)	37.5 (107 d)	75.0 (214 d)	125.0 (357 d)
2500 lx	12.5 (36 d)	25.0 (71 d)	75.0 (214 d)	150.0 (429 d)	250.0 (714 d)
5000 lx	25.0 (71 d)	50.0 (143 d)	150.0 (429 d)	300.0 (857 d)	500.0 (1429 d)

Table 2 also indicates the number of days in the exhibition that would result in the same accumulative light dose. The row with 0 lx indicates the reference subsamples that remained covered during the accelerated aging.

The number of 6 materials and the number of light intensities were chosen to optimize the recording surface of the IS instrument. For each of the six materials, $5 \times 6 = 30$ subsamples were cut out, to be used in the experiments. The samples were arranged to fit into the field-of-view (FOV) of the tested IS instrument (120 mm \times 120 mm) in order to optimize the duration of measurements and improve the quality of the results.

Round samples (\varnothing 5 mm) were cut taking care they were taken from a homogeneous area of each test material. The pieces were mounted on five buffered RagMat Museum Board 4 ply Natural, without liquid adhesive but instead using Filmoplast[®] by Neschen that covered only small margins of the samples as shown in Figure 5a.

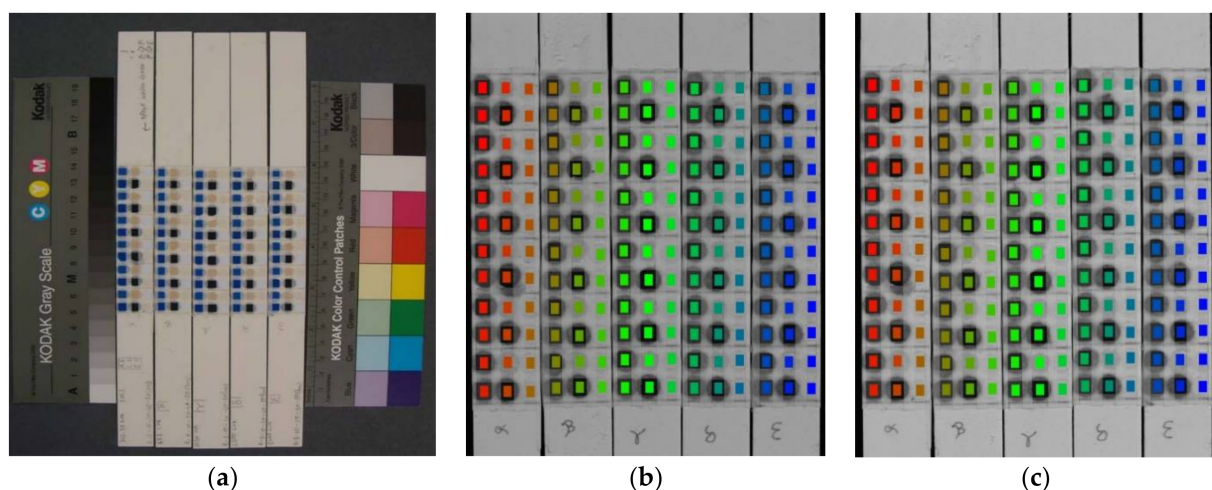


Figure 5. (a) The mounted samples used for the light ageing experiments. Rectangular regions-of-interest (ROI) defined on the IS datacube before (b) and after (c) the light ageing experiment. Each ROI is drawn in the same colour in the 680 nm spectral grayscale images in both recordings.

The resulting set of 180 sub-samples was measured with the IS instrument twice: before and after the accelerated light-ageing experiment. Each measurement results in a calibrated hyperspectral datacube (a stack of calibrated spectral images) that contains

a spectral reflectance curve for each image pixel. For each of the 180 material samples a region-of-interest (ROI) consisting of $38 \times 52 = 1976$ pixels was defined, which corresponds to an area = 2.3×3.2 mm. Any slight shift of the samples in the field-of-view of the instrument, visually detected in the second measurement with respect to the first measurement, was compensated by a corresponding shift of the ROI areas, see Figure 5b,c.

For each ROI, the mean spectral curve and the standard deviations (SD) over all 1976 pixels were calculated for both measurements. Figure 6 shows the mean spectral curves of one particular ROI for each test material before artificial ageing. The standard deviation reflects the combination of measurement noise of individual pixel values and the inhomogeneity of the material within the ROI area. Note that the peak in the curves of all samples at 380 nm is most likely caused by an imperfection of the corresponding spectral filter of the instrument, i.e., it is a measurement artefact rather than a reflectance characteristic of the samples.

For each sample, the difference spectrum was calculated by subtracting the corresponding ROI spectral curve before light ageing from the spectral curve of the same ROI after ageing. These difference spectra correspond to the spectral changes over the wavelength range of 365 to 1100 nm induced by ageing.

An estimate of the measurement error at each spectral band was obtained from the difference spectra as follows. For each spectral band, the mean value and standard deviation for all 30 difference values (5 reference subsamples of all 6 materials) were calculated. The mean value can be interpreted as a systematic error, whereas the standard deviation reflects a random contribution to the error. Measured difference values outside the range of the mean value ± 2 SD are considered to be statistically significant, i.e., the object has changed. However, since the wavelength-dependent measurement errors vary for the different materials, more conservative (i.e., larger) error limits can be derived by extending the ± 2 SD limits by the minimum and the maximum difference values for the particular material.

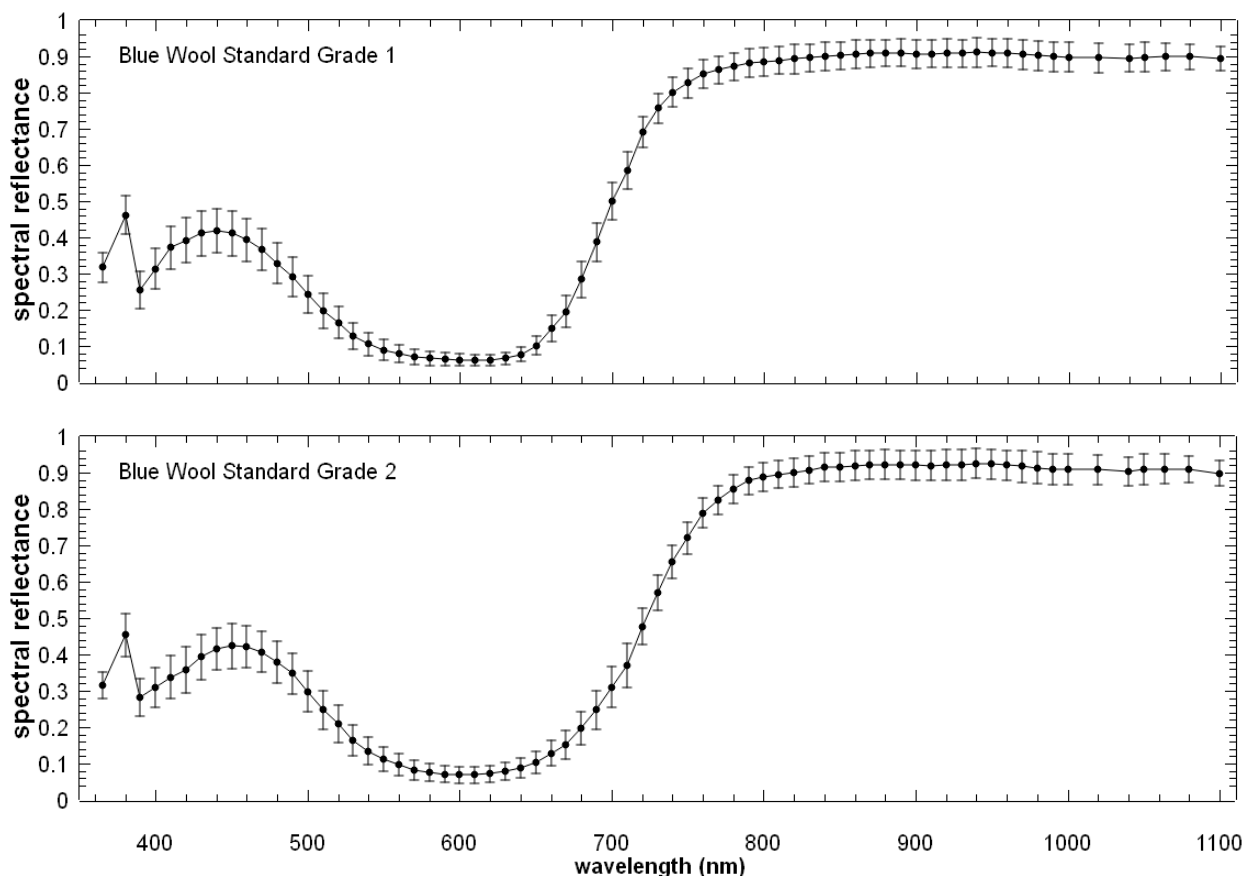


Figure 6. Cont.

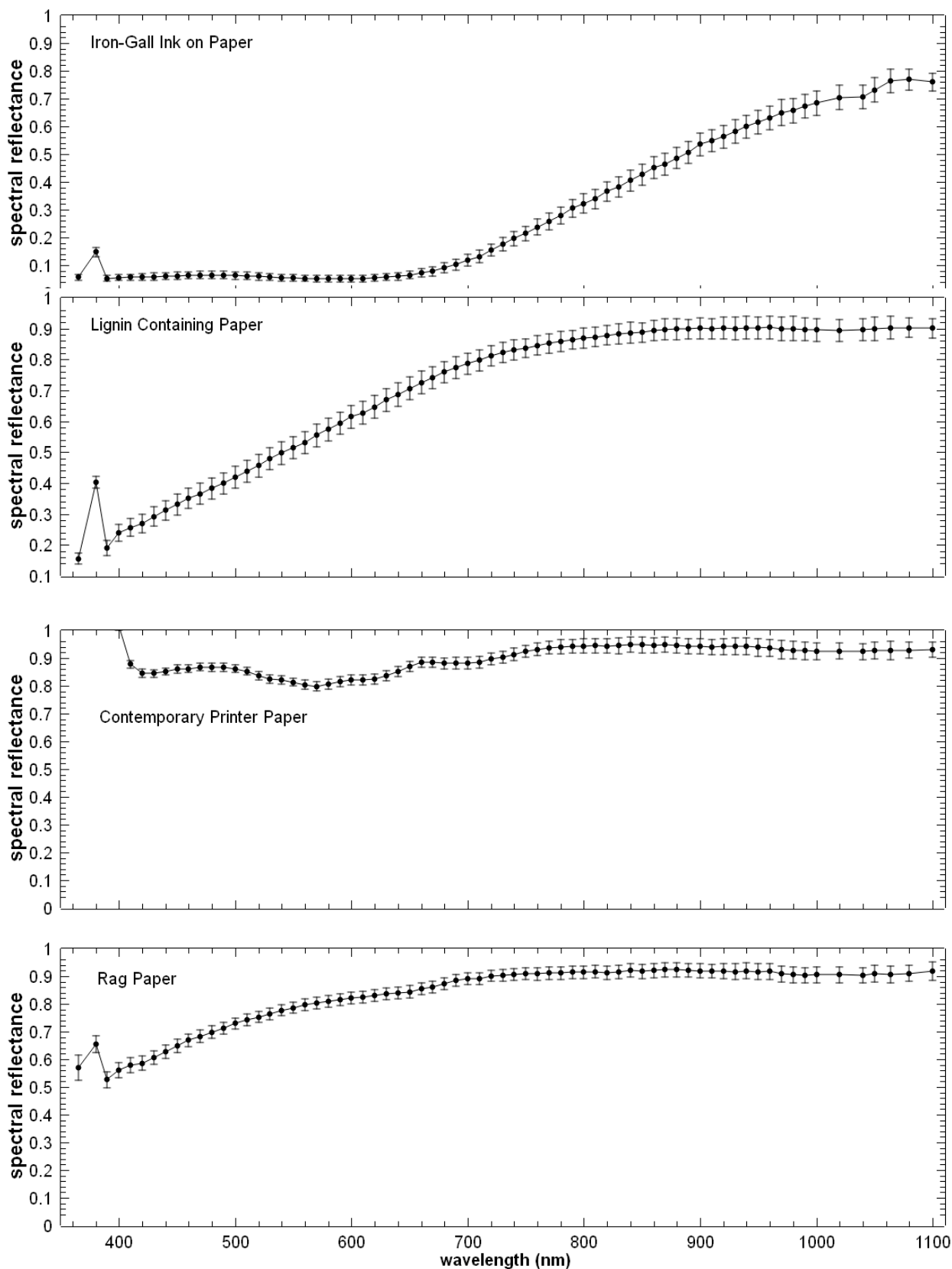


Figure 6. Mean reflectance spectra of the ROI of each of the 6 materials measured with the IS instrument before ageing (from top to bottom): Blue Wool Standard grade 1, Blue Wool Standard grade 2, iron = gall ink on paper, lignin-containing paper, contemporary printer paper, rag paper. The error bars indicate ± 1 SD at the corresponding wavelength.

When considering degradation of archival materials, an important criterion is whether such degradation can be detected visually (e.g., by comparison with colour charts). Therefore, in addition to the spectral differences at all wavelengths, the colour difference values ΔE_{2000} were calculated for samples before and after ageing. These results are reported in Table 3.

Table 3. Estimated errors for the calculated ΔE_{2000} colour difference values and standardized Euclidian vector distance values, Δ_{Euclid} , for the IS measurements of the aged test materials.

Material	$\varepsilon(\Delta E_{2000})$	$\varepsilon(\Delta_{Euclid})$
Blue Wool Standard Grade 1	0.19	0.00014
Blue Wool Standard Grade 2	0.36	0.00013
Iron-gall Ink on Paper	0.45	0.00015
Lignin Containing Paper	0.13	0.00012
Contemporary Printer Paper	0.15	0.00015
Rag Paper	0.21	0.00014

As an estimate for the measurement error $\varepsilon(\Delta E_{2000})$, for each material the maximum colour difference measured between the exposed and unexposed samples was used. It therefore takes into account the repeatability of the IS measurement itself, including any residual ROI positioning error and also any change in the reference samples not exposed to ageing. Any detected colour change $>\varepsilon(\Delta E_{2000})$ can thus be assumed to be a true change rather than measurement error. This means that $\varepsilon(\Delta E_{2000})$ defines the detection limit of the method, for the respective material. Note that for all materials, the measurement error $\varepsilon(\Delta E_{2000})$ is well below the threshold value of $\Delta E_{2000} = 0.7$, above which there is a 30% chance that a colour change is visually noticeable for a human observer.

The ΔE_{2000} value indicates whether a colour change induced by the ageing could be visibly detectable. Taking into account the particulars of human colour perception in combination with standardized illumination condition, reflectance changes in different wavelength regions are weighted differently and by definition, reflectance changes outside the visible range are not taken into account for colour measurements.

An alternative measure of spectral change that takes into account all wavelengths in the measured spectral range is the so-called standardized Euclidian distance Δ_{Euclid} . It is not based on (and limited by) human colour perception, and it uses all spectral values over the entire spectral range provided by the used instrument. The contribution from each wavelength to Δ_{Euclid} is weighted according to the estimated error. It is defined as:

$$\Delta_{Euclid} = \sqrt{\sum_i W_i \cdot (R_1(\lambda_i) - R_0(\lambda_i))^2} \quad (1)$$

where

$$W_i = \frac{\sigma^{-2}(\lambda_i)}{\sum_j \sigma^{-2}(\lambda_j)} \quad (2)$$

while the other symbols used are defined in Table 4. Note that all spectral measurements were carried out at the same spectral bands, which means that the sums in Equations (1) and (2) have the same number of terms for all samples. The standardized Euclidian distances are therefore comparable for all samples without the need to normalize for the number of spectral bands.

As an estimate for the measurement error $\varepsilon(\Delta_{Euclid})$ the maximum Δ_{Euclid} value determined for the 5 unexposed samples was used for each material reported in Table 1. Since the standardized Euclidian distance includes measurement data from additional spectral bands outside the visible range, there is the chance that allows the detection of changes of the monitored material before they can be detected by measurements in the visible range only.

Table 4. Symbols used in Equations (1) and (2).

Symbol	Description
Δ_{Euclid}	Standardized Euclidean distance of n-th spectrum from spectrum 0 recorded before any ageing
W_i	Weight factor at wavelength λ_i
$\sigma(\lambda_i)$ $\sigma(\lambda_j)$	Standard deviation over differences of reflectance values at wavelength λ_i or λ_j between measurements of the same sample, where the sample was not subjected to accelerated ageing
$R_0(\lambda_i)$	Spectral reflectance value at wavelength λ_i of a sample before ageing
$R_1(\lambda_i)$	Spectral reflectance value at wavelength λ_i of the same sample after ageing

3. Results

The eight different BWS samples were subjected to a number of IS measurements that correspond to 20 years of regular monitoring, in order to assess the impact. Before any IS measurements and after certain numbers of IS measurements, the samples were measured with the photospectrometer in order to quantify the impact of the multiple IS measurements on the materials with an independent instrument. Figure 7 shows for BWS1 the differences in the photospectrometer spectra recorded after different numbers of IS measurements with respect to the initial spectrum before any IS measurement. BWS grade 1 with the lowest light-fastness was chosen among the eight samples as it is deemed to be representative for the most light sensitive archival materials such as newspapers, photographs and watercolours. The grey and the red dashed curves indicate the estimated error of the photometer measurements with, respectively, $\pm 1\sigma(\lambda)$ and $\pm 2\sigma(\lambda)$ ranges around the mean of the spectral differences measured for the reference area where both measurements were exposed to the same number of IS measurement. After 16, 22, and 41 IS measurements, the differences in measured reflectance for the wavelength range of 530 to 650 nm are consistently outside the $\pm 2\sigma(\lambda)$ range. The photospectrometer is thus capable of detecting the corresponding small spectral differences in this wavelength range, which occur on the exposed area of the BWS1 sample after multiple IS measurements.

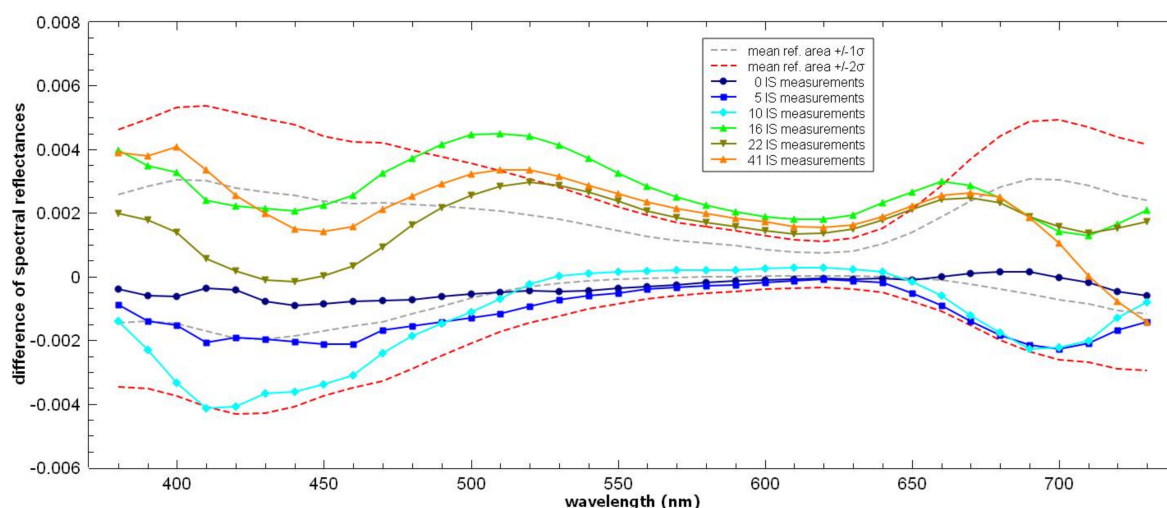


Figure 7. Changes of spectral reflectance values of BWS Grade 1 measured with the photospectrometer after increasing numbers of IS measurements as indicated. Additional dashed lines show the $\pm 1\sigma$ and $\pm 2\sigma$ intervals around the mean value from the unexposed reference areas at the corresponding wavelengths.

While comparing measurements at individual wavelengths is useful, it is possible that small, correlated changes in the spectra give rise to statistically significant differences

before they can be detected at any of the individual measurements. In the present case the main question was whether any changes caused by repeated IS measurements could become visible to the human eye.

Figure 8 shows ΔE_{2000} for BWS Grade 1 as a function of the number of repeated IS instrument measurements. As described in the Materials and Methods section of this article, the $\Delta E_{2000} = 0.27$ is the estimated error of the spectrophotometer measurement and values higher than this indicate statistically significant colour changes. The limit value of $\Delta E_{2000} = 1$ is per definition considered to be the smallest colour difference a trained human observer can detect. The $\Delta E_{2000} = 0.7$ level has been shown to be the threshold value above which the statistically more than 30% of the human observers are able to detect a difference in colour. All the measured colour differences remain below this more stringent threshold value for the 41 repeated IS measurements.

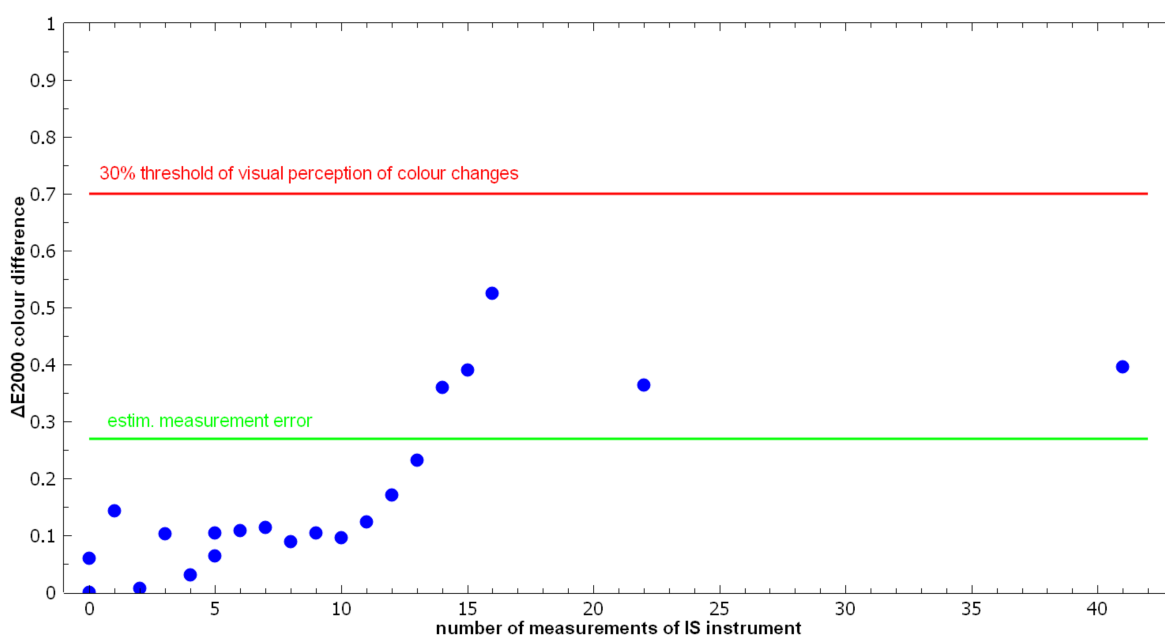


Figure 8. ΔE_{2000} of BWS Grade 1 as a function of the number of repeated IS instrument measurements. A value of 0.27 is the estimated measurement error of the spectrophotometer and 0.7 is the threshold value for visual perception of colour difference.

Results show that even very light-sensitive documents can be monitored with the SEPIA over periods of more than 20 years with the frequency of measurement of twice a year, before light exposure inherent to the measurement itself starts to effect any visible changes. These results are specific for the SEPIA device but other IS measurement systems could lead to similar results depending on their design. One of the key design features of the SEPIA instrument is that the wavelength selection for each spectral image is done inside the light sources. For each spectral image the measured object is irradiated only by the relatively low-intensity monochromatic light required to record this particular image. Other IS instrument concepts that rely on broadband illumination and sequential image recording with spectral filters at the camera expose the monitored objects to unnecessary high light doses and are therefore much less suitable for long-term monitoring. The camera lens and image sensor (CCD or CMOS) of the IS instrument has to be efficient in collecting the light reflected from the object, so that for a given light intensity the camera exposure time can be as short as possible. After the camera exposure has finished, the light source has to be switched off, so that the overall light dose received by the object during the entire measurement is minimized. At the time of the experiment, the Nationaal Archief was monitoring a range of circa 30 documents.

The Xrite spectrophotometer proved to be sensitive enough for control measurements as the colour changes induced in the most light-sensitive BWS became just measurable at the 15th repeated measurement, although still well below the visibility threshold. However, any further data analysis for the less light-sensitive BWS became obsolete with this, as even Grade 1 BWS was not affected significantly.

The second set of experiments addressed the sensitivity of IS measurements for detecting light-induced changes of six different materials. Figures 9 and 10 show the measured spectral changes for the six materials as induced by exposure to the maximum intensity of 5000 lux and a range of exposure periods. Please note the different y-axis scales in the diagrams of both figures. Figure 9 also includes the spectral changes at the minimum light intensity of 313 lux for BWS Grade 1. At the maximum light dose (i.e., at the maximum exposure time at the given intensity), and typically already at much lower light doses, all materials exhibit statistically significant spectral changes at several wavelengths.

For each material, the particular wavelength was determined where the maximum absolute spectral change was measured. The capability of the IS instrument to measure spectral differences in a given material can be expressed as the minimum light dose required to induce a spectral change that exceeds the measurement error at the material-specific wavelength with maximum change. The wavelengths and values of maximum change, the error limits at these wavelengths and the minimum detectable light doses of all materials are given in Table 5.

Table 5. For each material at the maximum light dose of 500 klx·h: wavelength of maximum spectral change (column 2); measured spectral change (column 3), corresponding error limit at this wavelength (column 4); light dose at the minimum detectable change (i.e., at the error limit, column 5); reference to the graph (column 6).

Material	Wave-Length (nm)	Spectral Change (%)	Error Limit (%)	Light Dose at min. Detectable Change (klx·h)	Corresponding Figure
Blue Wool Standard Grade 1	720	−11.5	−1.0	3.5	10
Blue Wool Standard Grade 2	740	−3.8	−0.5	30	10
Iron-gall Ink on Paper	820	−2.3	−0.2	65	11
Lignin-containing Paper	450	−2.6	0.3	60	11
Contemporary Printer Paper	390	−2.3	−0.7	70	11
Rag Paper	430	+2.6	+0.8	55	11

From the spectral reflectance curves measured with the IS instrument before and after accelerated ageing the function of induced colour change ΔE_{2000} vs. total light dose was calculated. Figure 11 shows the data for BWS Grade 1.

In line with the reciprocity principle [35], it would be expected that for a given light dose the same colour change is obtained regardless of the actual combination of light intensity and exposure duration. However, the data points corresponding to 5000 lx clearly show a slower increase than the rest. This could indicate deviation from reciprocity at high intensities, however, it might also reflect an uncertainty of the intensity levels in the light ageing setup. In any case, the dependence of colour change on light intensity is sufficiently low for the purpose of this experiment, i.e., to quantify the lowest light dose that induces colour change detectable by the IS instrument.

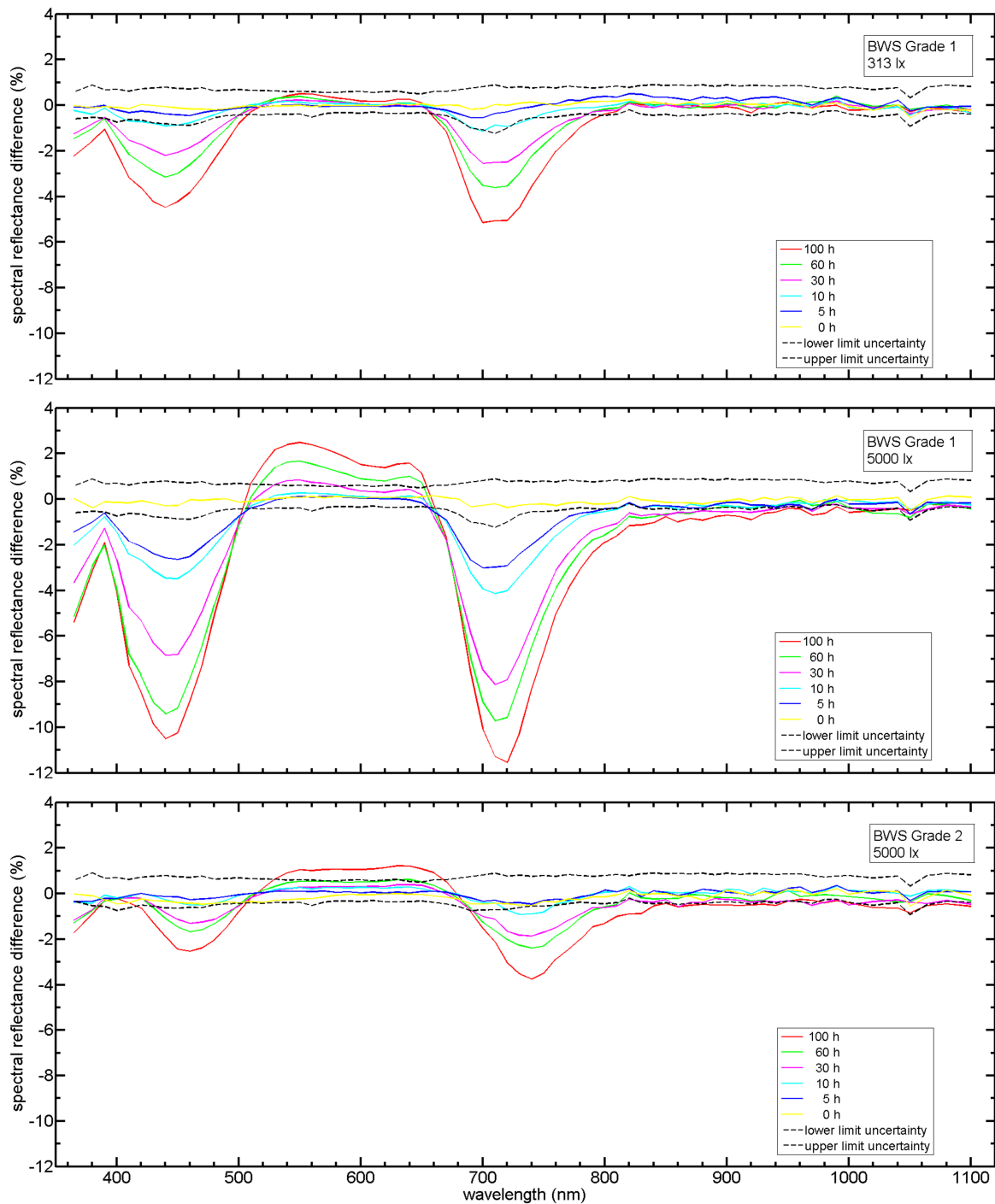


Figure 9. Differences in spectral reflectance values as a function of wavelength for BWS Grade 1 exposed to 313 lux and 5000 lux, and for BWS Grade 2 exposed to 5000 lux, for different durations as indicated. The dashed black curves indicate the upper and lower limits of the measurement uncertainty at each wavelength.

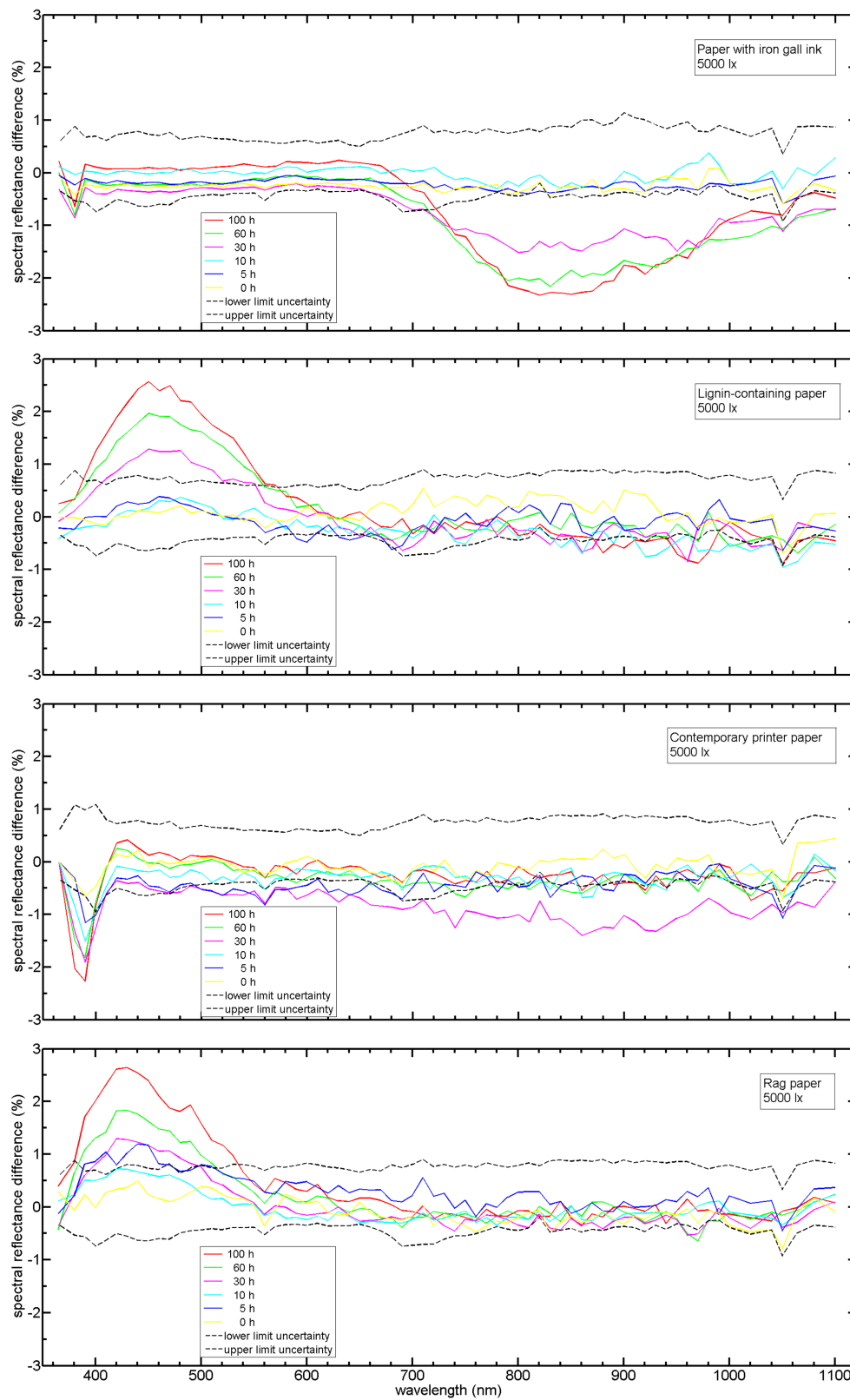


Figure 10. Differences in spectral reflectance values as a function of wavelength for four different materials (paper with iron gall ink, lignin-containing paper, contemporary printer paper, rag paper) exposed to 5000 lux for different durations as indicated. The dashed black curves indicate the upper and lower limit of the measurement uncertainty at each wavelength. For contemporary printer paper at wavelengths <400 nm, the curves are influenced by fluorescence. The changes induced by light ageing at these wavelengths can probably be attributed largely to break-down of these fluorescent components.

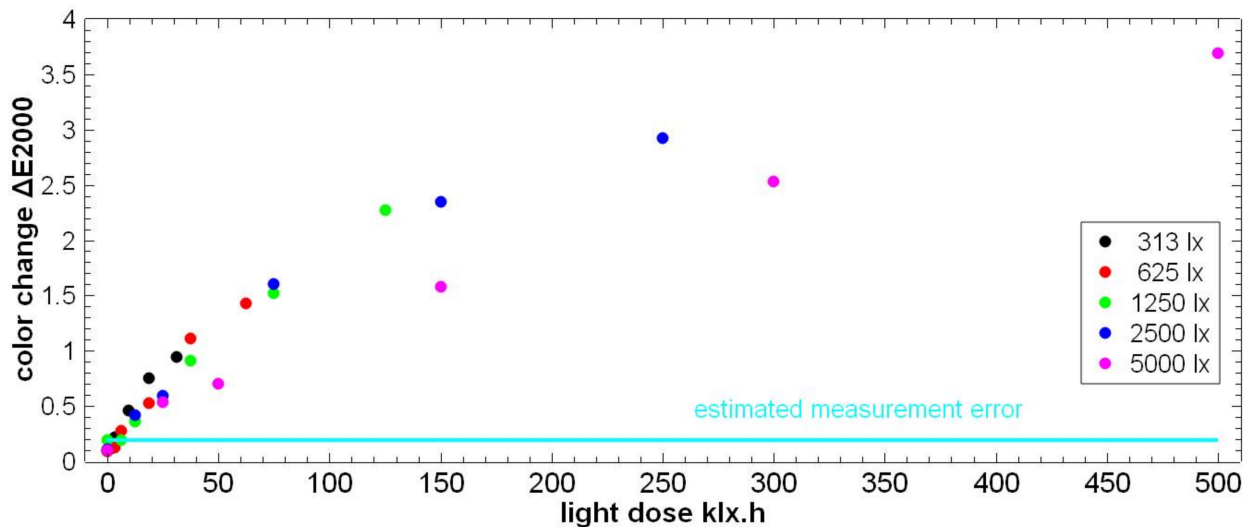


Figure 11. ΔE_{2000} as a function of light dose for BWS Grade 1, obtained at different combinations of light intensity and exposure duration during the light ageing experiment. The actual light intensities are as indicated. The maximum colour difference measured for unexposed samples is $\Delta E_{2000} = 0.19$, which is used to estimate the measurement error in Table 3.

For the BWS1 sample, the $\Delta E_{2000} = 0.7$ visibility threshold is obtained at light doses ~ 20 – 30 klx·h, corresponding to ~ 60 – 90 exhibition days at 50 lx, 7 h/day, from the halogen light sources as used in the exhibition *De Verdieping van Nederland*. Furthermore, the conservative estimation of $\Delta E_{2000} = 0.5$ as induced by IS measurements over 20 years can be estimated as equivalent to ~ 40 – 60 days of exhibition under the same conditions.

In addition to the ΔE_{2000} , the standardized Euclidian distance Δ_{Euclid} was calculated for the spectral reflectance curves measured after and before accelerated light ageing, as shown in Figure 12 for the BWS Grade 1.

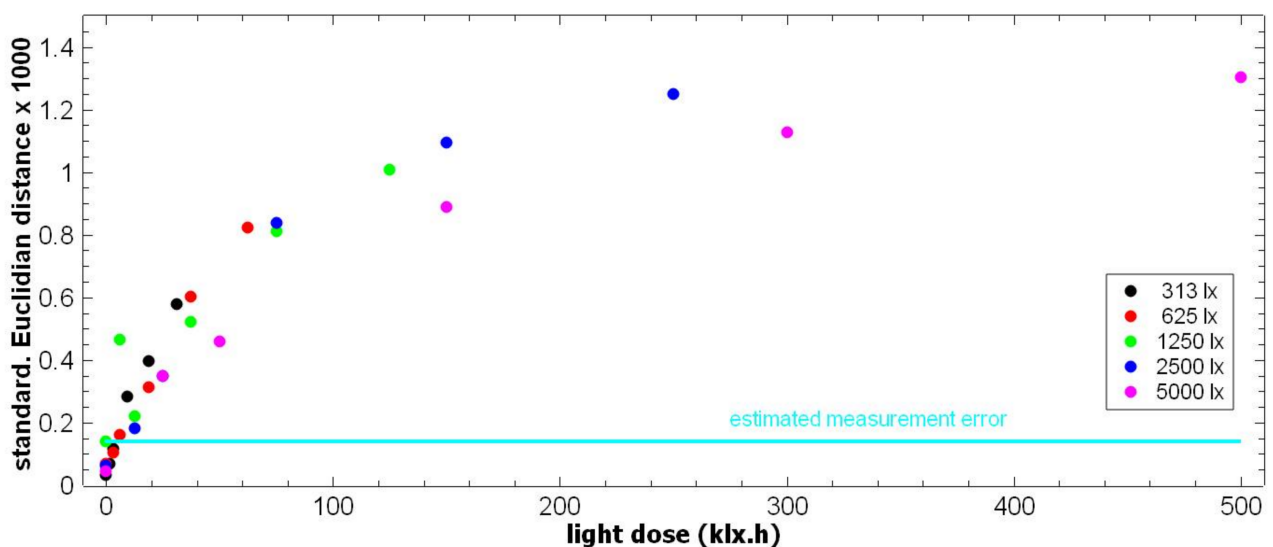


Figure 12. Standardized Euclidian distances, Δ_{Euclid} , for BWS Grade 1, as a function of light dose as obtained with different intensities, as indicated. The maximum distance measured for the unexposed samples is $\Delta_{\text{Euclid}} = 0.16 \times 10^{-3}$, which is used as an estimation of the measurement error in Table 3.

Tables 6 and 7 list ΔE_{2000} and Δ_{Euclid} , respectively, at the maximum light dose of 500 klx·h, for all the sample materials. As expected on the basis of Figures 9 and 10,

the biggest change is measured for BWS Grade 1 and the smallest change is measured for contemporary printer paper.

Based on the detection limits $\varepsilon(\Delta E2000)$ and $\varepsilon(\Delta_{Euclid})$ an estimate of the light dose required to induce the minimum detectable change was made for each material. The corresponding values are listed in the last column of Tables 6 and 7, respectively. The required light dose of 3.5 klx·h to achieve a detectable colour change in BWS Grade 1 samples corresponds to ~10 days of exhibition under the stated conditions.

Table 6. Colour change for each material at the maximum applied light dose of 500 klx·h, except in cases denoted with *, where the maximum was measured at the stated lower light dose. The light dose corresponding to the minimum detectable change is defined as the minimum light dose at which the measured colour change exceeds the measurement error $\varepsilon(\Delta E2000)$ as listed in Table 3. This minimum light dose is determined by linear interpolation of the measurement point just below and the point just above $\varepsilon(\Delta E2000)$.

Material	$\Delta E2000$ at 500 klx·h	$\varepsilon(\Delta E2000)$	Light Dose at $\varepsilon(\Delta E2000)$
Blue Wool Standard Grade 1	3.69	0.19	3.5 klx·h
Blue Wool Standard Grade 2	1.27	0.36	70 klx·h
Iron-gall Ink on Paper	0.40 (*150 klx·h) 0.61	0.45	≥ 500 klx·h
Lignin Containing Paper	1.2	0.13	20 klx·h
Contemporary Printer Paper	0.16 (*250 klx·h) 0.26	0.15	>500 klx·h
Rag Paper	0.96	0.21	22 klx·h

Table 7. Standardized Euclidian distance for each material at the maximum applied light dose of 500 klx·h, except in cases denoted with *, where the maximum was measured at the stated lower light dose. The light dose corresponding to the minimum detectable change is defined as the minimum light dose at which the measured spectral change exceeds the measurement error $\varepsilon(\Delta_{Euclid})$ as listed in Table 3. This minimum light dose is determined by linear interpolation of the measurement point just below and the point just above $\varepsilon(\Delta_{Euclid})$.

Material	Δ_{Euclid} at 500 klx·h	$\varepsilon(\Delta_{Euclid})$	Light Dose at $\varepsilon(\Delta_{Euclid})$ (klx·h)
Blue Wool Standard Grade 1	0.00130	0.00014	5
Blue Wool Standard Grade 2	0.00038	0.00013	60
Iron-gall Ink on Paper	0.00031	0.00015	135
Lignin Containing Paper	0.00026	0.00012	70
Contemporary Printer Paper	0.00013 (*150 klx·h) 0.00024	0.00015	>500
Rag Paper	0.00025	0.00014	70

For contemporary printer paper with its much higher light-fastness, the colour and the spectral changes at the maximum applied light dose of 500 klx·h is at the same level as the corresponding detection limits given by the estimated measurement errors. Note that the fact that the maximum colour and spectral difference were measured at lower light doses is also an effect of the measurement uncertainty. For the iron-gall ink on paper sample, the $\Delta E2000$ colour change measured at 500 klx·h is also just at the level of the measurement error so that this light dose can only be used as a lower limit. The Δ_{Euclid} value at 500 klx·h is about twice the estimated measurement error, allowing an estimate of 135 klx·h for the minimum detectable light dose.

Both ΔE_{2000} and Δ_{Euclid} are generic measures for spectral change. It can be expected that by using material-specific measures that give higher weights to those spectral regions where the strongest changes are induced, the sensitivity of the IS measurements for detecting light-induced changes can be further improved.

4. Discussion

This article describes a generally applicable approach to evaluation whether an imaging spectroscopic instrument is suitable as a tool for monitoring of archival documents. Depending on the object type to be investigated, instruments are typically selected based on their spectral range and resolution, their field-of-view and spatial resolution. However, in order to be useful for monitoring, an IS instrument has to fulfil two additional requirements:

1. Repeated measurements must not induce any significant additional spectral changes to the monitored object
2. Small spectral changes must be detectable before they become obvious visually.

We have shown that Requirement 1 can be tested by subjecting Blue Wool Standards to repeated measurements, corresponding to the intended duration of the monitoring schedule. The induced spectral change needs to be determined with an independent, sufficiently sensitive method, such as a spectrophotometer.

From a conservation point of view, the decision whether the predicted spectral changes induced by IS measurements themselves are acceptable or not must become part of the overall risk assessment of an institution's exhibition and monitoring schedule. A reasonable guideline would be that the spectral changes induced by measurements must be significantly less than those expected from exposure during exhibitions.

In the case study discussed here, the "SEPIA" hyperspectral imaging system was tested for an intended monitoring period of 20 years with an average of two measurements per year. The spectral changes induced by the tested IS instrument in Blue Wool Standard Grade 1 remained below the threshold for visually perceptible colour changes of $\Delta E_{2000} = 0.7$, which fulfils Requirement 1.

In order to test Requirement 2, sample materials representative of the monitored objects should be used in addition to standard reference materials. This is because the wavelength range and degree of spectral change depend on the material composition. Furthermore, the strength and spectral characteristics of light-induced change typically depend significantly on the irradiation spectrum. It is therefore advisable that the sample materials are exposed to accelerated degradation under conditions similar to those they are exposed to during exhibitions, in order to induce the same type of spectral change.

In our case study, four archival materials were subjected to accelerated ageing by 30 different combinations of light intensity and duration, corresponding to light doses of up to 500 klx·h. The deployed lamp type was the same as that used in the exhibition room *De Verdieping van Nederland* at the Nationaal Archief, to ensure that the same type of spectral change is induced as expected for exhibitions. The samples were irradiated with only moderate light intensities of up to 5000 lx and forced-air cooling was applied to minimize their temperature increase. The induced spectral changes should not be distorted significantly by any non-linearity of the material response with respect to the intensity (reciprocity-failure [36]) or by very high local sample temperature and low humidity. The spectral changes in the experiment are therefore expected to be comparable to those incurred by the materials over many years due to the normal exhibition schedule.

The changes were evaluated by calculating colour differences ΔE_{2000} and standardized Euclidian distances Δ_{Euclid} between the sample spectra measured before and after accelerated light ageing. The minimum light dose required to induce a detectable spectral change varied considerably from material to material. For the most light-sensitive Blue Wool Standard Grade 1, the detection limit for light-induced colour change corresponded to an exhibition period of ~10 days.

The instrument was thus shown to have an acceptably small impact on the materials, fulfilling Requirement 1, and acceptable high detection sensitivity for changes induced by exhibition lighting, i.e., also fulfilling Requirement 2.

5. Conclusions

In our research, the spectral change detection limit was determined on the basis of measurement repeatability over a time span of a few weeks. However, for long-term monitoring applications, long-term repeatability should be established. Future studies will have to look into practical calibration and validation procedures that are stable over long periods of time. In conclusion, imaging spectroscopic instruments can be valuable tools for monitoring the condition of archival documents and the present case study should be useful to establish the suitability of other instruments and similar case studies.

Author Contributions: Conceptualization, R.P.; methodology, R.P., M.E.K., M.S.; software, M.E.K.; formal analysis, R.P., M.E.K.; investigation, R.P.; resources, T.A.G.S. and G.d.B.; data curation, R.P. and M.E.K.; writing—original draft preparation, R.P.; writing—review and editing, M.S., M.E.K., R.M.G.; visualization, R.P., M.E.K.; supervision, M.S.; project administration, R.P.; funding acquisition, R.P., T.A.G.S., G.d.B. All authors have read and agreed to the published version of the manuscript.

Funding: This research received no external funding, but it was made possible thanks to the resources made available by the Nationaal Archief to Roberto Padoan for building the light-aging chamber and preparing and carrying out the measurements in 2014 during his work as books and paper conservator.

Conflicts of Interest: The authors declare no conflict of interest.

References

1. Fischer, C.; Kakoulli, I. Multispectral and Hyperspectral Imaging Technologies in Conservation: Current Research and Potential Applications. *Stud. Conserv.* **2006**, *51* (Suppl. 1), 3–16. [CrossRef]
2. Liang, H. Advances in Multispectral and Hyperspectral Imaging for Archaeology and Art Conservation. *Appl. Phys.* **2011**, *106*, 309–323. [CrossRef]
3. Padoan, R. Experimental Assessment of Impact and Monitoring Sensitivity of Imaging Spectroscopy on Historical Documents Used in Exhibitions. Master's Dissertation, Centre for Sustainable Heritage, University College London, London, UK, 2014.
4. ICON The Institute of Conservation. *The Institute of Conservation's Professional Standards*; ICON, The Institute of Conservation: London, UK, 2016; standard 1C.
5. ICOM International Council of Museums. *Code of Ethics for Museums*; ICOM International Council of Museums: Paris, France, 2018; article 4.1.
6. Balloffet, N.; Hille, J.; Reed, J.A. *Preservation and Conservation for Libraries and Archives*; American Library Association: Chicago, IL, USA, 2005; p. 2.
7. Millar, L.A. *Archives: Principles and Practices*; Facet Publishing: London, UK, 2017; p. 159.
8. British Standards BS 16893:2018 Conservation of Cultural Heritage, 2018. Available online: <https://shop.bsigroup.com/ProductDetail/?pid=00000000030324475> (accessed on 6 January 2021).
9. Valentini, G.; Comelli, D.; Toniolo, L.; Nevin, A. Advanced Imaging and Spectroscopy for the Conservation and Monitoring of Cultural Heritage. In *Renewable Energy and the Environment OSA Technical Digest (Online)*; Optical Society of America: Washington, DC, USA, 2013; paper EM4A.1. [CrossRef]
10. Picollo, M.; Cucci, C.; Casini, A.; Stefani, L. Hyper-Spectral Imaging Technique in the Cultural Heritage Field: New Possible Scenarios. *Sensors* **2020**, *20*, 2843. [CrossRef] [PubMed]
11. Hatzigiannakis, K.; Kristalia, M.; Philippidis, A.; Kokkinaki, O.; Kalokairinou, E.; Siozos, P.; Pouli, P.; Politaki, E.; Psaroudaki, A.; Dokoumetzidis, A.; et al. Monitoring and Mapping of Deterioration Products on Cultural Heritage Monuments Using Imaging and Laser Spectroscopy. In *International Conference on Transdisciplinary Multispectral Modeling and Cooperation for the Preservation of Cultural Heritage*; Communications in Computer and Information Science; Springer: Cham, Switzerland, 2019; Volume 962. [CrossRef]
12. Saunders, D. Colour Change Measurement by Digital Image Processing. *Natl. Gallery Bull.* **1988**, *12*, 66–77.
13. Saunders, D.; Cupitt, J. Image processing at the National Gallery: The VASARI Project. *Natl. Gallery Tech. Bull.* **1993**, *14*, 72–85.
14. Christian, L.; Georges, A.; Pascal, C.; Christofides, C.; De Christophe, D.; Ruven, P.; David, S.F.S. Crisatel: High definition spectral digital imaging of paintings with simulation of varnish removal. In *ICOM-CC: 13th Triennial Meeting, Rio de Janeiro 22–27 September 2002: Preprints*; James & James: London, UK, 2002; pp. 295–300.
15. European Commission. CORDIS Conservation Restoration Innovation Systems for Image Capture and Digital Archiving to Enhance Training, Education and Lifelong Learning. Available online: <https://cordis.europa.eu/project/id/IST-1999-20163> (accessed on 1 November 2020).

16. Liang, H.; Cupitt, S.; Cupitt, J. A New Multispectral Imaging System for Examining Paintings. *J. Imaging Sci. Technol.* **2005**, *49*, 551–562.
17. Ribes, A.; Brettel, H.; Schmitt, F.; Liang, H.; Cupitt, J.; Saunders, D. Calibration and Spectral Reconstruction for CRISATEL: An Art Painting Multispectral Acquisition System. *J. Imaging Sci. Technol.* **2005**, *49*, 563–573.
18. Havermans, J.; Aziz, H.A.; Scholten, H. Non Destructive Detection of Iron Gall Inks by Means of Multispectral Imaging Part 1: Development of the Detection System. *Restaurator* **2003**, *24*, 55–60. [CrossRef]
19. Havermans, J.; Aziz, H.A.; Scholten, H. Non Destructive Detection of Iron Gall Inks by Means of Multispectral Imaging Part 2: Application on original objects affected with Iron-Gall Ink Corrosion. *Restaurator* **2003**, *24*, 88–94. [CrossRef]
20. Fiorentin, P.; Pedrotti, E.; Scroccaro, A. A Multispectral Imaging Device for Monitoring of Colour in Art Works. In Proceedings of the IEEE Instrumentation and Measurement Technology Conference, Singapore, 5–7 May 2009; I2MTC. pp. 356–360.
21. Padoan, R.; Klein, M.E.; de Bruin, G.; Aalderink, B.J.; Steemers, T.A.G. Monitoring Ageing Processes of Archival Documents by Means of Quantitative Hyperspectral Imaging: A Part of the Hyperspectral Project at the Nationaal Archief (National Archives of the Netherlands). *Book Paper Group Annu. (AIC)* **2009**, *28*, 63–72.
22. France, F.G.; Christens-Barry, W.; Toth, M.B.; Toth, R.B.; Boydston, K. Advanced Image Analysis for the Preservation of Cultural Heritage. In *Computer Vision and Image Analysis of Art*; International Society for Optics and Photonics: Washington, DC, USA, 2010; pp. OE1–OE12.
23. Manfredi, M.; Zerbinati, O.; Robotti, E.; Mazzucco, E.; Gosetti, F.; Bearman, G.; France, F.; Shor, P. Technique Based on LED Multispectral Imaging and Multivariate Analysis for Monitoring the Conservation State of the Dead Sea Scrolls. *Anal. Chem.* **2011**, *83*, 6609–6618. [CrossRef]
24. Csefalvayova, L.; Strlic, M.; Karjalainen, H. Quantitative NIR Chemical Imaging in Heritage Science. *Anal. Chem.* **2011**, *83*, 5101–5106. [CrossRef] [PubMed]
25. Klein, M.E.; Aalderink, B.J.; Padoan, R.; De Bruin, G.; Steemers, T.A. Quantitative Hyperspectral Reflectance Imaging. *Sensors* **2008**, *8*, 5576–5618. [CrossRef] [PubMed]
26. British Standards. *Textiles Tests for Colour Fastness: Quality Control of Blue Wool Reference Materials 1 to 7*; BS EN ISO 105-B08:1999; British Standards: London, UK, 1999.
27. British Standards. *Conservation of Cultural Heritage: Guidelines and Procedures for Choosing Appropriate Lighting for Indoor Exhibitions*; PD CEN/TS 16163:2014; British Standards: London, UK, 2014.
28. Bacci, M.; Cucci, C.; Mencaglia, A.; Mignani, A.G.; Porcinai, S. Calibration and use of photosensitive materials for light monitoring in museums: Blue Wool Standard 1 as a case study. *Stud. Conserv.* **2004**, *49*, 85–98. [CrossRef]
29. CIE International Commission on Illumination. *Colorimetry—Part 6: CIEDE2000 Colour-Difference Formula*; ISO 11664-6:2014; CIE International Commission on Illumination: Vienna, Austria, 2014.
30. Pretzel, B. Now you see it, now you don't: Lighting decisions for the Ardabil carpet based on the probability of visual perception and rates of fading. In Proceedings of the 15th Triennial Conference on ICOM Committee for Conservation, New Delhi, India, 22–26 September 2008; Volume II.
31. Liu, Y.; Cigić, I.K.; Strlič, M. Kinetics of accelerated degradation of historic iron gall ink-containing paper. *Polym. Degrad. Stab.* **2017**, *142*, 255–262. [CrossRef]
32. Strlič, M.; Kolar, J.; Lichtblau, D.A. SurveNIR project: Non-destructive characterisation of historical paper. *Vic. Albert Mus. Conserv. J.* **2008**. Available online: <http://www.vam.ac.uk/content/journals/conservation-journal/issue-56/survenir-project-non-destructive-characterisation-of-historical-paper/> (accessed on 1 November 2020).
33. Rychlý, J.; Matisová-Rychlá, L.; Bukovský, V.; Pleteníková, M.; Vrška, M. The Progress of Ageing of Lignin-containing Paper Induced by Light and its Relation to Chemiluminescence—Temperature Runs. In *Macromolecular Symposia*; Special Issue: Polymers for Africa; WILEY-VCH Verlag: Weinheim, Germany, 2006; Volume 231.
34. TAPPI Technical Association of the Pulp & Paper Industry. Accelerated Light Aging of Printing and Writing Paper by Xenon-Arc Exposure Apparatus. TAPPI T 578, 2011. Available online: <https://imisrise.tappi.org/TAPPI/Products/01/T/0104T578.aspx> (accessed on 6 January 2021).
35. Feller, R.L. *Accelerated Aging Photochemical and Thermal Aspects*; The Getty Conservation Institute: Los Angeles, CA, USA, 1994; pp. 53–54. ISBN 0-89236-125-5.
36. Del Hoyo Meléndez, D.H.; Mecklenburg, M.F. An Investigation of the Reciprocity Principle of Light Exposures Using Microfading Spectrometry. *Spectrosc. Lett.* **2011**, *44*. [CrossRef]

Article

By the Hand of Angelos? Analytical Investigation of a Remarkable 15th Century Cretan Icon

Georgios P. Mastrotheodoros ^{1,2,*} , Marios Theodosis ³, Eleni Filippaki ² and Konstantinos G. Beltsios ⁴

¹ Conservation of Antiquities and Works of Art Department, West Attika University, Agiou Spyridonos, 12243 Aegaleo, Greece

² Institute of Nanoscience and Nanotechnology, NCSR ‘Demokritos’, Patr. Gregoriou E & 27 Neapoleos Str, 15341 Agia Paraskevi, Greece; e.filippaki@inn.demokritos.gr

³ Greek State Archives, D. Solomos Square, 29100 Zakynthos, Greece; mariostheodosis3@gmail.com

⁴ School of Chemical Engineering, National Technical University, Iroon Polytechniou 9, 15780 Zografou, Greece; kgbelt@mail.ntua.gr

* Correspondence: g.mastrotheodoros@inn.demokritos.gr

Received: 23 October 2020; Accepted: 13 November 2020; Published: 16 November 2020

Abstract: A 15th century St Theodoros icon of outstanding quality is on display at the Zakynthos Ecclesiastical Art Museum. On the basis of certain stylistic characteristics, this icon has been attributed to the legendary Cretan painter Angelos Akotantos. In order to explore the latter attribution, the icon was subjected to examination via multispectral imaging, while microsamples were investigated through an optical microscope (OM), a scanning electron microscope coupled with an energy dispersive analyzer (SEM-EDX), μ -Raman and X-ray diffraction (XRD). The data were evaluated in the light of the findings of recent analytical studies conducted on several genuine Angelos icons. Identified materials include gypsum, gold leaf, bole, natural ultramarine, lead white, charcoal, green earth, red lake, minium, cinnabar, and red and yellow ochres. The identified materials resemble those employed by Angelos, while the identification of ultramarine is of particular significance, as this extremely expensive and rather rare pigment was very often used by the particular painter. Moreover, multispectral imaging reveals notable painting technique similarities between the icon in consideration and known Angelos icons, while cross sections of corresponding samples exhibit almost identical structures. Overall, the present work considerably strengthens the suggestion that the St Theodoros icon in consideration was painted by Angelos and also widens our knowledge regarding the late Byzantine painting.

Keywords: pigment identification; preliminary drawing; gilding; Byzantine

1. Introduction

Religious panel paintings (“icons”) are an essential part of the Eastern Orthodox Christian Church ritual practices; hence, such artifacts have been continuously manufactured for more than 17 centuries [1]. In case of the artistry developed in the region of modern-day Greece, this long period is divided into three sub-periods, namely the Byzantine (330–1453), post-Byzantine (1453–1830) and modern periods (post-1830). The marking year 1453 corresponds to the capture of Constantinople (Byzantine Empire capital) by the Ottoman Turks, while 1830 corresponds to the declaration of the autonomy of the Greek state.

During the late 14th and early 15th centuries, icons of notably high quality were produced in the island of Crete (south Aegean Archipelago). As this artistic trend bears several idiomorphic characteristics, it has been designated as the “Cretan School of iconography”, and it is well known that

it considerably affected the development of the Orthodox religious painting throughout Greece and the Balkans [2]. Among the highlights of the Cretan painting stand several early 15th century icons of exquisite painting quality that bear the inscription “Χεῖρ Ἀγγέλου” ((by) “the hand of Angelos”). Interestingly, in the early 1960s M. Manoussakas spotted a Cretan painter’s will in the Venice State archives that is dated to the early 15th century (probably 1436) [3]; the testator was named Angelos Akotantos, and he made his will on the occasion of a trip to Constantinople. Soon after the Manoussakas publication, it was proven that the Angelos of the will was the painter of the aforementioned famous icons [4,5]. In order for the reader to get an idea of the importance of Angelos’ work, it is essential to note that the Cretan painting scholars acknowledge that he was indeed an outstanding painter of the 15th century and also that he “established and crystallized a large number of iconographic subjects in Cretan painting through his own work” [6]. Also, as for Angelos’ productivity, it is indicative to mention that more than 30 icons bearing his signature survive today, while some others are ascribed to him on the basis of pronouncedly idiomorphic stylistic characteristics [2,6].

The St Theodoros icon in consideration (Figure 1) dates from the second quarter of the 15th century (1425–1450) and has been recently ascribed—on the basis of stylistic criteria—to Angelos [7,8]. The icon originates from Crete and was once placed in the church of the Strofades monastery, from which it was later transferred to Zakynthos Island. It is worth noting that in 1953, the area of Zakynthos was struck by a series of strong earthquakes that destroyed many dwellings and infrastructures, including churches and monasteries. Unfortunately, during this event many of the Zakynthos icons were either destroyed by the fire that followed the earthquakes or “disappeared”; however, several hundred icons were rescued as a result of the tireless efforts of M. Chatzidakis and his co-workers [9]. St Theodoros icon survived this terrific disaster and is currently displayed at the Zakynthos Ecclesiastical Art Museum.



Figure 1. St Theodoros icon, Zakynthos Ecclesiastical Art Museum; the sampling spots are marked on the figure. Note that the painting has been transferred onto a new wooden panel.

The present work demonstrates how the analytical investigation of this very icon strengthens its assignment to Angelos Akotantos using a combination of technical evidence reported herein with related findings of other workers who previously studied several genuine Angelos icons [10–15]. The materials employed in the St Theodoros icon were identified through the meticulous investigation of microsamples’

cross sections, while the assessment of various technical aspects (pigment mixing, preliminary drawing, etc.) was assisted by the complementary use of multispectral imaging. Thus, authors managed to considerably strengthen the hypothesis that the St Theodoros icon is a work of Angelos, and also to widen the understanding of important details of late- Byzantine painting.

2. Materials and Methods

The icon (dimensions: 148.2 × 58.7 cm) was initially pictured using a MuSIS-MS multispectral camera (FORTH-Photonics, Heraklion, Greece) in the 1000 nm and the false-color infrared (IRFC) modes. Micro-samples (~1 mm × 1 mm) were removed from damaged areas using surgical scalpels (Figure 1), and, after preliminary stereoscope investigation, they were embedded in polyester resin, cross-sectioned and subjected to grinding and polishing (Pedemin-2, DAP-7, Struers, Ballerup, Denmark). Cross-sections were examined under an optical microscope (OM, DMRXP, Leica Microsystems, Wetzlar, Germany) at magnifications up to 200×, and, upon carbon coating (for conductivity purposes, using a Balzers' CED030 carbon vaporizer, Leica Microsystems, Wetzlar, Germany), through a scanning electron microscope coupled with an energy dispersive analyzer (SEM-EDX, Quanta Inspect D 8334, FEI, Hillsboro, Oregon, USA). Elemental compositions were estimated by using the built-in 'Genesis-Spectrum' software (EDAX Company, Mahwah, NJ, USA), in a standard-less quantification method mode that incorporates ZAF matrix corrections [16], and in combination with high accelerating voltage (25 kV) and optimal spectra collection parameters (a high count rate, long collection times, adequate DT%, etc. leading to high elemental peak to background ratios). Through the analysis of multi-elemental standard targets, it was demonstrated that this approach results in quantitative analysis with errors of circa ±3% for high concentration elements, and ±20% for low concentration ones (<5%). For each distinct pigment/phase, at least three EDX analyses were undertaken, targeting on different grains/areas; results were automatically normalized to 100% and the mean values were calculated. Due to the presence of the conductive carbon layer, carbon was not quantitatively estimated in organic/lake-type pigments. Micro-morphological characteristics were recorded using the SEM's backscattered electron detector (BSE), which permits for the differentiation of the observed phases on the basis of their atomic number. Also, the size of the various pigment grains along with the thickness of the gold leaves and the pertinent adhesives were determined using a built-in image processing tool of the SEM device (Table 1. Samples cross-sections were further examined under a μ -Raman device (inVia, Renishaw, Wotton-under-Edge, UK) using a low power (~0.01–1 mW) 514 nm laser; spectra were collected through a 100× magnification lens with repeated acquisitions of varying durations, and recorded in frequencies of 100–1800 cm^{-1} . A minor ground/gesso sample (<1mg) was pulverized and analyzed by using X-ray diffraction (XRD, 'D500', SIEMENS, Munich, Germany, equipped with a Cu-K α anticathode, diffraction pattern recorded in the range of 2–90° (2 θ) with a step size of 0.04° and a scan speed of 2 s per step). Note that during older conservation interventions, the painting and ground layers of the icon were detached from their original wooden substrate and placed onto a new one [7]; therefore the present authors did not employ techniques that pertain to wooden panel identification (e.g., x-ray radiography).

Table 1. EDX elemental analysis results, wt%, normalized to 100%. Abbreviations: n.d.: not determined.

Phase/Pigment	EDX Analysis Results (Elements, wt%)											Grain Size (µm)
	Na	Mg	Al	Si	S	Cl	K	Ca	Fe	Pb	Other	
Gesso/ground	0.1	1.0	0.3	1.6	38.8		58.3					n.d.
Lazurite	13.5		21.9	39.0	14.8	2.0	0.8	8.1				4–22
Green earth		5.1	2.9	45.2		1.3	12.5	4.3	28.7			6–23
Red lake	1.6	1.4	44.1	6.8	10.5	9.2	4.0	15.9	2.4		P (4.1)	n.d.
Red iron ochre		2.1	9.1	16.5		6.1	1.0	15.7	45.9		P (3.6)	4–5
Cinnabar					14.7						Hg (85.3)	0.8–7.0
Orange iron ochre	0.5	1.3	17.9	34.5	2.5	1.1	2.4	8.7	29.5		P/Ti (1.4/0.2)	1–5
Lead white									100.0			0.4–8.0
Minium									100.0			2–9
Charcoal												~0.5–2.0
	Gold leaf adhesives											
	Na	Mg	Al	Si	S	Cl	K	Ca	Fe	Pb	Other	Layer thickness (µm)
Yellow bole (campus)	0.4	1.4	18.3	35.1	5.8	0.6	1.8	13.6	22.8		Ti (0.3)	3–8
Mordant (highlights)	0.7	1.0	2.4	4.1		3.9	1.3	13.0	4.0	65.8	P (3.8)	2.5–7.0
	Gold leaves											
	Spot		EDX (elements wt%)					Leaf Thickness (µm)				
			Ag	Cu	Au							
	Background/"campus"		0.1	0.3	99.6							~0.4–0.6
	Gilded highlights on vestments		0.0	0.3	99.7							~0.4–0.6

3. Results

First, we present the results of the multispectral imaging, and the data that pertain to materials identification follow. The latter are presented in terms of the stratigraphy of a typical icon [17]: first the data on the ground/preparatory layer are presented, then the pigment palette is disclosed through the paint layers analysis results, and finally the data that pertain to gilded decorations are discussed.

3.1. Multispectral Imaging

The potential of infrared radiation to penetrate through the upper layers of paintings has been exploited in order to reveal layers that are invisible to the naked eye (such as underdrawings) [18,19] as well as for pigments identification [20]. In case of the St Theodoros icon, the inspection at 1000 nm revealed a wealth of information pertaining to the painting technique. The preliminary drawing is of a notably confident character, created by employing two techniques, namely brushstrokes and extremely thin (<30 μm , see next) incisions (Figure 2a,b). It is worth noting that in the case of the Saint's face and curly hair (where accuracy in sketch is of utmost importance), the drawing was rendered through thin brushstrokes (no incisions), while only few minor sketch-corrections were spotted in the corresponding areas (Figure 2c,d, arrow B). The preparatory paint layers that followed drawing (base colors/underpaintings [17]) were freely applied onto the ground (Figure 2d, arrow A), while the subsequent lighter tones and highlights were rendered with extremely accurate/skillful and fine brushstrokes (Figure 2). On the other hand, IRFC photography gave some hints on the employed pigments. For instance, the red mantle is rendered in an intense yellow-orange false color, thus implying the presence of cinnabar, while the differences in the false color of the "greenish" armor parts and the underwear garment around the Saint's waist indicate employment of different pigments (Figure 2e,f) [21].

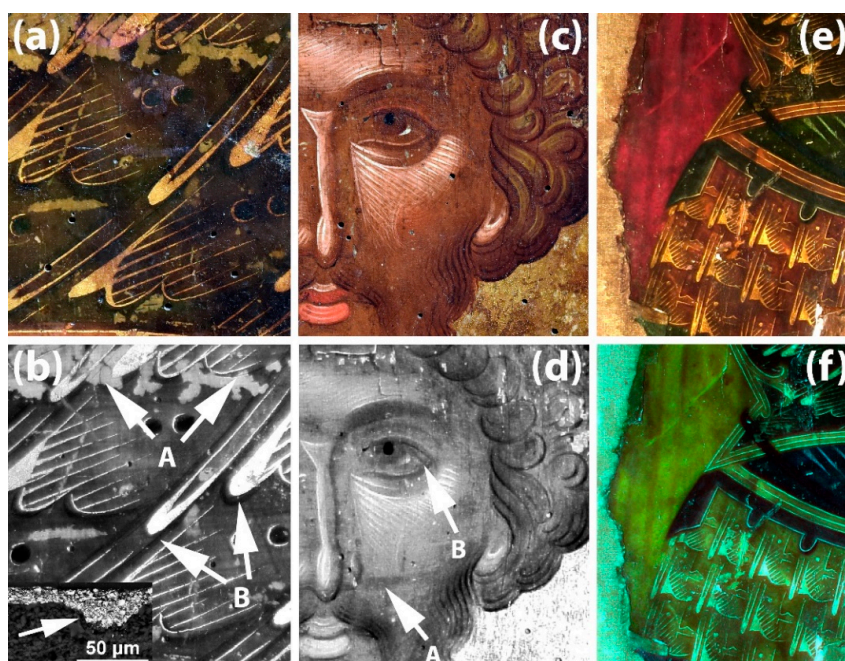


Figure 2. (a) Visible macro-detail of the armor. (b) Same area as in (a), pictured at 1000 nm. Preliminary drawing executed by incision (arrows "A") and brushstrokes ("B"); insert picture (lower left corner) shows an incision cross-section (scanning electron microscope (SEM), backscattered electron detector (BSE), 2000 \times). (c) St Theodore face, detail on visible light. (d) Same area as in (c), infrared (1000 nm). Arrow "A" points on preliminary paint layer brushstrokes, "B" on a minor sketch correction. (e) Detail, visible light. (f) The area figured in (d) as it was pictured in the false-color infrared (IRFC) mode.

3.2. Ground/Gesso

During the microscopic probing of the cross-sections, it was observed that the preparatory ground layer consists of up to eight distinct sub-layers of $\sim 50\text{--}150\ \mu\text{m}$ thickness, which correspond to the successive gesso coatings applied onto the wooden panel (Figure 3a). XRD and μ -Raman analyses revealed that the inorganic ground component is gypsum ($\text{CaSO}_4\cdot 2\text{H}_2\text{O}$), which was probably mixed with an organic gluing agent [17]. For instance, the relevant μ -Raman spectrum shows a characteristic shift at $\sim 1008\ \text{cm}^{-1}$ that corresponds to the ν_1 (SO_4) symmetric stretching mode of gypsum (Figure 4a) [22]. In addition, the ground layer contains minor admixtures of black, red and yellow pigments (see insert on Figure 3a).

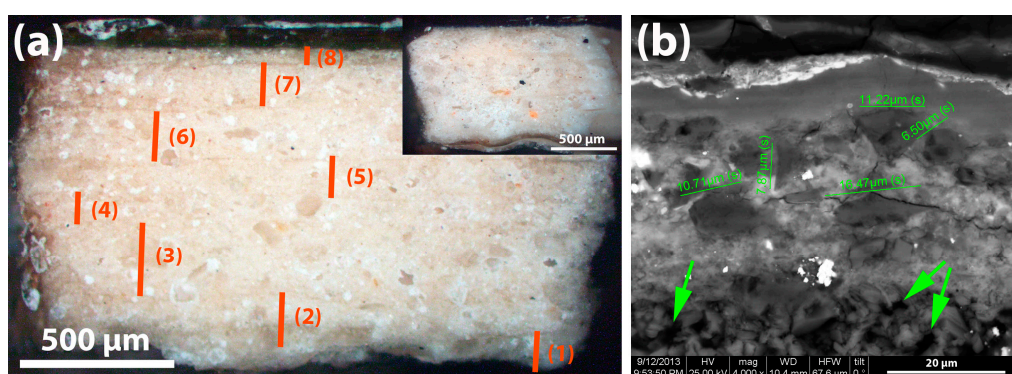


Figure 3. (a) Multiple ground layers, optical microscope (OM), 50 \times . The insert picture shows scattered grains of black and yellow pigments in the ground (OM, 50 \times). (b) Natural ultramarine grains and their maximum dimensions; arrows point on charcoal particles that lay into the lazurite substrate (SEM, BSE, 4000 \times).

3.3. Paint Layers

Pigments employed in the St Theodoros icon were identified through SEM-EDX and μ -Raman spectroscopy (Table 1 and Figure 4). Thus, a palette consisting of nine distinct pigments was revealed: natural ultramarine, green earth, two types of iron ochre, cinnabar, minium, red lake, charcoal and lead white (Table 1 and Figure 4). The extremely expensive and rather rare ultramarine pigment was identified through its characteristic Raman spectrum (ν_1 stretching vibration mode and ν_2 bending vibration mode of S_3^- , at $548\ \text{cm}^{-1}$ and $258\ \text{cm}^{-1}$, respectively [23]) and its elemental composition (Table 1), while the characteristic conchoidal fracture features of the relevant grains and the detection of minor calcite (natural impurity) verify the natural origin of the particular pigment (Figures 3b and 4b, Table 1) [23,24].

In the case of the green pigment, authors were unable to collect Raman spectra. However, the EDX analysis revealed that the pertinent grains are mainly composed of silicon, iron, potassium and magnesium, and this elemental composition evidently shows employment of green earth (Table 1) [28,29]. Similarly, the use of two iron ochre varieties was attested to through SEM-EDX analyses, as the deep-red and the yellowish ochre differ drastically in terms of elemental composition (especially as regards the content of iron, calcium, silicon and chlorine, see Table 1). In addition, the grains of these two pigments are of a notably small size ($0.5\text{--}5\ \mu\text{m}$), and this is so in the case of cinnabar and lead white as well ($0.5\text{--}8\ \mu\text{m}$, see Figure 5a). Note that a cinnabar Raman spectrum is displayed on Figure 4c; the characteristic shifts at 253 , 282 and $343\ \text{cm}^{-1}$ originate from a totally symmetric A_1 and degenerated E transverse modes (E_{TO}) respectively [30]. The employment of these thin-grained pigment fractions reflects intense grinding and suggests meticulous pigment preparation.

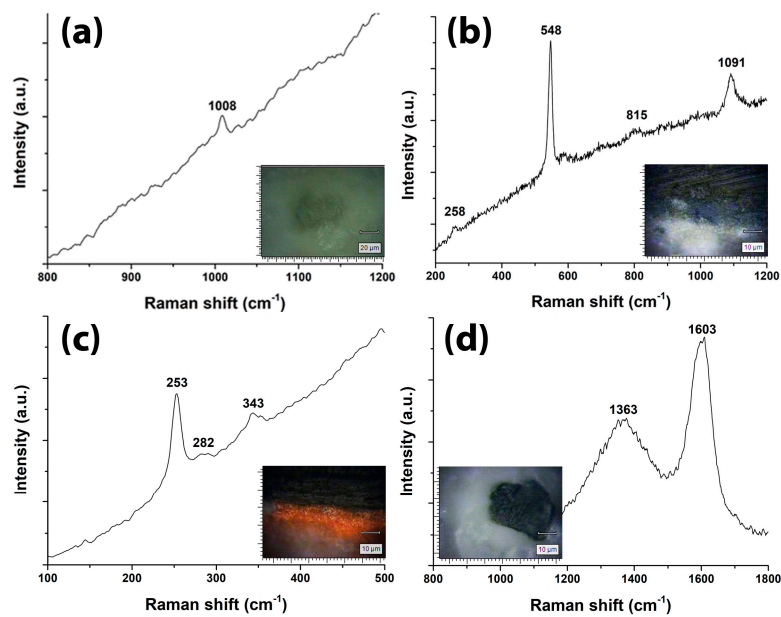


Figure 4. Characteristic μ -Raman spectra of St Theodoros icon ground and pigments. (a) Gypsum, characteristic peak at 1008 cm^{-1} . (b) Natural ultramarine, Raman shifts at 258 , 548 , 815 and 1091 cm^{-1} . (c) Cinnabar, shifts at 253 , 282 and 343 cm^{-1} . (d) Carbon black, characteristic shifts at 1363 and 1603 wavenumbers. Insert figures show indicative individual pigment grains that were analyzed. For libraries of pigment Raman spectra, the reader is directed to [25–27].

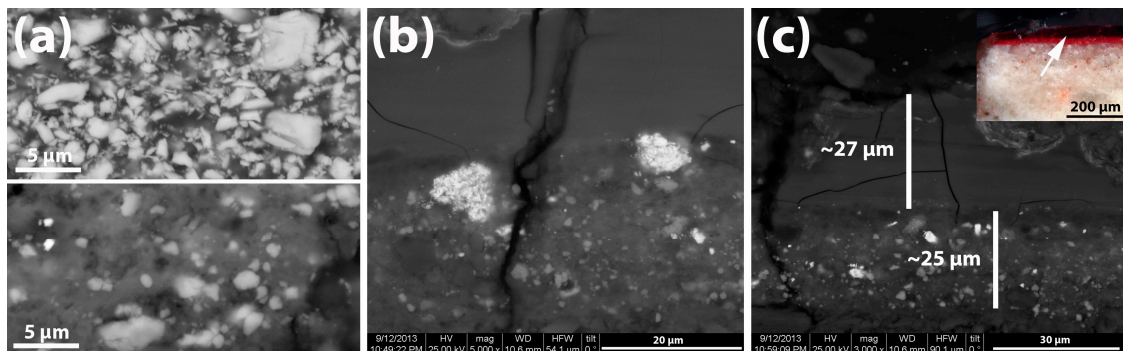


Figure 5. (a) Notably small grains of ochre (bottom) and cinnabar (up); SEM, BSE, $10,000\times$. (b) Minium grains (big bright particles) among ochre (gray particles); SEM, BSE, $5000\times$. (c) Lake glaze (upper layer, uniform) on top of an ochre and lead white substrate (bottom layer, spotted) (SEM, BSE, $3000\times$). Insert picture: the same sample under OM, the arrow points on the glaze ($100\times$).

On the other hand, a few minium grains were spotted among red ochre particles, therefore it seems probable that the minium was added in order to slightly adjust the hue of the ochre (Figure 5b). Of special interest is the case of the deep-red lake, which was used as a glaze (translucent paint layer) that covers an ochre plus lead white paint layer (Figure 5c), which is in fact a technique quite commonly applied in Cretan icons [31]. Here the lake organic coloring compound could not be identified, yet the elevated phosphorous ($4.1\text{ wt}\%$) is compatible with the employment of insect dye [32]. Finally, charcoal of plant origin was applied as a preliminary paint layer in the areas rendered in lazurite (Figure 3b) and as a minor addition in various paint layers. Charcoal was also used to render the preliminary drawing (Figure 6b), while a minute amount of the same pigment was included in the ground layer/gesso (Figure 3a). The corresponding Raman spectra show the typical G and D bands of carbon at $\sim 1600\text{ cm}^{-1}$ and $\sim 1360\text{ cm}^{-1}$, respectively [33].

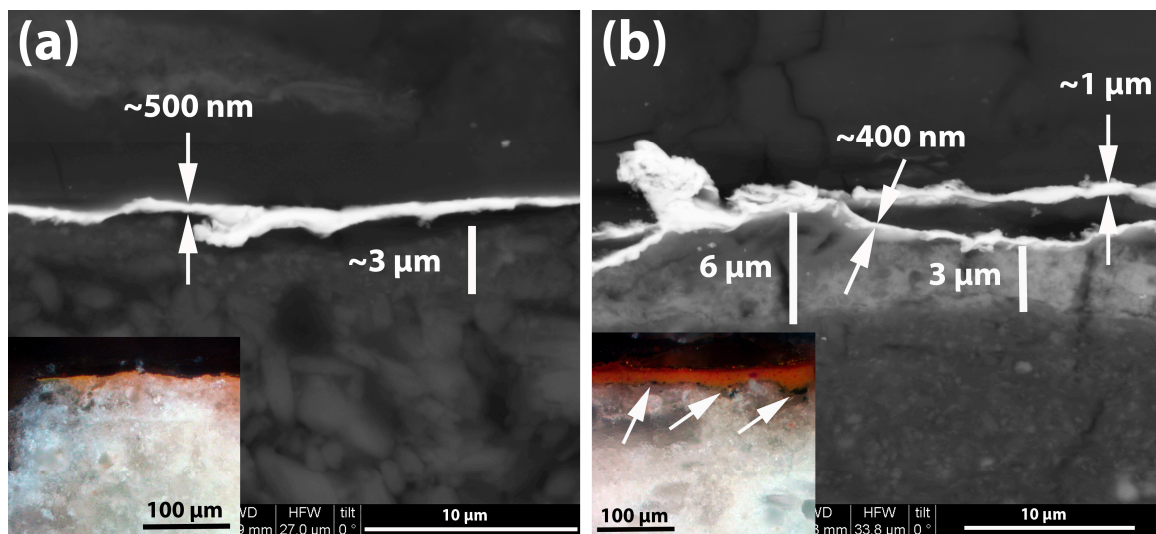


Figure 6. (a) Background image: thin gold leaf (bright layer) on a bole substrate (dark gray substrate, 3.12 μm marker); BSE, 10,000 \times . Insert picture: same sample, OM, 200 \times ; note the yellow bole layer. (b) Background image: Double gold leaf (uppermost bright layers) on a lead-mordant (bright substrate); BSE, 8000 \times . Insert picture: same sample under OM, arrow points on charcoal grains that lay on the white gesso and correspond to preliminary drawings (200 \times).

3.4. Gilded Pictorial Elements

The icon background (“campus”) along with the highlights of the armor and certain vestment details (e.g., bracelets) are rendered in gold tones. Micro-samples investigation revealed that these particular pictorial elements are in fact gilded with high purity ($\text{Au} > 99 \text{ wt } \%$) and extremely thin ($< 1 \text{ micron}$) gold leaves (Figure 6, Table 1). The latter have been applied by employing two distinct gluing agents, a yellow iron-rich clayey bole in case of the background and a lead-containing mordant in the highlights (Table 1). These adhesives pertain to the two most common—in the framework of painting—gilding techniques, namely water and mordant/oil gilding, respectively [34,35]. It shall be mentioned that the gold leaf thickness determination was achieved through inspection of high magnification SEM images, using a built-in image processing software (Figure 6) therefore some overestimation is possible [35,36].

4. Discussion

Through the analytical investigation of the St Theodoros icon, authors were able to identify the employed painting materials (except of the organics) and techniques, and now, a crucial question arises: how can these data contribute towards the assessment of painter’s identity? To this end, the analytical data were compared to the findings of previous studies of Angelos’ known (signed) works [10–12,14,15], and evaluated in the light of analytical investigations of other high-quality Cretan icons [31,37–39]. It is thus shown that the icon in consideration can indeed be assigned to Angelos.

According to the pertinent studies, Angelos’ works show a series of specific technical characteristics, that when seen as a whole constitute a rather idiomorphic painting manner. In detail, the gypsum grounds contain always a bit of charcoal and ochres [11,32] (probably added for the purpose of modifying the gesso color) and this is also the case for the St Theodoros icon (Figure 3a), though the incorporation of pigments in grounds is an uncommon practice for post-Byzantine painting [39,40]. As for the gilded backgrounds, Angelos always used a yellow bole substrate to apply the gold leaves on [10,11,15], and yellow is the bole of the St Theodoros icon as well (Figure 5a). Yet, it seems that the red-colored boles were extensively used during 15th century [38], and, hence, the employment of a yellow bole is a very important component of Angelos’ ‘fingerprint’.

Angelos' palette comprised of 11 pigments, including common ones such as charcoal, ochres and green earth, as well as some valuable and less frequently used ones, such as lazurite and azurite [10,11,13,15]. At first sight, it appears that there is no relevance between this palette and the idiomorphic character of Angelos' paintings. However, the use of natural ultramarine deserves special attention. It is well known that this very pigment was circulating in various grades, the best of which possessed an extremely high cost [24,41]. As is evident by the photomicrographs in Daniilia et al. [11], Angelos' paintings bear first-grade lazurite with grains that usually measure above 10 microns, and this is also the case for the St Theodoros lazurite (Figure 3b). On the other hand, previous analytical studies have shown that lazurite was rather rarely employed in icon painting [29,31] and this indeed adds much value to the identification of ultramarine in the St Theodoros icon.

On the other hand, Angelos' paintings show some idiomorphic technical characteristics that resulted in the typical extremely skillful manner detected by archaeologists. In detail, Angelos always rendered the preliminary drawing/sketch by combining thin brushstrokes and very shallow incisions [10,12]. Sometimes the incised drawing could be rather extensive [15]; however, the facial features and the details of flesh and hair parts were always rendered by thin and extremely skillful brushstrokes, they were never incised [10,12,15], and this is regarded a typical characteristic of Angelos' work [14]. Therefore, the fact that the same technique has been applied in the St Theodoros icon is regarded as a notable clue towards assigning the icon to Angelos (Figures 2 and 6b). For comparison purposes, we present an example of preliminary drawing on another high-quality Cretan icon. The artifact in consideration (which is of a slightly later date, i.e., the early 16th century) is the left wing of a Royal Doors pair depicting the Annunciation of Virgin Mary that is currently on display at the Byzantine Museum of Ioannina (BMI), Greece (Figure 7a). In this case, the preliminary drawing incisions are considerably deeper than those of St Theodoros icon (~90 μm /Figure 7b versus ~20 μm /Figure 2d, respectively), while the facial characteristics and hair details are pronouncedly incised (Figure 7c).

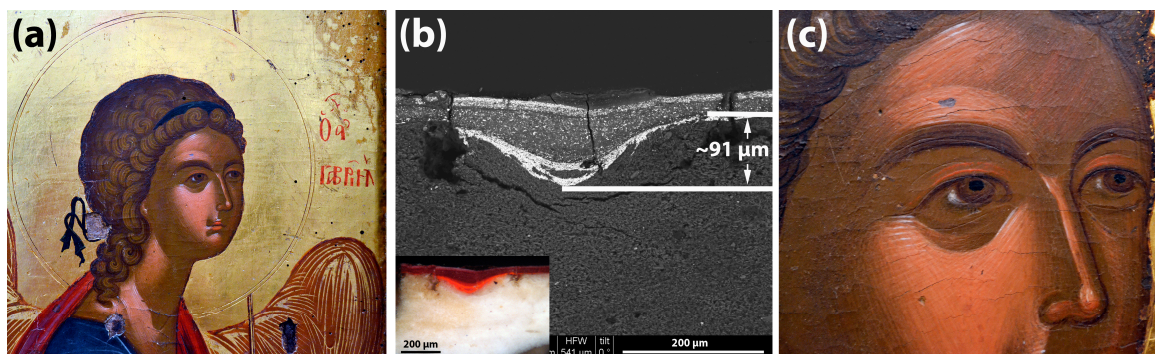


Figure 7. (a) Royal Doors, BMI, detail of Archangel Gabriel, left wing. (b) Background image: deep preliminary drawing incision (~91 microns) BSE, 500 \times . Insert picture: same sample under OM, 100 \times . (c) Detail of Archangel Gabriel face, sketch incisions on the facial characteristics are evident.

What is more, the St Theodoros icon shows notable similarities to the Angelos' works as regards the pigment mixtures and paint layer stratigraphy/application methods employed to render specific pictorial elements. In order to highlight the importance of this aspect, it should be kept in mind that the art of Eastern Orthodox iconography is based on a series of rules and dictations that more or less define the materials and techniques to be used when painting an icon. For instance, there are several post-Byzantine painting manuals that offer detailed recipes for the preparation of specific underpaint colors and the corresponding lighter tones [17,42]. Hence, the materials and techniques 'fingerprint' of a Late-Byzantine or Early Post-Byzantine icon painter cannot contain too many unusual features.

In the flesh parts, Angelos used a preparatory paint layer (underpainting/"proplasma") consisting of yellow ochre, cinnabar, hematite, lead white and charcoal, that was freely applied onto the ground

in the form of thin layers [10,11]. It is worth mentioning that the latter rarely exceed 25 μm in thickness [10,13], and that the freehand application of this underpainting is a characteristic that is documented on all Angelos icons [10]. In case of the St Theodoros icon, IR photography (Figure 2) revealed that the flesh underpainting was applied with an identical manner to the one seen on Angelos' paintings. In addition, the cross-section of a corresponding microsample (St Theodoros left hand) shows intriguing similarities in the stratigraphy and composition level with flesh samples from Angelos' icons [10,11,13]. The underpainting in St Theodoros flesh consists of yellow ochre, cinnabar, red ochre, lead white, charcoal and a bit of green earth (Figure 8a). Older studies of Angelos paintings had failed to spot green earth in flesh underpaints, thus leading some scholars to conclude that this is a notable deviation of Angelos from his contemporary painting trends [10]. Nevertheless, this pigment was recently identified in a genuine Angelos icon [13] and in the icon studied herein, implying thus that some parts of the full spectrum of Angelos materials and techniques might still be unknown; in addition, certain features might be specific to particular artistic periods of Angelos.

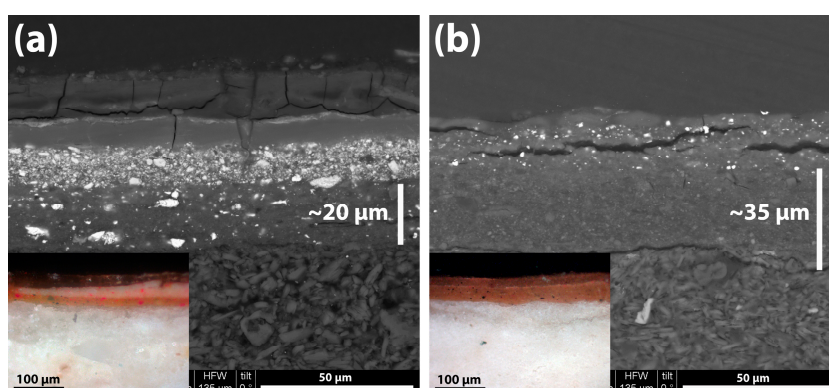


Figure 8. (a) Sample from the flesh section of St Theodoros, cross-section. Background image: BSE, 2000 \times ; perpendicular line marks the underpainting that contains numerous cinnabar grains (bright particles). Insert picture: same sample, OM, 200 \times . (b) Sample from the Annunciation icon, flesh part. Background image: BSE, 2000 \times . The perpendicular line marks the underpainting, note the absence of cinnabar. Insert picture: same sample under OM, 200 \times .

Finally, in order to highlight the rather idiomorphic character of Angelos' flesh painting manner (which is documented in the St Theodoros icon), the icon discussed herein was compared to a relevant high-quality Cretan icon (Annunciation, royal doors, Figure 7). Cross-sections from flesh parts of the two works are shown in Figure 8. The layered structure of St Theodoros sample (Figure 8a) is practically identical to the stratigraphy seen in samples from several Angelos paintings (see for instance the figures in row "a" of Table 1, pages 102–103 in [10]). The characteristic features in both cases (St Theodoros icon and signed Angelos paintings) are the following: (a) the thinness (usually $\sim 20 \mu\text{m}$) and color of the underpainting (pale yellowish-brown); (b) the consistent addition of cinnabar in the latter; and (c) the application of only one—yet significantly brighter—middle tone (lead white + cinnabar + ochre) on the base color. The final touches/highlights consist of pure lead white and are applied directly on the middle tone [10,13]. In contrast, the sample from the Annunciation icon shows an underpainting of moderate thickness ($\sim 35 \mu\text{m}$) that contains no cinnabar (Figure 8b), while the lighter flesh tones were built with at least two brighter (containing more lead white) paint layers (only the first is shown in Figure 8b).

5. Conclusions

By critically assessing the data acquired through the analytical investigation of the St Theodoros icon, it was documented that the painter of this high-quality icon employed materials and painting techniques which are remarkably similar to those characterizing works of the renowned Angelos painter. In brief, the preliminary drawing was rendered in the typical Angelos manner, namely through

a combination of brushstrokes and notably thin incisions; the facial characteristics were rendered through extremely skillful drawing. Similarly, flesh parts were painted with the same technique as the one encountered in Angelos' works. Other common features of the studied artifact and Angelos' icons include the addition of pigments in the gesso ground, the employment of high-grade lazurite for rendering blues and the use of yellow bole for gilding backgrounds. Although some of these techniques/materials do characterize icons of other Cretan painters of the same period, their simultaneous appearance in a single icon, along with the corresponding stylistic characteristics (archaeological perspective), collectively constitute a safe fingerprint of an Angelos painting.

Author Contributions: Conceptualization, G.P.M.; methodology, G.P.M., M.T. and E.F.; validation, G.P.M. and K.G.B.; formal analysis, G.P.M.; investigation, G.P.M. and K.G.B.; resources, G.P.M.; data curation, G.P.M. and M.T.; writing—original draft preparation, G.P.M.; writing—review and editing, G.P.M., K.G.B. and E.F.; visualization, G.P.M.; supervision, K.G.B.; project administration, G.P.M.; funding acquisition, G.P.M. All authors have read and agreed to the published version of the manuscript.

Funding: This research received no external funding.

Acknowledgments: G.P.M. expresses his gratitude towards the Alexander S. Onassis Public Benefit Foundation for providing a Ph.D. scholarship. His eminence Dionysius, Metropolitan of Zakynthos, and the Abbey and the Abbot of the Monastery of St Dionysius in Zakynthos, along with the General Directorate for the Restoration, Museums and Technical Works and the Directorate for Byzantine and Post-Byzantine Antiquities (both are divisions of the Greek Ministry of Culture and Sports) are sincerely acknowledged for providing sampling permissions. Special thanks are due to George Mitrikas (INN, NCSR 'Demokritos') for providing access to μ -Raman. Finally, G.P.M. thanks Giannis Kefallinos for providing accommodation during field-work in Zakynthos island.

Conflicts of Interest: The authors declare no conflict of interest.

References

1. Vokotopoulos, P. *Byzantine Icons*; Ekdotiki Athinon: Athens, Greece, 1995.
2. Χατζηδάκης, Μ. *Ελληνες ζωγράφοι μετά την Αλωση (1450–1830)* [*Greek Painters After the Fall of Constantinople (1450–1830)*]; Kentro Neoellinikon Ereunon: Athens, Greece, 1987.
3. Μανουσάκας, Μ. Η διαθήκη του Αγγέλου Ακοτάντου (1436), αγνώστου κρητικού ζωγράφου (πίν.52-53). *Δελτίον Χριστιανικής Αρχαιολογικής Εταιρείας* **1962**, *20*, 139. [CrossRef]
4. Cattapan, M. I pittori Pavia, Rizo, Zafuri da Candia e Papadopulo dalla Canea. *Thesaurismata* **1977**, *14*, 199–238.
5. Vassilaki, M. *The Painter Angelos and Icon-Painting in Venetian Crete*; Ashgate/Variorum: Farnham, UK, 2009.
6. Vassilaki, M. *The Hand of Angelos: An Icon Painter in Venetian Crete*; Lund Humphries: Farnham, UK, 2010.
7. Μυλωνά, Ζ. *Μουσείου Εκκλησιαστικής Τέχνης Ιεράς Μονής Στροφάδων και Αγίου Διονυσίου* [*Museum of Ecclesiastical Art of the Holy Monastery of Strofades and Saint Dionysius*]; Αποστολική Διακονία της Εκκλησίας της Ελλάδος: Athens, Greece, 2011.
8. Αχειμάστου-Ποταμιάνου, Μ. *Εικόνες της Ζακύνθου* [*Icons of Zakynthos*]; Ιερά Μητρόπολη Ζακύνθου και Στροφάδων: Athens, Greece, 1997.
9. Ζήβας, Δ.Α. *Ζάκυνθος 1953–2003* [*Zakynthos 1953–2003*]; Περίπλους: Athens, Greece, 2003.
10. Milanou, K.; Vourvopoulou, C.; Vranopoulou, L.; Kalliga, A.E. Angelos painting technique. A description of panel construction, materials and painting method based on a study of seven signed icons. In *Icons by the Hand of Angelos: The Painting Method of a Fifteenth-Century Cretan Painter*; Milanou, K., Vourvopoulou, C., Vranopoulou, L., Kalliga, A.E., Eds.; Benaki Museum: Athens, Greece, 2008; pp. 19–114.
11. Daniilia, S.; Minopoulou, E.; Andrikopoulos, K.S.; Karapanagiotis, I. Analysis of organic and inorganic materials and their application on icons by Angelos. In *Icons by the Hand of Angelos: The Painting Method of a Fifteenth-Century Cretan Painter*; Milanou, K., Vourvopoulou, C., Vranopoulou, L., Kalliga, A.E., Eds.; Benaki Museum: Athens, Greece, 2008; pp. 115–150.
12. Alexopoulou, A.; Kaminari, A. Study and documentation of an icon of Saint George by Angelos using infrared reflectography. In *Icons by the Hand of Angelos: The Painting Method of a Fifteenth-Century Cretan Painter*; Milanou, K., Vourvopoulou, C., Vranopoulou, L., Kalliga, A.E., Eds.; Benaki Museum: Athens, Greece, 2008; pp. 151–162.

13. Milanou, K.; Vourvopoulou, C.; Vranopoulou, L.; Kalliga, A.E. A technological examination of Cretan icons dating from the end of the 14th to the middle of the 15th century. *Μουσείο Μπενάκη* **2016**, *13–14*, 251–272, (In Greek, with English abstract).
14. Μιλάνου, Κ.; Βουρβοπούλου, Χ.; Βρανοπούλου, Λ.; Καλλιγιά, Α. Ο άγιος Νικόλαος με υπογραφή ‘Χειρ Αγγέλου’. Παρατηρήσεις σχετικές με τα υλικά κατασκευής και την τεχνική του έργου [Saint Nikolaos (icon) signed ‘By the hand of Angelos’. Observations on the materials and techniques of the artifact]. In X.A.E. *28ο Συμπόσιο Βυζαντινής και Μεταβυζαντινής Αρχαιολογίας και Τέχνης*; Simmetria: Athens, Greece, 2008; pp. 62–63.
15. Stassinopoulos, S. An icon of St Nicolaos with scenes from his life by the painter Angelos. Conservation and technical analysis. *Μουσείο Μπενάκη* **2016**, *13–14*, 223–250, (In Greek, with English abstract).
16. Heinrich, K.F.J. Strategies of electron probe data reduction. In *Electron Probe Quantitation*; Springer: Berlin/Heidelberg, Germany, 1991; pp. 9–18.
17. Dionysios of Fournā. *The “Painter’s Manual” of Dionysius of Fournā: An English Translation [from the Greek] with Commentary of cod. gr. 708 in the Saltykov-Shchedrin State Public Library, Leningrad*; Oakwood: London, UK, 1996.
18. Cosentino, A. Infrared technical photography for art examination. *e-PRESERVATION Sci.* **2016**, *13*, 1–6.
19. Boer, J.R.J.V.A.D. Infrared Reflectography: A Method for the Examination of Paintings. *Appl. Opt.* **1968**, *7*, 1711–1714. [CrossRef]
20. Cosentino, A. Identification of pigments by multispectral imaging; a flowchart method. *Heritage Sci.* **2014**, *2*, 8. [CrossRef]
21. Moon, T.; Schilling, M.R.; Thirkettle, S. A Note on the Use of False-Color Infrared Photography in Conservation. *Stud. Conserv.* **1992**, *37*, 42. [CrossRef]
22. Sarma, L.P.; Prasad, P.S.R.; Ravikumar, N. Raman Spectroscopic Study of Phase Transitions in Natural Gypsum. *J. Raman Spectrosc.* **1998**, *29*, 851–856. [CrossRef]
23. Osticioli, I.; Mendes, N.; Nevin, A.; Gil, F.P.; Becucci, M.; Castellucci, E. Analysis of natural and artificial ultramarine blue pigments using laser induced breakdown and pulsed Raman spectroscopy, statistical analysis and light microscopy. *Spectrochim. Acta Part A Mol. Biomol. Spectrosc.* **2009**, *73*, 525–531. [CrossRef]
24. Plesters, J. Ultramarine blue, natural and artificial. In *Artist’s Pigments, Vol. 2*; Ashok Roy, Ed.; National Gallery of Art: Washington, DC, USA, 1993; pp. 37–65.
25. Bell, I.M.; Clark, R.J.; Gibbs, P.J. Raman spectroscopic library of natural and synthetic pigments (pre- ≈ 1850 AD). *Spectrochim. Acta Part A Mol. Biomol. Spectrosc.* **1997**, *53*, 2159–2179. [CrossRef]
26. Burgio, L.; Clark, R.J.H. Library of FT-Raman spectra of pigments, minerals, pigment media and varnishes, and supplement to existing library of Raman spectra of pigments with visible excitation. *Spectrochim. Acta Part A Mol. Biomol. Spectrosc.* **2001**, *57*, 1491–1521. [CrossRef]
27. Caggiani, M.; Cosentino, A.; Mangone, A. Pigments Checker version 3.0, a handy set for conservation scientists: A free online Raman spectra database. *Microchem. J.* **2016**, *129*, 123–132. [CrossRef]
28. Grissom, C.A. Green earth. In *Artists Pigments: A Handbook of Their History and Characteristics*; Feller, R.L., Ed.; National Gallery of Art: Washington, DC, USA, 1986; pp. 141–168.
29. Mastrotheodoros, G.P.; Beltsios, K.G.; Bassiakos, Y. On the blue and green pigments of post-Byzantine Greek icons. *Archaeometry* **2020**, *62*, 774–795. [CrossRef]
30. Botticelli, M.; Maras, A.; Candeias, A. μ -Raman as a fundamental tool in the origin of natural or synthetic cinnabar: Preliminary data. *J. Raman Spectrosc.* **2019**, *51*, 1470–1479. [CrossRef]
31. Karapanagiotis, I.; Lampakis, D.; Konstanta, A.; Farmakalidis, H. Identification of colourants in icons of the Cretan School of iconography using Raman spectroscopy and liquid chromatography. *J. Archaeol. Sci.* **2013**, *40*, 1471–1478. [CrossRef]
32. Kirby, J.; Spring, M.; Higgitt, C.; National Gallery. The Technology of Red Lake Pigment Manufacture: Study of the Dyestuff Substrate. Available online: www.nationalgallery.co.uk (accessed on 10 October 2020).
33. Tomasini, E.; Siracusano, G.; Maier, M. Spectroscopic, morphological and chemical characterization of historic pigments based on carbon. Paths for the identification of an artistic pigment. *Microchem. J.* **2012**, *102*, 28–37. [CrossRef]
34. Mactaggart, P.; Mactaggart, A. *Practical Gilding*; Archetype: London, UK, 2002.
35. Mastrotheodoros, G.P.; Beltsios, K.G.; Bassiakos, Y.; Papadopoulou, V. On the Metal-Leaf Decorations of Post-Byzantine Greek Icons. *Archaeometry* **2017**, *60*, 269–289. [CrossRef]

36. Mastrotheodoros, G.P.; Anagnostopoulos, D.F.; Beltsios, K.G.; Filippaki, E.; Bassiakos, Y. Glittering on the Wall: Gildings on Greek Post-Byzantine Wall Paintings. In *Communications in Computer and Information Science*; Springer: Berlin/Heidelberg, Germany, 2019; Volume 962, pp. 397–404. [CrossRef]
37. Valianou, L.; Wei, S.; Mubarak, M.S.; Farmakalidis, H.; Rosenberg, E.; Stassinopoulos, S.; Karapanagiotis, I. Identification of organic materials in icons of the Cretan School of iconography. *J. Archaeol. Sci.* **2011**, *38*, 246–254. [CrossRef]
38. Karapanagiotis, I.; Minopoulou, E.; Valianou, L.; Daniilia, S.; Chryssoulakis, Y. Investigation of the colourants used in icons of the Cretan School of iconography. *Anal. Chim. Acta* **2009**, *647*, 231–242. [CrossRef]
39. Mastrotheodoros, G.P. Pigments and Various Materials of Post-Byzantine Painting. Ph.D. Thesis, University of Ioannina, Ioannina, Greece, 2016.
40. Mastrotheodoros, G.P.; Beltsios, K.G.; Bassiakos, Y.; Papadopoulou, V. On the Grounds of Post-Byzantine Greek Icons. *Archaeometry* **2015**, *58*, 830–847. [CrossRef]
41. Cennini, C. *The Craftsman's Handbook*; Dover Publications: Mineola, NY, USA, 1954.
42. Mastrotheodoros, G.P.; Beltsios, K.G. Sound Practice and Practical Conservation Recipes as Described in Greek Post-Byzantine Painters' Manuals. *Stud. Conserv.* **2018**, *64*, 42–53. [CrossRef]

Publisher's Note: MDPI stays neutral with regard to jurisdictional claims in published maps and institutional affiliations.



© 2020 by the authors. Licensee MDPI, Basel, Switzerland. This article is an open access article distributed under the terms and conditions of the Creative Commons Attribution (CC BY) license (<http://creativecommons.org/licenses/by/4.0/>).

Article

Ag-Nanostars for the Sensitive SERS Detection of Dyes in Artistic Cross-Sections—*Madonna della Misericordia* of the National Gallery of Parma: A Case Study

Maria Sole Zalaffi ¹, Ines Agostinelli ², Najmeh Karimian ¹ and Paolo Ugo ^{1,*}

¹ Department of Molecular Sciences and Nanosystems, University Ca' Foscari of Venice, Via Torino 155, 30172 Venezia Mestre, Italy; mariasole.zalaffi@unive.it (M.S.Z.); najmeh.karimian@unive.it (N.K.)

² Restoration Laboratory of the National Gallery of Parma, Piazzale della Pilotta 15, 43121 Parma, Italy; ines.agostinelli@beniculturali.it

* Correspondence: ugo@unive.it

Received: 29 September 2020; Accepted: 10 November 2020; Published: 12 November 2020

Abstract: In historical paintings, the detection of low amounts of pigments and dyes by Raman spectroscopy can sometimes be challenging, in particular for fluorescent dyes. This issue can be overcome by using SERS (surface-enhanced Raman spectroscopy) which takes advantage of the properties of nanostructured metal surfaces to quench fluorescence and enhance Raman signals. In this work, silver nanostars (AgNSs) are applied for the first time to real art samples, in particular to painting cross-sections, exploiting their effective SERS properties for pigment identification. The case study is the *Madonna della Misericordia* of the National Gallery of Parma (Italy). Cross-sections were analyzed at first by optical microscopy, SEM-EDS, and micro-Raman spectroscopy. Unfortunately, in some cross-sections, the application of conventional Raman spectroscopy was hindered by an intense background fluorescence. Therefore, AgNSs were deposited and used as SERS-active agent. The experimentation was successful, allowing us to identify a modern dye, namely copper phthalocyanine. This result, together with the detection of other modern pigments (titanium white) and expert visual examination, allowed to reconstruct the painting history, postdating its realization from the 15th century (according to the Gallery inventory) to 19th century with a heavy role of recent (middle 20th century) restoration interventions.

Keywords: silver nanostars; surface enhanced Raman spectroscopy; cross-sections; copper phthalocyanine; blue pigment; analytical diagnostics; National Gallery of Parma; *Madonna della Misericordia*

1. Introduction

Nowadays the scientific approach plays a key role in the conservation-restoration of cultural heritage, which is necessary not only to sort out conservation issues but also to answer diagnostic inquiries. The analysis of the composition of a work of art follows a precise analytical protocol which starts from the visual analysis (optical microscopy in visible and UV light, IR reflectography), then it involves the use of elemental and molecular non-destructive techniques (X-rays fluorescence spectroscopy), scanning electron microscopy (SEM), attenuated total reflection-Fourier transform infrared (ATR-FTIR) spectroscopy, Raman spectroscopy, up to eventually resorting to micro-destructive ones (gas chromatography and mass spectrometry, high performance liquid chromatography). Indeed, since they are composite materials, works of art must be studied in their three-dimensionality in order to take into account all the layers underneath the superficial one. For this reason, transversal micro-sample, the so-called cross-section, once embedded in resins or salts, represent the ideal condition for an exhaustive analysis. Cross-sections should contain all the layers of which the work of art is composed:

support, ground layer, priming, paint layer, varnish, and glaze. The complexity of the layering and the variety of material employed (binders, pigments, dyes, varnishes) depend on several factors: the period and place of execution, the artist, the restoration interventions, etc. Cross-sections can tell us the story of a work of art: by performing analyses directly on each layer, we can map the materials employed and organize the layers in a reliable sequence [1,2].

Chemical information on the composition of the layers of a cross-section can be obtained by analytical techniques characterized by spatial resolution capabilities. Typically, localized elemental information is obtained by SEM combined with electron dispersive spectroscopy (EDS) while molecular data are obtained by using vibrational spectroscopies combined with optical microscopy, such as micro-FTIR or micro-Raman spectroscopy.

In particular, Raman spectroscopy represents one of the most employed techniques in diagnostics thanks to the following advantages: non-destructiveness, efficient in situ performance, high spatial resolution (up to 1 μm), presence of Raman bands in the “fingerprint” region of the spectra, capability of discriminating between different crystalline structures, and to resolve weak Raman signals of the analyte from water and glass [3,4]. On the other hand, Raman spectroscopy presents some disadvantages which can hamper its widespread use. Raman scattering is weak (spectroscopic cross-section of 10^{-28} cm^2/mol), as a result, it can be obscured by the much more intense fluorescence (spectroscopic cross-section of 10^{-16} cm^2/mol) emitted by organic molecules with conjugated electronic structures, such as the colorants. The low sensitivity of Raman spectroscopy and the presence of fluorescence can hinder the detection of dyes, in particular, when present at low concentration levels.

Surface enhanced Raman spectroscopy (SERS), observed for the first time by Fleischmann, Hendra, and McQuillan in 1973 [5], helps to overcome these shortcomings. This technique takes advantage of the optical properties of nanostructured metal surfaces, in particular silver, which locally enhance the electromagnetic field, at the same time quenching the fluorescence. As a consequence, a dramatic enhancement of the Raman signal is detected for molecules in close contact with the nanomaterial so facilitating their detection [6].

The SERS technique has been employed in the field of cultural heritage (see ref. [2] for a recent review), in particular, for the analysis of colorants directly on fibers, micro-fragments, and cross-sections [7–9]. Typically, the materials chosen for this purpose are spherical silver nanoparticles, prepared as colloidal dispersion by using the Lee–Meisel method [10,11]. Recently, other nanomaterials have shown higher effectiveness in producing significant SERS effects, including anisotropic nanostructures such as silver nanostars (AgNSs) [12–15]. Due to their stellate shape composed of a central core and many pods, these particular nanoparticles are expected to absorb photons in different spectral regions, namely around 370–380 nm and in the near infrared region and, when excited with red-light laser beams, AgNSs show Raman enhancement factors in excess to 10^6 [16–18]. Gold and silver nanostars (Au/AgNSs) can be obtained employing different reagents and reduction methodologies. Among the different synthetic methods proposed for the preparation of AgNSs [13,16–25], the one-pot method recently proposed by A. García-Leis et al. [14,15], looks particularly attractive for its feasibility and reproducibility. It involves the reduction of the metallic precursor (AgNO_3) by a reducing agent (hydroxylamine) in the presence of a capping agent (trisodium citrate) and additive (NaOH). Here, we propose for the first time, as far as we know, the use of AgNSs prepared with the above method, to detect dyes in painting cross-sections. The efficiency of AgNSs as SERS substrates has been tested in our lab on other kinds of samples such as thiols adsorbed on metals, including metal nanofibers [15], and lake pigments, indicating the superiority of AgNSs over spherical silver nanoparticles [26].

As a case example, the methodology was applied to cross-sections from the Madonna della Misericordia, an altarpiece kept by the National Gallery of Parma, Italy. The study took advantage of recent restoration intervention on the paint, with the goal to obtain information on the history of this work of art, in particular, to identify original pictorial layers and the role of previous restoration or even repainting interventions. In this study, Raman spectroscopy was applied together with other

diagnostic tools, demonstrating that SERS with the help of AgNSs is effective in detecting organic and metalorganic dyes at trace levels, which are not detectable by means of “regular” Raman spectroscopy.

A case study is exposed in this paper, illustrating how AgNSs can be applied to a cross section of a real painting for diagnostics purposes, confirming that this kind of SERS substrate can be effective for the sensitive detection of organics and metallorganics employed in the field of cultural heritage.

2. Materials and Methods

2.1. The painting “Madonna della Misericordia” from the National Gallery of Parma

The Madonna della Misericordia (Inv. 450) at the National Gallery of Parma is an oil on panel painting, 192 × 82 cm, which represents Virgin Mary housing under her mantle the clients, two ladies and two gentlemen, kneeling at her left and right, respectively. It is completed by a painted frame characterized by two lateral *paraste*, a central rose and a *predella* decorated by three saints (Figure 1).

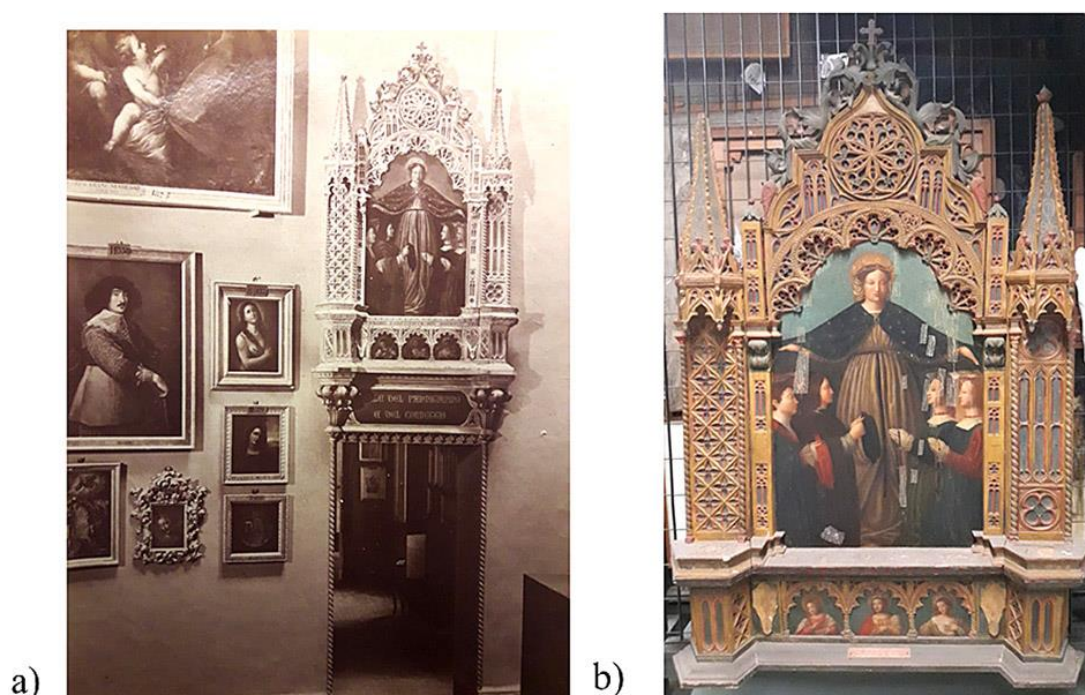


Figure 1. Pictures showing the Madonna della Misericordia (a) at the entrance of Parmigianino and Correggio’s display rooms in the 19th century and (b) in the picture gallery where it has been displayed until 2018.

This painting arrived at the Gallery in 1868, coming from the Cappuccini’s monastery in Borgo Santa Chiara, Parma [27]. The director of the Gallery, Corrado Ricci, attributed this painting to an anonymous painter belonging to the school of Cremona of the 15th century [28]. The painting underwent important restoration interventions (insertion of wedges into the panel to level it—*sverzatura*—which is the main cause of cracks on the pictorial layer, numerous re-paintings, etc.) carried out in 1896 by G. Frenguelli [28] and in 1951 by L. Arrigoni [29]. The present study was performed during a restoration intervention of the painting performed in 2018 and 2019.

2.2. UV-Visible Absorption Spectroscopy

UV-Visible absorbance spectra were recorded with a Perkin-Elmer Lambda 40 spectrophotometer equipped with a Peltier-Elmer PTP6 (Peltier temperature programmer) apparatus. The Ag colloids samples were diluted 1:3 in water.

2.3. Transmission Electron Microscopy (TEM)

Transmission electron microscopy (TEM) and high resolution TEM (HRTEM) analysis were performed using a JEOL 3010 high resolution electron microscope (0.17 nm point-to-point resolution at Scherzer defocus), operating at 300 kV, equipped with a Gatan slow-scan CCD camera (model 794) and an Oxford Instrument EDS microanalysis detector Model 6636. Drops of colloidal solutions were deposited on holey-carbon copper grids and let dry at room temperature before analysis.

2.4. SEM-EDS

SEM and EDS analysis on selected spots of the cross sections were performed at the University Ca' Foscari of Venice (Department of Molecular Sciences and Nanosystems), using a TM3000 Hitachi tabletop scanning electron microscope coupled with a X-ray microanalysis system (SwiftED3000); conditions for recording the EDS spectra were: acquisition time 30.0 s; process time 5 s; accelerating voltage 15 kV.

2.5. Micro-Raman Spectroscopy

The SERS measurements were performed at the University of Southampton, during a stage of MSZ at the School of Chemistry. A Renishaw 2000 Raman spectrometer was employed to carry out both Raman and SERS measurements. The excitation laser employed was a Renishaw 785 nm laser and a CCD detector. The maximum power of the laser is 100 mW, but lower powers were used during the data acquisition, typically 0.05% and 1% (0.05 and 1 mW) to avoid to damage the samples. The collection time was 10 s for one accumulation. The spectrometer was equipped with a Leica DMLM series microscope. In order to collect scattered light at the sample, a microscope objective with a 50× magnification was employed with a short working distance (0.37 mm—numerical aperture 0.75). Noise filters and background correction were used for clarity when necessary.

2.6. Preparation of the Cross-Sections

The samples for the cross sections were taken by the restorer, using a micro scalpel, cutting triangular millimeter sized fragments containing all the layers composing the painting. Then, they were placed into cells of a silicon rubber mold on an already hardened resin layer. At this point, the embedding resin was prepared under the fume hood using some mL of unsaturated orthophthalic polyester resin (purchased from G. Angeloni, Venice) and few drops of hardener (methyl-ethyl-ketone peroxide). The components were stirred until the mixture was completely homogenous. Eventually, the resin was poured into the cells and left to dry for two days. Once the resin cured, the polishing procedure started. The cross sections were polished manually using silicon carbide paper with decreasing grain sizes. Different grit size were used (P120-P500-P800-P4000-P6000-P8000-12000, of an average size from 130 to 4 μm) and progressively replaced into the lapping machine, equipped with a magnetic rotating disk and water cooling system, from the coarsest to the finest one. The sections were pressed onto the abrasive papers for some minutes and frequently observed at the stereomicroscope to check the level of polishing. This procedure ended when the samples were reached from the long side of the resin blocks.

2.7. Ag Nanostars Colloid: Preparation and Application on the Cross Sections

AgNSs were synthesized using the method proposed by A. García-Leis et al. [14], using analytical grade reagents and water purified with a Milli-Q system (Millipore). Four solutions were required:

- Sodium hydroxide solution: NaOH (0.02 g) dissolved in water (10 mL) to get a 0.05 M solution.
- Hydroxylamine solution: NH₂OH (18 μL) at 50% w/v in water (5 mL).
- Silver nitrate solution: AgNO₃ (0.0017 g) dissolved in water (10 mL) to obtain a 1·10⁻³ M solution.
- Trisodium citrate solution: of C₆H₅O₇Na₃·2H₂O (0.114 g) dissolved in water (10 mL) to get a 0.045 M solution.

Next, 500 μL of the NaOH and 500 μL of the hydroxylamine solutions were mixed in a flask and stirred at 670 rpm with a magnetic stirrer for one minute. Then, 9 mL of the AgNO_3 solution were added and the mixture kept under stirring for 5 min. Afterwards, 100 μL of the citrate solution were dropped in the flask, stirring for approximately 15 min, i.e., until it developed a dark green color. The reduction of Ag^+ ions was achieved by hydroxylamine, but this process, at room temperature, is very slow. In order to make the long arms of these spiky nanoparticles grow faster, citrate was added. The complete growth of the star-shaped NPs, starting from a spherical faceted morphology, takes more or less 48 h. Therefore, the colloidal solution of AgNSs was concentrated by centrifuging three times at 8000 rpm in a 1.5 mL Eppendorf centrifuge tube from 500 μL of colloid. After each centrifugation step, 400 μL of supernatant were removed and replaced by the same quantity of colloid. Before centrifuging, nanoparticles which got stuck at the bottom, were redispersed. After this procedure, 2 μL of the concentrated AgNSs dispersion were deposited on the cross section by means of a micropipette. Once completely dried, the sample was ready to be analyzed with the $\mu\text{-Raman}$ spectrometer.

3. Results and Discussion

3.1. Synthesis and Characterization of AgNSs

The macroscopic optical properties and TEM image of the AgNSs are shown in Figure 2, while Figure S1 shows the extinction spectra of the colloidal suspension of AgNSs [16]. This colloid presents a dark green color (Figure 2A) and, as shown by TEM analysis, is indeed composed by a monodisperse suspension of AgNSs (Figure 2B). A typical AgNS presents a central core of around 50 nm diameter and a variable number of pods arranged in an octahedral structure reaching an overall dimension of approximately 200 nm. The growth starts from spherical seeds of Ag reduced by hydroxylamine, then, in the following 48 h, the pods start taking shape thanks to the citrate ions in the presence of NaOH, which directs the growth of the branches [14,15].

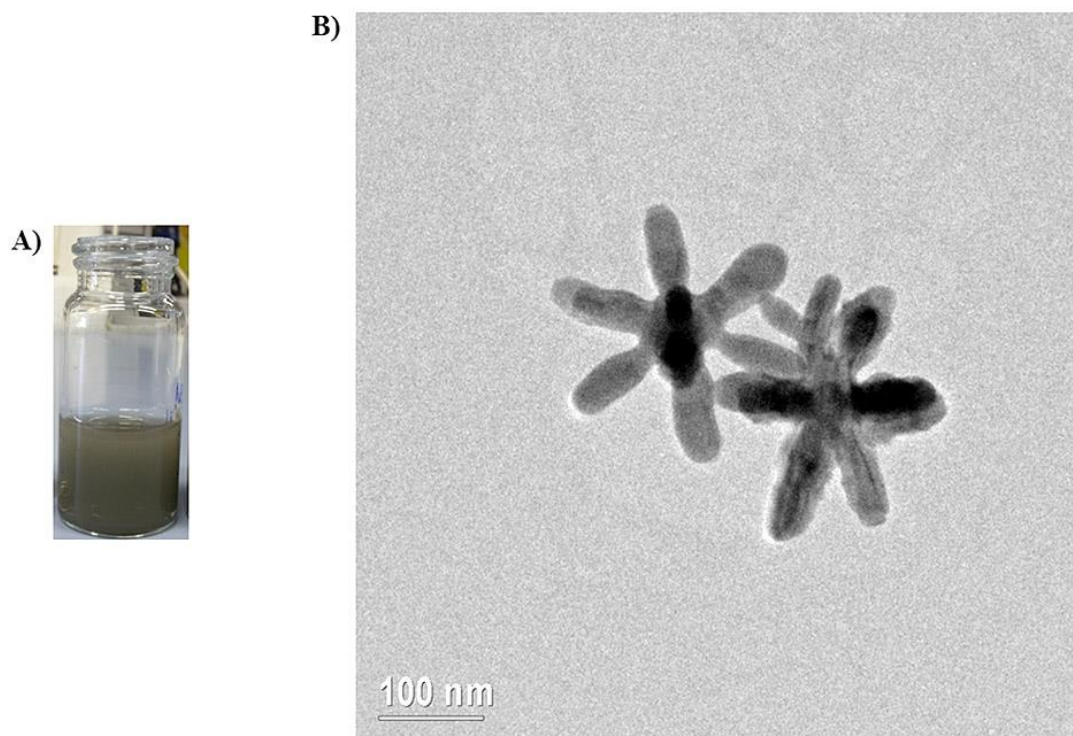


Figure 2. (A) Photograph showing the macroscopic appearance of the colloidal suspension of Ag nanoparticles; (B) relevant TEM image of the nanoparticles obtained.

The UV-Vis-NIR extinction spectrum of the colloidal dispersion of AgNSs (see Figure S1) presents features in agreement with the previous literature [15–17], namely an absorption peak with maximum extinction at 370 nm, followed by a progressive increase in extinction in the NIR region, starting approximately for $\lambda > 550$ nm. Further details on the general characterization of the AgNSs synthesized here are described elsewhere [16].

3.2. Cross-Sections Analysis: Bluish Background (CS7), an Exemplificative Study

The preliminary analyses were fundamental to plan the sampling areas (see SM). Indeed, mapping the more recently retouched areas of over painting was necessary to avoid them during the sampling. Seven cross-sections were sampled from the painting and the *predella*, and six from the frame. Each one was taken in order to answer specific questions about the materials employed in every layer of the stratigraphy at those precise points (Figure 3). For the sake of brevity, only the most important and relevant results are presented (see SM).



Figure 3. Sampling map of the numbered cross sections (CS) in the (a) panel and (b) frame (CS5 is an erratic sample).

The analysis of CS7, sampled in the bluish background behind the Virgin Mary and the clients, is the most exemplificative in the context of the present study. Figure 4a shows the exact area where CS7 was sampled and, once embedded in a polyester resin block, it was analyzed using 50 \times magnification (Figure 4b) and optical microscope in reflected light (Figure 4c). At high magnifications (50 \times), all the layers composing the painting are visible. Starting from the bottom, we can find the ground layer, made of gypsum, which is necessary to make the support even and homogeneous, in this case, the wood panel. Then, it is possible to note the paint layer made up of a mixture of blue and white grains. The peculiar feature is that this sequence is repeated: a new ground and paint layer were added on the original ones in more recent times. Apparently, they may be composed of the same materials, but this must be investigated by means of elemental and molecular analyses.

First of all, the cross section was examined by SEM. The analysis of data in Figure 5 confirms the presence of four layers: the 1st ground (I) (around 150 μm), characterized by light elements

(darker areas); the 1st paint layer (II) ($\approx 70 \mu\text{m}$) composed by grains of quite light elements in a heavier matrix (brighter areas); the 2nd ground layer (III) ($\approx 50 \mu\text{m}$) and the 2nd paint layer (IV) ($\approx 15 \mu\text{m}$), both containing mainly light elements with some brighter spots which indicate the presence of heavy elements. EDS analysis provided important information on the elemental composition of the layers. EDS spectra inserted in Figure 5 confirm the presence of Ca and S in the 1st ground layer, which agree with the likely use of gypsum (CaSO_4). The peak of Cu in the grains and the one of Pb in the matrix of the 1st paint layer suggest the presence of a blue copper pigment such as azurite [$\text{Cu}_3(\text{CO})_2(\text{OH})_2$] mixed with a white lead pigment, probably lead white [$(\text{PbCO}_3)_2 \cdot \text{Pb}(\text{OH})_2$]. Ca and S are detected also in the 2nd ground layer, indicating again the presence of gypsum. Finally, the 2nd paint layer is mainly characterized by the presence of Ti, Si, Al, Na, S, Cu, and some Cr. The presence of Ti suggests the use of titanium white, TiO_2 , a modern pigment introduced in 1920 [30].

Additional EDS spectra were recorded, focusing on the bluish grains present in the 2nd paint layer, revealing the presence of S, Ba, Cr, and Co (see Figure 6). The detection of S and Ba can agree with the presence of barite, BaSO_4 . This natural occurring mineral has been synthetically produced from the beginning of the nineteenth century to be extensively employed both as filler in the formulations of colors [31] and used in the preparation of TiO_2 [30]. Cr and Co could be attributed to the presence of a bluish chromium-based pigment: cobalt chromite, CoCr_2O_4 (PB36, cobalt chromite blue-green spinel) often substitutes the historically genuine cerulean blue (PB35, cobalt stannate), the latter being introduced in 1860 as a pigment [32]. Unfortunately, no Raman or SERS spectral evidence allowed to confirm this supposition.

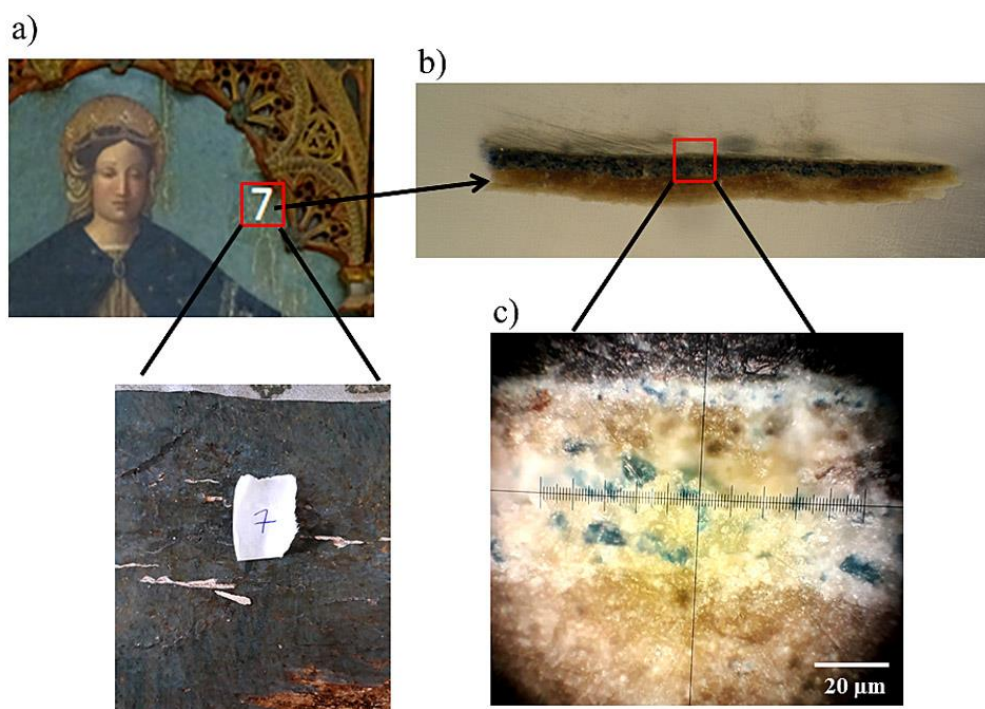


Figure 4. (a) The sampling area of CS7 is marked on the picture; (b) CS7 analyzed using the stereomicroscope, a transversal sample (1–2 mm) embedded in a resin block showing all the layers the painting is composed of; (c) magnification of the cross section (objective of the microscope 50 \times) showing from the bottom to the top the original ground and paint layer and a more recent coat composed of a new ground and paint layer.

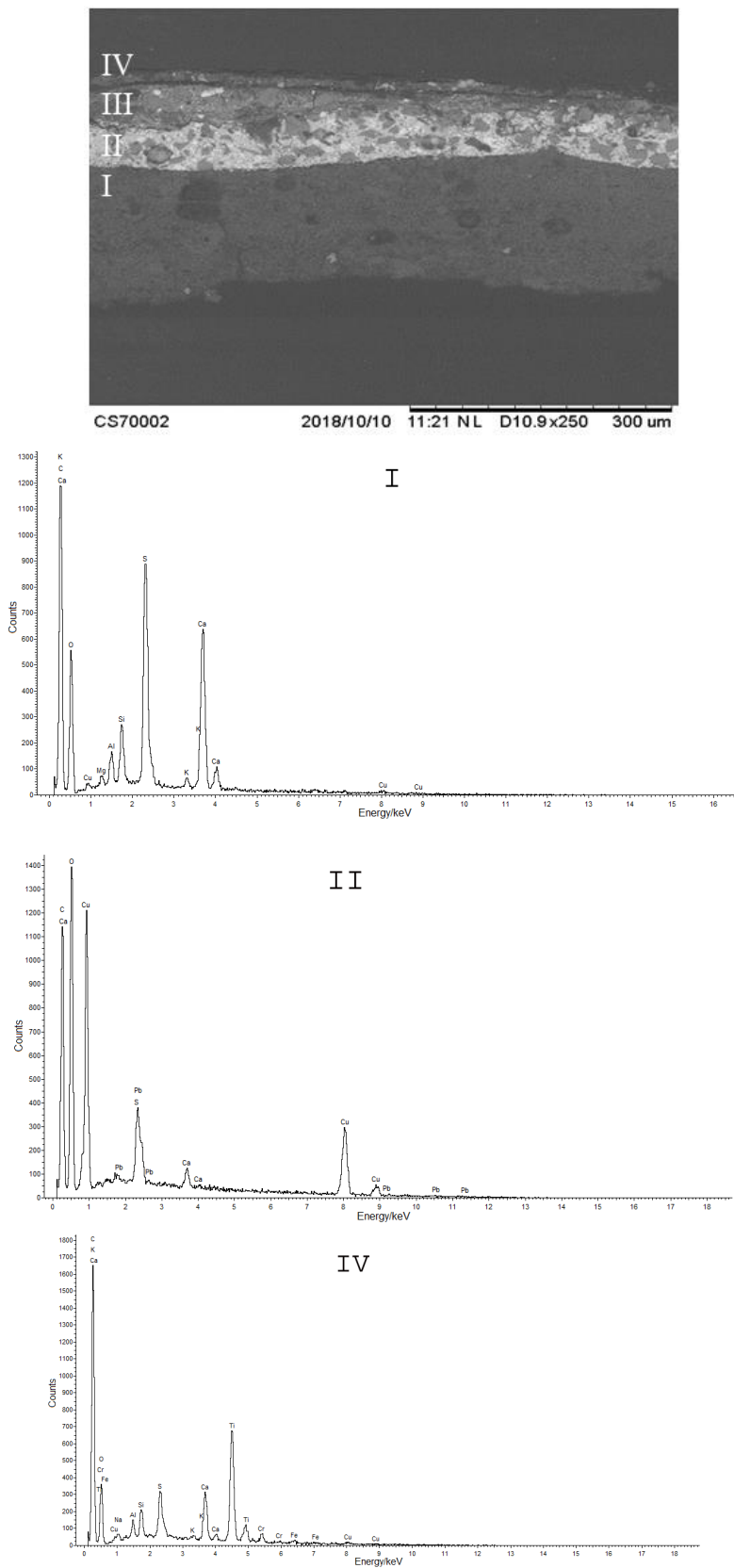


Figure 5. SEM image of CS7 and EDS spectra recorded on the I, II, and IV layers (the EDS spectrum of the III layer is comparable with that of layer I).

In order to obtain information at a molecular level, micro-Raman spectroscopy was applied. Figure 7 shows the Raman spectra recorded analyzing defined points on the magnified cross section, indicated in Figure 7a. The two ground layers were confirmed to contain gypsum, whose spectrum presents the typical band at $1009 \text{ (strong) cm}^{-1}$ (Figure 7b) [33]. Comparison with literature spectra [33] proved that the 1st paint layer contains azurite, as indicated by the bands at 1578 (weak) , 1423 (medium) , 1096 (m) , 832 (w) , 770 (m) , 401 (s) , 247 and 83 (m) cm^{-1} (Figure 7c), and lead white, whose bands are detected at 1055 (s) and 401 (m) cm^{-1} (Figure 7d).

The results of the Raman analyses performed on the 2nd paint layer are exposed below. The presence of titanium white (PW6) in the form of anatase, was confirmed by the detection of its typical bands at 640 (m) , 510 (m) , 397 (m) and 143 (s) cm^{-1} (Figure 8) [32].

The Raman characterization of the bluish pigment, due to the scarcity of grains and the tiny thickness of the layer, is particularly challenging. The Raman spectrum recorded on this layer allowed us to identify ultramarine blue: sodium polysulphide-aluminosilicate (PB29, $\text{Na}_{6-10}\text{Al}_6\text{Si}_6\text{O}_{24}\text{S}_{2-4}$, which is responsible for the Raman band at $548 \text{ cm}^{-1} \text{ (s)}$ (the bands in gray belong to titanium white) (Figure 9) [34]. This attribution is supported by the detection of Si, Na, Al, S in the EDS spectrum reported in Figure 5IV. Natural ultramarine is a mineral called *lazurite*, a complex sulfur-containing sodium aluminosilicate based on a body-centered cubic lattice. Synthetic ultramarine was synthesized in 1828 by Jean Baptiste Guimet in Paris and then rapidly adopted by artists [35]. Note that natural and synthetic ultramarine blue provide comparable spectral signatures and cannot be distinguished by Raman analysis.

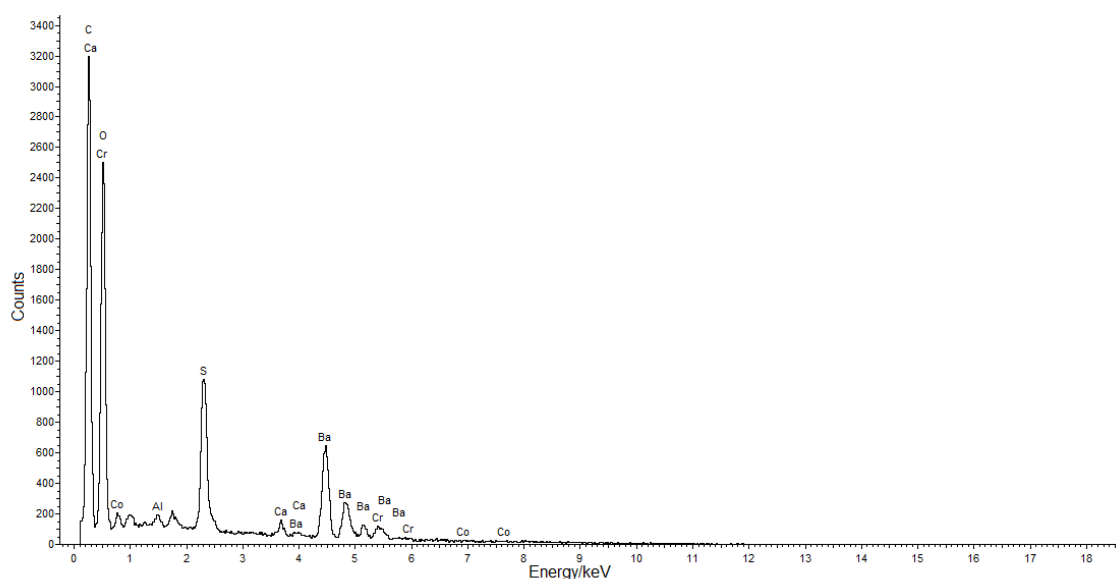


Figure 6. EDS spectrum performed on blue grain of the 2nd paint layer of CS7.

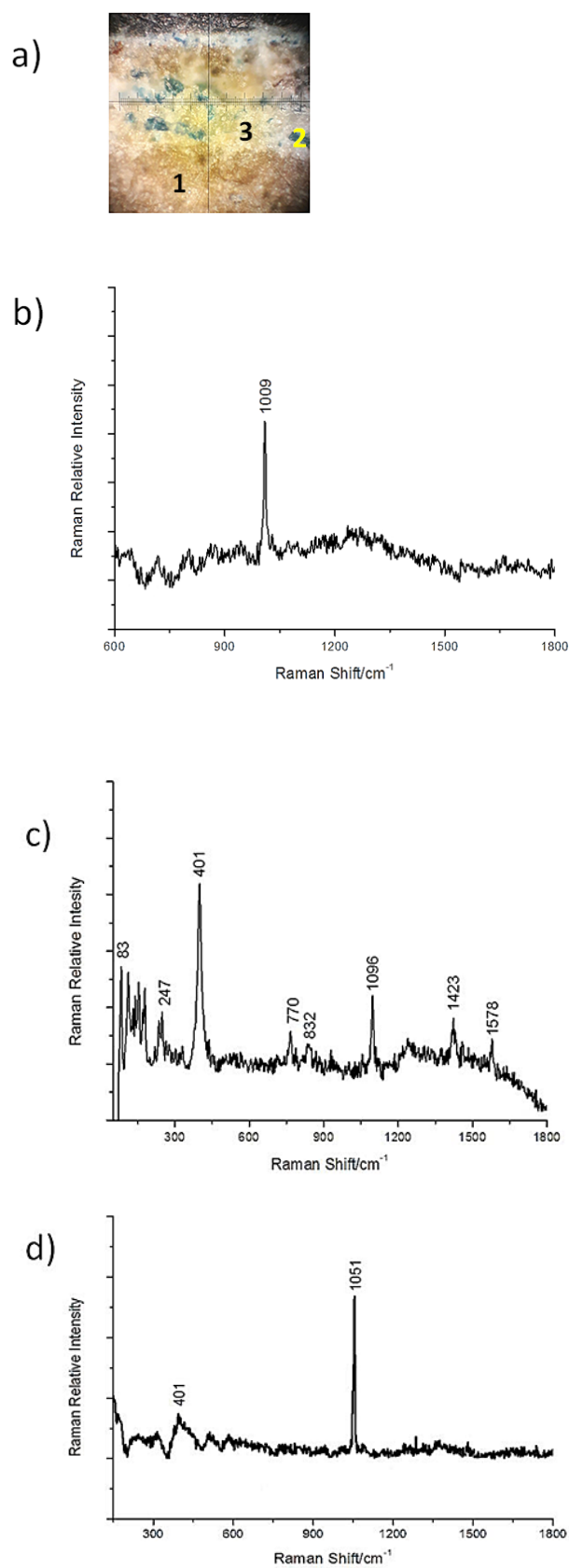


Figure 7. (a) Optical micrograph of CS7 (50×); (b–d) Raman spectra on CS7 revealing: (b) in the 1st and 2nd ground layers, at point 1, the spectral features typical of gypsum; in the 1st paint layer, (c) at point 2 the features of azurite, and (d) at point 3, of lead white.

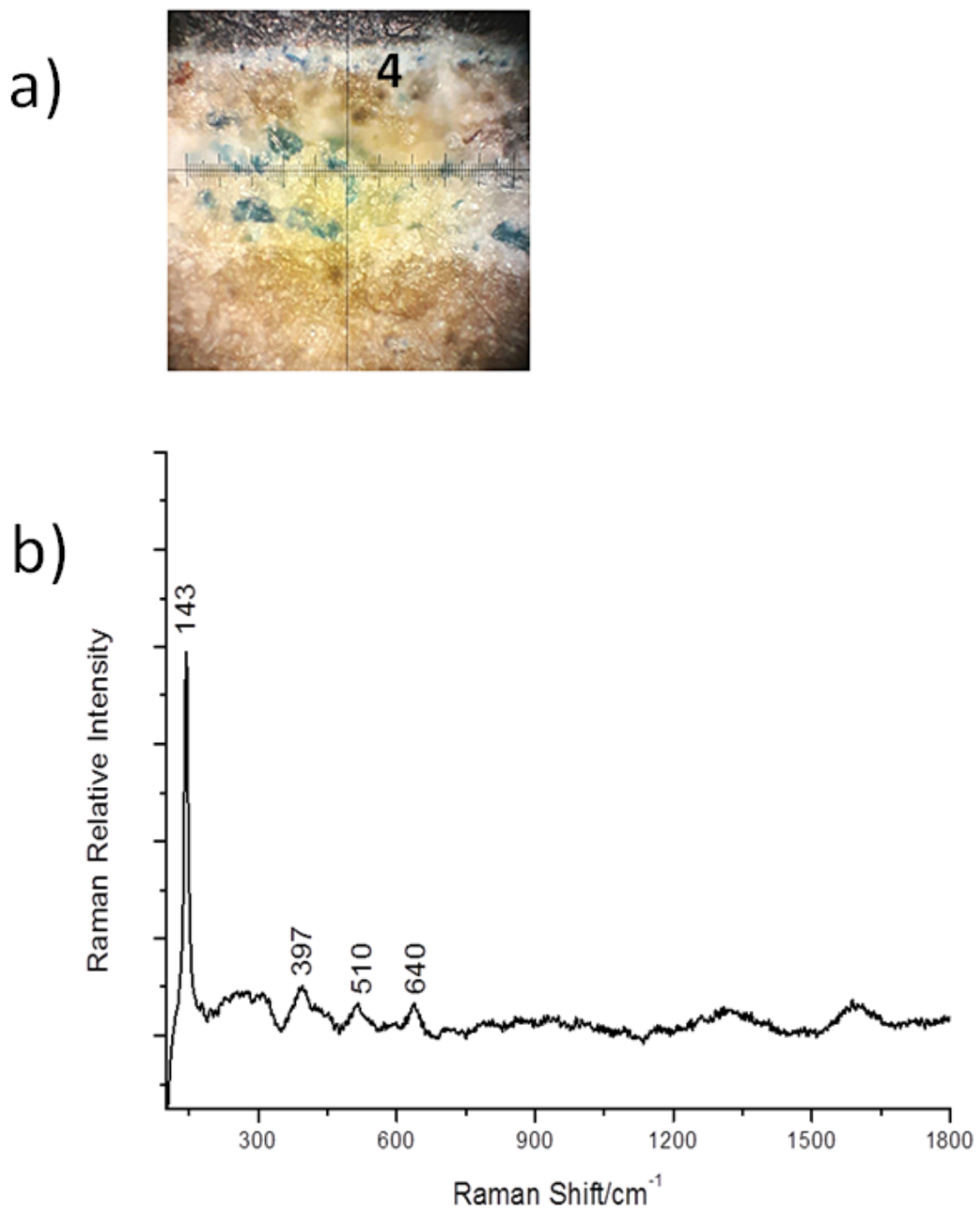


Figure 8. (a) Optical micrograph (50 \times) and (b) Raman spectrum recorded at point 4 on the 2nd paint layer of CS7, showing the spectral features of titanium dioxide.

During the analysis of the blue layer, we noticed that some spots gave strong fluorescence while others did not. Indeed, the spectrum in Figure 9 refers to the non-fluorescent grains. Comparing the results obtained with the composition of the most common contemporary color tubes, it was clear that the presence of synthetic ultramarine alone was unlikely since this pigment is often mixed with synthetic organic dyes [36]. Normal Raman spectroscopy did not provide spectra useful to solve this diagnostic issue because of the fluorescence, typically generated by some organic dyes and pigments (Figure 10a). For this reason, we opted to employ the SERS technique using AgNSs as signal enhancers and fluorescence quenchers, in order to amplify the Raman spectrum of the fluorescent grains. After addition of the Ag nanostars [14], the spectrum shown in Figure 10b was collected.

The fluorescent background is now dramatically lowered and a defined spectrum emerges being characterized by detectable bands at 1566 (m), 1514 (s), 1438 (w), 1400 (w), 1379 (m), 1349 (s), 1303 (m), 1142 (w), 1104 (s), 1002 (m), 720 (m), 679 (s), 649 (m), and 585 (w) cm^{-1} . Comparison with literature data indicate that these features corresponds to those of copper alpha-phthalocyanine (PB 15:2) [37–39], a synthetic pigment. A detailed comparison of the experimental and the reference bands of PB 15:2 is reported in Table S1 in Supplementary Materials. Interestingly, the presence of PB 15:2 agrees with the presence of the Cu signals in the EDS spectrum in Figure 5II. Organic phthalocyanines and their metal complexes were synthesized at the beginning of the twentieth century and are widely used as blue and green pigments until the present time [40]. Note that the band at 211 cm^{-1} is produced by the interaction of Ag with ions present in the colloidal solution of nanoparticles [41].

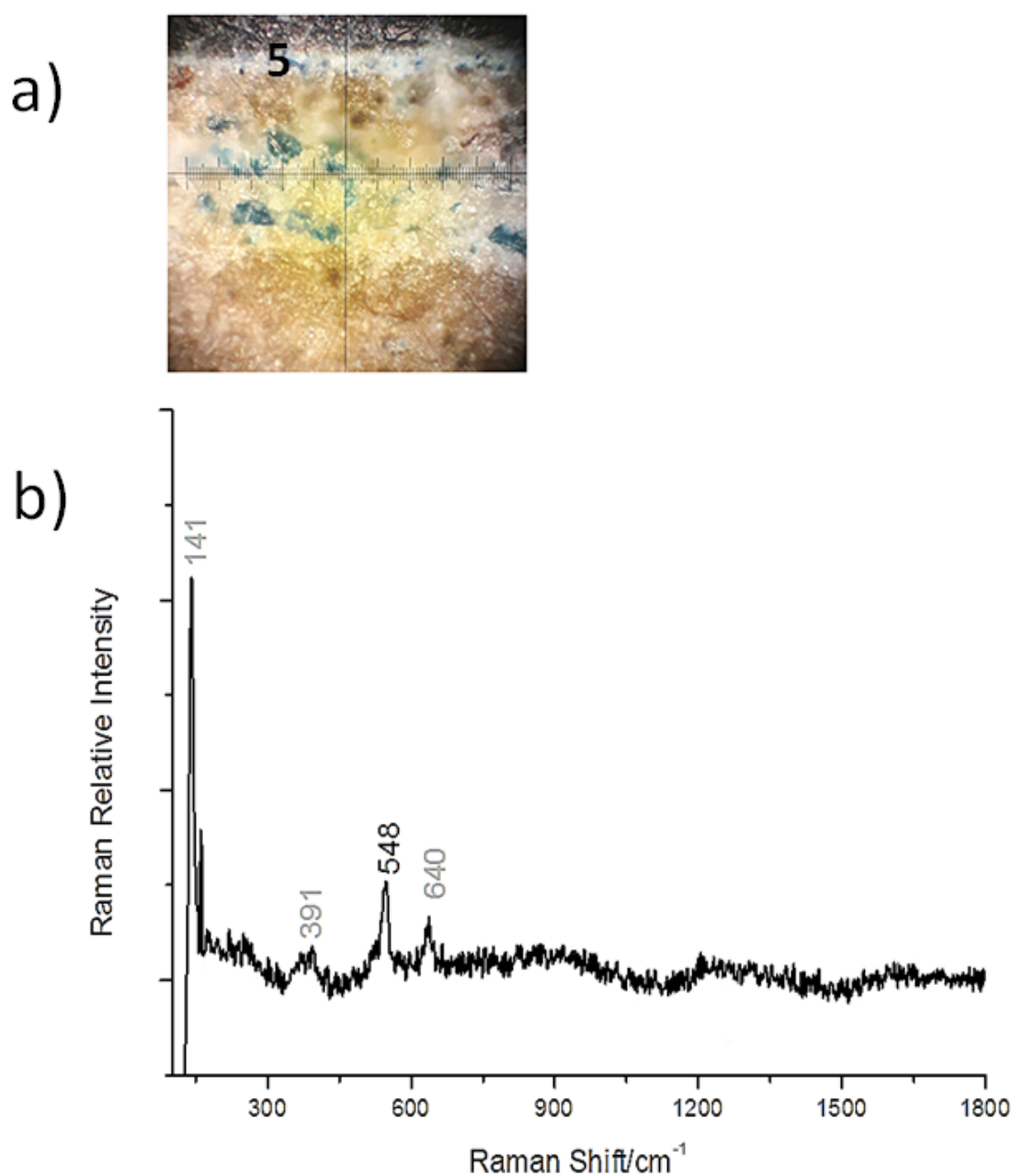


Figure 9. (a) Optical micrograph (50 \times) and (b) Raman spectrum recorded at point 5 on the 2nd paint layer of CS7, showing the spectral features of ultramarine blue.

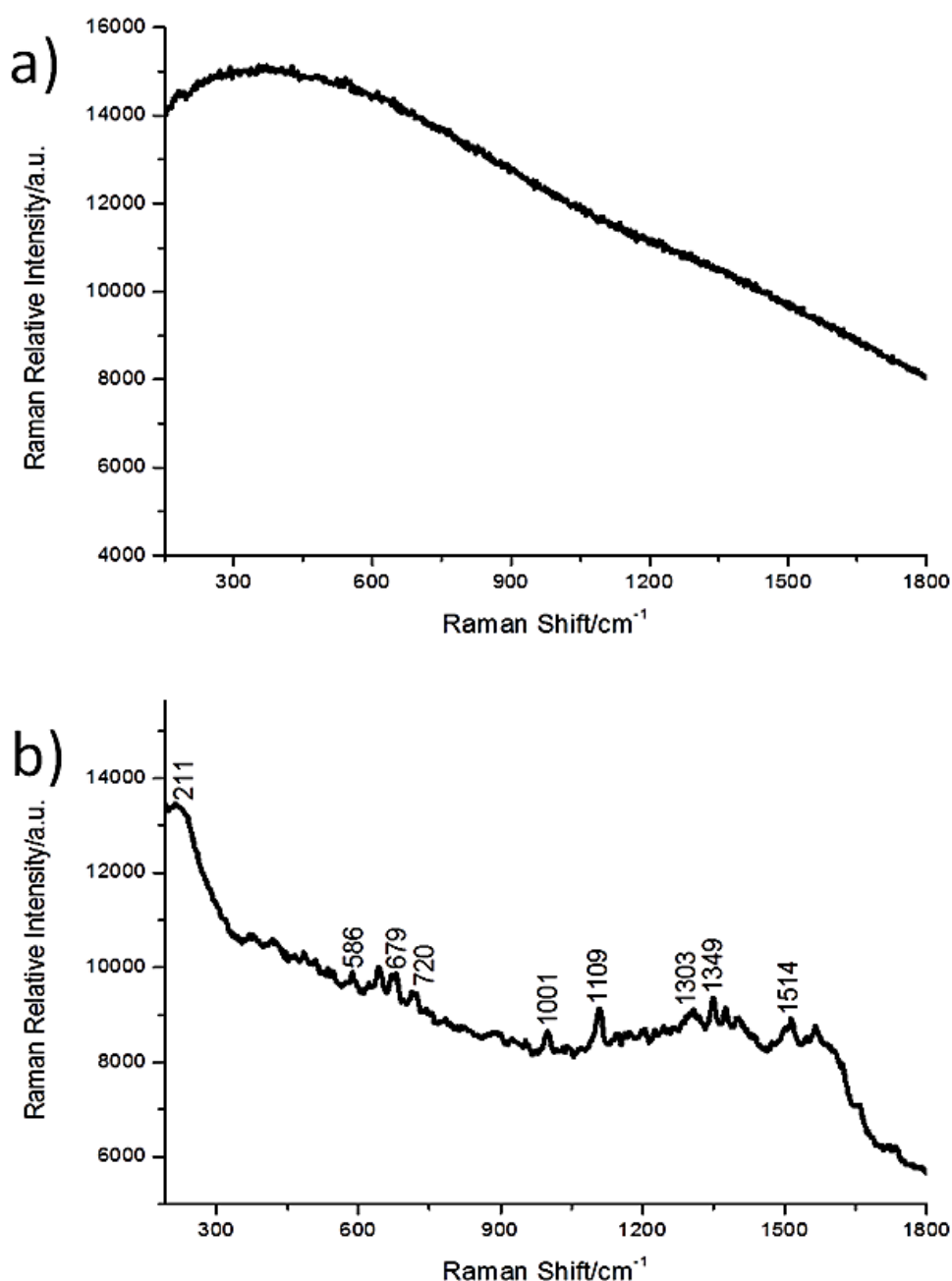


Figure 10. (a) Raman spectrum of the blue organic dye in 2nd paint layer of CS7, which resulted completely fluorescent; (b) SERS spectrum of the blue dye, recorded after AgNSs deposition, showing the spectral features of copper phthalocyanine.

4. Conclusions

The overall results obtained with this investigation on the Madonna della Misericordia of the Parma National Gallery are summarized in Table S1 in Supplementary Materials. In particular, the careful analysis of the cross section CS7 from the Madonna della Misericordia, combined with general visual and instrumental investigation on the painting, revealed at least two moments of execution. In particular, referring to the blue area from which CS7 was sampled, a probably older paint layer characterized by the presence of azurite and lead white was discerned. Over this, separated by a gypsum ground overlayer, a second layer of paint was found which contains modern components such as titanium white, copper phthalocyanine blue, and barite. These findings can indicate that the painting was realized in the 19th century and heavily remodeled during the restoration works of

the 20th century. This dating is in substantial opposition to the temporal collocation reported in the inventory of the gallery which attributed the painting to the 15th century [28]. The extensive study of this work of art led to particularly interesting results: the scientific together with the stylistic analyses enabled to achieve a more accurate and precise dating, underlining the importance of adopting a scientific approach in the field of cultural heritage.

From an analytical diagnostic viewpoint, this study demonstrates the real-world applicability and practical usefulness of AgNSs as highly effective agents to achieve SERS detection of Raman signals for identifying pigments such as copper phthalocyanine, whose fluorescence hampers their detection by means of regular Raman spectroscopy. The one-pot, easy synthesis of AgNSs, together with their easy applicability on cross-sections or other kinds of samples, make their use highly practicable as SERS enhancers for real world cultural heritage diagnostics.

Supplementary Materials: The following are available online at <http://www.mdpi.com/2571-9408/3/4/74/s1>.

Author Contributions: Conceptualization, M.S.Z., I.A., P.U.; formal analysis, M.S.Z., N.K., P.U.; investigation, M.S.Z., N.K.; methodology, M.S.Z., I.A., N.K., P.U.; project administration, I.A., P.U.; supervision, I.A. and P.U.; validation, M.S.Z., I.A., P.U.; visualization, M.S.Z., P.U.; writing—original draft preparation, M.S.Z., I.A., P.U.; writing—review and editing, M.S.Z., I.A., N.K. and P.U. All authors have read and agreed to the published version of the manuscript.

Funding: This research received no external funding.

Acknowledgments: The Monumental Complex of the Pilotta and the National Gallery of Parma, in particular, the museum director Simone Verde and Maria Cristina Quagliotti of the administrative staff are sincerely thanked for the possibility of analyzing the painting Madonna della Misericordia. Philip N. Bartlett, University of Southampton, UK, is thankfully acknowledged for providing access to Raman and SERS instrumentation and for useful suggestions for improving the quality of the manuscript. We thank Danilo Bersani, University of Parma, for useful discussion on the Raman spectra. At University Ca' Foscari of Venice, we acknowledge the assistance of Eleonora Balliana and Elisabetta Zendri for the preparation of the cross-sections and Patrizia Canton for TEM analysis.

Conflicts of Interest: The authors declare no conflict of interest.

References

1. Pinna, D.; Galeotti, M.; Mazzeo, R. Scientific examination for the investigation of paintings. In *A Handbook for Restorers*; Centro Di of Edifimi srl: Florence, Italy, 2011.
2. Zalaffi, M.S.; Karimian, N.; Ugo, P. Review—Electrochemical and SERS Sensors for Cultural Heritage Diagnostics and Conservation: Recent Advances and Prospects. *J. Electrochem. Soc.* **2020**, *167*, 037548. [CrossRef]
3. Smith, G.D.; Clark, R.J.H. Raman microscopy in archaeological science. *J. Archaeol. Sci.* **2004**, *31*, 1137–1160. [CrossRef]
4. Wiesinger, R.; Pagnin, L.; Anghelone, M.; Moretto, L.M.; Orsega, E.F.; Schreiner, M. Pigment and Binder Concentrations in Modern Paint Samples Determined by IR and Raman Spectroscopy. *Angew. Chem. Int. Ed.* **2018**, *57*, 7401–7407. [CrossRef] [PubMed]
5. Fleischmann, M.; Hendra, P.J.; McQuillan, A.J. Raman spectra of pyridine adsorbed at a silver electrode. *Chem. Phys. Lett.* **1974**, *26*, 163–166. [CrossRef]
6. Le Ru, E.C.; Blackie, E.; Meyer, M.; Etchegoin, P.G. Surface Enhanced Raman Scattering Enhancement Factors: A Comprehensive Study. *J. Phys. Chem. C* **2007**, *111*, 13794–13803. [CrossRef]
7. Jurasekova, Z.; Del Puerto, E.; Bruno, G.; García-Ramos, J.V.; Sanchez-Cortes, S.; Domingo, C. Extractionless non-hydrolysis surface-enhanced Raman spectroscopic detection of historical mordant dyes on textile fibers. *J. Raman Spectrosc.* **2010**, *41*, 1455–1461. [CrossRef]
8. Pozzi, F.; Lombardi, J.R.; Leona, M. Winsor & Newton original handbooks: A surface-enhanced Raman scattering (SERS) and Raman spectral database of dyes from modern watercolor pigments. *Heritage Sci.* **2013**, *1*, 23. [CrossRef]
9. Idone, A.; Aceto, M.; Diana, E.; Appolonia, L.; Gulmini, M. Surface-enhanced Raman scattering for the analysis of red lake pigments in painting layers mounted in cross sections. *J. Raman Spectrosc.* **2014**, *45*, 1127–1132. [CrossRef]

10. Lee, P.C.; Meisel, D. Adsorption and surface-enhanced Raman of dyes on silver and gold sols. *J. Phys. Chem.* **1982**, *86*, 3391–3395. [CrossRef]
11. Cañamares, M.V.; Garcia-Ramos, J.V.; Gómez-Varga, J.D.; Domingo, C.; Sanchez-Cortes, S. Comparative Study of the Morphology, Aggregation, Adherence to Glass, and Surface-Enhanced Raman Scattering Activity of Silver Nanoparticles Prepared by Chemical Reduction of Ag+Using Citrate and Hydroxylamine. *Langmuir* **2005**, *21*, 8546–8553. [CrossRef]
12. Guerrero-Martínez, A.; Barbosa, S.; Pastoriza-Santos, I.; Liz-Marzán, L.M. Nanostars shine bright for you. *Curr. Opin. Colloid Interface Sci.* **2011**, *16*, 118–127. [CrossRef]
13. Wang, Y.; Camargo, P.H.C.; Skrabalak, S.E.; Gu, H.; Xia, Y. A Facile, Water-Based Synthesis of Highly Branched Nanostructures of Silver. *Langmuir* **2008**, *24*, 12042–12046. [CrossRef]
14. Garcia-Leis, A.; Garcia-Ramos, J.V.; Sanchez-Cortes, S. Silver Nanostars with High SERS Performance. *J. Phys. Chem. C* **2013**, *117*, 7791–7795. [CrossRef]
15. Zalaffi, M.S.; Litti, L.; Canton, P.; Meneghetti, M.; Moretto, L.M.; Ugo, P. Preparation and characterization of Ag-nanostars@Au-nanowires hierarchical nanostructures for highly sensitive surface enhanced Raman spectroscopy. *Nano Express* **2020**, *1*, 020006. [CrossRef]
16. Kumar, P.S.; Pastoriza-Santos, I.; Rodríguez-González, B.; De Abajo, F.J.G.; Liz-Marzán, L.M. High-yield synthesis and optical response of gold nanostars. *Nanotechnology* **2008**, *19*, 015606. [CrossRef]
17. Litti, L.; Reguera, J.; De Abajo, F.J.G.; Meneghetti, M.; Liz-Marzán, L.M. Manipulating chemistry through nanoparticle morphology. *Nanoscale Horiz.* **2020**, *5*, 102–108. [CrossRef]
18. Rodríguez-Lorenzo, L.; Álvarez-Puebla, R.A.; Pastoriza-Santos, I.; Mazzucco, S.; Stéphan, O.; Kociak, M.; Liz-Marzán, L.M.; De Abajo, F.J.G. Zeptomol Detection Through Controlled Ultrasensitive Surface-Enhanced Raman Scattering. *J. Am. Chem. Soc.* **2009**, *131*, 4616–4618. [CrossRef]
19. Pastoriza-Santos, I.; Liz-Marzán, L.M. N,N-Dimethylformamide as a Reaction Medium for Metal Nanoparticle Synthesis. *Adv. Funct. Mater.* **2009**, *19*, 679–688. [CrossRef]
20. Yuan, H.; Khoury, C.G.; Hwang, H.; Wilson, C.M.; A Grant, G.; Vo-Dinh, T. Gold nanostars: Surfactant-free synthesis, 3D modelling, and two-photon photoluminescence imaging. *Nanotechnology* **2012**, *23*, 075102. [CrossRef]
21. Yamamoto, M.; Kashiwagi, Y.; Sakata, T.; Mori, H.; Nakamoto, M. Synthesis and Morphology of Star-Shaped Gold Nanoplates Protected by Poly(N-vinyl-2-pyrrolidone). *Chem. Mater.* **2005**, *17*, 5391–5393. [CrossRef]
22. Bakr, O.M.; Wunsch, B.H.; Stellacci, F. High-Yield Synthesis of Multi-Branched Urchin-Like Gold Nanoparticles. *Chem. Mater.* **2006**, *18*, 3297–3301. [CrossRef]
23. Zhou, M.; Chen, S.; Zhao, S. Preparation of Branched Gold Nanocrystals by an Electrochemical Method. *Chem. Lett.* **2006**, *35*, 332–333. [CrossRef]
24. Li, Z.; Li, W.; Camargo, P.H.C.; Xia, Y. Facile Synthesis of Branched Au Nanostructures by Templating Against a Self-Destructive Lattice of Magnetic Fe Nanoparticles. *Angew. Chem. Int. Ed.* **2008**, *47*, 9653–9656. [CrossRef] [PubMed]
25. Lu, L.; Kobayashi, A.; Tawa, K.; Ozaki, Y. Silver Nanoplates with Special Shapes: Controlled Synthesis and Their Surface Plasmon Resonance and Surface-Enhanced Raman Scattering Properties. *Chem. Mater.* **2006**, *18*, 4894–4901. [CrossRef]
26. Zalaffi, M.S. Metal Nanostructures Decorated with Silver Nanostars: A Novel Highly Efficient Substrate for Dyes and Pigments Detection. Ph.D. Thesis, Università degli Studi di Trieste and Università Ca' Foscari, Venezia, Italy, 2019.
27. da Campagnola, S. L'arte nella chiesa e nel convento di s. Maria Maddalena e dell'Immacolata (già S. Caterina). In *I Cappuccini a Parma: Quattro secoli di vita*; da Mareto, F., Ed.; Istitografico tiberino: Rome, Italy, 1961.
28. Ricci, C. *La Regia. Galleria di Parma*; Batteil: Parma, Italy, 1896.
29. Fornari-Schianchi, L.; Riccomini, E. *Galleria Nazionale di Parma, Catalogo delle opere dall'antico al Cinquecento*; Ricci, F.M., Ed.; Franco Maria Ri: Milan, Italy, 1997.
30. Laver, M. Titanium dioxide whites in Artists' Pigments. In *A Handbook of Their History and Characteristics*, 3rd ed.; Fitzhugh, E.W., Ed.; National Gallery of Art: Washington, DC, USA, 1997; Volume 3.
31. Feller, R.L. Barium Sulphate—Natural and Synthetic in Artists' Pigments. In *A Handbook of Their History and Characteristics*; Feller, R.L., Ed.; Cambridge University Press: Cambridge, UK, 1986; Volume 1, pp. 255–283.
32. Newman, R. Chromium oxide greens in "Artists" Pigments. In *A Handbook of Their History and Characteristics*, 3rd ed.; Fitzhugh, E.W., Ed.; National Gallery of Art: Washington, DC, USA, 1997; Volume 3.

33. Burgio, L.; Clark, R.J.H. Library of FT-Raman spectra of pigments, minerals, pigment media and varnishes, and supplement to existing library of Raman spectra of pigments with visible excitation. *Spectrochim. Acta Part A Mol. Biomol. Spectrosc.* **2001**, *57*, 1491–1521. [CrossRef]
34. Caggiani, M.; Cosentino, A.; Mangone, A. Pigments Checker version 3.0, a handy set for conservation scientists: A free online Raman spectra database. *Microchem. J.* **2016**, *129*, 123–132. [CrossRef]
35. Plesters, J. Ultramarine Blue, Natural and Artificial in Artists' Pigments. In *A Handbook of their History and Characteristics*; Feller, R.L., Ed.; Cambridge University Press: Cambridge, UK, 1986; Volume 1, pp. 37–61.
36. Available online: www.maimeri.it (accessed on 15 July 2020).
37. Scherrer, N.C.; Stefan, Z.; Françoise, D.; Annette, F.; Renate, K. Synthetic organic pigments of the 20th and 21st century relevant to artist's paints: Raman spectra reference collection. *Spectrochim. Acta Part A Mol. Biomol. Spectrosc.* **2009**, *73*, 505–524. [CrossRef] [PubMed]
38. Defeyt, C.; Strivay, D. PB15 as 20th and 21st artists' pigments: Conservation concerns. *e-PS* **2014**, *11*, 6–14.
39. Harroun, S.G.; Bergman, J.; Jablonski, E.; Brosseau, C.L. Surface-enhanced Raman spectroscopy analysis of house paint and wallpaper samples from an 18th century historic property. *Analyst* **2011**, *136*, 3453. [CrossRef]
40. Dahlen, M.A. The Phthalocyanines a New Class of Synthetic Pigments and Dyes. *Ind. Eng. Chem.* **1939**, *31*, 839–847. [CrossRef]
41. Cañamares, M.; Garcia-Ramos, J.; Domingo, C.; Sanchez-Cortes, S. Surface-enhanced Raman scattering study of the anthraquinone red pigment carminic acid. *Vib. Spectrosc.* **2006**, *40*, 161–167. [CrossRef]

Publisher's Note: MDPI stays neutral with regard to jurisdictional claims in published maps and institutional affiliations.



© 2020 by the authors. Licensee MDPI, Basel, Switzerland. This article is an open access article distributed under the terms and conditions of the Creative Commons Attribution (CC BY) license (<http://creativecommons.org/licenses/by/4.0/>).

Article

Exploring the Dzi Bead with Synchrotron Light: XRD, XRF Imaging and μ -XANES Analysis

Averie Reinhardt ¹, Renfei Feng ² , Qunfeng Xiao ², Yongfeng Hu ² and Tsun-Kong Sham ^{1,*} 

¹ Department of Chemistry, Western University, 1151 Richmond Street, London, ON N6A 5B7, Canada; areinha2@uwo.ca

² Canadian Light Source, 44 Innovation Boulevard, Saskatoon, SK S7N 2V3, Canada;

Renfei.Feng@lightsource.ca (R.F.); Qunfeng.Xiao@lightsource.ca (Q.X.); Yongfeng.hu@lightsource.ca (Y.H.)

* Correspondence: tsham@uwo.ca

Received: 16 August 2020; Accepted: 10 September 2020; Published: 15 September 2020

Abstract: The origin of Dzi beads, also called “tian zhu”, has always been a mystery. These beads come in a variety of patterns, shapes and sizes. They have cultural and heritage significance in Tibet and areas surrounding the Himalayas. The most recognized beads are those with the “eye” pattern. They are said to ward off evil spirits. Due to their reputation, the demand for Dzi beads has increased in Asia. Herein, we report a study of a Dzi bead with a three-eye pattern using X-ray diffraction (XRD), X-ray fluorescence (XRF), X-ray absorption near edge structure (XANES) and imaging techniques. This is a novel area for Dzi bead research using X-rays from a synchrotron light source to determine the chemical composition of the bead, if the pattern is natural or man-made or if the bead is genuine or a replica. These techniques revealed the bead to be composed of agate (silicon dioxide). An interesting feature on the bead’s surface was the etched rings, which were observed to contain regular copper hot spots on their circumference. Our results suggest that the Dzi bead was genuine and started out as an earth-formed agate, with the pattern crafted.

Keywords: Dzi bead; agate; X-ray diffraction; X-ray fluorescence; X-ray absorption near edge structure; X-ray imaging

1. Introduction

The origin of Tibetan Dzi beads, also known as “tian zhu” (heaven’s pearl) or commonly accepted as Tibetan beads, has always been a mystery. They first appeared between 2000 and 1000 BC in countries surrounding the Himalayas. Authentic Dzi beads are found primarily in Tibet, according to Bolin [1]. There are many legends about how these beads came to be. This is because the Tibetan people believe the beads are of supernatural origin [2]. One story tells of semigods owning them as ornaments. It is said that the beads would be thrown away if they became imperfect in any way. This story explains why Dzi beads are never found in perfect condition [1,2]. Another story is perhaps more well-known and widespread, describing the Dzi beads to be insects. The story tells of a man in the mountains who supposedly threw his hat over such an insect, petrifying it. This petrified insect is said to have been a Dzi bead [1,2]. There are a multitude of other stories that have been told, including the Dzi bead being found in the horns of slaughtered animals as well as in dung [1–3]. The people of Tibet hold these beads in high regard and consider them heritage gems; they are reluctant to sell them for low sums, especially to those in the Western world. Therefore, there has been very little scientific research conducted on them. It is generally accepted, however, that Dzi beads are made from agate, a form of chalcedony quartz with a chemical composition of SiO₂ [1–3].

It is said that the owner or wearer of a Dzi bead is protected from catastrophe. The Dzi bead supposedly wards off evil spirits that might have ill effects on the wearer [1,2]. While being worn,

if the bead breaks or chips, it is thought to have served its purpose and has absorbed the energy of a catastrophic event that was intended for the wearer. Thus, the effects of the bead are rendered useless, as it is no longer regarded as “pure” [1,2]. The only time a Dzi is deliberately broken is for medicinal purposes. Doctors in Tibet use powder from the beads mixed with herbs to treat ailments such as epilepsy [1,2].

In Ebbinghouse and Winsten’s article, they mention three techniques that have been recorded for creating Dzi beads [2]. The first technique for creating a white pattern on a natural stone background involves the painting of an alkali substance onto the surface of the bead and then firing the whole bead [3–5]. The area that has been painted then turns white, and this continues through the surface into the Dzi bead interior [6,7]. The second technique creates a black design on a whitened background. The whitening is done with the aforementioned technique on the entire bead, and then the dark pattern is painted with a chemical such as copper nitrate [8]. Using similar techniques, the third type of Dzi is a black design on a natural stone background [2–8]. It should also be noted that drill bits made of reed in the old days and then copper were used to drill holes in the crafting process. Bolin’s book (p. 29) also describes similar treatments in the craft, including darkening with plant sugar and heat, beaching and white line etching with natron (a naturally occurring mixture of sodium carbonate decahydrate, $\text{Na}_2\text{CO}_3 \cdot 10\text{H}_2\text{O}$, and sodium bicarbonate, NaHCO_3 , along with small amounts of sodium chloride and sodium sulfate) and protecting the desired areas with grease, clay, etc. [1].

The Tibetan people only regard certain Dzi beads as real or “pure”. Dzi beads come in a varied array of patterns, shapes and sizes. A set of patterns that are universally recognized as “pure” are the “eye” patterns, as shown in Figure 1a,b together with representative fakes (Figure 1c) and the three-eye specimen we used in this investigation, Figure 1d,e. Every pattern holds a different meaning and benefit to the wearer [1–3]. The most highly coveted Dzi bead is the nine-eye bead. This bead symbolizes the nine planets, holds the activity of the entire universe and possesses the wisdom of humanity [1,2], and it is said to assist the owner in gaining wealth, good health, success, power, compassion and glory [1–8].

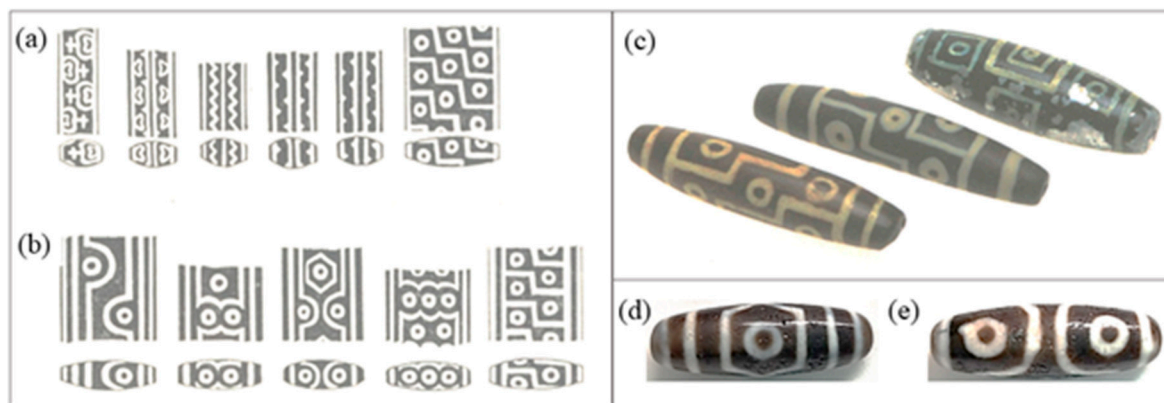


Figure 1. Dzi bead patterns. (a) The most precious Dzi beads. (b) Beads that are of lesser value than (a) but are most recognized and worn as traditional ornaments [2]. (c) Dzi bead imitations. Left to right: plastic with metal core, polymer clay and painted aluminum [4]. (d,e) Photograph of the Dzi bead used in this study, showing a one-eye pattern on one side and a two-eye pattern on the opposite side. The middle column in (b) depicts what the three-eye bead looks like when unfolded.

Tibetans have created criteria for what makes a Dzi bead valuable. As mentioned, the bead must have a desirable pattern that is considered “pure”. A Dzi bead must possess a round cross-sectional shape and not appear thin [1,2]. As noted above, the Dzi bead must not be broken or chipped, as this is said to reflect the fact that it has already served its purpose. When held up to the sun, the bead should be translucent or reveal any internal flaws with the pattern, although there are exceptions [1,2]. Tibetans know how to identify a genuine Dzi bead from a fake; however, imitations have been created because these beads are so valuable.

The demand for Dzi beads in Asian regions has increased and spurred the production of replicas. Some replicas have such minute details that they must be observed more closely under a microscope or cut open to reveal if they are fake. In most cases, it has been identified that a replica weighs less than the original [4]. Other replicas are fitted with a metal center to imitate the weight of the real beads. Dzi bead replicas are usually made of plastic, glass or a light metal such as aluminum; examples are shown in Figure 1c [4].

The objective of this work is to investigate the pattern, the elemental and chemical composition as well as the structure of a three-eye Dzi bead using conventional laboratory techniques, such as optical microscopy and scanning electron microscopy (SEM), and advanced X-ray techniques from a synchrotron source. X-ray diffraction (XRD) reveals the crystal structure and, hence, mineral formation of the bead; X-ray fluorescence (XRF) reveals its elemental composition; and X-ray absorption near edge structure (XANES) reveals the local structure of a selected element of interest. Using a micro-X-ray beam, we can conduct microscopy and microanalysis of the different patterns of the specimen. We have gained considerable experience over the years in the research and development of these techniques [9] and are encouraged by our recent success in retrieving high-resolution images from badly tarnished daguerreotypes [10–12], the first public photographs in human history. The applications of X-rays from synchrotrons in art and archaeology have also been reviewed recently [13]. Based on these techniques, we will attempt to investigate if the specimen is genuine or fake, if the pattern is natural or man-made and if there is any evidence for the crafting methods we noted above, as described by Bolin and Ebbinghouse and Winsten [1,2]. We show below that we can provide some positive answers for these questions in this preliminary study using synchrotron radiation.

2. Materials and Methods

2.1. The Three-Eye Dzi Bead

The three-eye bead investigated in this work was purchased in a jewelry store in Chengdu, Sichuan, China, and it came with an authenticity certificate (Figure S1). The bead was sliced in the middle, as shown in Figure S2. Slicing was carried out in the Department of Earth Sciences at Western University. A MK Diamond brand tile saw with a diamond embedded blade was used to slice the Dzi bead into several pieces. The bead was cut open to reveal the interior for further imaging. It should be noted that the middle piece was chipped, which is not unexpected from a hard stone like agate. A small piece was ground to powder. Both the slices and the powder specimens were used for XRD measurements.

2.2. Optical and Scanning Electron Microscope, Energy-Dispersive X-ray Spectroscopy

The optical microscope used was a Mitutoyo WF with a ZEISS Axiocam 1Cc5 color Charge Coupling Device (CCD) camera. The magnifications available were 5×, 10×, 20× and 100×. The Dzi bead was affixed to the glass of the stage with a sticky carbon tab to ensure its stability. The scanning electron microscope was a LEO/ZEISS 1540XB instrument. Both the optical and SEM measurements were made in Western's Nanofabrication Facility. Images were collected from a piece of the Dzi bead, specifically on the outer surface of the bead. Special attention was paid to the etched rings on the surface. The Energy Dispersive X-ray (EDX) detector model was the N-Max 50 by Oxford Instruments. This detector was coupled to the SEM, and the emitted fluorescent X-rays from the sample surface were collected to perform a complete elemental analysis on specific sections on the Dzi bead surface.

2.3. XRD

XRD was used to characterize the surface of the light and dark regions; the edge of a slice and a powder sample of the Dzi bead were investigated to determine its structure. Powder XRD was conducted with a Rigaku Ru200BVH diffractometer equipped with a Co K_{α} ($\lambda = 1.8 \text{ \AA}$) X-ray source. The diffraction patterns were measured over a 2θ range of 2° to 82° . The diffraction patterns of quartz (SiO_2), graphite

and copper oxide, CuO, were used as references to compare with the crystal structure of the Dzi bead. The reason for a graphite and copper oxide reference will become clear in the discussion below. XRD of the Dzi bead surface and the edge of a slice was conducted using the VESPERS (Very Sensitive Elemental and Structural Probe Employing Radiation from a Synchrotron) beamline of the Canadian Light Source [14]. It is a hard X-ray beamline equipped with optical elements to deliver a polychromatic beam (pink beam) and multibandpass monochromatic beams (using a double-multilayer and double-crystal monochromator with Si(111) crystals, respectively) as well as microbeam (using a Kirkpatrick-Baez (KB) mirror) capabilities for XRD, XRF and imaging [14,15]. Using VESPERS (Very Sensitive Elemental and Structural Probe Employing Radiation from a Synchrotron), XRD was performed with monochromatic X-rays at 8 keV (1.55 \AA) ~ Cu K_{α} and 12 keV ($\lambda = 1.03 \text{ \AA}$), and the diffracted beam was detected by a Pilatus 1M pixel area detector. The diffraction rings were converted to intensity versus 2θ plots for easy comparison with the references. It should be noted that monochromatic X-rays from the synchrotron are tunable in energy, of a higher energy resolution and at least 10^4 times brighter than those of laboratory sources, making the technique more desirable for faster acquisition and higher-quality data for Rietveld refinement, and the microbeam ($\sim 5 \text{ \mu m}$) allows for small area diffraction and imaging.

2.4. X-Ray Microbeam Analysis: XRF and XANES

XRF and imaging experiments were conducted using the Very Sensitive Elemental and Structural Probe Employing Radiation from a Synchrotron (VESPERS) [14,15] and the Soft X-ray Microanalysis Beamline (Soft X-ray Microanalysis Beamline (SXRMB)) [16,17] beamline of the Canadian Light Source. The former produces monochromatic hard X-rays from 5 to 30 keV, and the latter delivers tender X-rays from 1.7 to 10 keV. With VESPERS, an X-ray energy of 10 keV was selected for XRF excitation, which is above the Cu K-edge (edge: 8979 eV; K_{α_1} : 8048 eV), an element of interest in our pursuit, providing a good cross-section and, hence, fluorescence yield from other first-row transition elements at the K-edge, such as Fe (edge: 7112 eV; K_{α_1} : 6404 eV). The SXRMB beamline is equipped with a double-crystal monochromator with dual crystal sets of InSb(111) and Si(111) crystals. The former is used for Si K-edge studies with a slightly better photon throughput. It is also equipped with a tender X-ray microprobe endstation that is capable of tracking elements such as Si (K-edge: 1840 eV; K_{α_1} at 1740 eV), K (K-edge: 3608 eV; K_{α_1} : 3314 eV) and all the way up to Fe (K-edge: 7112 eV; K_{α_1} : 6404 eV). The micro-X-ray beam was scanned over the sample (fixed beam position with sample moving) with a pixel size of $\sim 5 \times 5$ and $\sim 10 \times 10$ microns for VESPERS and SXRMB, respectively, while the intensity of the relevant fluorescent X-ray was tracked by silicon drift detectors. Elemental maps were produced with the normalized fluorescence yield of the element of interest and analyzed with standard imaging software.

XANES tracks the modulation of the X-ray absorption coefficient of an element above an absorption edge. The modulation, often appearing as oscillations arising from the interference of the forward- and backscattered photoelectron by surrounding atoms, contains all the information about the local structure of the absorbing atom (the absorption coefficient of a free atom is monotonic), such as the identity of the neighboring atom, its interatomic distance from the absorbing atom and its local dynamics (root mean displacement from the equilibrium distance). The simplest but most powerful use of XANES is its fingerprinting features since different local environments will exhibit different yet specific features in XANES. Thus, microbeam XANES provides additional information beyond XRF in that it provides not only elemental information but also chemical information. The power of these capabilities in the X-ray microanalysis of the Dzi bead specimen will become apparent below.

3. Results and Discussion

3.1. Optical and SEM Observations

The optical and SEM images are shown in Figure 2 together with the EDX analysis. A close inspection of the patterns revealed that in addition to the familiar eye and dark and light stripes, there were etched rings, as is apparent from Figure 1. Observation under the optical microscope did not

reveal any clear boundaries between the white ring and the dark background. Figure 2a displays the photographs of the one-eye and two-eye side of the bead together with the optical microscopy, and Figure 2b displays the SEM images showing a representative etched ring. These rings were all over the surface. In addition, from the slice in Figure S2, one could see the white region extended considerably into the bead; this confirms the report of Ebbinghouse and Winsten on the crafting of the white patterns that the white region extends significantly below the surface [2].

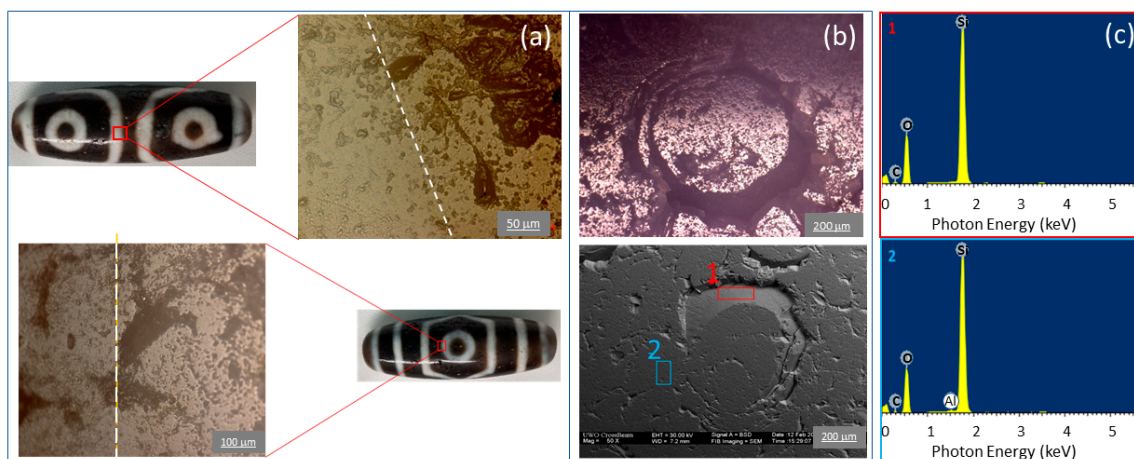


Figure 2. (a) The approximate boundary between the light and dark areas of the bead's pattern (depicted with a white dashed line), as observed using an optical microscope. (b) Optical (top) and scanning electron microscopy (SEM) (bottom) image of the etched rings that are all over the surface of the bead in both the light and dark regions and across the boundary. (c) EDX from two specified areas denoted 1 and 2 in the SEM (Electron High Tension (EHT): 30 kV). Dominant components are Si and O, as expected for agate.

One can also see from Figure 2b that the etched rings were about 1 mm in diameter and clearly exhibited cracks and crevices, as can be seen in both the optical and SEM images. EDX recorded in the selected area marked with blue and red rectangles identified Si and O as the dominant elements, with a tiny amount of Al in the flat region in Figure 2c. This finding immediately confirms the elemental composition of the Dzi bead was consistent with that of agate (quartz).

3.2. XRD

Figure 3 shows a comparison of the lab and synchrotron XRD recorded with (a) a powder sample of the Dzi bead and (b) the edge of a slice of the Dzi bead, respectively. The XRD using VESPERS was collected with a microbeam and an area-sensitive detector, yielding diffraction rings that were then converted to the 2θ display (Figure 1b and Figure S3) with the same scale as Co $K\alpha$ for ease of comparison. From Figure 3a, one clearly sees that the Dzi bead powder exhibited a pattern characteristic of α -quartz (vertical lines), supporting the EDX results that the materials making up the Dzi bead were SiO_2 quartz. There was, however, a small but noticeable peak marked by the arrow. This conspicuous peak was not seen in the synchrotron data (Figure 3b), where a comparison was also made with the XRD of graphite and CuO. The latter had no match, e.g., CuO had strong peaks at 2θ between 30° and 40° (not shown), strongly indicating that this peak likely came from graphite. It should be noted that both graphite and CuO appear black.

From the above analysis, the Dzi bead was made of SiO_2 (quartz) and appeared to be genuine. A graphite signature was detected in the powder sample but not from microdiffraction at the edge of a slice; presumably, the latter probed a much smaller area than the powder sample examined with a large beam and a relatively macroscopic sample, although possible carbon contamination during the grinding process cannot be ruled out.

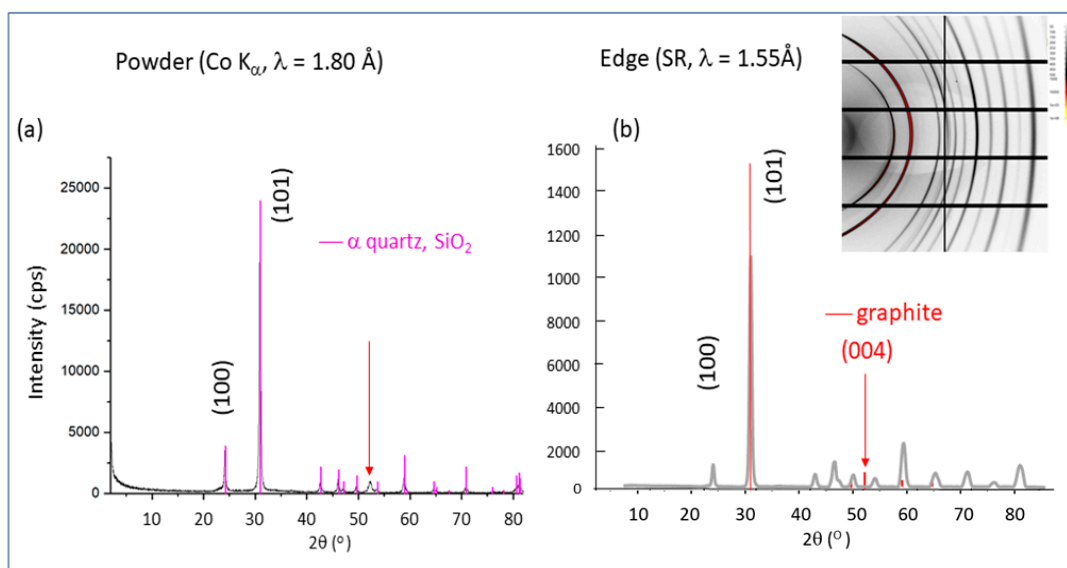


Figure 3. (a) Representative X-ray diffraction (XRD) of DZI powder ground from a broken piece recorded using lab X-rays from a Co anode ($\lambda = 1.8 \text{ \AA}$). The corresponding XRD pattern of quartz (PDF 46-1045) is also shown in purple vertical lines. A conspicuous peak not belonging to quartz is marked with an arrow, which is consistent with graphite (004) diffraction. (b) XRD from the edge of a slice of DZI bead obtained with 8 keV X-rays using the VESPERS beamline converted to the same 2θ scale as Co $K\alpha$ for ease of comparison. The insert shows the diffraction rings from the Pilatus detector, which has been converted to the intensity- 2θ pattern as shown. The XRD pattern of graphite (PDF 41-1487) is also shown as vertical red lines. The conspicuous peak seen in the powder sample is absent.

3.3. XRF, Imaging and Micro-XANES Analysis

Figure 4 shows the XRF map of elements in a region of interest covering both dark and light areas. XRF tracks the specific X-ray emissions from elements, e.g., Cu $K\alpha$ X-ray emissions arise from the radiative de-excitation upon the removal of a 1s electron from a Cu atom (2p electron filling a 1s core hole, emitting an X-ray photon). While XRF can be excited by any high-energy radiation—most commonly electrons, as in SEM, EDX and X-rays—a synchrotron X-ray has the advantage over EDX using SEM in that, in addition to being many orders of magnitude brighter than laboratory X-rays, one can tune the excitation energy to just above an absorption edge of interest to enhance absorption and, hence, the intensity of the fluorescence or, under favorable conditions, to avoid an unwanted fluorescence signal by tuning the X-ray to below the edge of an unwanted element.

Let us first discuss the XRF results from VESPERS, a hard X-ray beamline where we used 12 keV X-rays, which will be able to excite Ca and all first-row transition elements, yielding characteristic $K\alpha$ and $K\beta$ X-rays; the $K\alpha$ was used to track elements of interest.

From Figure 4a,b, we can see the etched rings covering the surface regardless of the dark and light regions. The scan covered an area of $\sim 1.1 \times 1.1 \text{ mm}$, as marked by the red square. It began in a dark region and ended in a light region, covering ~ 50 – 50 of both the light and dark region. From Figure 4c, it is apparent that the most interesting feature was the hot spots seen in the element maps of Ca, Fe and Cu, especially Cu. The location of these rings had no correlation with the dark and light regions of the surface. Let us now concentrate on the Cu map. The spots were $\sim 20 \text{ }\mu\text{m}$ in diameter and aligned regularly along the circumference of the ring, with a spacing of $\sim 100 \text{ }\mu\text{m}$. The maps of Ca, Fe and Cu could be directly overlaid on each other. To determine the chemical composition of the Cu, we conducted Cu K-edge XANES measurements with a microbeam at the hot spots. Figure 5a,b shows a magnified image of this region, which reveals that the etched ring spanned both the light and dark regions. Figure 5c displays the micro-XANES of a hot spot ($5 \times 5 \text{ }\mu\text{m}$) recorded in the Cu $K\alpha$

fluorescence yield compared with the XANES of the reference compounds, Cu metal, Cu₂O and CuO, representing the 0, +1 and +2 oxidation states of Cu. It should be noted that despite low count rates in micro-XANES, the signal we obtained (eight scans) required about an hour, and it already clearly confirms that the hot spot Cu was from CuO. The discovery of CuO led us to compare the XRD data with those of CuO XRD patterns, and there was no sign of any CuO peaks seen in the bead's data, as noted in the XRD section above. This indicates that the amount of CuO was either amorphous or very small and not detectable in the XRD.

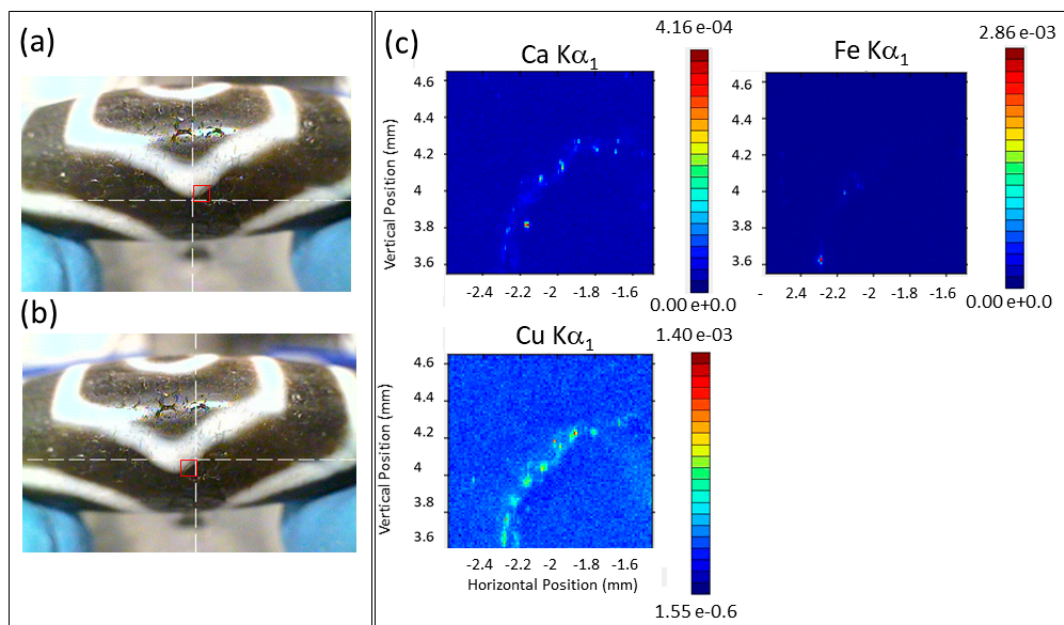


Figure 4. (a,b) show the starting and ending point of the scan (crosshairs), respectively, of the region marked with a square. (c) X-ray fluorescence (XRF) maps of several elements, Ca, Fe and Cu, are shown (XRF data are stored in a Multichannel Analyzer (MCA); counts within an energy window characteristic of the element are tracked and color-coded). These maps show hot spots on the circumference of the etched ring, most apparent in the case of Cu. The size of the hot spot is $\sim 20 \mu\text{m}$, with $\sim 100 \mu\text{m}$ spacing along the circumference.

While the experiment using VESPERS provided fruitful results, its energy was not suitable to track SiO₂, the major component of agate based on which Dzi beads are made and crafted. We next conducted measurements with the SXRMB beamline using its tender X-ray microprobe endstation. SXRMB is designed for tender X-ray (1.7–5 keV) investigations, with accessible photon energy extending to 10 keV [16,17].

The microprobe provides a beam size of $\sim 11 \times 11 \mu\text{m}$ across this energy range with KB mirror focusing [17]. To investigate the Si K-edge, we used InSb(111) crystals in the double-crystal monochromator. XRF, imaging and micro-XANES were all conducted in a vacuum chamber; a Si drift detector was used to track the fluorescent X-rays. Figure 6a shows the optical image of the area of interest. Figure 6b displays the XRF maps excited at a photon energy of 7130 eV, just above the Fe K-edge, and selected regions of interest (ROI), marked with color-coded boxes. Figure 6c–e is the XRF maps of Si, K, Ca and Fe of selected ROI, respectively. While the etched rings were apparent, instead of looking more like holes in the Cu map, the Si in Figure 6a shows the optical image from the video camera; it again shows that the etched rings were all over the surface. The boxes define the area where XRF maps of relevant elements were collected, as shown in Figure 6b, from Si, K, Ca and Fe $K_{\alpha 1}$ emissions. It can be clearly seen that the rings contained extruding Si materials, while other elements appeared to be less defined or depleted in the case of K, which tracked Si well in the ring circumference. It was desirable to see if the Si map was correlated with the Cu image obtained using VESPERS (Figure 5). While Cu mapping using SXRMB was difficult due to low flux at the Cu K-edge, we were

able to track the Cu distribution while tracking Si and other element maps at 7130 eV by observing the Cu K_{α} produced by second-order radiation (14260 eV). The results are shown in Figure S4 for ROI displayed in Figure 6d; one can see that despite the weak signal, there was a good correlation between Cu and Si.

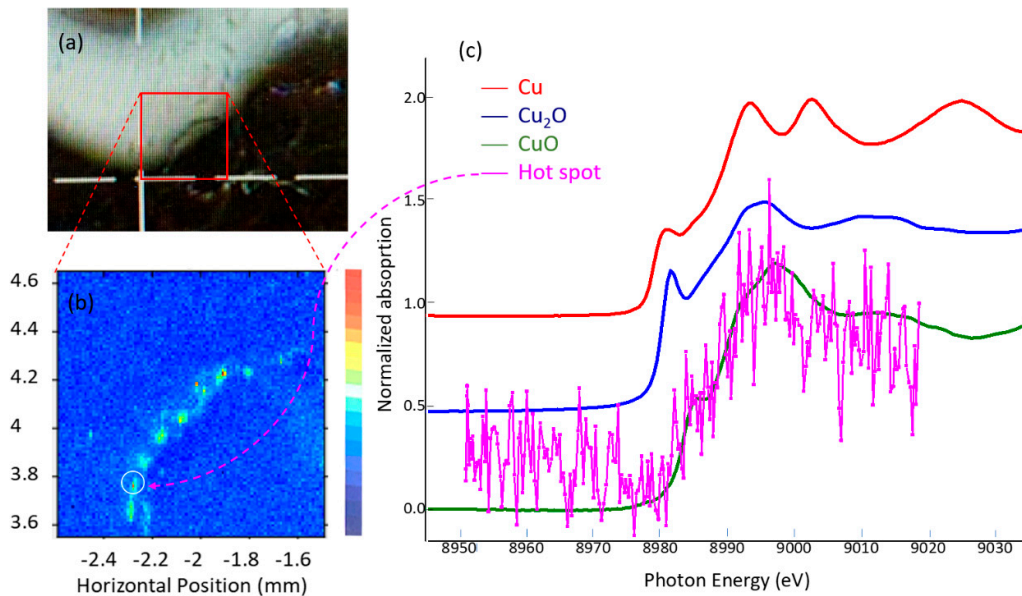


Figure 5. (a) Optical image of the magnified region of the etched ring inside the region of the XRF map. (b) XRF map from Cu showing the hot spots and the circled hot spot where micro-X-ray absorption near edge structure (XANES) has been obtained. (c) Cu K-edge micro-XANES from a hot spot circled in (b), obtained with a microbeam ($5 \times 5 \mu\text{m}$) together with the references, Cu metal, Cu_2O and CuO .

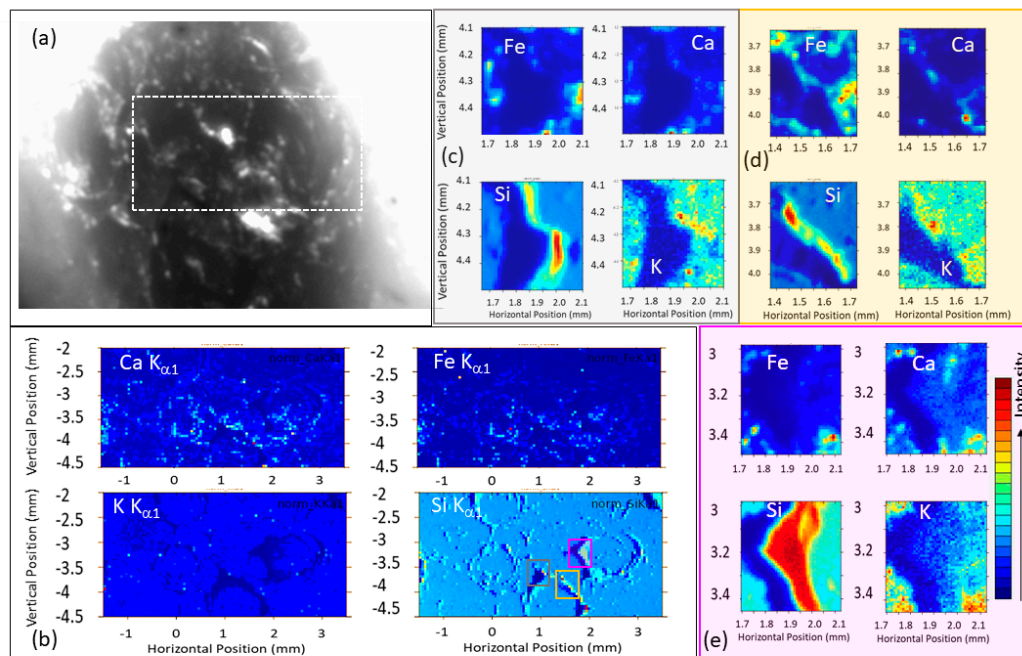


Figure 6. (a) Optical image of the Dzi bead surface; the rectangle encloses the region of the XRF maps shown in (b). (b) XRF map from Ca, K, Si and Fe as noted; the color-coded boxes in the Si map define the regions of interest (ROI) displayed in (c–e) with the same color code, where all four elements are tracked; the color code is also shown.

Figure 7 displays the Si K-edge micro-XANES of four spots from hot to cold. We can see that the XANES for all the spots was nearly identical except for spot 2, which was at the edge of the crack and

showed a slight broadening of the resonances, indicating some disorder. They were characteristic of the XANES of quartz (inset), with the white line (spike at the edge jump) at ~ 1848 eV, arising from the Si $1s$ to t_2 transition in the tetrahedral surrounding of Si in quartz. We have also conducted micro-XANES in different ROIs depicted in Figure 6c,d and found similar results (not shown) with no irregularities.

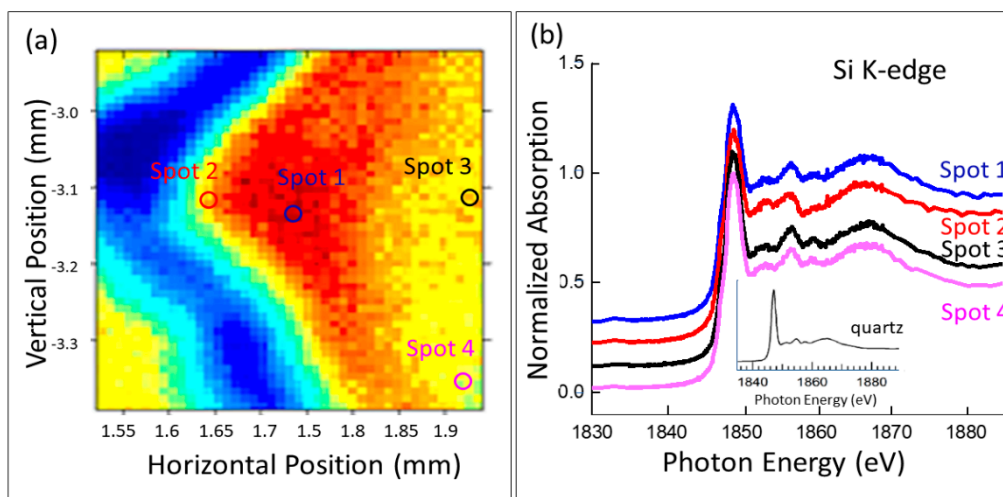


Figure 7. (a) Si map of a ROI of the Dzi bead sample, as shown in Figure 6e, where four spots (single pixel of $11 \times 11 \mu\text{m}$) were selected for micro-XANES analysis as marked. Spot 1 is the hot spot, spot 4 is the cold spot, spot 2 is at the edge of a crack and spot 3 is with moderate intensity. (b) Si K-edge XANES of selected spots. The spectral features are unmistakably characteristic of quartz SiO_2 (inset).

4. Discussion

We have presented and analyzed all data from XRD, XRF imaging and micro-XANES of selected regions of the Dzi bead. We now attempt to understand what these results mean in connection with the questions we set out to explore: (1) what is this three-eye Dzi bead made of, (2) is it genuine or fake and (3) how was the crafting done?

We begin with the first question. Based on the XRD, XRF mapping and XANES, there is absolutely no doubt that this sample was made of SiO_2 (quartz) consistent with an agate origin. For the second question, since it is generally agreed by Dzi bead collectors and traders that Dzi beads are made of agate, our observations clearly show that it was made of SiO_2 (quartz), which eliminates all the fake possibilities illustrated in Figure 2c (plastic with metal core, polymer clay and painted aluminum).

The third question is perhaps the most interesting yet challenging and is most relevant to our analysis. Based on the descriptions of Bolin [1] and Ebbinghouse and Winsten [2], there are many ways to inspect Dzi beads and how they are crafted. We will focus on the surface-etched rings; the dark and light pattern; and how the XRF map, especially the Cu pattern we found in this analysis, may reveal how this three-eye Dzi bead was crafted.

From the optical image, we see that it showed well-defined light (white) and dark patterns, and the surfaces were covered with etched rings; these are the general characteristics of Dzi beads. Upon slicing the bead in half, we could see that the piece was translucent, and the white pattern did extend considerably into the bulk, as described by Ebbinghouse and Winsten [2]. None of the SEM, EDX, XRD and XRF mapping techniques showed any clear boundary between the light and the dark region, however. XRD of the powder showed the presence of graphite, while microdiffraction of the edge of the slice did not. It is unclear whether this is due to the sensitivity of the microbeam looking at a very small area or whether the powder was contaminated by carbon during the grinding process. This awaits future exploration. The presence of graphite may be related to light absorption in the dark region, however.

The most interesting finding was the hot spots of Cu on the circumference of the etched ring. In both Bolin's book [1] and the work of Ebbinghouse and Winsten [2], drilling with small bits and

the use of alkaline material and copper nitrate, $\text{Cu}(\text{NO}_3)_2$, were mentioned as agents put on the bead surface, followed by firing for whitening and darkening functions, respectively. The regular separation (~ 1 mm) of the Cu spots of ~ 20 μm in size could be speculated to be the tiny drill holes to facilitate diffusion of chemicals used in the pattern formation. The presence of CuO in all the Cu hot spots was likely the result of the following reaction upon firing:



In addition to Cu, Ca and Fe were also found with both 12.0 keV (VESPERS) and 7.13 keV (SXRMB) excitation photon energy in the XRF map overlaying that of the Cu. K was also found in the tender X-ray map (not looked for in VESPERS); the origin of Ca is less clear, and Fe may have come from the tools used in crafting. It should be noted, however, that Fe is also commonly found in agate as a trace element, while Ca and K are not [18]. Compared to the Si map, which showed extruding pilings of SiO_2 on the circumference of the rings, the Cu spots appeared to be more like tiny pits. The Si and Cu map were correlated (Figure S4). It is also interesting to note that while we found CuO from the micro-XRF, it could not be detected in the XRD.

Finally, our preliminary finding was consistent with the descriptions noted in the literature [1,2]. Presumably, a piece of translucent agate was polished into shape and treated with alkaline solution. SiO_2 is slightly acidic, and a potash solution could do the etching (dissolving SiO_2), and the light region could come from the increased porosity. The use of pyrolytic $\text{Cu}(\text{NO}_3)_2$ and firing would produce CuO, which appears black. The origin of regular hot spots of CuO on the ring was possibly from drilling. The presence of graphite remains a mystery; repeated XRD measurements of various regions of the bead (not powder) revealed no crystalline carbon. The origin of carbon requires further investigation, although if plant sugar was used for darkening under heat and reed drill bits were used, it could be a source of carbon.

5. Conclusions

We have reported the preliminary results of an exploration of the mysterious Dzi beads by studying a three-eye bead using laboratory-based optical microscopy and SEM and the advanced synchrotron techniques including XRD, XRF imaging and micro-XANES. The specimen, including the surface, the edges and the interior after slicing, was inspected with an optical microscope and SEM. The crystal structure from a powder specimen, the surface and the edges of a sliced piece were subjected to XRD. They all showed the structure of quartz (SiO_2). While there appeared to be a trace of graphite in the former, it was not detected in the latter. XRF imaging also shows that the bead was made of SiO_2 ; in addition to SiO_2 , there were regular Cu hot spots, as well as Fe, Ca and K at lower concentrations on the circumference of the etched rings. We can conclude, from the material perspective, that the three-eye bead specimen was genuine, and the patterns (dark and light as well as the etched rings), which were apparent to the naked eye, were crafted. The discovery of regular small pits containing copper oxide (CuO) on the circumference, which correlated with the SiO_2 map, and the presence of potassium were consistent with the crafting methods described in the literature [1,2].

Finally, while we have not fully answered the question on the origin of these beads nor expect to do so with a single specimen, in a broader context that will require further studies of representative samples from various regions and times, we are optimistic that the tools and the methodologies introduced here will play a significant role in future studies.

Supplementary Materials: The following are available online at <http://www.mdpi.com/2571-9408/3/3/56/s1>, **Figure S1.** The three-eye Dzi bead purchased from a jewelry piece came with an authenticity certificate and a bag. **Figure S2.** (a) The slicing plan for the Dzi bead as seen lengthwise. (b) A depiction of the Dzi bead slicing plan as seen from one end of the bead, looking down the hole that runs lengthwise through the bead. (c) Dzi bead post-slicing. (d) Dzi bead after ultrasound bath. **Figure S3.** Glazing XRD (left panel) of the surface light and dark regions (red dot on the right panel) using 12 keV (1.03 Å) X-rays. Despite the intensity variation, the patterns are identical. **Figure S4.** Cu $K\alpha$ map recorded based on second order radiation at the Fe K-edge excitation compared with corresponding maps for Si, Fe and Ca.

Author Contributions: A.R. conducted most of the lab measurements at Western; R.F. and T.-K.S. conducted measurements at the VESPERS and Q.X., Y.H. and T.-K.S. conducted measurements at the SXRMB; T.-K.S. initiated the project and provided funds for the research. All authors participated in data analysis and discussion. All authors have read and agreed to the published version of the manuscript.

Funding: This research was supported by the Canada Research Chair (CRC) program and a Natural Science and Engineering Research Council (NSERC) Discovery Grant. Research was in part conducted at the Canadian Light Source which is supported by Canada Foundation for Innovation (CFI), National Research Council (NRC), Canadian Institute of Health Research (CIHR), NSERC, and the University of Saskatchewan.

Conflicts of Interest: The authors declare no conflict of interest.

References

1. Bolin, T. *The Complete Book of Dzi Beads*; Amazon Digital Services LLC: Seattle, WA, USA, 2018.
2. Ebbinghouse, D.; Winsten, M. Tibetan dZi (gZi) Beads. *Tibet J.* **1988**, *13*, 38–56.
3. The Myth and Mystery of Tibetan Dzi Stone Beads. Owlcation. 2017. Available online: <https://owlcation.com/social-sciences/The-Myth-and-Mystery-of-Tibetan-Dzi-Stone-Beads> (accessed on 18 November 2019).
4. Liu, R.K. Stone Beads and Their Imitations. *Beads J. Soc. Bead Res.* **1999**, *10*, 13–18.
5. Beck, H.C. Etched Carnellian Beads. *Antiqu. J.* **1933**, *XIII*, 384–398. [CrossRef]
6. Beck, H.C. The Beads from Taxilia. In *Memoirs of the Archeological Survey of India*; The Manager of Publications: Delhi, India, 1933.
7. Beck, H.C. The magical Properties of Beads. *Bead J.* **1976**, *2*, 32–39.
8. Bellasis, A.F. Further Observations on the Ruined City of Brahmanabad Sind. *J. Bombay Branch R. Asiat. Soc.* **1857**, *V*, 468–474.
9. Kozachuk, M.S.; Sham, T.K.; Martin, R.R.; Nelson, A.J.; Coulthard, I.; McElhone, J.P. Recovery of Degraded-Beyond-Recognition 19th Century Daguerreotypes with Rapid High Dynamic Range Elemental X-ray Fluorescence Imaging of Mercury L Emission. *Sci. Rep.* **2018**, *8*, 9565. [CrossRef] [PubMed]
10. Kozachuk, M.S.; Sham, T.K.; Martin, R.R.; Nelson, A.J.; Coulthard, I. Eyeing the past: Synchrotron μ -XANES and XRF imaging of tarnish distribution on 19th century daguerreotypes. *J. Synchrotron Radiat.* **2019**, *26*, 1679–1686. [CrossRef] [PubMed]
11. Kozachuk, M.S.; Sham, T.K.; Martin, R.R.; Nelson, A.J.; Coulthard, I.; Smieska, L.; Woll, A.R. Recovering Past Reflections: X-ray Fluorescence Imaging of Electrocleaned 19th Century Daguerreotypes. *Heritage* **2019**, *2*, 37. [CrossRef]
12. Kozachuk, M.S.; Sham, T.K.; Martin, R.R.; Nelson, A.J.; Coulthard, I. Exploring tarnished daguerreotypes with synchrotron light: XRF and μ -XANES analysis. *Herit. Sci.* **2018**, *6*, 12. [CrossRef]
13. Paterson, D.; Howard, D. Special issue in art and archaeology. *Synchrotron Radiat. News* **2019**, *32*. [CrossRef]
14. Feng, R.; Gerson, A.; Ice, G.; Reiningger, R.; Yates, B.; McIntyre, S. VESPERS: A beamline for combined XRF and XRD measurements. In Proceedings of the Synchrotron Instrumentation 9th International Conference, AIP CP879, Daegu, South Korea, 7 February 2007; pp. 872–874.
15. Feng, R.; Dolton, W.; Igarashi, R.; Wright, G.; Bradford, M.; McIntyre, S. Commissioning of the VESPERS Beamline at the Canadian Light Source. In Proceedings of the AIP Conference, Melbourne, Australia, 6 July 2010; Volume 1243, pp. 315–318.
16. Hu, Y.F.; Coulthard, I.; Chevrier, D.; Wright, G.; Igarashi, R.; Sitnikov, A.; Yates, B.W.; Hallin, E.L.; Sham, T.K.; Reiningger, R. Preliminary Commissioning and Performance of the Soft X-ray Micro-characterization Beamline at the Canadian Light Source. In Proceedings of the AIP Conference, Melbourne, Australia, 6 July 2010; Volume 1234, pp. 343–346.
17. Xiao, Q.; Maclennan, A.; Hu, Y.; Hackett, M.; Leinweber, P.; Sham, T.K. Medium-energy microprobe station at the SXRMB of the CLS. *J. Synchrotron Radiat.* **2017**, *24*, 333–337. [CrossRef] [PubMed]
18. Gotze, J.; Tichomirowa, M.; Fuchs, H.; Pilot, J.; Sharp, Z.D. Geochemistry of agates: A trace element and stable isotope study. *Chem. Geol.* **2001**, *175*, 523–541. [CrossRef]



© 2020 by the authors. Licensee MDPI, Basel, Switzerland. This article is an open access article distributed under the terms and conditions of the Creative Commons Attribution (CC BY) license (<http://creativecommons.org/licenses/by/4.0/>).

Article

Investigation of the Pigments and Glassy Matrix of Painted Enamelled Qing Dynasty Chinese Porcelains by Noninvasive On-Site Raman Microspectrometry

Philippe Colomban ^{1,*} , Burcu Kırmızı ^{1,2} , Bing Zhao ³, Jean-Baptiste Clais ⁴, Yong Yang ⁵ and Vincent Droguet ⁶

¹ MONARIS UMR8233, Sorbonne Université, CNRS, 4 Place Jussieu, 75005 Paris, France; kirmizi@yildiz.edu.tr

² Department of Conservation and Restoration of Cultural Property, Faculty of Architecture, Yıldız Technical University, Yıldız Yerleşkesi B Blok, Beşiktaş, 34349 İstanbul, Turkey

³ CRCAO UMR8155, CNRS, Collège de France, 75005 Paris, France; bing.zhao@college-de-france.fr

⁴ Département des Objets d'art, Musée du Louvre, quai François Mitterrand, 75001 Paris, France; jean-baptiste.clais@louvre.fr

⁵ Department of Fine Arts, Palace Museum, Beijing 100009, China; yangyong@dpm.org.cn

⁶ Château-Musée de Fontainebleau, Place Charles de Gaulle, 77300 Fontainebleau, France; Vincent.droguet@culture.gouv.fr

* Correspondence: philippe.colomban@sorbonne-universite.fr or philippe.colomban@upmc.fr

Received: 24 July 2020; Accepted: 14 August 2020; Published: 17 August 2020

Abstract: A selection of 15 Chinese painted enameled porcelains from the 18th century (Qing dynasty) was analyzed on-site by mobile Raman and XRF microspectroscopy. The highly prized artifacts are present in the collections of the Musée du Louvre in Paris and Musée Chinois at Fontainebleau Castle in France. In the painted enamels, pigments such as Naples yellow lead pyrochlore, hematite, manganese oxide and carbon and opacifiers such as lead arsenates were detected. The glassy matrices of the enamels mainly belonged to lead-rich and lead-alkali glass types according to the Raman spectra obtained. The glaze and body phases of the porcelain artifacts were also analyzed. The detection of lead arsenate apatite in some of the blue enamels was significant, indicating the use of arsenic-rich European cobalt ores (smalt) and possibly mixing with Asian cobalt. This characteristic phase has also been identified in French soft-paste porcelains and glass decor and high-quality Limoges enamels from the same period. Based on the shape of the Raman scattering background, the presence of colloidal gold (Au⁰ nanoparticles) was identified in red, orange and pink enamels. Different types of Naples yellow pigments were also detected with Sb-rich, Sn-rich and mixed Sb–Sn–(Zn, Fe?) compositions in the yellow enamels. The results were compared to previous data obtained on Chinese *cloisonné* and painted enameled metalware and Limoges enamels as well as French enameled watches.

Keywords: porcelain; enamels; China; 18th century; Raman microspectroscopy; pXRF; pigments; arsenic; cobalt; Naples yellow

1. Introduction

Technological aspects of ceramic production in the past were not only affected by the mastery and innovation of the local craftsmen but the transfer of technology coming out of cultural interactions between societies. This is well-reflected in the choice of the raw materials used and the firing conditions as well as in decorative processes such as enameling. Regarding porcelain production in the Far East, a long-distance technological transfer is known to have been conducted by Portuguese Jesuit missions in Japan at the beginning of the 17th century [1–3]. Historical records of the Chinese court and Jesuit mission [4–8] also both demonstrated the importation of European enamels and ingredients as well as

the venue of European craftsmen who had expertise in enameling techniques at the Qing court at the end of 17th century. These enamels are called “*falangcai*” (珐彩 from *falang*, a homonym of the “French” character in Chinese) and/or “*yangcai*”, (洋彩 “foreign colors”) [9], which are deposited generally over the glaze, the latter being fired beforehand with the porcelain body. Although porcelain production was first achieved in China historically, the craft of enameling is generally suggested to have benefited with Western contacts as early as the 14th century via the Silk Road [10–15].

Scientific analyses of various Chinese [10–15] and European [11,16–18] enameled artifacts have previously confirmed the use of a blue enamel precursor (usually called “smalt”) based on European cobalt ores and Naples yellow lead pyrochlore pigments typical of European recipes in enameled metalware and porcelains produced during the Qing dynasty. Furthermore, the use of the European “Cassius purple” method to prepare pink to purple porcelain enamels (the so-called *Famille rose*) with colloidal gold had been well-established for decades [19]. Due to the rareness of artifacts produced at the Beijing Imperial Palace Workshop (*falangzuo* (珐琅作), enamel workshop) and, consequently, the lack of fragments of such artifacts, most of the studies have been conducted with noninvasive techniques, in particular on-site with Raman and X-ray fluorescence (XRF) mobile instruments [10–14,16–18,20], which are well-suited for the in situ study of outstanding objects in their secure locations [20–24].

UTF8gsn We present here an on-site noninvasive Raman study of Chinese porcelain masterpieces assigned to have been produced at the beginning of the 18th century (Yongzheng (1723–1735) and beginning of Qianlong (1735–1796) reigns) belonging to the collections of the Louvre Museum and Chinese Museum at Fontainebleau Castle in France. One artifact has also been analyzed with a mobile XRF microspectrometer. A comparative approach was carried out with the first Raman study focused on porcelains produced at the end of the Kangxi reign (1661–1722) and the beginning of the Yongzheng reign [12] and with painted enameled metalware of the same collections [14] as well as other types of European enameled artifacts [11,16–18].

2. Methods and Artifacts

2.1. Artifacts

The porcelains analyzed are listed in Table 1 and shown in Figures 1–5. They belong to the collections of the Musée du Louvre (Department of Fine Art Objects) in Paris and Musée Chinois at Fontainebleau Castle, which is located close to Paris. Artifacts from the Fontainebleau Chinese Museum were part of the collection of Napoléon III (1808–1873, president of the French Republic from 1848 to 1852 and then emperor up to 1870) and the Empress Eugénie (1826–1920), while some of the artifacts from the Louvre Museum belonged to the collection of Adolphe Thiers (1797–1877), former president of the French Republic. Indeed, following the Universal Exhibitions, the European elites of the second part of the 19th century took a great interest in Chinese and Japanese ceramics and built up collections rich in exceptional pieces. Most of the artifacts studied here were assigned, based on a stylistic examination of their shape and decor, to have been made during the Yongzheng reign (1722–1735) or just afterwards. The corpus studied includes four cups, five plates, one milk pot, one saucer lid, one teapot and three bottles, which were analyzed by Raman microspectrometry. Only the TH457 bottle was also analyzed by portable XRF (pXRF). Some of the artifacts have rather similar counterparts in other museum collections (Table 1). Four artifacts display painted enamel decor with exceptional quality, such as the plates with roosters (TH487, Figure 1) and tigers (R1056, Figure 2) and especially the TH457 (Figure 3), F1371C (Figure 4) and F1341C (Figure 5) bottles. Close-up views of the painted flower-and-bird decor on the TH457 bottle and the flower decor on the F1341C bottle and F1429C teapot display the high sharpness of the drawing without any diffusion of the colors outside the areas delimited by (black) lines. The F1371C bottle shows a technique inspired by *cloisonné* enameled metalware in which the decor is first made by incision in order to avoid diffusion of the colors, somewhat similar to the *sgraffito* technique.

Table 1. Information about the studied artifacts regarding their collections and time assignments along with special remarks (see [25–27]).

Artifacts	Inventory Number	Collection	Artifacts	Inventory Number	Size	Artifacts
	R1041 cup			1722–1735	H:3.9 D: 7.2	Similar cups at the British Museum (FRANKS 703), at the Fitzwilliam Museum (OC.29-1936) and at the Art Gallery of Greater Victoria (1991.014.021)
	R1045 cup			1730–1745	H:4 D:7	Similar cup saucer at Rijksmuseum (AK-NM-13720-A) [25]
	R1048 cup			1740–1760	H:4 D:7	China, Guangzhou workshop?
	R1135 cup			ca. 1750–1760	H:3.7 D:6.6	China, Guangzhou workshop?
	R1006 dish	Baronne Salomon de Rothschild bequest		1740–1760?	D~10	
	R1177 saucer lid		Louvre Museum		D:11.5	Series with the coat of arms of an English family, S. Jones de Stepney or J. Bromwell Jones or his son or brother [25,26].
	SN284 milk pot			ca. 1735	H:11 D:6.8	
	R1056 plate			1722–1735	D:19	With 3 tigers as decor
	R1175 (2) plate			1735	H:1.7 L:13.2	With the coat of arms of an English family (see above)
	R1025 dish			1740–1750	H:3.2 D:23	With CFB monogram
	TH487 dish	A. Thiers Coll.		1730–1735		With 2 roosters drawn

Table 1. Cont.

Artifacts	Inventory Number	Collection	Artifacts	Inventory Number	Size	Artifacts
	TH457 bottle	A. Thiers Coll.		1735–1796	H:30.9 D:12	
	F1371C bottle			1730/35–1750/60	H:19 D:30	
	F1429C teapot	Napoléon Emperor Coll.	Fontaine bleau Castle (Musée Chinois)	Qianlong period (1736–1795)	H:13 D:12 A:19	Jingdezhen Imperial Factory of Porcelain
	F1341C bottle			End of Yongzheng period (~1730–1735)	H:30 D:15	



Figure 1. The cups and plate analyzed. The remote head with optic fibers connected to the laser source and the spectrometer is shown at the bottom. A laser focusing on the R1041 cup exhibits the high translucency of the porcelain (see Table 1 for details).



Figure 2. The detailed images of the plates and milk pot analyzed (see Table 1 for details).



Figure 3. The detailed images of the TH457 bottle (the neck has undergone a restoration process; see Table 1 for details).

2.2. Mobile Raman Microspectrometry

The high value of the porcelain artifacts made it necessary to conduct the noninvasive Raman analyses in the exhibition or storage rooms of the Musée du Louvre (Paris) and Musée Chinois (Fontainebleau Castle). A mobile Raman setup from HORIBA Scientific Jobin Yvon (Longjumeau, France) was used for the on-site measurements. This setup was composed of an HE532 spectrometer (920 lines/mm grating; resolution $\sim 4\text{ cm}^{-1}$), a remote optical device called SuperHead (Figure 1) and a 532 nm 300 mW Ventus laser source (Laser Quantum, Fremont, CA, USA), which were connected to each other by optic fibers. The SuperHead incorporates long working distance x50 (surface analyzed: $\sim 10\text{--}20\ \mu\text{m}^2$; in-depth: $\sim 5\text{--}20\ \mu\text{m}$) and x200 (surface analyzed: $\sim 1\ \mu\text{m}^2$; in-depth: $\sim 1\text{--}2\ \mu\text{m}$) microscope objectives for the green laser illumination and the collection of scattered light. Details about the procedures have already been published [13,17,18,20].

2.3. Mobile X-ray Fluorescence Microspectrometry

Portable XRF (pXRF) measurements were performed without any contact between the instrument and the artifact using an ELIO instrument (ELIO, XGLab/Bruker, Italy). This setup consisted of a miniature X-ray tube system with a Rh anode (max voltage of 50 kV, max current of 0.2 mA, a 1 mm collimator determining a rather similar surface) and a large-area silicon drift detector (SDD) ($50\ \text{mm}^2$ active area). Details about the procedure have already been published; it should be noted the information thickness during the analysis of the enamel was estimated to be $\sim 4\ \mu\text{m}$ at Si K_{α} , $130\ \mu\text{m}$ at Cu K_{α} , $220\ \mu\text{m}$ at Au L_{α} and $\sim 2.5\ \text{mm}$ at Sn K_{α} [18].

3. Results and Discussion

3.1. Body Phase Identification

Raman spectra (Figures 6–13) have been recorded on the glaze-free body for the different artifacts (see Figure 6A (R1045), Figure 7A (TH457), Figure 8B (R1175) and Figure 9A,B (R1006 and SN284)). In these spectra, the narrow main peak of quartz (SiO_2) was observed at ca. $460\ \text{cm}^{-1}$ [28,29], shifted down to lower wavenumbers than that of the isolated quartz mineral ($\sim 463\ \text{cm}^{-1}$) due to the compressive stress of the glassy matrix on the quartz grains. A broader component at ca. $480\ \text{cm}^{-1}$ was also observed (see e.g., Figures 7A and 9B), characteristic of a glassy aluminosilicate phase forming the porcelain body in between acicular mullite crystals forming a 3D network [30,31]. The mullite phase was generally not detected with a mobile Raman spectrometer due to the operating conditions of the mobile setup and poor intensity of the mullite Raman spectrum. Only in the body spectrum of the R1045 cup (Figure 6A(a)) could very small features at ~ 960 and $1130\ \text{cm}^{-1}$ be considered to come from the mullite phase [28]. The Raman spectrum of the glaze, fired at a high temperature with the porcelain body, was rather similar, but the intensity of the ~ 490 to $505\ \text{cm}^{-1}$ broad component was stronger, and the quartz peak was mostly weaker, as observed for the glaze spectra of the R1045 and R1041 cups (Figure 6A(b),C(b)).

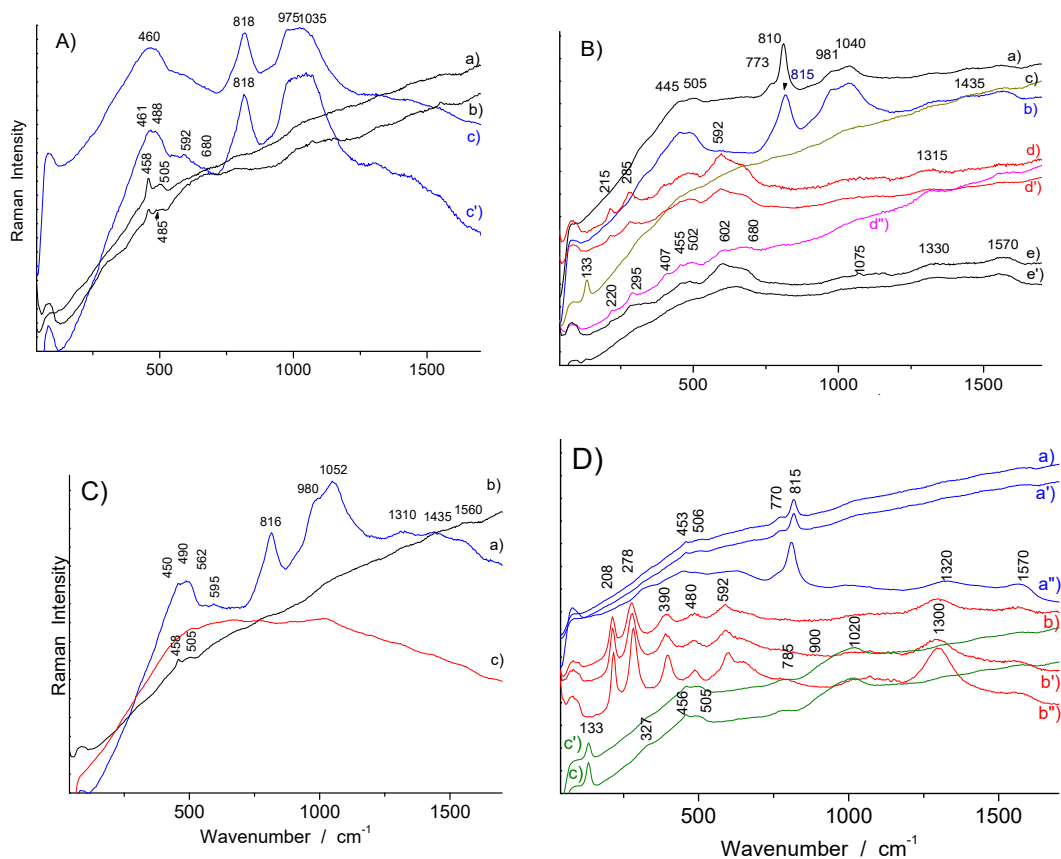


Figure 6. Representative Raman spectra recorded on the body, glaze and painted enamels of the porcelains: **(A)** R1045 cup (a) body, (b) white, (c,c') blue; **(B)** R1048 cup (a) white, (b) blue, (c) yellow, (d,d',d'') red, (e,e') black (line); **(C)** R1041 cup (a) blue (flower), (b) colorless glaze, (c) pink; **(D)** R1135 cup (a,a',a'') blue, (b,b',b'') red (eye), (c,c') green areas.

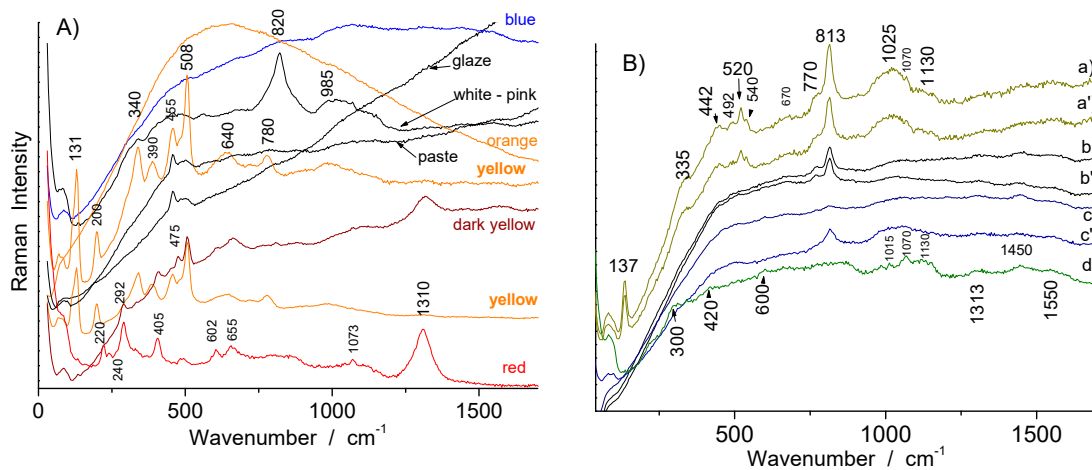


Figure 7. Representative Raman spectra recorded on the body, glaze and painted enamels of the TH457 **(A)** and F1371C bottles **(B)**: (a,a') white, (b,b') dark blue, (c,c') celadon (green), (d) yellow-green.

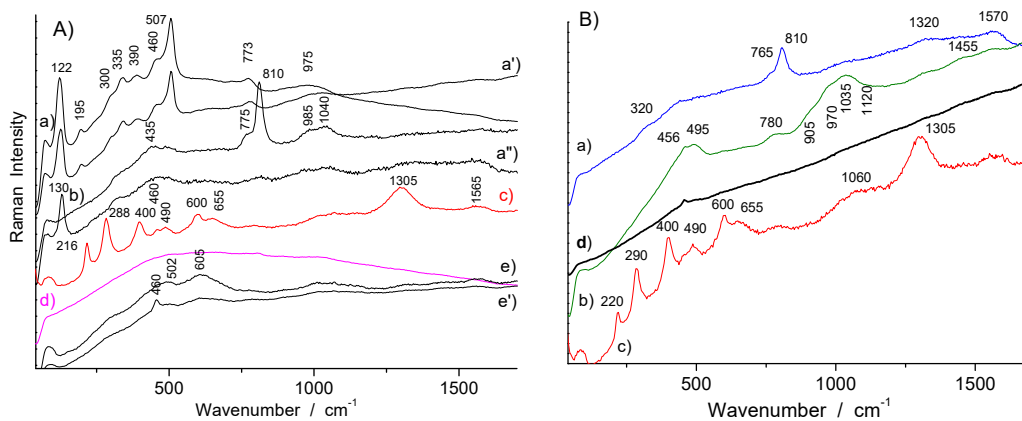


Figure 8. Representative Raman spectra recorded on the painted enamels of the R1175 large plate (A) (a,a',a'') (marli) yellow, (b) (marli) blue, (c) orange (coat), (d) red (flower), (e,e') (marli) black; and small plate (B) (a) blue, (b) green, (c) red (line), (d) body.

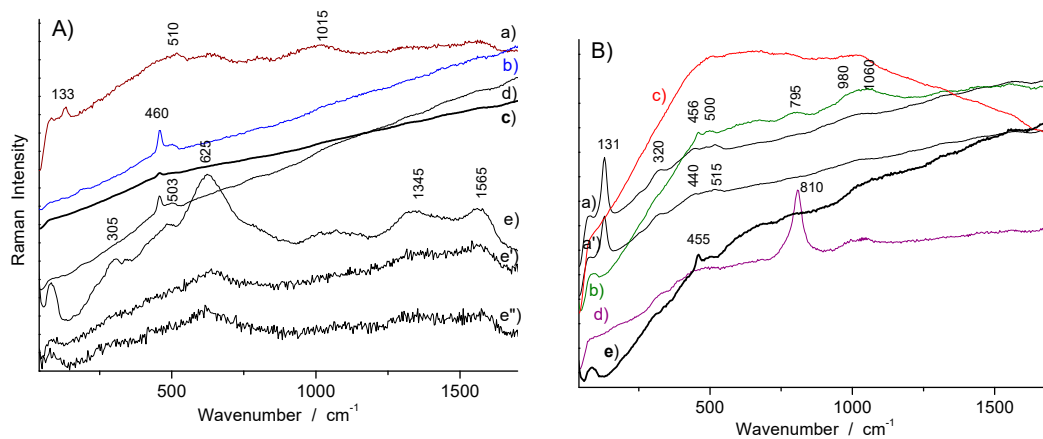


Figure 9. Representative Raman spectra recorded on the body, glazes and painted enamels of the R1006 dish (A) (a) light yellow, (b) blue glaze, (c) colorless glaze, (d) body, (e,e',e'') black (e' and e'' corresponded to very short counting times, and e, to 500 accumulations); and SN284 pot (B) (a,a') yellow, (b) green, (c) red (flower), (d) pink (textile), (e) body.

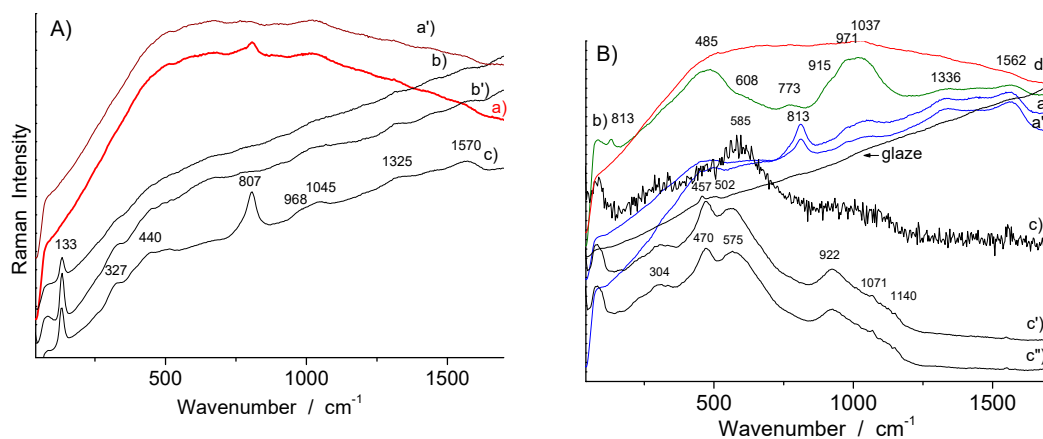


Figure 10. Representative Raman spectra recorded on the painted enamels of the TH487 plate: (A) (a,a') red, (b,b') yellow (cock), (c) (marli) light yellow; (B) (a,a') blue, (b) green, (c,c',c'') black (c, very short counting time), (d) red.

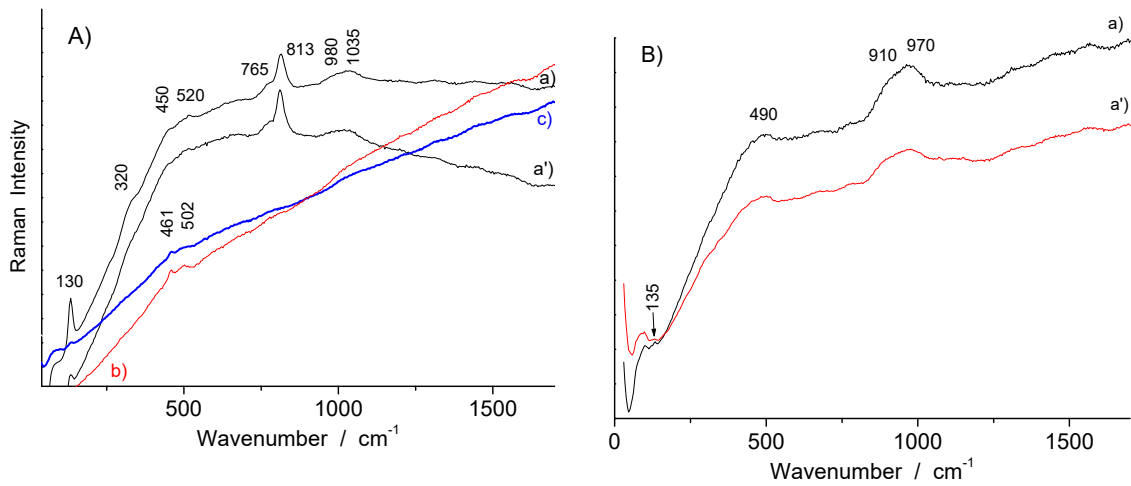


Figure 11. Representative Raman spectra recorded on the glaze and painted enamels of the R1056 tiger plate (A) (a,a') white (tiger belly), (b) pink, (c) glaze; and SN284 pot (B) yellow.

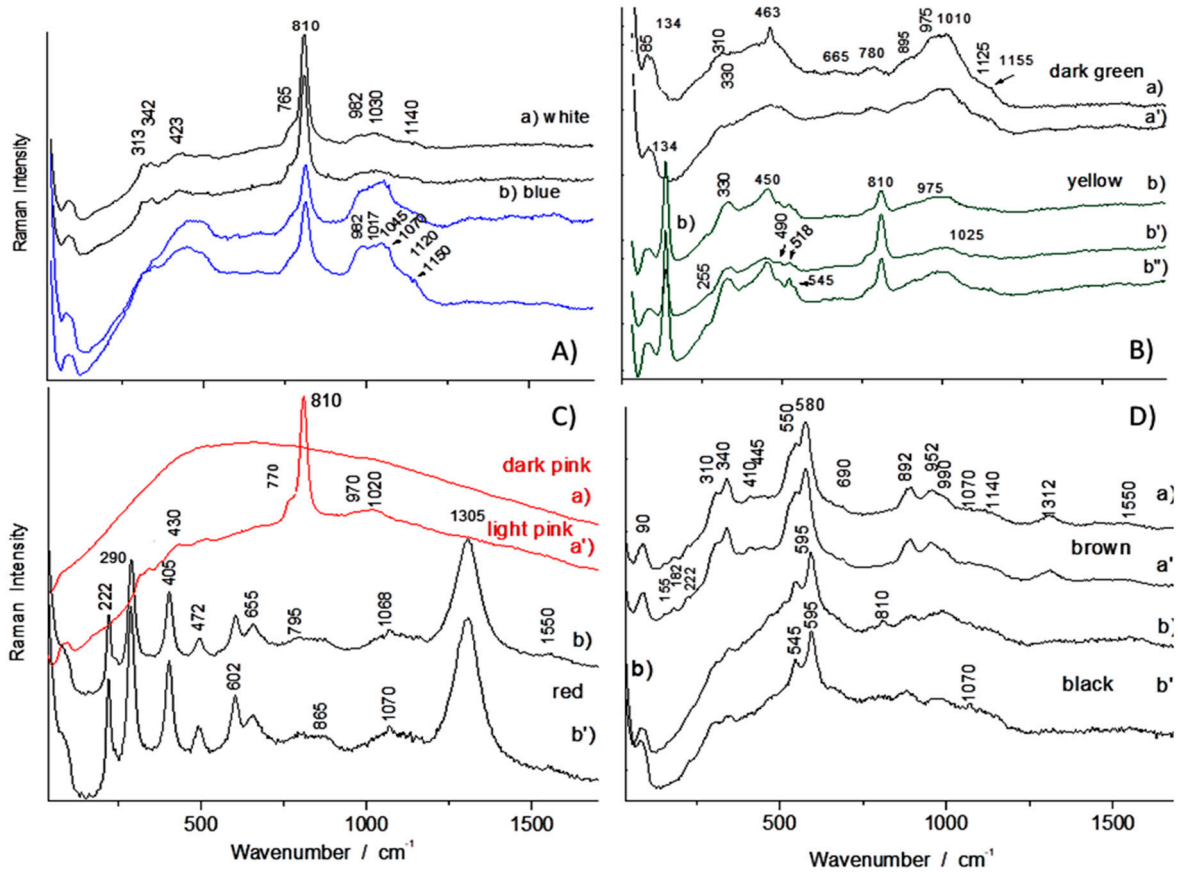


Figure 12. Representative Raman spectra recorded on the F1429C teapot for different colored painted enamels: (A) white (a) and blue (b) enamels; (B) dark green (a,a') and yellow (b,b',b'') enamels; (C) pink (a,a') and red (b,b') enamels; (D) brown (a,a') and black (b,b') enamels.

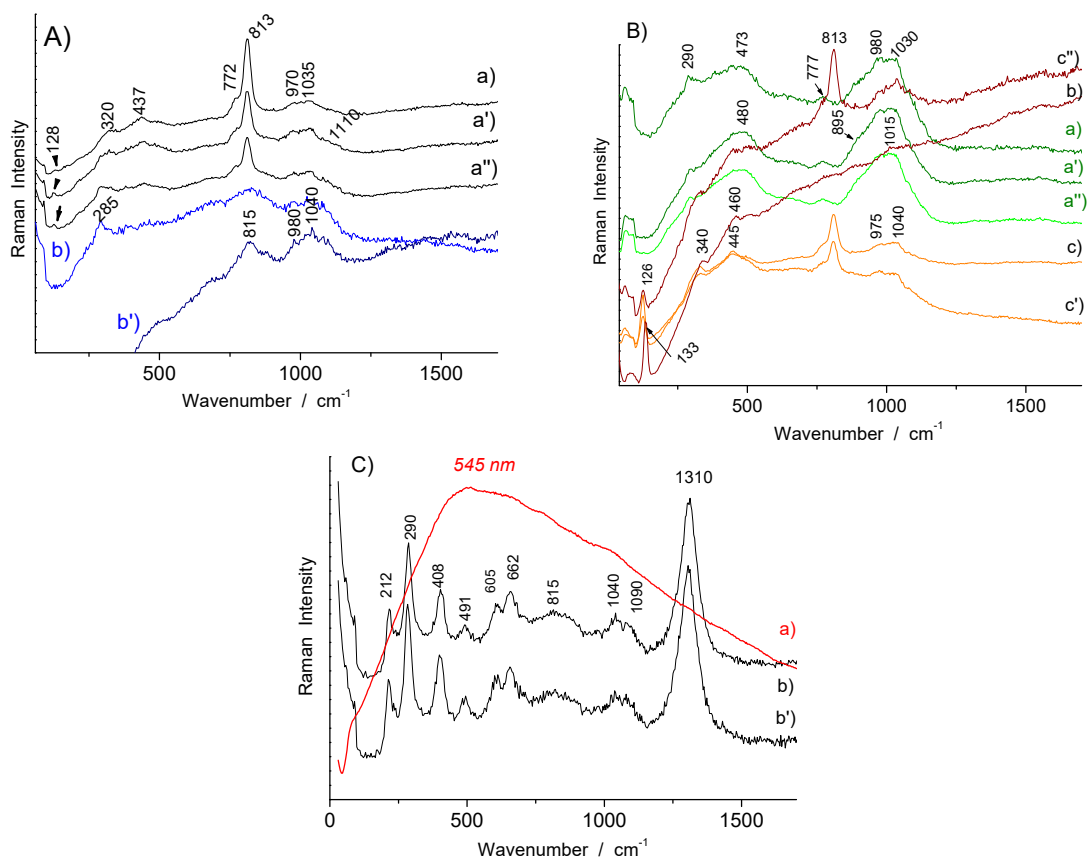


Figure 13. Representative Raman spectra recorded on the painted enamels of the F1341C bottle: (A) white (a,a',a'') and blue (b,b'); (B) green (a,a',a'') light green) and yellow (b,c,c''); (C) orange (a) and red (b,b').

3.2. Phase Identification in Colored Glaze/Enamels

Different phases were identified by Raman analysis for the different colored areas of the Chinese painted enameled porcelains, such as white, blue, yellow (and green), red (purple to red) and pink (Table 2).

Table 2. Characteristic pigments/opacifiers identified in the different colored painted enamels (overglaze) of the Chinese porcelains analyzed. The decor made with imported European recipes is expressed in bold (NY: Naples yellow, br: broad, nr: narrow, sh: shoulder, s: small).

Color	Artifact	Identified Phase(s)	Characteristic Raman Peak (cm ⁻¹)	Remarks
White (colorless glaze)	R1006, R1041, R1056, R1175, TH457, TH487	quartz	455–460	
		glassy aluminosilicate	~485 (br)	
White (overglaze)	F1371C, R1048, R1056	As apatite	~813 (nr), ~770 (sh)	White type 1
White-pink (overglaze)	TH457	arsenate	820 (br)	White type 2
Blue (overglaze)	R1175 (s), R1135, F1371C, F1429C	As apatite	~810 (nr), ~775 (sh)	Blue type 1
	TH487, R1045, R1048, R1041	arsenate	~815 (br)	Blue type 2

Table 2. Cont.

Color	Artifact	Identified Phase(s)	Characteristic Raman Peak (cm ⁻¹)	Remarks
Blue (glaze)	R1006	glassy silicate (+ quartz)	460, 503	Blue type 3 Smalt?
Yellow (overglaze)	R1175, TH457	Sb-rich NY pyrochlore	~122/130, ~335, 508	
	R1175, R1006, R1048, TH487, SN284, R1135	Sn-rich NY pyrochlore	~130–133, ~455	
	TH487, R1056	Sn-rich NY pyrochlore + arsenate	~133, 327, 440, ~810–820 (broad)	
Yellow-green (overglaze)	F1429C, F1341C?, TH457	Sb–Sn–(Zn, Fe?) NY pyrochlore + As apatite	134, 330, 450, 480–490, 518, 810, 770 (sh)	
	R1135	Sn-rich NY pyrochlore + As-apatite	~133, 330, 815, 770	
Green (overglaze)	R1135	Sn-rich NY pyrochlore	~130–133, 330, 455	
Blue-green (overglaze)	TH487	Sn-rich NY pyrochlore + arsenate	~133, 330, 440, ~810	
Dark yellow (overglaze)	TH457	Feldspar? + hematite	~508 + 220, 292, ~1310	
Red (overglaze)	TH457, R1175, R1048, R1135	hematite	220, 292, ~1310	
	SN284, R1175 (large), TH487	Au ⁰ + arsenate	Fluorescence background peaking at ~500 + ~810	
Orange (overglaze)	TH457, SN284	Au ⁰	Fluorescence background peaking at ~600	
	R1175, R1041, TH487	Au ⁰ + arsenate	Fluorescence background + ~820	
	R1175	hematite	220, 290, ~1305	
Pink (rose) (overglaze)	SN284	Arsenate + Au ⁰ ?	~810 + fluorescence background at ~500	
	R1041, F1429C	Au ⁰	Fluorescence background at ~500	
Black (overglaze)	TH487	Mn oxide	470–575	
	R1175, R1048, TH487	Mn spinel/oxide (+ carbon)	502–605 (+1330–1570)	
	R1006	Spinel (Mn?) (+ carbon)	625 (+1330–1565)	
Brown	F1429C	Mn oxide	550, 580, 892	

3.2.1. Arsenic-Based Phases

In the painted enamels analyzed, the detection of two types of arsenic-based phases was significant. The first type refers to lead alkali arsenate apatite, recognized with the narrow (ca. 810–813 cm^{-1}) peak and a well-defined shoulder at $\sim 770\text{--}775 \text{ cm}^{-1}$ [12–14,17,18,32–34], characteristic of the As–O stretching mode of apatite, for which a composition close to $\text{Na}_{1-x-y}\text{K}_x\text{Ca}_y\text{Pb}_4(\text{AsO}_4)_3$ ($x = 0.1$ and $y = 0.5$) has been deduced in a French soft-paste porcelain [34]. This type of opacifying phase was found in some of the enamels analyzed, mostly in white and blue as well as light pink and yellow ones [11–14,17,18,34], as observed in Figure 6B(a) (R1048), Figure 6D(a,a') (R1135), Figure 7B(a,a'),(b,b') (F1371C), Figure 8A(b), Figure 8B(a) (R1175), Figure 10A(a), Figure 11A(a,a'), Figure 12A(a,b), Figure 12B(b,b',b'') and Figure 12C(a') (F1429C). In the case of blue enamels, lead arsenate apatite typically forms as a result of a reaction between arsenic coming from the cobalt source (smalt) and the lead-based enamel/glaze (see further) during the firing process. Its composition also depends on various fluxing species, such as Na(K) and Ca, present in the enamel/glaze matrix [3]. Raman spectra of these enamels displayed the characteristic signature of lead arsenate apatite along with that of the glassy silicate matrix, indicating that the blue was obtained by dissolution of Co^{2+} ions in the glassy matrix [29]. The bands expected due to the precipitation of cobalt aluminate or cobalt silicate (see further) were also not detected. Cobalt ores with an arsenic-rich composition are characteristic of European sources used between ~ 1500 and 1800 [17,18,35,36]. In particular, raw cobalt arsenide mined from the Erzgebirge (the Ore Mountains) in Saxony (Germany) were mixed with potassium glass to produce blue smalt, which was then exported as a coloring agent for glasses/enamels and paint for easel paintings during the 16th–17th centuries [3,36,37]. The detection of lead arsenate apatite could also be due to deliberate addition of an arsenic compound for opacification, especially in the case of the white enamels analyzed [34]. This phase has also been identified in the previous analytical studies of 18th–19th-century Chinese porcelains produced during the Qing dynasty [11–14] as well as in the blue decor of 17th- and 18th-century French enameled glass [16], enameled metalware [10,11,18] and soft-paste porcelains [17,34].

The second type of arsenate phase was characterized by a much broader (ca. 815–820 cm^{-1}) peak (Figure 6A(c,c') (R1045 blue), Figure 6B(b) (R1048 blue), Figure 6C(a) (R1041 blue), Figure 7A (TH457 white-pink), Figure 10A(c) (TH487 yellow) and Figure 13A(b') (F1341C blue)). An intermediate shape between those of the two arsenate phases was observed for Figure 9B(d) (SN284 pink). This broad arsenate band has already been observed in Kangxi Chinese porcelains for the blue areas [12–14] as well as certain French enameled productions [11,16–18]. The broadening of the As–O stretching modes may have arisen from the poor crystallinity or small size of the arsenate apatite crystals or from structural distortions differentiating the AsO_4 tetrahedra (only one strong peak with A_1 symmetry is expected for the stretching mode of an XO_4 tetrahedron). However, arsenates with different composition and structures from apatites (e.g., feldspar) have also been identified in Italian and Spanish majolica enamels [38–41]. Microdestructive analyses to be performed on porcelain shards, such as μ -diffraction, μ XRF and/or transmission electron microscopy analyses, are needed to identify more precisely the arsenic-based phases given the ca. 815 cm^{-1} broad band.

The two signatures observed in the blue enameled areas indicated the use of cobalt ores rich in arsenic, i.e., cobalt ores imported from Europe [11,15–18] or a mixture of Asian (Mn- and Fe-rich) [3,13,36,42–46] and European (As-rich) cobalt ingredients. However, the rareness—and high cost—of European ingredients led Japanese potters, and likely Chinese ones, to mix with Asian ingredients. This point will be discussed further using the XRF spectra obtained.

3.2.2. Lead Pyrochlore (Naples Yellow)

A second important outcome of this study was the detection of at least two types of Naples yellow lead pyrochlore pigments in the yellow and green painted enamels of the porcelains. Naples yellow refers to a variety of synthetic lead antimonate pigments with a pyrochlore structure, prepared by mixing lead oxide with various compounds, including mainly antimony and tin, in the presence of various fluxing agents [1,3,12,13,18,47–54]. This pigment, in the form of Sb- or Sn-rich types,

has been used as a glass and glaze pigment since antiquity [55–57] and as a painting pigment after the Quattrocento/Renaissance [53,54]. Possible variations of the pigment might also include the addition of zinc, iron and silicon elements [14,18,49,50]. The adjustment of the proportions of these compounds at varying firing temperatures allows for the production of modified forms of the pigment displaying different hues. The composition of Naples yellow type pigments is therefore nonstoichiometric with the incorporation of various cations into the lead pyrochlore structure ($\text{Pb}_{2-x}\text{M}'_x\text{M}_2\text{-yM}''_y\text{O}_{7-\delta}$ with $\text{M}, \text{M}'' = \text{Sb}, \text{Sn}, \text{Fe}, \text{Si}, \text{Zn}$; $\text{M}' = \text{RE}$). This phase is built with two sublattices, one of (big) Pb^{2+} cations, the second of (small, covalent-bonded) cations forming tetrahedral and octahedral entities sharing some oxygen atoms. During the firing process of the enamels, composition of the pigment used may be further affected with other species present in the enamel matrix (Fe, Si, Sn, etc.) [14,18,50,58,59]. Some of these incorporating elements may also have different speciations (e.g., Sn^{2+} or Sn^{4+} , Sb^{3+} or Sb^{5+} , Fe^{2+} or Fe^{3+}), and furthermore, the oxygen nonstoichiometry very much depends on the conditions of the firing process (reducing/oxidizing conditions).

In practice, the lead pyrochlore pigment can be prepared as a powder in advance and then mixed with the glass/glaze powder before deposition, the so-called “*anime*” and “*corpo*” recipes [57,60,61]. Alternatively, all the ingredients can be mixed together to obtain the yellow glass/glaze powder. In the first method, the grains of lead pyrochlore are rather big ($>> \mu\text{m}$), while in the other, the homogeneous nucleation on cooling gives rise to small precipitates ($< \text{a few } \mu\text{m}$). With a high-magnification microscope objective, a single pigment grain could be analyzed, and the Raman spectrum obtained was strong without a background, and almost no signature of the glassy matrix was recorded (see e.g., Figure 7A—TH457 yellow; see also in ref. [34]). In the case of nucleation, both the signature of lead pyrochlore precipitates and glass were recorded together with a significant background (e.g., Figure 6D(c,c')).

In the last decades, several Raman spectrometry studies performed on various pottery glazes, glasses and enamels [1–3,11–18,47–52,57–59] as well as oil paintings [53–56] allowed for the identification of Naples yellow lead pyrochlore pigments. In general, these pigments have a very characteristic Raman signature, which basically includes the strong stretching mode peaks of Pb ions at the low-wavenumber region ($\sim 115\text{--}145 \text{ cm}^{-1}$) and $\text{M}/\text{M}''\text{-O}$ stretching modes from ~ 300 to 600 cm^{-1} . Furthermore, Sb-rich pyrochlore pigment is mainly distinguished by strong peaks at $\sim 110\text{--}130$ and $\sim 505 \text{ cm}^{-1}$, while Sn-rich-type pigment exhibits stronger peaks at $\sim 130\text{--}135$, ~ 335 and 450 cm^{-1} (the Sn–O stretching mode) with the disappearance of the $\sim 505 \text{ cm}^{-1}$ peak [10,13,18,47–52]. Zn-containing mixed lead pyrochlores exhibit a medium $450\text{--}480 \text{ cm}^{-1}$ component [18]. Although Sn-rich lead pyrochlore was observed in most of the yellow and green enameled areas (Figure 6B(c) (R1048), Figure 6D(c,c') (R1135), Figure 9A(a) (R1006), Figure 9B(a,a') (SN284), Figure 10A(b,b') (TH487), Figure 11A(a) (R1056) and Figure 13B(c,c') (F1341C)), Sb-rich compositions were clearly observed in the yellow enamels of the TH457 bottle from the Thiers Collection (Figures 3 and 7A) and the R1175 plate with an English family's coat of arms (Figures 2 and 8 A(a,a')). Mixed lead pyrochlores were also observed in some cases (Figure 7B(a,a') (F1371C) and Figure 12 B(b,b',b'') (F1429C)). As a second piece of proof, the XRF spectrum recorded on the yellow enamel of TH457 showed both Sn and Sb signals (Figures 14 and 15).

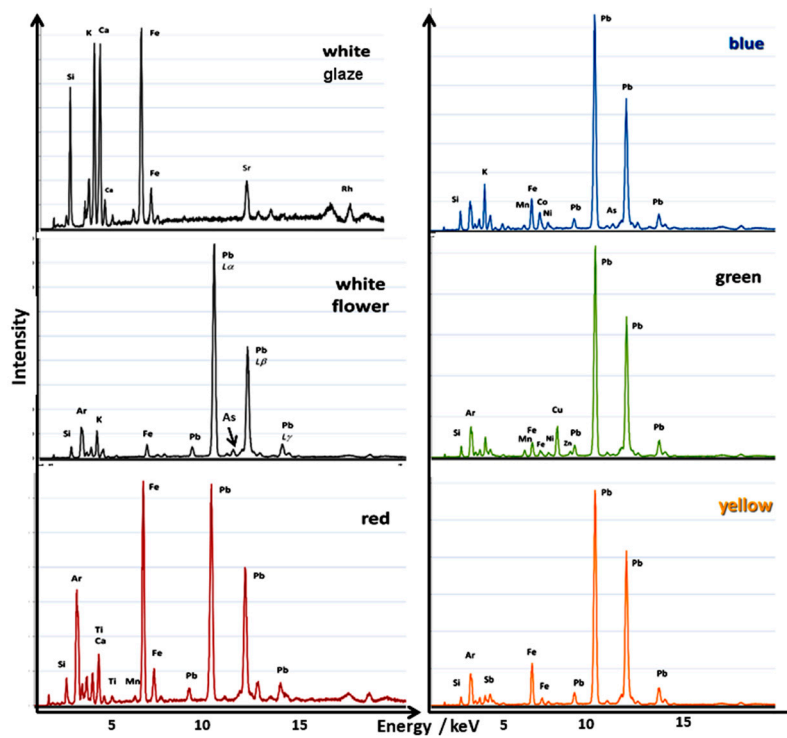


Figure 14. Representative portable XRF (pXRF) spectra recorded on the TH457 bottle for the glaze and different painted enamels.

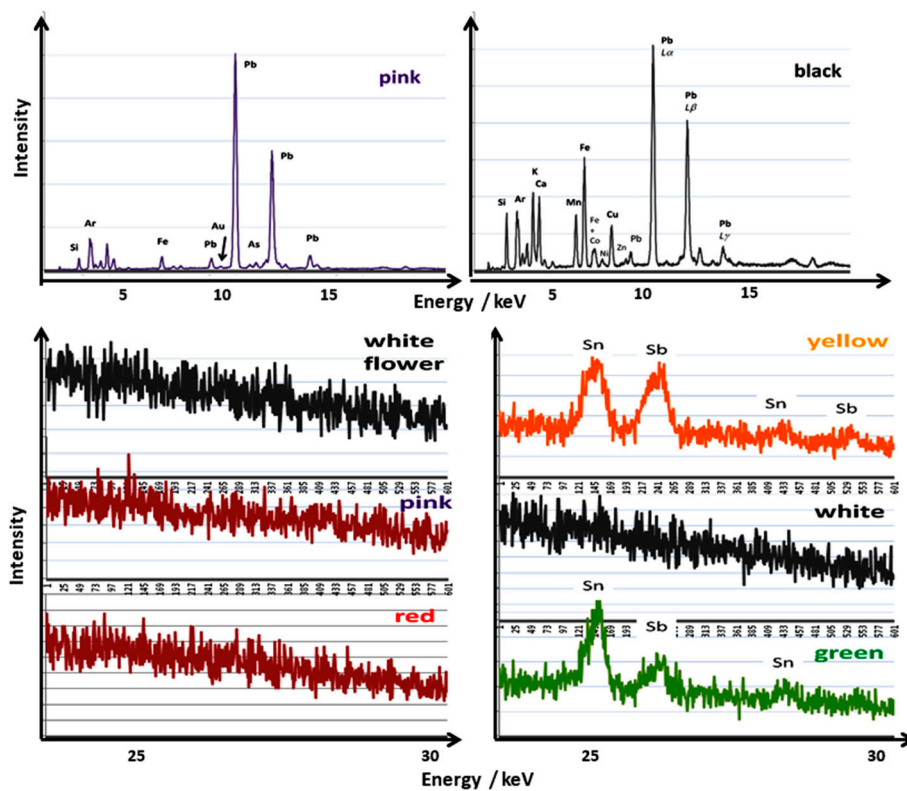


Figure 15. Representative pXRF spectra recorded on the TH457 bottle for pink and black enameled areas; bottom: zoom in on the energy window characteristics of Sn and Sb elements for different areas.

3.2.3. Red to Violet Colors

The last important characteristic of the painted enameled porcelains analyzed was the presence of different methods for obtaining red-related colors. The use of hematite or gold nanoparticles was identified in the painted enamels to obtain red, orange to pink/purple hues (Table 2). In only two artifacts, the TH457 bottle (Figures 3 and 7A, white-pink and red) and R1175 plates (Figures 2 and 8A(c,d), orange and red; and Figure 8B(c), red), the use of both methods was observed. Hematite has a well-defined Raman signature, with a strong (ca. 1305–1310 cm^{-1}) mode (resonance signal of magnon mode under green laser excitation) and narrow peaks between 200 and 600 cm^{-1} [62,63] (see e.g., Figure 6D(b,b',b''), Figure 7A, Figure 8A(c),B(c) and Figure 12C(b,b')). The magnon mode is very sensitive to the particle size of hematite [63] and the oxygen stoichiometry [62], with small particles giving an orange-red color [29]. Broadening of hematite peaks indicates a partial substitution of iron with other elements, possibly Ti and Al coming from the iron sources [29].

A specific Raman feature referred to the use of gold nanoparticles dispersed in the glassy matrix of the enamel (this type of enamel is at the origin of the label “*Famille rose*” [15,19], with a characteristic broad fluorescence background peaking at $\sim 500\text{--}600$ cm^{-1} under a green laser, corresponding to ~ 500 nm on the absolute scale [14,18]; see Figure 6C(c) (R1041), Figure 7A (TH457), Figure 8A(d) (R1175), Figure 9B(c) (SN284), Figure 10A(a,a'),B(d) (TH487), Figure 12C(a) (F1429C) and Figure 13C(a) (F1341C)). This method was first experimented with in 17th-century France by the glassmaker Bernard Perrot and then some years later by Johann Kunckel in Germany and certainly by others in Italy before [16,18,64–67]. The presence of gold was also confirmed by pXRF analysis (see arrow on Figure 15—pink, in which the small Au L_{α} peak is obvious), with a hardly visible peak well-identified by data fitting. In addition, it is important to note that a very small band characteristic of the As–O stretching band at ca. 820 cm^{-1} could be detected along with the fluorescence background characteristic of the use of colloidal gold (seen clearly in Figure 10A(a,a') (TH487) and less intensely in Figure 9B(c) (SN284) and Figure 13C(a) (F1341C)). This band corresponds to the use of Perrot’s preparation route for obtaining the colloidal gold precipitate using an arsenic salt, which is different from that of Kunckel, who made use of a tin salt instead [16]. Similar Raman signatures were observed for painted Chinese enameled wares of the same period [14] as well as on French enameled watches [18].

3.3. Glassy Matrix

Raman spectra of the glazes/painted overglaze enamels showed the characteristic signature of glassy silicates, which basically include Si–O bending and stretching bands in the range ~ 500 and ~ 1000 cm^{-1} , respectively. A comparison of the Si–O stretching band components and the area ratio of the Si–O bending/stretching band has proved to be very efficient for the compositional classification of different glass/glaze/enamel types based on experimental Raman data obtained for a great deal of ancient glassy objects [68–71] as well as on Density Functional Theory calculations [72]. The glazes were aluminosilicate glazes, with the Si–O stretching bands varying between ca. 900 and 1200 cm^{-1} . The painted enamels analyzed displayed a broad and strong band varying between ~ 920 and 1070 cm^{-1} with various shoulders/components, indicating mainly lead-based compositions [69–71], as observed for soft-paste porcelains [17] and enameled metalware [14,18]. In some of the spectra, the intensity of the Si–O bending modes near 500 cm^{-1} appeared to be equal to or weaker than that of the stretching modes at 950–1050 cm^{-1} (see e.g., Figure 6A(c),C(a), Figure 10B(b) and Figure 13B(a',a'')). This indicates a polymerization ratio close to less than 1, according to firing at temperatures inferior to 900–1000 $^{\circ}\text{C}$ [68,71]. The painted enamels can be further classified into three main glass types (Table 3) based on representative glass (and glaze) types [12,13,16,68,69] and previous studies conducted on Chinese *cloisonné* and painted enamels [10,14,73–76]: (i) lead-rich glass with the strongest component at ca. 920 to 1020 cm^{-1} (Type I); (ii) lead (earth) alkali glass with the strongest component at ca. 1030 to 1060 cm^{-1} (Type IIa), with rather similar-intensity components at ca. 980 and 1040 cm^{-1} (Type IIb); and (iii) lead (earth) alkali glass with the strongest component at ca. 1070 cm^{-1} (Type III). Some of the yellow, green and black enamels belonged to the lead-rich type of glass, with their strongest component

at low wavenumbers, which indicates a low degree of polymerization and firing at low temperatures (the addition of Naples yellow increases the lead content). Most of the painted enamels (white and blue) belonged to the lead alkali type of glass (the addition of smalt increases the potassium content), with their strongest component shifted to higher wavenumbers (up to ca. 1060 cm^{-1}) accompanied by a similar low wavenumber component to the lead-rich glass. The glass compositions of the painted enamels did not show much variety, indicating a limited number of firings over the transparent glaze.

Table 3. SiO_4 stretching components of the glassy matrix of the painted enamels analyzed (strongest; shoulder/weak) and comparison with Chinese enameled metalware (Lead alkali glass: L-a; Lead-rich glass: L-rich).

Artifact	Si–O Stretching Components (cm^{-1})	Color	Glass Type	Observed in Cloisonné Metalware [14]	Observed in Painted Metalware [14]
F1371C	<u>1025</u> , <u>1130</u>	White, blue	L-a IIa		
R1048	<u>980</u> , <u>1040</u>	White	L-a IIa	Blue and white	<i>Not observed except F1440C</i>
	<u>975</u> , <u>1040</u>	Blue	L-a IIa		
	<u>1075</u>	Black, yellow, red	L-a III		
R1056	<u>980</u> , <u>1035</u>	White	L-a IIa		
TH457	<u>985</u> , <u>1130</u>	White pink	L-rich I	Yellow and black Green-yellow	<i>Yellow and turquoise yellow and green</i>
	<u>985</u>	Yellow	L-rich I		
	<u>1070</u>	Dark yellow, red, blue	L-a III		
R1175	<u>985</u> , <u>1040</u>	Blue	L-a IIa	See above	Green
	<u>975</u>	Yellow	L-rich I	See above	
	<u>985</u> , <u>1040</u>	Black	L-a IIb	Green	
	<u>905</u> , <u>970</u> , <u>1035</u> , <u>1120</u>	Green, orange, red	L-a IIa		
TH487	<u>975</u> , <u>1050</u>	Blue	L-a IIa	See above	
	<u>970</u> , <u>1045</u>	Yellow	L-a IIa		
	<u>920</u> , <u>1140</u>	Black	L-rich I		
	<u>915</u> , <u>971</u> , <u>1037</u>	Green, red	L-a IIb		
R1045	<u>975</u> , <u>1035</u>	Blue, white	L-a IIb		
R1041	<u>980</u> , <u>1050</u>	Blue, pink	L-a IIa		
R1006	<u>1015</u>	Yellow	L-rich I		
	<u>1020</u>	Black	L-rich I		
SN284	<u>980</u> , <u>1060</u>	Yellow, red, pink	L-a IIa		
R1135	<u>1020</u>	Green, blue, red	L-rich I		
F1341C	<u>970</u> , <u>1035</u>	White, blue	L-a IIb		
	<u>980</u> , <u>1030</u>	Green	L-a IIb		
	<u>1040</u> , <u>1090</u>	Red	L-a IIa		
F1429C	<u>980</u> , <u>1030</u> , <u>1140</u>	White, blue	L-a IIa		
	<u>970</u> , <u>1020</u>	Light pink	L-a IIa		
	<u>900</u> , <u>975</u> , <u>1010</u> , <u>1130</u>	Yellow	L-rich I		
	<u>900</u> , <u>975</u> , <u>1010</u> , <u>1125</u>	Green	L-a IIb		

3.4. XRF Analysis

One of the porcelain artifacts, the TH457 bottle, was analyzed by pXRF. This artifact exhibits the most sophisticated decor, and its shape is well-suited for XRF analysis using a portable instrument since the analyzed area must be roughly perpendicular to the instrument [18]. Additionally, the distance between the instrument and the artifact must be small ($\sim 10\text{ mm}$), and flat areas are required. Figures 14 and 15 show the representative XRF spectra recorded on the white glaze and the different

overglaze enamels (white, blue, green, red, yellow, pink and black) in the 1–22 keV range, where most of the peaks characteristic of major and minor elements were observed. Figure 15 shows details of the 24–30 keV range, where peaks of tin and antimony elements could be compared visually.

As expected for porcelains, the glaze showed elements characteristic of a glassy aluminosilicate porcelain glaze fired at a high temperature [1–3,28–31] with high levels of potassium, calcium and silicon (Table 4). Significant iron content was also obvious in the (colorless) glaze. The high whiteness of the glaze, in association with some iron impurities, demonstrated a firing process under a reducing atmosphere that imposed Fe^{2+} speciation. These ions lead to a weak blue coloration, reinforcing the “whiteness” of the glaze for human eyes. Strontium, an impurity of calcium, was detected at a significant level. Light elements such as sodium could not be detected due to their low atomic number. All overglaze enamels were lead-rich: all the L_{α} , L_{α} , L_{α} XRF transitions of the lead element were clearly observed. A comparison between the relative intensity of lead and potassium or calcium peaks indicated the lower content of lead in the black enamels.

Table 4. The glaze and overglaze painted enamels analyzed by pXRF. (Major-minor-traces).

Glaze	Elements
White	Si, K, Ca, Fe–Sr
Overglaze enamel	
Blue	Si, Pb–K, Co, Fe, As–Ni, Mn
White	Si, Pb–K, Fe, Ca, As–Ni
Green	Si, Pb–Cu, Fe, K, Ca, Sn, Zn–Mn, Ni, (Co?)
Yellow	Si, Pb–K, Sb, Fe, Sn–Ni
Red	Si, Fe, Pb–K, Ca, Ti–Mn
Pink	Si, Pb–K, Ca, Fe, As–Au, Ni
Black	Si, K, Ca, Pb, Fe–Mn, Co, Cu–Ni, Zn

The XRF spectrum of the blue overglaze enamel showed strong lead peaks; pronounced arsenic, iron and cobalt peaks; and weak manganese and nickel peaks. Arsenic was also observed in the white overglaze enamel (flower decor) as well as in the pink one. Arsenic content is visually detected by the small As K_{β} peak just before the Pb L_{α} one, the As K_{α} peak being at the same position as the strong Pb L_{α} one. Confirmation was carried out with the software fitting. Note the high intensity of the potassium peak in blue, according to the use of smalt. The presence of nickel and manganese was due to the impurities found in the cobalt ore used (Table 4). The intensity of the iron peak was rather similar for all overglaze enamels. The presence of manganese was thus consistent with the implication that Asian and European cobalt ingredients were mixed. The detection of arsenic was also significant in relation to the type of the cobalt ore. The red overglaze enamel displayed significant iron peaks, in accordance with the Raman identification of hematite (Figure 7A). Minor amounts of titanium and traces of manganese were also observed, possibly coming from the hematite source. The pink overglaze enamel displayed minor amounts of iron, also indicating the use of hematite. In addition to that, the detection of gold traces was significant, confirming the use of colloidal gold for obtaining the desired hue. The presence of arsenic was also in accordance with the use of Perrot’s technique.

The yellow overglaze enamel showed distinct peaks of iron together with minor amounts of antimony and tin, indicating the use of a complex (Fe) Sb-rich Naples yellow lead pyrochlore pigment (see Section 3.2). A similar type of this pigment also seemed to have been used for the green overglaze enamel, with a higher amount of tin and some zinc. Antimony was detected in the low-energy range, but a magnification of the 24–30 keV range (Figure 15) showed the variable content of tin and antimony elements more clearly. The green enamel additionally included copper, which contributes to color formation, together with manganese, nickel and zinc. It was difficult to see if cobalt was also present.

Iron was clearly observed in the black overglaze enameled areas (Table 4). Black enamel was obviously obtained with a mixture of iron and manganese in the presence of copper (and cobalt?), according to the Raman identification of manganese-rich oxide (spinel) (see e.g., Figure 6B(dd') (R1048), Figure 8A(e) (R1175), Figure 9A(e,e',e'') (R1006) and Figure 10B(c',c'') (TH487)). It is important to note that relative intensities of lead and silicon elements measured on the black lines were intermediate between those measured on other overglaze enamels and that of the glaze. This is due to the limited thickness of the black lines: the XRF spectrum (Figure 15) both displayed the contribution of the black line plus those of adjacent areas, the glaze on one side and the colored overglaze on the other side. All the data obtained by pXRF were in perfect agreement with the Raman data.

4. Comparison with Painted Enameled Metalware

The characteristics of porcelain and metal enameling were expected to be very much linked to each other in terms of the pigments/opacifiers used and the firing conditions employed. At the end of the 17th and early 18th century in China, enameling workshops both in charge of metal and porcelain enameling were established in the Forbidden City by the Jesuit mission to satisfy the demand of the Kangxi Emperor [4–8]. These workshops are considered to have been in close contact with each other [27]. The present study has shown that the material characteristics and production technology of 18th-century Chinese painted enameled porcelains and the painted enameled metalware of the same period are very similar. Pigments/opacifiers of European origin, such as Naples yellow lead pyrochlore pigment (yellow to green enamels), colloidal gold (red, orange and pink enamels) and lead arsenate phases (white and blue enamels) as well as similar lead-based glass compositions were identified in both of the enameled ware types. However, with the present state of knowledge, some differences can be noted on the diffusion of these new technologies in China. Tables 5 and 6 chronologically compare the appearance of European technologies for blue, white, yellow/green and red/pink enamels of porcelain and metalware, respectively.

Table 5. Chronological summary of the innovative technologies evidenced in Chinese enameled porcelains (A: arsenic-based apatite).

Period (Assignment Based on Decor Style)	Porcelain	Specific Technologies	Remarks	Refs
Final period of Kangxi reign (<1722)	G1710 vase	<u>Ming blue</u> <u>H-red</u> Sn-N.y.(s)	“Biyu tang zhi” mark Famille verte/Famille noire J.p.k.	[12]
	G822 dish	Sn-N.y. (s) <u>H-red</u>	“Da Qing Kangxi nian zhi” mark Famille verte J.I.F	[12]
	G5696 bowl	<u>Ming blue</u> <u>H-red</u> Sn/Sb-N.y.(s)	“Da Qing Kangxi nian zhi” mark doucai J.I.F	[12]
	G5250 bowl	As-blue; <u>Ming blue</u> Sb-N.y.; Sn-N.y. Au° Cassiterite?	“Kangxi yu zhi” mark huafalang P.w.	[12,17]
	G3361 water dropper	As-blue As-white Sn-N.y. Au°	“Da Qing Kangxi nian zhi” mark Famille rose J.I.F.	[12]

Table 5. Cont.

Period (Assignment Based on Decor Style)	Porcelain	Specific Technologies	Remarks	Refs
Yongzheng reign (1723–1735)	R1006 cup	<u>Ming blue</u> Sn-N.y.		This work
	R1056 dish	As-white Sn-N.y.		This work
	R1041 cup	As-blue Au°		This work
	MG4806 bowl	<u>Ming blue</u> Sb-N.y. (s)	“Yongzheng yu zhi” mark huafalang/yangcai J.I.F.	[12]
	MG913 bowl	As-blue As-white Sn-N.y. (s) <u>H-red</u>	“Yongzheng yu zhi” mark huafalang/yangcai J.I.F.(?)	[12]
	MG7368 bowl	<u>Ming blue</u> N.y. (s) <u>H-red</u>	“Da Qing Yongzheng nian zhi” mark, doucai J.p.k.	[12]
	R1175 dish	As-blue (A) CaF ₂ (?), Au° Sn/Sb-N.y., <u>H-red</u>		This work
	TH487 dish	As-blue Sn/Sb-N.y. Au°		This work
	F1341C bottle	As-blue Sn-N.y. Au°; <u>H-red</u>		This work
	SN284 milk pot	As-blue (A) Sn-N.y. Au°		This work
Qianlong reign (>1735–1750)	SN284 cup	Sn-N.y. Au°		This work
	Shard bowl	As-blue As-white <u>H-red</u> Sn-N.y. (yellow) Sb-N.y. (green)	From Palace excavation	[13]
	R1045 cup	As-blue		This work
	F1429C teapot	As-blue(A) Sb-Sn-Y.y. Au°		This work
	TH457 bottle	<u>Ming blue</u> Sn-N.y. Sb-Sn-N.y. Au°, <u>H-red</u>		This work
	F1371C bottle	As-white As-blue (A) Sn-N.y.		This work
	R1025 dish	As-blue (A) Au°		This work
R1048 cup	As-white, As-blue Sn-N.y., <u>H-red</u>		This work	

Table 5. Cont.

Period (Assignment Based on Decor Style)	Porcelain	Specific Technologies	Remarks	Refs
Qianlong reign (1750–1800)	MG3668 teapot	As-blue, Au ^o As-white Sn-Sb-N.y.	Yixing p.k.	[12]
	MG9604 teapot	As-blue As-white Sb-N.y.	Yixing p.k.	[12,17]

P.w.: palace workshop; J.I.F.: Jingdezhen Imperial Factory; J.p.k.: Jingdezhen private kiln; As-blue: European cobalt; Sb-N.y.: Sb-rich Naples yellow; Sn-N.y.: Sn-rich Naples yellow; s: small intensity; *ancient Ming technology: Asian blue; hematite red*; MGxxxx: Musée national des arts asiatiques—Guimet inventory number.

Table 6. Chronological summary of the innovative technologies evidenced in Chinese enameled metalware [14].

Period	Painted	Specific Technologies	Cloisonné	Specific Technologies	Remarks
Final period of Kangxi reign (<1722)			F1448C	Sb-Sn-N.y. Sn-N.y. Cassiterite Au ^o	Palace workshop?
Qianlong reign (1735-1750)	R957	As-white As-blue As-blue (A)			Guangzhou
Qianlong reign (1750-1775)		Sn-N.y.	F1735C	Sb-Sn-N.y. Sn-N.y.	Qianlong mark
	F1440C	As-blue Sb-N.y. Sn-N.y. Au ^o			
Qianlong reign (<1775-1800)	R958	As-blue (A) As-white Sn-N.y. Au ^o			Guangzhou
	R975	As-blue Sb-Sn-N.y. Au ^o ?			Guangzhou
			F1501	As-blue Sb-Sn-N.y. Sn-N.y. Au ^o ?	Palace workshop
			F1467.1/.2	Sb-N.y. Sn-N.y. Au ^o	
	F1467.1/.2	As-blue Sb-N.y. Sn-N.y. Cassiterite			Qianlong mark
Qianlong reign (>1800)?	F1698C	As-blue Sn-N.y.			Guangzhou

Regarding the blue overglaze enamels studied so far, the change from Ming blue (made with Asian cobalt ores) to As-rich blue (pure European cobalt ores or mixing with Asian ones) is suggested

for the artifacts assigned to the end of the Kangxi reign on the basis of the decor style. It seems that both types of blue were used in the MG5250 “Imperial” bowl [12]. This bowl also exhibited the Raman spectrum characteristic of the use of colloidal-gold-based (*Famille rose*) enamel. Naples yellow pyrochlore, tin-rich, was the first European technology imported, but the addition of antimony was expected in the MG5696 “Imperial” bowl [12]. A weak signal of cassiterite was even detected in a similar shard [17]. It can be also noted that the MG5250 bowl is assigned to have been made at the palace workshop; the same innovative technology of enameling was observed for the MG3361 pencil water dropper assigned to have been made at the Jingdezhen Imperial Factory [12]. This indicates a very rapid transfer of technology from the palace workshop managed under the Jesuits’ guidance to the imperial kilns at Jingdezhen. The Sn-rich Naples yellow (in yellow and green enamels) appears to have been used more frequently than the Sb-rich homologue up to the mid-18th century. The addition of Naples yellow increased the lead content. The use of cassiterite seems to be exceptional, and its use must be confirmed by an examination of shard sections of similar artifacts.

It is worth mentioning that cassiterite was identified in the painted enamels of the metalware, as an opacifier, for a Kangxi *cloisonné* metalware piece and the exceptional painted and *cloisonné* Qianlong ewers from the French emperor’s collection. Regarding enameled porcelain, Sn- and Sb-rich Naples yellow pyrochlores appear to have been used since the final period of the Kangxi reign. The same conclusions can be drawn for the use of colloidal gold for red to pink colors. By comparison, it appears that almost all enameled metalware was prepared with the European technologies, including As-rich cobalt, although enamel traditional recipes such as Ming blue were used simultaneously with new ones (Ming blue was used for underglaze decor). More artifacts must be analyzed to confirm this point.

5. Conclusions

The present on-site Raman study of intact Chinese painted enameled porcelains from the 18th century sheds light on the materials (pigments/opacifiers, colorants, glass types of glazes/enamels and body phases) and the technology used during their production. The study also provides a comparative approach for the technical aspects of painted enameled porcelains and contemporaneous enameled metalware regarding the different reigns of the Qing dynasty. The use of the same on-site analytical protocol for these artifact groups is advantageous for comparing the data obtained. The outcomes are significant in terms of the know-how transfer (materials/techniques) from Europe to China by the Jesuit mission at the end of the 17th century.

From the (limited) number of objects studied, it appears that the first innovations were the different types of Naples yellow lead pyrochlore pigments and then the use of European cobalt during the later years of the Kangxi reign for enameled porcelains. Cassiterite appeared first during the same period in certain *cloisonné* enamel wares. The detection of cassiterite traces in a Kangxi enamel is assigned to (the effect of) the use of Sn-rich Naples yellow that induced precipitation of cassiterite. Its addition to adjust the hue is also possible. More artifact studies are needed to clarify this point. Yongzheng enameled objects made use of European recipes for blue, yellow and rose; the opacification with different As phases was identified. Unfortunately, only one metalware piece from the Yongzheng period has been studied [14]. Studies of a larger number of objects are required, in particular to study the technology transfer from the Imperial Palace to the Jingdezhen imperial kilns and to private kilns in Jingdezhen or Guangzhou [27] to really have a statistical view of the number of porcelains on which the lead-based enamels were deposited directly on the body and not on the glazed body [77].

Author Contributions: Conceptualization, P.C. and B.Z.; methodology, P.C.; validation, P.C. and B.K.; investigation, P.C.; resources, B.Z., J.-B.C., Y.Y. and V.D.; writing—original draft preparation, P.C.; writing—review and editing, P.C. and B.K.; funding acquisition, P.C. and B.Z. All authors have read and agreed to the published version of the manuscript.

Funding: This research was funded by the French Agence Nationale de la Recherche ANR EnamelFC project—19-CE27-0019-02 and by the Partenariat ‘Hubert Curien’ PHC-Cai Yuanpei Campus France–China cooperative program.

Acknowledgments: M. Gironda from ELIO, XGLab/Bruker is kindly acknowledged for recording the XRF data. C. Gougeon from the Louvre Museum and S. Paronetto from Fontainebleau Castle are acknowledged for their help in the preparation of the measurement campaigns. J. Defretin is acknowledged for providing historical information on some artifacts. Yong Lei and Huawen Liu from the Palace Museum, Department of Analysis and Conservation and Professor Ludovic Bellot-Gurlet from MONARIS (Laboratoire de la MOlécule au Nano-objet: Réactivité, Interaction & Spectroscopies) are kindly acknowledged for many discussions. This work has been conducted under the framework of the Laboratoire International Associé CNRS–Palace Museum TrEnamel and Campus France PHC-Cai Yuanpei programs.

Conflicts of Interest: The authors declare no conflict of interest.

References

1. Montanari, R.; Alberghina, M.F.; Casanova Municchia, A.; Massa, E.; Pelagotti, A.; Pelosi, C.; Schiavone, S.; Sodo, A. A polychrome Mukozuke (1624–1644) porcelain offers a new hypothesis on the introduction of European enameling technology in Japan. *J. Cult. Herit.* **2018**, *32*, 232–237. [CrossRef]
2. Montanari, R.; Murakami, N.; Alberghina, M.F.; Pelosi, C.; Schiavone, S. The Origin of overglaze-blue enameling in Japan: New discoveries and a reassessment. *J. Cult. Herit.* **2019**, *37*, 94–102. [CrossRef]
3. Montanari, R.; Murakami, N.; Colombari, P.; Alberghina, M.F.; Pelosi, C.; Schiavone, S. European Ceramic technology in the Far East: Enamels and pigments in Japanese art from the 16th to the 20th century and their reverse influence on China. *Herit. Sci.* **2020**, *8*, 48. [CrossRef]
4. Shih, C.F. Evidence of East-West exchange in the eighteenth century: The establishment of painted enamel art at the Qing Court in the reign of Emperor Kangxi. *Natl. Palace Mus. Res. Quarterly* **2007**, *24*, 45–94.
5. Zhou, S.Z. *Research on Painted Enamels Porcelain Ware from the Qing Court*; Wenwu Chubanshe: Beijing, China, 2008.
6. Lili, F. *La Céramique Chinoise*; China Intercontinental Press: Beijing, China, 2011.
7. Xu, X.D. Europe-China-Europe: The Transmission of the Craft of Painted Enamel in the Seventeenth and Eighteenth Centuries. In *Goods from the East, 1600–1800 Trading Eurasia*; Berg, M., Ed.; Houndmills, Basingstoke, Palgrave Macmillan: Hampshire, UK, 2015; pp. 92–106.
8. Zhao, B.; Wang, G.; Biron, I.; Colombari, P.; Hilaire-Pérez, L. La circulation des techniques de l'émail entre la France et la Chine du XVIIème au XIXème siècle. *Le CNRS en Chine Bulletin* **2016**, *21*, 21–25. Available online: http://www.cnrs.fr/derci/IMG/pdf/cnrsenchine_21_fr_final_pour_le_site_cnrs.pdf (accessed on 23 July 2020).
9. Zhou, L.L. Discussion on Falangcai Enamels-and the Difference between Falangcai and Yangcai. *Shanghai Bowuguan Jikan* **2000**, *8*, 210–226.
10. KIRMIZI, B.; Colombari, P.; Quette, B. On-site analysis of Chinese Cloisonné enamels from fifteenth to nineteenth centuries. *J. Raman Spectrosc.* **2010**, *41*, 780–790.
11. Colombari, P.; Arberet, L.; KIRMIZI, B. On-Site Raman Analysis of 17th and 18th Century Limoges Enamels: Implications on the European Cobalt Sources and the Technological Relationship between Limoges and Chinese Enamels. *Ceram. Int.* **2017**, *43*, 10158–10165. [CrossRef]
12. Colombari, P.; Zhang, Y.; Zhao, B. Non-invasive Raman analyses of *huafalang* and related porcelain wares. Searching for evidence for innovative pigment technologies. *Ceram. Int.* **2017**, *43*, 12079–12088. [CrossRef]
13. Colombari, P.; Ambrosi, F.; Ngo, A.-T.; Lu, T.-A.; Feng, X.-L.; Chen, S.; Choi, C.-L. Comparative analysis of wucan Chinese porcelains using mobile and fixed Raman microspectrometers. *Ceram. Int.* **2017**, *43*, 14244–14256. [CrossRef]
14. Colombari, P.; KIRMIZI, B.; Zhao, B.; Clais, J.-B.; Yang, Y. Non-invasive on-site Raman study of pigments and glassy matrix of the 17th–18th century painted enamelled Chinese metal wares: Comparison with French enamelling technology. *Coatings* **2020**, *10*, 471. [CrossRef]
15. Giannini, R.; Freestone, I.C.; Shortland, A.J. European cobalt sources identified in the production of Chinese *famille rose* porcelain. *J. Archaeol. Sci.* **2017**, *80*, 27–36. [CrossRef]
16. Colombari, P.; KIRMIZI, B. Non-invasive on-site Raman study of polychrome and white enamelled glass artefacts in imitation of porcelain assigned to Bernard Perrot and his followers. *J. Raman Spectrosc.* **2020**, *51*, 133–146. [CrossRef]
17. Colombari, P.; Lu, T.-A.; Milande, V. Non-invasive on-site Raman study of blue-decorated early soft-paste porcelain: The use of arsenic-rich (European) cobalt ores—Comparison with *huafalang* Chinese porcelains. *Ceram. Int.* **2018**, *44*, 9018–9026. [CrossRef]

18. Colomban, P.; Kırmızı, B.; Gougeon, C.; Gironde, M.; Cardinal, C. Pigments and glassy matrix of the 17th-18th century enamelled French watches: A non-invasive on-site Raman and pXRF study. *J. Cult. Herit.* **2020**. [CrossRef]
19. Kingery, W.D.; Vandiver, P.B. The Eighteenth-Century Change in Technology and Style from the *Famille-Verte* Palette to the *Famille-Rose* Palette. In *Technology and Style*; Kingery, W.D., Ed.; Ceramics and Civilization Serie; The American Ceramic Society: Columbus, OH, USA, 1986; Volume 2, pp. 363–381.
20. Colomban, P. On-site Raman study of artwork: Procedure and illustrative examples. *J. Raman Spectrosc.* **2018**, *49*, 921–934. [CrossRef]
21. Colomban, P. The on-site/remote Raman analysis with mobile instruments: A review of drawbacks and success in cultural heritage studies and other associated fields. *J. Raman Spectrosc.* **2012**, *43*, 1529–1535. [CrossRef]
22. Vandenabeele, P.; Edwards, H.G.M.; Jehlička, J. The role of mobile instrumentation in novel applications of Raman spectroscopy: Archaeometry, geosciences, and forensics. *Chem. Soc. Rev.* **2014**, *43*, 2628–2649. [CrossRef]
23. Madariaga, J.M. Analytical chemistry in the field of cultural heritage. *Anal. Methods* **2015**, *7*, 4848–4876. [CrossRef]
24. Simsek, G.; Unsalan, O.; Bayraktar, K.; Colomban, P. On-site pXRF analysis of glaze composition and colouring agents of “Iznik” tiles at Edirne mosques (15th and 16th-centuries). *Ceram. Int.* **2019**, *45*, 595–605. [CrossRef]
25. Defretin, J. *La Datation de la Porcelaine “Coquille D’euf” D’exportation du Musée du Louvre, Mémoire, 2nd Cycle—Histoire de L’art Appliquée Aux Collections*; Ecole du Louvre: Paris, France, 2020.
26. Howard, D.S. *Chinese Armorial Porcelain*; Heirloom & Howard Ltd.: London, UK, 2003; Volume 2, p. 155.
27. Tang, H. ‘The Colours of Each Piece’: Production and consumption of Chinese Enamelled Porcelain, c.1728-c.1780. Ph.D. Thesis, Warwick University, Warwick, UK, March 2017. Available online: <http://wrap.warwick.ac.uk/91791> (accessed on 26 June 2020).
28. Colomban, P.; Treppoz, F. Identification and differentiation of ancient and modern European porcelains by Raman macro and micro-spectroscopy. *J. Raman Spectrosc.* **2001**, *32*, 93–102. [CrossRef]
29. Colomban, P.; Sagon, G.; Faurel, X. Differentiation of antique ceramics from the Raman spectra of their coloured glazes and paintings. *J. Raman Spectrosc.* **2001**, *32*, 351–360. [CrossRef]
30. Carty, W.M.; Senapati, U. Porcelain-raw materials, processing, phase evolution, and mechanical behavior. *J. Am. Ceram. Soc.* **1998**, *81*, 3–20. [CrossRef]
31. Sciau, P.; Noé, L.; Colomban, P. Metal nanoparticles in contemporary potters’ masterpieces: Lustre and red “pigeon blood” potteries as models to understand the ancient pottery. *Ceram. Int.* **2016**, *42*, 15349–15357. [CrossRef]
32. Manoun, B.; Azdouz, M.; Azrou, M.; Essehli, R.; Benmokhtar, S.; El Ammari, L.; Ezzahi, A.; Ider, A.; Lazor, P. Synthesis, Rietveld refinements and Raman spectroscopic studies of tricationic lacunar apatites $\text{Na}_{1-x}\text{K}_x\text{Pb}_4(\text{AsO}_4)_3$ ($0 < x < 1$). *J. Mol. Struct.* **2011**, *986*, 1–9.
33. Van Pevenage, J.; Lauwers, D.; Herremans, D.; Verhaeven, E.; Vekemans, B.; De Clercq, W.; Vincze, L.; Moens, L.; Vandenabeele, P. A combined spectroscopic study on Chinese porcelain containing *ruan-cai* colours. *Anal. Methods* **2014**, *6*, 387–394. [CrossRef]
34. Colomban, P.; Maggetti, M.; d’Albis, A. Non-invasive Raman identification of crystalline and glassy phases in a 1781 Sèvres Royal Factory soft paste porcelain plate. *J. Eur. Ceram. Soc.* **2018**, *38*, 5228–5233. [CrossRef]
35. Kissin, S.A. Five element (Ni-Co-As-Ag-Bi) veins. *Geosci. Can.* **1992**, *19*, 113–124.
36. Colomban, P. Rocks as blue, green and black pigments/dyes of glazed pottery and enamelled glass artefacts—A review. *Eur. J. Mineral.* **2014**, *25*, 863–879. [CrossRef]
37. Berrie, B.H. Mining for Color: New Blues, Yellows, and Translucent Paint. *Early Sci. Med.* **2015**, *20*, 308–334. [CrossRef]
38. Pradell, T.; Molina, G.; Molera, J.; Pla, J.; Labrador, A. The use of micro-XRD for the study of glaze color decorations. *Appl. Phys. A* **2013**, *111*, 121–127. [CrossRef]
39. Viti, C.; Borgia, I.; Brunetti, B.; Sgamellotti, A.; Mellini, M. Microtexture and microchemistry of glaze and pigments in Italian Renaissance pottery from Gubbio and Deruta. *J. Cult. Herit.* **2003**, *4*, 199–210. [CrossRef]
40. Pérez-Arantegui, J.; Resano, M.; Garcia-Ruiz, E.; Vanhaecke, F.; Roldan, C.; Ferrero, J.; Coll, J. Characterization of cobalt pigments found in traditional Valencian ceramics by means of laser ablation-inductively coupled

- plasma mass spectrometry and portable X-ray fluorescence spectrometry. *Talanta* **2008**, *74*, 1271–1280. [CrossRef] [PubMed]
41. Pérez-Arantegui, J.; Montull, B.; Resano, M.; Ortega, J.M. Materials and technological evolution of ancient cobalt-blue-decorated ceramics: Pigments and work patterns in tin-glazed objects from Aragon (Spain) from the 15th to the 18th century AD. *J. Eur. Ceram. Soc.* **2009**, *29*, 2499–2509. [CrossRef]
 42. Colomban, P.; Sagon, G.; Huy, L.Q.; Liem, N.Q.; Mazerolles, L. Vietnamese (15th century) blue-and-white, tam thai and “luster” porcelains/stoneware: Glaze composition and decoration techniques. *Archaeometry* **2004**, *46*, 125–136. [CrossRef]
 43. Figueiredo, M.O.; Silva, T.P.; Veiga, J.P. A XANES study of cobalt speciation state in blue-and-white glazes from 16th to 17th century Chinese porcelains. *J. Electr. Spectrosc. Relat. Phenom.* **2012**, *185*, 97–102. [CrossRef]
 44. Dias, M.I.; Prudêncio, M.I.; de Matos, M.A.P.; Rodrigues, A.L. Tracing the origin of blue and white Chinese Porcelain ordered for the Portugese market during the Ming dynasty using INAA. *J. Archaeol. Sci.* **2013**, *40*, 3046–3057. [CrossRef]
 45. Simsek, G.; Colomban, P.; Wong, S.; Zhao, B.; Rougeulle, A.; Liem, N.Q. Toward a fast non-destructive identification of pottery: The sourcing of 14th–16th century Vietnamese and Chinese ceramic shards. *J. Cult. Herit.* **2015**, *16*, 159–172. [CrossRef]
 46. Fischer, C.; Hsieh, E. Export Chinese Blue-and-white porcelain: Compositional analysis and sourcing using non-invasive portable XRF and reflectance spectroscopy. *J. Archaeol. Sci.* **2016**, *80*, 14–26. [CrossRef]
 47. Sandalinas, C.; Ruiz-Moreno, S. Lead-tin-antimony yellow—Historical manufacture, molecular characterization and identification in seventeenth-century Italian paintings. *Stud. Conserv.* **2004**, *49*, 41–52. [CrossRef]
 48. Sandalinas, C.; Ruiz-Moreno, S.; Lopez-Gil, A.; Miralles, J. Experimental confirmation by Raman spectroscopy of a Pb-Sn-Sb triple oxide yellow pigment in sixteenth-century Italian pottery. *J. Raman Spectrosc.* **2006**, *37*, 1146–1153. [CrossRef]
 49. Pereira, M.; de Lacerda-Aroso, T.; Gomes, M.J.M.; Mata, A.; Alves, L.C.; Colomban, P. Ancient Portuguese ceramic wall tiles (Azulejos): Characterization of the glaze and ceramic pigments. *J. Nano Res.* **2009**, *8*, 79–88. [CrossRef]
 50. Rosi, F.; Manuali, V.; Miliani, C.; Brunetti, B.G.; Sgamellotti, A.; Grygar, T.; Hradil, D. Raman scattering features of lead pyroantimonate compounds. Part I: XRD and Raman characterization of Pb₂Sb₂O₇ doped with tin and zinc. *J. Raman Spectrosc.* **2009**, *40*, 107–111. [CrossRef]
 51. Pelosi, C.; Agresti, G.; Santamaria, U.; Mattei, E. Artificial yellow pigments: Production and characterization through spectroscopic methods of analysis. *E-Preserv. Sci.* **2010**, *7*, 108–115.
 52. Kirmizi, B.; Colomban, P.; Blanc, M. On-site Analysis of Limoges enamels from 16th to 19th centuries. *J. Raman Spectrosc.* **2010**, *41*, 1240–1247. [CrossRef]
 53. Dik, J.E.; Hermens, R.; Peschar, H. Schenk, Early production recipes for lead antimonite yellow in Italian art. *Archaeometry* **2005**, *47*, 593–607. [CrossRef]
 54. Dik, J. Scientific analysis of historical paint and the implications for art history and art conservation. The case studies of naples yellow and discoloured smalt. Doctorate Thesis, University of Amsterdam, Amsterdam, The Netherlands, 2003. Available online: <https://dare.uva.nl/search?identifier=98d80b7d-a63e-450b-a984-611a3d0c0cfe> (accessed on 14 August 2020).
 55. Bell, I.M.; Clark, R.J.H.; Gibbs, P.J. Raman spectroscopic library of natural and synthetic pigments (pre-~1850 AD). *Spectrochim. Acta Part A* **1997**, *53*, 2159–2179. [CrossRef]
 56. Colomban, P. The destructive/non-destructive identification of enamelled pottery and glass artifacts and associated pigments—A brief overview. *Arts* **2013**, *2*, 77–110. [CrossRef]
 57. Neri, E.; Morvan, C.; Colomban, P.; Guerra, M.P. Prigent, Late Roman and Byzantine Mosaic opaque Glass-ceramics Tesserae (5th–9th century). *Ceram. Int.* **2016**, *42*, 18859–18869. [CrossRef]
 58. Rosi, F.; Manuali, V.; Grygar, T.; Bezdicka, P.; Brunetti, B.G.; Sgamellotti, A.; Burgio, L.; Seccaroni, C.; Miliani, C. Raman scattering features of lead pyroantimonate compounds: Implication for the non-invasive identification of yellow pigments on ancient ceramics. Part II. In situ characterisation of Renaissance plates by portable micro-Raman and XRF studies. *J. Raman Spectrosc.* **2011**, *42*, 407–414. [CrossRef]
 59. Cartechini, L.; Rosi, F.; Miliani, C.; D’Acapito, F.; Brunetti, B.G.; Sgamellotti, A. Modified Naples yellow in Renaissance majolica: Study of Pb-Sb-Zn and Pb-Sb-Fe ternary pyroantimonates by X-ray absorption spectroscopy. *J. Anal. Atom. Spectrom.* **2011**, *26*, 2500–2507. [CrossRef]

60. Biron, I.; Chopinet, M.-H. Colouring, Decolouring and Opacifying Glass. In *Modern Methods for Analysing. Archaeological and Historical Glass*, 1st ed.; Janssens, K., Ed.; John Wiley & Sons Ltd.: London, UK, 2012; pp. 49–66.
61. Verita, M.; Maggetti, M.; Sagui, L.; Santopadre, P. Colors of Roman Glass: An Investigation of the Yellow Sectilia in the Gorga Collection. *J. Glass Stud.* **2013**, *55*, 21–34.
62. Froment, F.; Tournié, A.; Colomban, P. Raman identification of natural red to yellow pigments: Ochre and iron-containing ores. *J. Raman Spectrosc.* **2008**, *39*, 560–568. [CrossRef]
63. Owens, F.J.; Orosz, J. Effect of nanosizing on lattice and magnon modes of hematite. *Solid State Commun.* **2006**, *138*, 95–98. [CrossRef]
64. Hunt, L.B. The true story of Purple of Cassius. *Gold Bull.* **1976**, *9*, 134–139. [CrossRef]
65. Colomban, P. The Use of Metal Nanoparticles to Produce Yellow, Red and Iridescent Colour, from Bronze Age to Present Times in Lustre Pottery and Glass: Solid State Chemistry, Spectroscopy and Nanostructure. *J. Nano Res.* **2009**, *8*, 109–132. [CrossRef]
66. Geysant, J. Secret du verre rouge transparent de Bernard Perrot et comparaison avec celui de Johann Kunckel. In *Bernard Perrot (1640-1709): Secrets et Chefs-d'œuvre des Verreries Royales d'Orléans, Catalogue*; Musée des Beaux-Arts d'Orléans, SOMOGY Editions d'Arts: Paris, France, 2010; pp. 51–54.
67. Louis, C. Gold nanoparticles in the past: Before the Nanotechnology Era. In *Gold Nanoparticles for Physics, Chemistry and Biology*; Louis, C., Pluchery, O., Eds.; Imperial College Press: London, UK, 2012; pp. 1–27.
68. Colomban, P. Polymerisation Degree and Raman Identification of Ancient Glasses used for Jewellery, Ceramics Enamels and Mosaics. *J. Non-Cryst. Solids* **2003**, *323*, 180–187. [CrossRef]
69. Colomban, P.; Tournié, A.; Bellot-Gurlet, L. Raman Identification of glassy silicates used in ceramic, glass and jewellery: A tentative differentiation guide. *J. Raman Spectrosc.* **2006**, *37*, 841–852. [CrossRef]
70. Colomban, P.; Paulsen, O. Non-destructive Raman Determination of the Structure and Composition of Glazes by Raman Spectroscopy. *J. Am. Ceram. Soc.* **2005**, *88*, 390–395. [CrossRef]
71. Colomban, P. *Non-Destructive Raman Analysis of Ancient Glasses and Glazes*, in *Modern Methods for Analysing Archaeological and Historical Glass*, 1st ed.; Janssens, K., Ed.; John Wiley & Sons Ltd.: London, UK, 2012; pp. 275–300.
72. Labet, V.; Colomban, P. Vibrational properties of silicates: A cluster model able to reproduce the effect of “SiO₄” polymerization on Raman intensities. *J. Non-Cryst. Solids* **2013**, *370*, 10–17. [CrossRef]
73. Su, Y.; Qu, L.; Duan, H.; Tarcea, N.; Shen, A.; Popp, J.; Hu, J. Elemental analysis-aided Raman spectroscopic studies on Chinese cloisonné wares and painted enamels from the Imperial palace. *Spectrochim. Acta A-Mol. Biomol. Spectrosc.* **2016**, *153*, 165–170. [CrossRef] [PubMed]
74. Henderson, J.; Tregear, M.; Wood, N. The technology of sixteenth- and seventeenth century Chinese Cloisonné enamels. *Archaeometry* **1989**, *31*, 133–146. [CrossRef]
75. Shih, C.F. *Radiant Luminance: The Painted Enamelware of the Qing Imperial Court*; The National Palace Museum of Taipei: Taipei, Taiwan, 2012.
76. Wood, N. *Chinese Glazes: Their Origins, Chemistry and Recreation*; A & C Black: London, UK, 1999.
77. Shi, N.C. Analyse Scientifique des Couleurs Falang D'objets Conservés au Palais ou Retrouvés en Contexte Archéologique. In Proceedings of the French-Chinese Meeting on Enamelling Technology, Collège de France, Paris, France, 10 September 2019.



© 2020 by the authors. Licensee MDPI, Basel, Switzerland. This article is an open access article distributed under the terms and conditions of the Creative Commons Attribution (CC BY) license (<http://creativecommons.org/licenses/by/4.0/>).

Article

On-Site VIS-NIR Spectral Reflectance and Colour Measurements—A Fast and Inexpensive Alternative for Delineating Sediment Layers Quantitatively? A Case Study from a Monumental Bronze Age Burial Mound (Seddin, Germany)

Vincent Haburaj ^{1,*} , Moritz Nykamp ¹ , Jens May ², Philipp Hoelzmann ¹ and Brigitta Schütt ¹ 

¹ Freie Universität Berlin, Institute of Geographical Sciences, 12249 Berlin, Germany;

m.nykamp@fu-berlin.de (M.N.); philipp.hoelzmann@fu-berlin.de (P.H.); brigitta.schuett@fu-berlin.de (B.S.)

² Brandenburgisches Landesamt für Denkmalpflege und Archäologisches Landesmuseum, 15806 Zossen, Germany; jens.may@bldam-brandenburg.de

* Correspondence: vincent.haburaj@fu-berlin.de

Received: 22 May 2020; Accepted: 19 June 2020; Published: 25 June 2020

Abstract: Quantitative sediment analyses performed in the laboratory are often used throughout archaeological excavations to critically reflect on-site stratigraphic delineation. Established methods are, however, often time-consuming and expensive. Recent studies suggest that systematic image analysis can objectivise the delineation of stratigraphic layers based on fast quantitative spectral measurements. The presented study examines how these assumptions prevail when compared to modern techniques of sediment analysis. We examine an archaeological cross-section at a Bronze Age burial mound near Seddin (administrative district Prignitz, Brandenburg, Germany), consisting of several layers of construction-related material. Using detailed on-site descriptions supported by quantitatively measured sediment properties as a measure of quality, we compare clustering results of (i) extensive colour measurements conducted with an RGB and a multispectral camera during fieldwork, as well as (ii) selectively sampled sedimentological data and (iii) visible and near infrared (VIS-NIR) hyperspectral data, both acquired in the laboratory. Furthermore, the influence of colour transformation to the CIELAB colour space (Commission Internationale de l’Eclairage) and the possibilities of predicting soil organic carbon (SOC) based on image data are examined. Our results indicate that quantitative spectral measurements, while still experimental, can be used to delineate stratigraphic layers in a similar manner to traditional sedimentological data. The proposed processing steps further improved our results. Quantitative colour measurements should therefore be included in the current workflow of archaeological excavations.

Keywords: digital archaeology; image classification; stratigraphy; landscape archaeology; sediment analysis; spectroscopy; proximal sensing

1. Introduction

Stratigraphic documentation and interpretation are crucial parts of archaeological research. Since the emergence of the archaeological discipline, researchers have been concerned with the identification of methods that allow more objectivity in stratigraphic delineation and interpretation. The fundamental work of, e.g., Harris [1] is meanwhile complemented by a progressing digitisation of fieldwork (e.g., [2]) and a growing number of on-site measurements and analyses carried out in various

laboratories in the aftermath of an excavation. These techniques comprise, e.g., the establishment of soil colour standards (cf. [3,4]), geochemical analyses of sediments (e.g., [5–7]), the analysis of thin sections (e.g., [8]), or the analysis of pollen [9] and phytoliths [10].

The overall objectivity of stratigraphic interpretation clearly benefits from these techniques. Nevertheless, the initial on-site delineation of stratigraphic layers (i.e., stratigraphic documentation) remains partly influenced by the perception of the respective researcher at work. As pointed out by Zhang and Hartemink [11] and Haburaj et al. [12], statistical analysis of RGB and multispectral images of soil profiles can be utilised to semi-automatically delineate stratigraphic units. These derived units are based on the physical measurement of the sediments' spectral reflectance and allow the respective researcher to critically face up to his or her delineation.

Building upon these developments, our study further explores the potential of visible and near-infrared (VIS-NIR, 400–700–2500 nm) spectral data for archaeological fieldwork. Due to its non-destructive character and the moderate extent of necessary sample preparation, spectroscopy in general has the potential to save time and costs during fieldwork (e.g., [12–15]). Working with an archaeological cross-section from a Bronze Age burial mound from Brandenburg, northern Germany, we investigate how traditional geochemical sediment analyses, selective spectroscopic measurements, and extensive RGB and multispectral image data can be used to objectivise archaeological field documentation by quantitatively capturing stratigraphic layers. Using a detailed on-site description supported by quantitatively measured sediment properties (grain size composition, water content, and soil organic carbon content) as a measure of quality, we compare clustering results of (i) extensive colour measurements (i.e., image data) acquired with an RGB and a multispectral camera during fieldwork, as well as clustering results of selectively sampled (ii) portable energy-dispersive X-ray fluorescence spectrometer (p-ED-XRF) data and (iii) visible and near infrared (VIS-NIR) hyperspectral data, both acquired in the laboratory. This experimental approach allows us to illustrate the benefits and shortcomings of systematic spectral measurements as a complementary or alternative method for stratigraphic documentation, delineation, and interpretation.

The characteristics of the recorded diffuse reflectance spectra of the sediments are directly linked to their chemical and physical composition (e.g., [13]). Within the last two decades, an increasing number of publications were devoted to the prediction of soil properties via VIS-NIR spectroscopy (e.g., [16–20]). Soriano-Disla et al. [21] deliver an extensive overview on the predictability of multiple soil properties via visible, near-infrared, and mid-infrared spectral data. We therefore examined how the conducted image classification performs when using additional input data: We were able to calibrate a prediction model for soil organic carbon (SOC) based on the recorded spectral signal and created a raster containing predicted SOC values for the entire profile. Several authors have argued that the CIELAB colour space (Commission Internationale de l'Éclairage) shows a clear benefit regarding quantitative analyses (e.g., [22–27]). The CIELAB colour space consists of three values: L^* is the vertical axis and is defined by lightness, while a^* and b^* represent the chromaticity (a^* : Red/green; b^* : Yellow/blue). We examined colour transformation to the CIELAB colour space, as it was found to be highly effective when analysing soil profiles (e.g., [28]). Hereby, our overarching aim remains the delineation of stratigraphic layers rather than the quantitative examination of sediment properties.

Our results indicate the importance of quantitatively measuring sediment colours—be it selective or extensive—as they constitute an additional layer of documentation during an archaeological excavation, which can be acquired easily and render the on-site archaeological documentation and interpretation more transparent and reproducible. The study at hand is presented as an experimental investigation, which allows us to assess the potential of VIS-NIR spectral sensors for archaeological fieldwork.

Study Site

The Bronze Age burial mound of Seddin (colloquial: ‘King’s Grave’, German: Königsgrab Seddin), which was discovered in 1899, is widely known for its tremendous size and the valuable funerary goods made from bronze, iron, glass, and stone (e.g., [29–31]). It was dated to approximately 800 BC (period V of the Nordic Bronze Age) and has a central role in the regional cultural landscape, which today covers the north-west of the federal state of Brandenburg and southern Mecklenburg [32,33]. While past studies found the surroundings of the burial mound to be heavily shaped by human influence, which occurred during the Bronze Age [31,34], the ‘King’s Grave’ keeps an outstanding position, both regarding its geographical location and its rich physical characteristics. Estimates by May [35] see the total height of the mound between eight and ten metres. The burial mound is separated spatially from smaller groups of burial mounds in the surrounding area. It is located on a slight spur, surrounded by multiple waterbodies [31]: 900 m east of the burial mound runs the river Stepenitz, and in the north and south, two of the river’s tributaries delimit the burial mound from its surroundings (Figure 1). The parent material is dominated by Pleistocene deposits, composed mostly of fine to coarse glaciofluvial sand with little or no gravel [36]. West and south of the burial mound, clayey to sandy silt can be found. In the hollows, associated with the two tributaries of the Stepenitz (Figure 1), muck soil of a sand–humus mixture dominates, which overlies fluvial and periglacial deposits [36]. The relief of the surrounding landscape is characterised by a smooth, rather levelled topography that is dissected by depressions and river valleys. Regarding the wider vicinity, several burial mounds of similar size are known but have mostly been destroyed and lack any archaeological record [31,37]. Regardless of the nature of these undocumented burial mounds, their sheer amount reflects the importance of this landscape during the late Bronze Age. Brunke et al. [38] see the ‘King’s Grave’ of Seddin as the clearest manifestation of an accumulation of wealth and power in this area around the middle reaches of the Stepenitz.

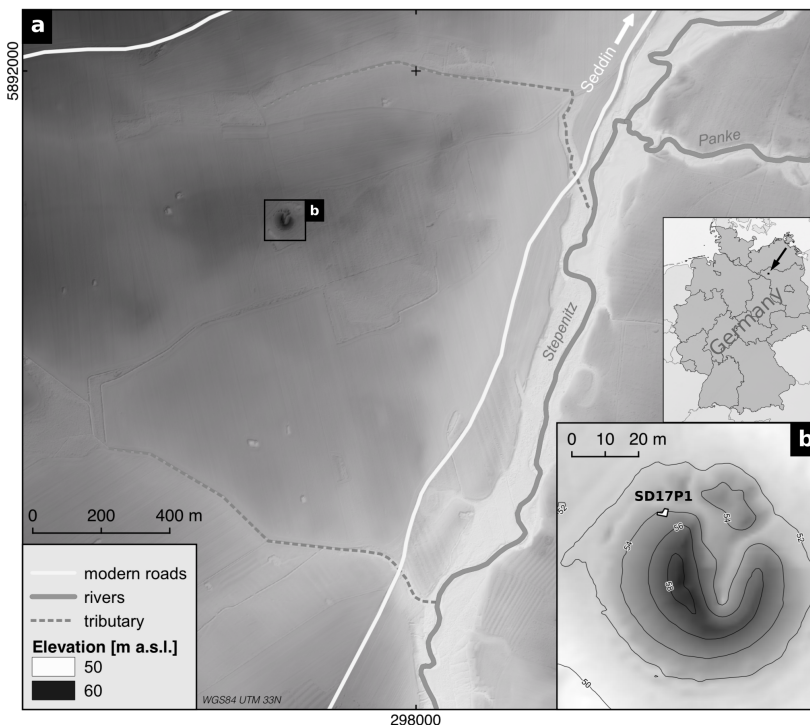


Figure 1. Location of the study site: (a) Surroundings of the burial mound; (b) location of section SD17P1. Elevation data: LiDAR-based DEM (1×1 m) by Geobasis-DE/LGB 2013 (R. Hesse; modified).

Within this study, we examine section SD17P1 (297601 E, 5891584 N; WGS84; UTM 33N), which was documented in 2017 during an excavation on the north-western slope of the Bronze

Age burial mound of Seddin. The investigated section faces north, is approximately 3.2 m high, and consists mainly of anthropogenic layers: Only the lowermost 20–40 cm are interpreted as the buried local soil (Figure 2c,E), which was dated by three ^{14}C -AMS ages to the ninth century BC [33]. The remaining part of the profile consists of discrete layers, which were piled up during the construction of the burial mound with alternating layers of stone and sand that were deposited on top of each other. In addition, there is a horizontally running, thin, dark layer, which crosses the lowest artificial sand layer (Figure 2c,C). The type of construction with stone layers at hand is congruent with the findings of Brunke et al. [38], who examined the south-eastern side of the burial mound in 2013. However, the diagonal segmentation and orientation of sand layers B and D is only present in SD17P1. The topmost stone layer of SD17P1 most likely represents the Bronze Age surface, which would, in addition to the prominent position of the mound, emphasise its monumental character (cf. [33]).

All analyses carried out in this study focus on the parts of the profile that lie above the lowest layer of stones, which is approximately 200 cm below the surface of the burial mound. Layer E (local soil) is therefore excluded from the processing (Figure 2c).

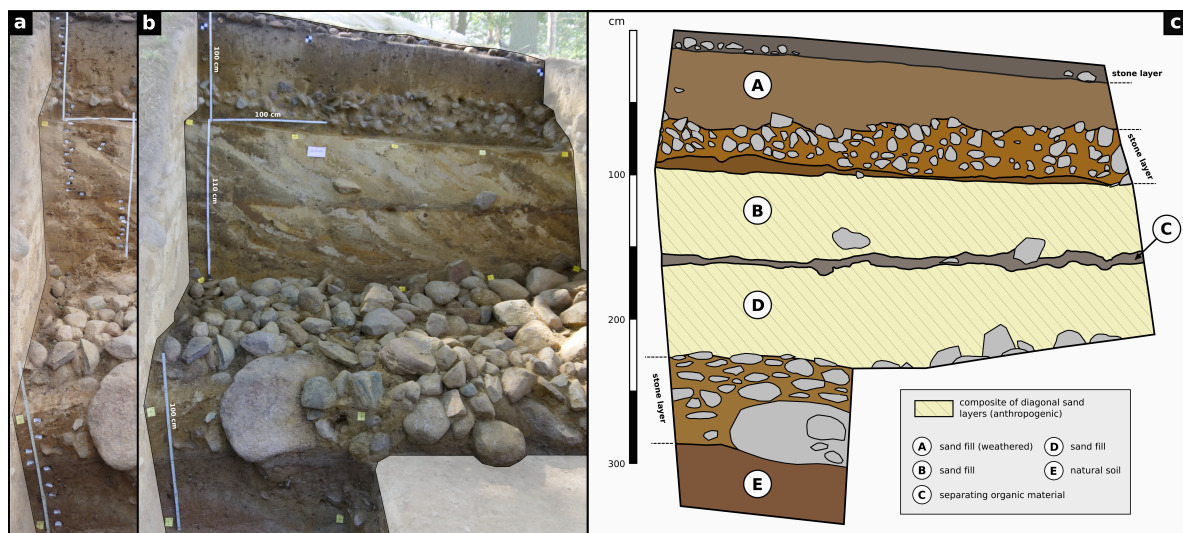


Figure 2. Archaeological section examined. (a) Location of the sediment samples taken; (b) overview of the section; (c) drawing of the archaeological section examined. Layers A to D are part of the anthropogenically created burial mound. Layers B and D consist of numerous diagonal layers, which are summarised here. Colour and texture of the sediments were documented during fieldwork and are presented in Figure 5 along with the sedimentological record (Section 3.1). Layer E is interpreted as the local soil that was buried during the construction of the burial mound [33] and is excluded from all analyses.

2. Materials and Methods

Our experimental design involves the measurement of selective data based on sediment samples extracted from the archaeological profile and extensive image data acquired during fieldwork. The workflow is depicted in Figure 3, and a more detailed documentation of the data processing along with scripts for the programming language R is given in Online Resources 1–3 (in Supplementary Materials).

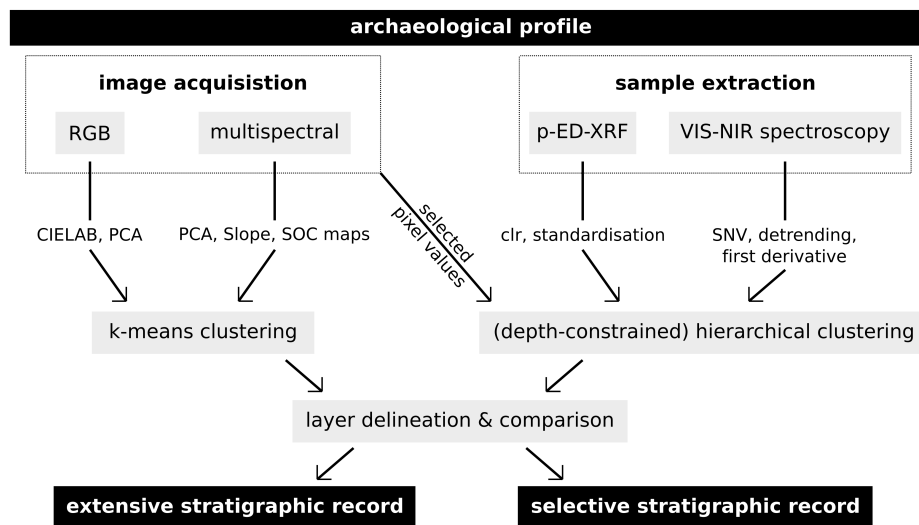


Figure 3. Schematic depiction of our workflow. Image processing included principle component analysis (PCA), derivation of slope rasters, colour transformation to CIELAB (Commission Internationale de l’Eclairage), and the prediction of soil organic carbon (SOC). The standardised centred log ratio (clr) of the data acquired with the portable energy-dispersive X-ray fluorescence spectrometer (p-ED-XRF) was used. Spectroscopic measurements of the sampled material were processed using standard normal variate (SNV) transformation with detrending applied to the first derivative of the $\log(1/R)$ transformed spectrum. This allowed us to create stratigraphic delineations based on extensive and selective data and to compare the performance of colour and spectral measurements to traditional p-ED-XRF data.

2.1. Laboratory Sediment Analyses

Analyses were performed using the topmost 31 samples, extracted from the eastern part of the profile and vertically covering a depth of 6 to 194 cm, thus excluding the natural soil of layer E (Figure 2a). Samples were extracted and stored in airtight bags to minimise errors when measuring water content. We densely sampled layers B and D to consequently capture the variability between the single obliquely bedded sand layers. Stratigraphic (sub)layers were described regarding colour and texture using the Munsell soil colour chart [39] and the German manual of soil mapping [40] respectively.

Further laboratory analyses of the sediments followed after the determination of the water content and sample preparation, including crushing of aggregates, separation of coarse components with a 2-mm sieve, and homogenising of the subsamples for carbon and portable energy-dispersive X-ray fluorescence spectrometer (p-ED-XRF) analyses in a vibrating disc mill.

2.1.1. Water Content

The water content was determined gravimetrically. The moist samples were weighed, heated in a drying cabinet at 105 °C until a constant weight was reached, cooled down to room temperature in a desiccator, and weighed again. The water content was calculated according to [41] and reported in mass%.

2.1.2. Soil Organic Carbon

The total carbon content of the samples was determined using a TruSpec CHN analyser by Leco (St. Joseph, Michigan, USA). Additionally, a small portion of the powdered material from all samples was tested for its carbonate content using 9.9% HCl acid. None of the samples showed signs of carbonate, which is why the measured total carbon content is interpreted as the total organic carbon content. During measurement, the samples were dry combusted at 950 °C in an oxygen atmosphere, and carbon fluxes were quantified by infrared spectroscopy. The results were calibrated using certified

reference material (CRM; Leco 502–309; 12.29 ± 0.37 mass% C; Leco 502–308; 3.6 ± 0.29 mass% C; reproducibility was <2% RSD) and are reported as soil organic carbon (SOC) in mass%.

2.1.3. pH Value

The pH values of the samples were measured in a 1:2.5 solution of 10 g of dried sediment and 25 mL of 0.01 M KCl using a handheld pH meter (Hanna Instruments, Woonsocket, Rhode Island, USA) with a resolution of 0.1.

2.1.4. Grain Size

The particle size distribution for the fraction ≤ 1 mm was determined with a laser diffraction particle size analyser LS13 320 by Beckman-Coulter (Brea, California, USA). The samples were sieved with a 1-mm sieve and bi-distilled water together with about 0.5 g $\text{Na}_4\text{P}_2\text{O}_7$ as an anti-coagulation agent. The samples were placed in an overhead shaker for 24 h and ultrasonic treated for 5 min directly before the measurement. The prepared samples were put into a liquid sample divider and two subsamples were measured with three independent runs each. The six measurements per sample were averaged to obtain the sample's grain size distribution [42]. Particle sizes are defined according to [40] and reported in vol%.

2.1.5. Element Concentrations

Analysis of element concentrations was conducted with a Niton XL3t portable energy-dispersive X-ray fluorescence spectrometer (p-ED-XRF) by Thermo Scientific (Waltham, Massachusetts, USA). Internal parameter calibration was set to 'mining mode' and all measurements were recorded in %. Two certified reference materials (CRMs) were used for quality control: GBW07312 (stream sediment; National Research Center for Certified Reference Materials in China) and NCS DC 73387 (soil; China National Analysis Center for Iron and Steel). The CRMs were measured repeatedly after every eight samples. Since this study does not examine any absolute elemental concentrations but, rather, the overall variability throughout the profile, the CRMs were used only to ensure validity of the measured data. Recovery values were therefore not examined quantitatively.

Further processing of the p-ED-XRF data was necessary to produce reliable measurement results. Measurements with a value smaller than or equal to three times the $1-\sigma$ error were discarded. Following Schmidt et al. [43], the remaining results were analysed using a compositional data approach to manage the consistent sum-constrained model [44] via R [45]. Elements were only processed if the number of values below the limit of detection did not exceed 10% of the respective measurements. Subsequently, the data were transformed using centred log-ratio (clr; [44]):

$$z = clr(x) = [\ln(x_1/g(x)), \ln(x_2/g(x)), \dots, \ln(x_D/g(x))], \quad (1)$$

where $g(x) = [x_1 \times x_2 \times \dots \times x_D] \times 1/D$ is the geometric mean of all parts of the observation $x = [x_1, x_2, \dots, x_D]$. This transformation was conducted using the compositions package for R [46]. Prior to the conducted cluster analysis, the data were additionally standardised using a robust z-transformation.

2.1.6. Visible and Near-Infrared Spectroscopy

Visible and near-infrared reflectance of the sediment samples was captured using an FieldSpec II spectroradiometer by ASD (Malvern, Worcestershire, UK). Samples were measured before and after homogenisation. This allowed us to indicate an influence of material, which may be coating quartz grains and, therefore, over-represented in the unground samples (e.g., fine clay or Fe oxides, see [21]), and likewise to assess the general influence of grinding and homogenisation on sediment colour [47]. Reflectance was measured between 350 and 2500 nm in 1 nm steps. Measurements were acquired in a darkroom, where each sample was uniformly illuminated by two halogen lamps to minimise the casting of shadows. Samples were spread homogeneously on a plate, and the fibre optic cable of the

spectroradiometer was placed above the samples (Online Resource 3 in Supplementary Materials). Each spectrum was averaged from 50 single measurements to compensate for uneven sediment texture. A white reference was captured every 15 min to minimise variation between the measurements and to acquire normalised reflectance values in the range [0, 1].

The raw spectral information showed a high noise content below 450 nm and above 2300 nm, as well as several smaller aberrations. The spectra were therefore smoothed using a Savitzky–Golay filter of second polynomial order with a width of 21 values [48]. This was conducted with the *hsdar* package for R [49]. Due to the high amount of noise below 450 nm, the spectral data were limited to the range between 450 and 2500 nm for further processing (Figure 4).

Several studies recommend analysing spectral absorbance rather than spectral reflectance (e.g., [23,50]). Spectral reflectance R was therefore transformed into absorbance $A = \log(1/R)$, which allows for a better correlation of the signal with sedimentological data.

As an increase of overall reflectance was observed after homogenisation of the samples, several processing steps were carried out to compensate for this (Figure 4). Building upon Stenberg et al. [50], baseline correction was conducted by calculating the first derivative, which eliminated the existing baseline shift [51]. Furthermore, this step enhanced weak spectral signals. Since this step also introduced additional noise, the baseline corrected spectra were then smoothed using a Savitzky–Golay filter of second polynomial order with a width of 21 values. Subsequently, scatter correction was performed by a standard normal variate (SNV) transformation and de-trending [52]. These pre-processing steps allow for the direct comparison of the spectra of homogenised and non-homogenised samples as well as an enhancement of relevant spectral peaks and a reduction of, e.g., overall curvature [50]. A more detailed documentation of the workflow is delivered in Online Resource 3 (Supplementary Materials).

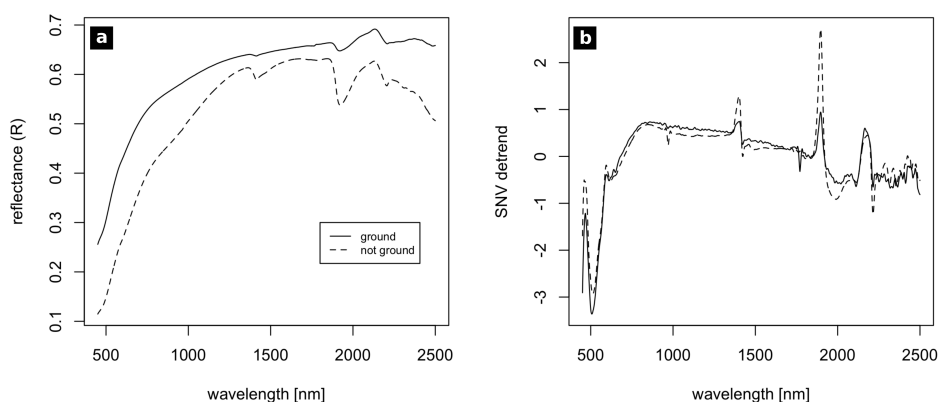


Figure 4. Exemplary spectral signal (450–2500 nm, sample no. 10) before (a) and after (b) pre-processing. Standard normal variate (SNV) transformation with detrending was applied to the first derivative of the $\log(1/R)$ transformed spectrum.

2.2. Image Acquisition

Digital RGB photographs of section SD17P1 were taken using a 24.3 MP mirrorless camera with a 2.8/16 mm lens (Sony ILCE-6000, Sony SEL-16F28, by Sony, Tokyo, Japan). Multispectral imaging was carried out using a Micro-MCA snapshot camera with six spectral channels (Table 1) by TetraCam (Chatsworth, California, USA). Central wavelengths and FWHM (full width half maximum) of the Sony ILCE-6000 RGB camera have been previously published by Haburaj et al. [12] and used throughout this study.

Using optical measurement systems, the lighting of the profile needs to be controlled and documented. Images were captured under natural diffuse daylight. Apart from smaller diffuse shadows in the corners, the section was captured under uniform lighting conditions. The cameras were placed on a tripod and centred in front of the respective section. Rotation of the cameras was limited

to a minimum, and black-and-white reference targets were placed in the section, which allowed us to overlay and merge images manually afterwards while keeping spatial distortions at a minimum.

Table 1. Technical specifications of the camera systems used; central wavelengths of the spectral channels blue, green, red, red edge, NIR1, and NIR2.

	Sony ILCE-6000	TetraCAM MicroMCA-6
B	485 nm	490 nm
G	540 nm	550 nm
R	595 nm	680 nm
red edge	-	720 nm
NIR1	-	800 nm
NIR2	-	900 nm
spatial resolution	5696 × 4272 px	1280 × 1024 px
colour depth	8 bit	10 bit

The RGB images were converted into 8-bit TIF format and normalised to the range [0, 1] via feature-scaling. Six multispectral images were recorded in TetraCam RWS-format (each containing one spectral channel and stored in three 8-bit layers, labelled red, green, and blue) and, to allow further processing, converted into six 10-bit TIF-format images using the formula provided by the manufacturer.

Since the used multispectral camera consists of an array of six separate cameras and the images were acquired from a distance of approximately five metres, a significant spatial offset between the spectral channels was present and required manual band alignment. The proprietary processing software PixelWrench2 contains an option for minimising this offset, which was used successfully by, e.g., Retzlaff [53]. This solution, however, is more suitable for images acquired during remote sensing, as they keep a certain minimal distance from the subject, therefore keeping the spatial offset at acceptable levels. Our ground-based approach, on the contrary, included an offset that was too high and, therefore, was corrected through the pairwise manual selection of reference points. The resulting multispectral images were normalised to the range [0, 1] via feature scaling.

2.3. Image Analysis

2.3.1. Image Pre-Processing

To allow for the comparison of the classification results via spatially consistent image data, the recorded RGB and multispectral images were processed by manually registering 12 reference points (overlapping geometries and artificial black-and-white targets) for thin plate spline [54] transformation (TPS) with nearest neighbour resampling, carried out with the Georeferencer plugin in QGIS (v2.18). This resulted in overlying images, which are necessary to assess the quality of the final results. All non-sediment objects captured in the images were masked manually. Aside from external disturbances like grass patches and other vegetation, this included the prehistoric stone layers that are separating the sediment layers from one another (Figure 2). This step was conducted using the raster package for R [55]. Minimising the impact of image noise and smaller disturbances within the profile, the images were filtered spatially using the raster package for R [55]. To keep the geometric alteration as low as possible and, likewise, to minimise the influence of outliers, we chose a median filter with a window size of 21 by 21 pixels (multispectral data) and 101 by 101 pixels (RGB data) for spatial filtering. The window size was scaled according to the respective spatial resolution and set to quite high values, since our main interest was in the main strata. The sediment layers examined did not include flakes of, e.g., brick, charcoal, or mortar, which renders the loss of texture detail in the image data acceptable [12].

2.3.2. Slope Rasters

Various derivatives of raster data show a positive impact on classification results. According to Haburaj et al. [12], the spectral slope between red, green, and blue channels—while introducing more noise—can help to identify organic material in the images. Slope rasters were therefore created for both the RGB and the multispectral image data, leading to two and five additional raster layers, respectively.

2.3.3. Principal Component Analysis

Additional raster layers were created by performing a principle component analysis (PCA, conducted via [56]) on the RGB image and the multispectral image. The number of principle components was set to two, since this delivered an acceptable explained cumulative variance (Online Resource 1 in Supplementary Materials).

2.3.4. CIELAB

The colour spaces CIELAB, CIE-Yxy, and Munsell are suited for the analysis of iron oxide content in soils and sediments [57,58]. The CIELAB colour space shows a clear benefit regarding quantitative analyses and was used throughout the presented study, since CIELAB coordinates are often influenced by soil and sediment properties: CIELAB lightness L^* is often regarded to be related with organic matter, and CIELAB chromaticity coordinates a^* and b^* were proven to be related with different iron oxide concentrations (cf. [27,57,59]). While these relations are measurable, authors generally conclude that the specific relation is highly dependent on the material examined and often cannot be transferred between different soil types [27].

The recorded image data were therefore transformed into the CIELAB colour space using the `convertColor()` function for R. The CIE standard illuminant D65 was used as reference white, since its properties are close to real indirect daylight as present during fieldwork. The multispectral data were modified so that only the red, green, and blue bands were transformed. The produced raster layers were used as additional input for classification with the intent of adding a rough measurement of lightness and, more importantly, iron oxide content.

2.3.5. Soil Organic Carbon

Numerous studies have examined the prediction of soil organic carbon (SOC) via the spectral signal [17–20,60–63]. Most recent publications tend to stress the better accuracy of machine learning algorithms [13], especially when predicting more complex soil properties. For the prediction of SOC, however, linear regression models have proven to deliver robust predictions with acceptable accuracy. Since our study solely aims for the rough delineation of strata and our number of prediction variables is quite low, ordinary least squares (OLS) regression was chosen as a rather straightforward prediction model. As already pointed out by Bumgardner et al. [60], the overall reflectance in the visible part of the spectrum decreases when the organic matter content increases. For this reason, only the first four image bands of the multispectral image were used as input data for the prediction of SOC (450, 550, 680, and 720 nm). SOC measurement results were assigned to a set of training pixels, which were extracted from the image bands based on the respective sampling locations. Training pixels comprise all pixels of the digitised sample location. As the number of pixels is quite small due to the limited spatial resolution of the images, further processing of the pixel values via, for example, mean values of random subsets (as suggested for bigger data sets by, e.g., [63]) was not conducted. The fitted model was used for prediction of SOC based on all image pixels. Model fitting was performed with the `stats` package for R [45] and prediction using the `raster` package for R [55].

2.4. Cluster Analysis

Unsupervised classification of the processed data was conducted to semi-automatically delineate stratigraphical (sub)units from (i) the image data and their derivatives and (ii) multiple parameters

of the sedimentological data. This type of classification does not require the definition of training areas and, thus, assumptions prior to the performance of the classification; it therefore excludes the researcher's subjective perception [12]. The on-site delineation by local archaeological experts in combination with the results of the quantitative sedimentological analyses was used as a reference to discuss the quality of the results.

2.4.1. Sedimentological Data

Unsupervised classification of the sediment properties examined was used to verify stratigraphic delineation conducted during fieldwork. The most recent work of Schmidt et al. [43] shows that hierarchical clustering of element concentrations may be used to classify sediment data for stratigraphic delineation and interpretation. Building upon their work, we applied cluster analysis of Manhattan distances performed with Ward's method (e.g., [64]). Additionally we examined the benefit of depth-constrained clustering [65] using CONISS [66]. The number of clusters/groups is based on the layers identified in Figure 2c: Four main layers (A, B, C, D) and two additional layers, representing the sediment parts within the stone layers. The total number of six clusters was increased to 10 clusters for depth-constrained clustering, now including transitional layers between the main layers. Both clustering approaches were conducted for (i) the pre-processed element concentrations (p-ED-XRF), the pre-processed spectra of the (ii) ground and (iii) unground sediment samples, and (iv) the median pixel values of the RGB and (v) multispectral images, extracted from the sampling locations.

2.4.2. Image Data

In past studies, k-means clustering was successfully applied for the analysis of soil data (e.g., [11,12,62]). In this study, clustering was carried out in the spectral domain using the k-means algorithm proposed by Hartigan and Wong [67]. Partitioning into clusters was performed using a random sample, consisting of 10% of the pixels of the respective raster stack [45,55] in order to reduce computational time. The maximum number of iterations allowed was set to 50, and three random sets were created as seed points. The resulting partition was used for prediction via the *clue* package for R [68].

Following Haburaj et al. [12], multiple combinations of the processed image data were used as input for the k-means clustering: All image derivatives created were combined with one another to assess the influence of each processing step regarding image noise and cluster quality. All combinations examined are presented in the supplemental material (Online Resource 1 in Supplementary Materials).

The number of clusters was set to 15, allowing the inclusion of potential disturbances and transitional layers in comparison to the six clusters of the sedimentological data. This rather high number of clusters leads to the necessity of subsequent manual grouping of the clusters with respect to the on-site stratigraphic documentation. This step was conducted in QGIS (v2.18). As argued by Haburaj et al. [12], manual grouping should be conducted attentively, as it allows for a more transparent documentation of the where and how of drawing borders between layers.

Evaluation of the image clustering results was carried out manually and by a visual interpretation of the homogeneity of the resulting clusters, as well as their conformity with the delineation of stratigraphic layers depicted in Figures 2 and 5.

3. Results

3.1. Sedimentological Record

The measured sediment properties of the section examined allow a detailed description of the layers depicted in Figure 2. Layer A is characterised by a water content of c. 5%, an average SOC concentration of around 1%, acidic pH values (top A: < 3.5, basis A: 4.5), and high concentrations of silt compared to the other layers (Figure 5). At the top of layer B (sublayer 5), a peak of water content is visible (c. 10%). Layers B and D show strong variation between their individual sublayers, averaging at

around 5% water content, acidic pH values between 3.5 and 4.5, and low SOC concentrations (<0.2%). The dark, thin horizontal layer C shows a peak in water content (c. 10%) and a slight increase of silty material and SOC content compared to the surrounding materials (Figure 5).

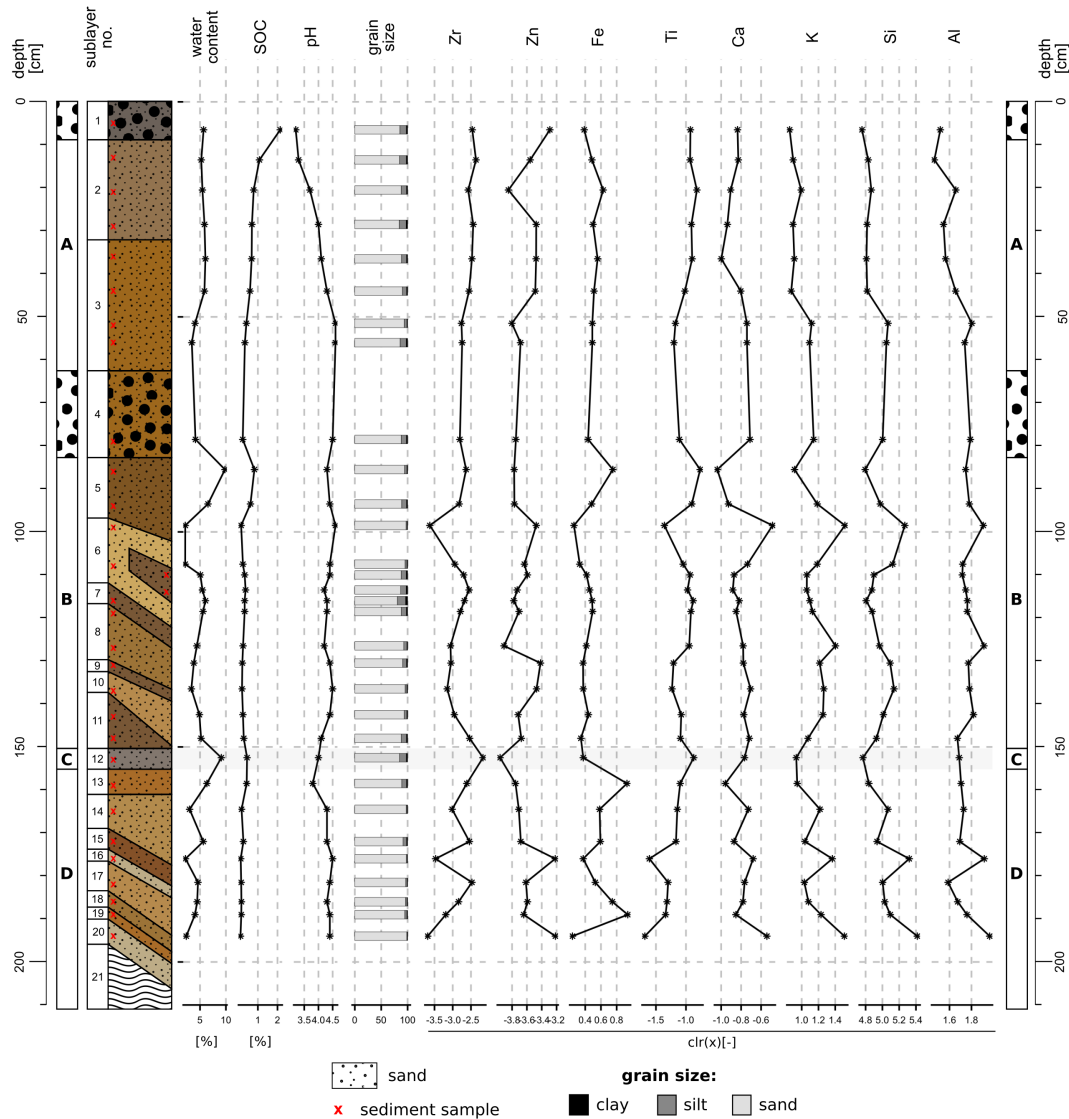


Figure 5. Sedimentological record of SD17P1 (layers A, B, C and D). Sediment colour and texture [69] as documented during fieldwork, location of samples, and respective results of the sediment analyses performed. Centred log-ratio (clr) transformed contents of relevant elements measured with the p-ED-XRF device.

During pre-processing of the p-ED-XRF data, we excluded several elements due to their insignificance or erroneous measurements. The following eight elements showed valid measurements and were processed: Zr, Zn, Fe, Ti, Ca, K, Si, and Al. Concentrations of these elements are heterogeneous in the lower parts of the examined profile (layers B, C, D), while layer A repeatedly shows continuous trends of element concentrations from its top to its bottom (Figure 5).

3.2. Clustering Results—Sedimentological Data

Clustering results (groups) of the p-ED-XRF data are documented in Figure 6. The groups produced by depth-constrained hierarchical cluster analysis of the transformed element concentrations

capture the main stratigraphic layers of the profile and, together with the on-site delineation and the sedimentological record (Figure 5), serve as a reference for the quality of all clustering results: Groups 1 and 2 cover areas of dark material, which are characterised by high water contents and are situated in layer A and at the top of layer B (sublayer 5, see Figures 5 and 6). Layer C is grouped together with the surrounding materials of layers B and D in the results of both clustering approaches.

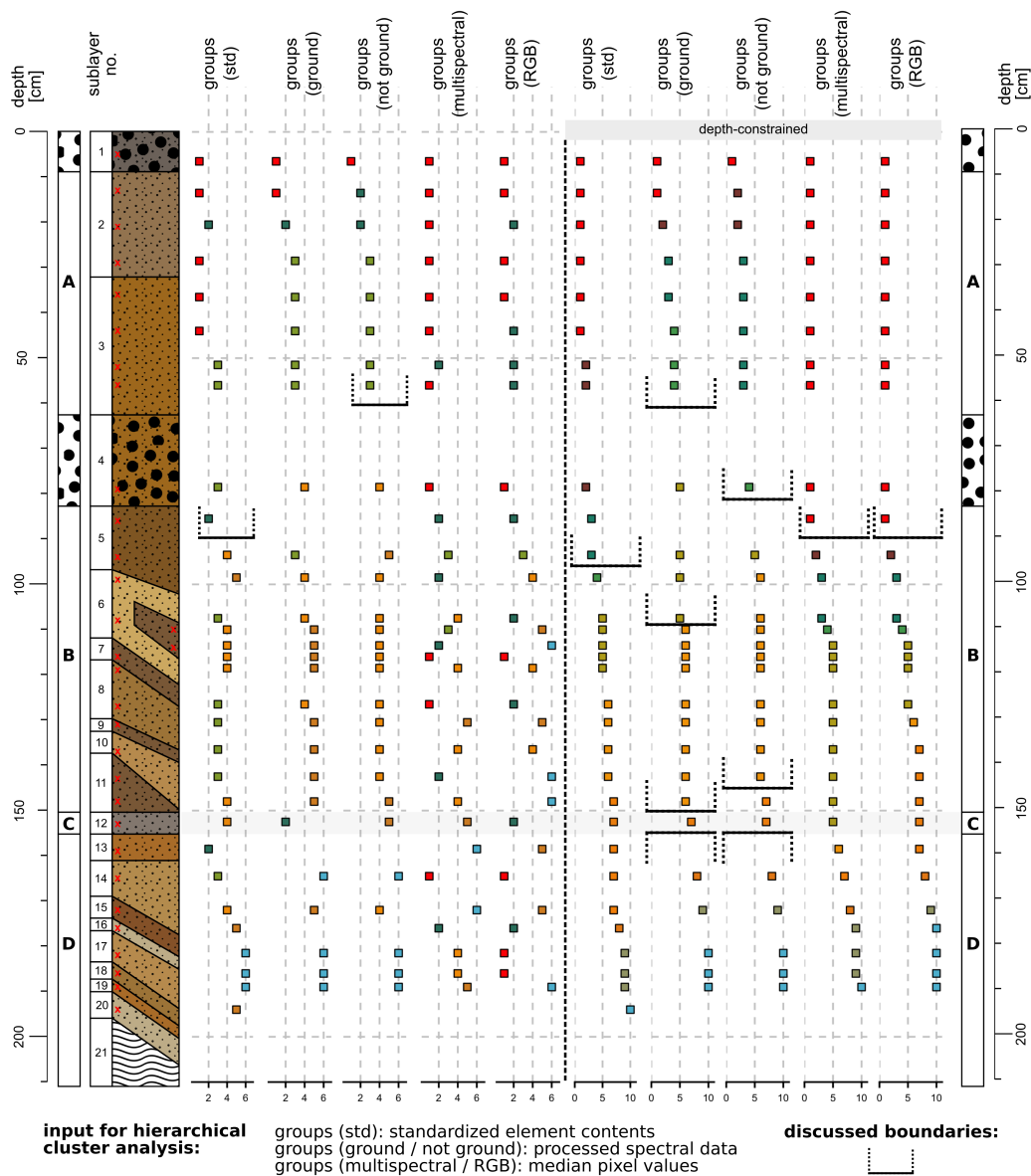


Figure 6. Clustering results (groups) of SD17P1 (layers A, B, C and D). Sediment colour and texture [69] as documented during fieldwork, location of samples, and respective results of the hierarchical and the depth-constrained hierarchical cluster analyses of the following data: p-ED-XRF data, selectively measured spectral data (450–2500 nm), and median pixel values extracted from image data. Colours of samples indicate groups obtained from the cluster analyses. Six groups (six colours) were obtained from the hierarchical clustering and ten groups (ten colours) from the depth-constrained hierarchical clustering. Boundaries discussed in the text are highlighted.

Clustering of the pre-processed spectra of the samples showed a noteworthy influence of grinding. While layer C is grouped with the topmost layer in the ground data, it is grouped with the darker part of layer B when samples are not ground (Figure 6). Both ground and not ground samples clearly

delineate data of layer A from the rest of the data in the clustering results. Layer C is assigned to a separate group in the ground data only. Compared to the results of the p-ED-XRF data, the groups produced on the basis of the spectral data are spatially more consistent. Depth-constrained clustering increases this consistency (Figure 6).

Groups produced by the clustering of both RGB and multispectral pixel data capture layer A homogeneously. Additionally, the hierarchical clustering assigns darker parts of layers B and D to groups 1 and 2. The clustering of the RGB data groups layers A and C, while the clustering of the multispectral data groups layer C with the darker parts of layer B. Both data sets assign the topmost part of layer B (sublayer 5, see Figure 6) to groups 1 and 2. Including depth-constrained clustering showed a positive effect on group homogeneity for both RGB and multispectral-based clustering results; layer A and sublayer 5 are captured as one single group. Both depth-constrained cluster approaches of the pixel data, however, do not capture layer C, but group it together with the surrounding materials of layers B and D.

3.3. Clustering Results—Image Data

Multiple band combinations were tested as input for the performed image classification via k-means clustering. While all combinations have problems capturing the thin horizontal layer C, the results shown in Figure 7 indicate clear benefits when using specific bands: Using the RGB data, the most homogeneous classification results were derived from a combination of the raw RGB bands, two principle components, and two slope rasters (Figure 7b). The summarised groups produced by the cluster analysis roughly represent the stratigraphic (sub)layers. Clustering the same band combination of the multispectral data (Figure 7c) produced results of similar quality. Nevertheless, two major differences have to be pointed out: (1) Multispectral data succeed in separating layer A from the rest of the profile, and (2) RGB data capture layer C more precisely in the spatial domain. Layer C is grouped with materials from layer A in the results produced using RGB data, while the multispectral data clustering results group it together with parts of layers B and D (see Online Resource 1 (in Supplementary Materials) for all band combinations).

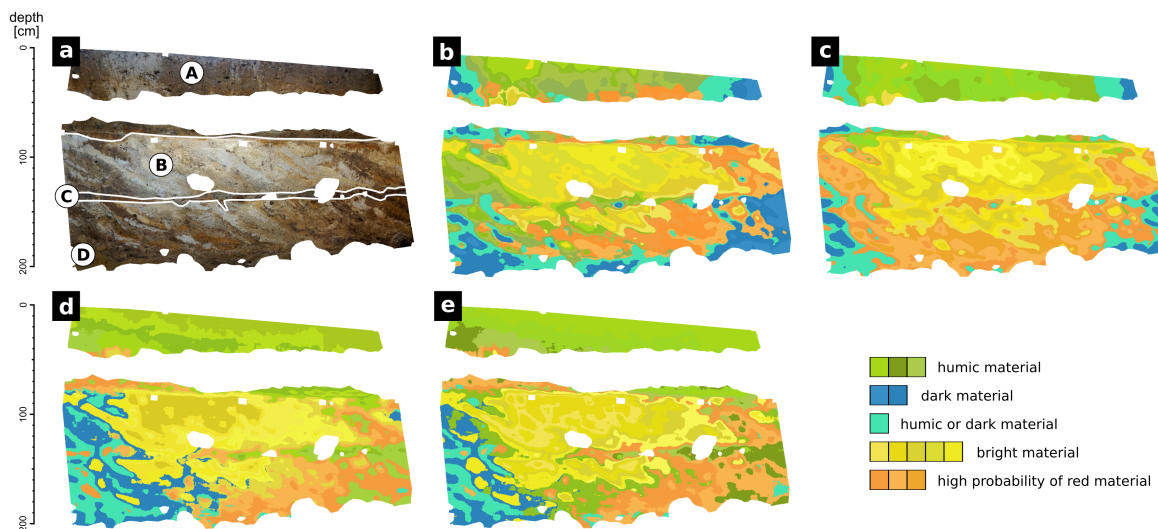


Figure 7. Results of the performed image classification of the upper part of SD17P1; stone layers were masked manually prior to processing. (a) Profile as perceived during fieldwork with layer borders (white) according to Figure 2 (layers A, B, C and D). Classification results of (b) an RGB composite (raw data, slopes, PCA results), (c) a multispectral composite (raw data, slopes, PCA results), (d) a multispectral composite (slopes, CIELAB), and (e) a multispectral composite (slopes, predicted SOC, CIELAB chromaticity coordinates a and b). Colour shades represent individual groups produced from k-means clustering, while summarised groups are indicated by a common hue.

4. Discussion

4.1. Image Data

Our image classification results of the RGB data are consistent with the results of other studies (e.g., [11,12,28,70]). The combination of raw RGB bands, two principle components, and two slope rasters (as proposed by [12]) produced similar results to those of the equally processed multispectral bands. Furthermore, processing of the multispectral data improved the classification results significantly, allowing us to minimise the impact of lighting differences successfully.

Transformation to CIELAB coordinates did not deliver any benefit for the RGB data: Neither replacing the RGB bands with their CIELAB counterparts, nor using the image bands containing chromaticity coordinates a^* and b^* separately led to better clustering results (Online Resource 1 in Supplementary Materials). This is different for the multispectral data, as both the CIELAB data based on the multispectral data and SOC data show a significant influence on the clustering results (Figure 7d,e). A combination of slope bands and CIELAB bands eliminates the influence of slightly shadowed areas on the left and right sides of the profile. This leads to more homogeneous results, which is mostly visible in layer A and the righthand parts of layers B and D. As a consequence layer C is—while grouped with the material of layer A—captured more reliably than with the other multispectral band combinations. Another notable result is the similar performance of (i) the combination of slope bands with all CIELAB bands (Figure 7d) and (ii) the combination of slope bands with the CIELAB chromaticity bands a^* and b^* and the SOC raster (Figure 7e). Classification results are nearly identical, only showing small differences in the lower part of the profile.

We observed similarities between the clustering results of band combinations including the SOC raster and, alternatively, the CIELAB lightness raster. Nevertheless, the transferability of these results to other sites has to be examined critically and individually for each case. The noticed relation between SOC and lightness rasters is already proposed by other authors (e.g., [27,59]), who examined this phenomenon in detail and concluded that the relation is highly dependent on the local circumstances. However, if quantitative examination of SOC as conducted by, e.g., Steffens et al. [62] cannot be included into the workflow due to technical or financial limitations, we propose CIE lightness to be a rough indicator of the spatial variance of SOC, while keeping in mind that water content also influences lightness significantly (e.g., [50,60]). Our results support the strong correlation of CIELAB image bands and SOC, as observed for high-contrast soil profiles, for example, by Zhang and Hartemink [28].

The initially proposed significance of CIELAB chromaticity coordinates for the examination of iron oxide concentrations could not be confirmed for our experimental design. The examination of iron oxides based on CIE a^* and b^* as proven by, e.g., Vodyanitskii and Kirillova [27] possibly requires a more sophisticated approach, including the mathematical prediction via, e.g., partial least squares regression or machine learning algorithms, as applied for other sediment properties by, e.g., Daniel et al. [71], Viscarra Rossel and Behrens [72], or Morellos et al. [73]. Other factors that could be responsible for the poor performance of our approach include the limited presence of iron in the profile examined: Elemental Fe concentration is below 1% (see Online Resource 2 in Supplementary Materials) throughout the examined samples. This would correspond to a maximum of c. 1.4% Fe_2O_3 , given that all Fe would result from hematite. A future approach should consider a camera setup with fewer limitations regarding spectral range and resolution. Using a hyperspectral VIS-NIR device would allow the examination of Fe in far more detail [13,60,74]. This would also allow the analysis of further sediment properties, like grain size based on the spectral signal [50,75–77].

More generally speaking, our results support the usage of the CIELAB colour space as a standard for documentation during archaeological excavations. The observed good performance of the CIELAB datasets supports the scientific relevance of the CIELAB colour space, which was previously proposed by other authors [47,78]. For the last decades, this colour space gained popularity in the geosciences and, meanwhile, is widely used in numerous studies (cf. [14]). Many authors noted the clear advantages over the RGB or Munsell colour systems (e.g., [22,23,26]): CIELAB is a mathematically defined colour

space that is free to use and suitable for quantitative analyses. In future studies, the proposed quantitative examination of colour differences throughout archaeological profiles by transformation to CIELAB could be complemented by additional colour difference formulas like CIEDE2000 to assess possible benefits [79].

4.2. Sedimentological Data

By quantitatively analysing sediment properties, we were able to explain several characteristics of the profile in detail. Clustering results suggest that the topmost parts of layer B (sublayer 5) are related to layer A or the intermediate stone layer. The observed high values of water content and SOC suggest sublayer 5 to be either related to construction work (compression by overlying stones) or resembling (together with the overlying stones) a prehistoric surface, which would have been of similar character to the topmost stone layer described by May [35]. Similarly to sublayer 5, the colour of layer C seems to be influenced mainly by a high water content. However, slightly increased SOC may also indicate a prehistoric surface here. The observed similarities also explain why layer C is often clustered with layer A or sublayer 5.

The performed hierarchical cluster analysis of the examined sediment properties produced similar results for the p-ED-XRF data and the recorded VIS-NIR data (Figures 5 and 6). We see this as an indicator that selective or extensive spectroscopy should be considered a fast and efficient alternative to laboratory analyses when one is aiming for the delineation of layers or an objective confirmation of the observed variance in a profile. Spectroscopy in comparison to laboratory analyses is easy and fast to apply, non-destructive, cost-efficient in the long term, and also more environmentally friendly. While our study supports the idea of using spectroscopy during archaeological excavations due to the aforementioned benefits, the methodological approach should still be considered experimental—currently, clear limitations regarding the ease of use and the on-site applicability exist.

Throughout our study, depth-constrained clustering generally improved the results, which supports preferability of this method when clustering layers, as, e.g., Schmidt et al. [43] proposed. Depth-constrained clustering also improved clustering results of the sampled pixel values significantly (Figure 6) and—with the exception of layer C—captured overall variability of the profile. Layer C is generally treated similarly in the image data and the selective data, as it is either clustered with layer A or darker parts of layers B and D. It is also noteworthy that layer C was captured most accurately by the spectral data of ground sediment samples, which underlines the potential of VIS-NIR spectroscopy for stratigraphic analyses. In addition, both the selective pixel-based approach and the extensive image-based approach distinguish between layer A and the rest of the profile.

4.3. Shortcomings and Benefits of Spectral Measurements

Our study exposes that quantitative colour measurements during fieldwork can help with stratigraphic delineation and interpretation, be it based on selective or extensive data. Combining these measurements with semi-automated classification algorithms, we were able to increase objectivity and transparency of the delineation of stratigraphic (sub)layers in a similar manner to that if using common sedimentological data. In particular, depth-constrained hierarchical clustering should be considered a useful tool when analysing stratigraphic sequences quantitatively. Depending on the respective research question, future studies should consider the measurement of VIS-NIR spectral data as an alternative to other analytical methods, which are often time-consuming and destructive. For example, spectral measurements could offer a fast and quantitative way of documentation on rescue excavations.

We were able to successfully transfer the image analysis workflow proposed by Haburaj et al. [12] to the archaeological profile SD17P1 from the burial mound of Seddin. Moreover, we want to stress the significant improvements we could add to this process by adding CIELAB data and SOC information, both derived from the multispectral data. The observed similarities between the clustering results

of band combinations, including the SOC raster and, alternatively, the CIE lightness raster, suggest that time-consuming and expensive SOC prediction can be replaced with a fast transformation of the image data to the CIELAB colour space. The noticed benefits should especially be kept in mind when one is working under heterogeneous fieldwork conditions, as CIELAB and slope rasters clearly help to overcome uneven lighting conditions. If intra- or inter-site comparability of the colour and spectral measurements is required, image acquisition should include distinct colour calibration [80,81].

The output of the conducted comparisons suggests that the selective spectral information measured from sediment samples produces similar clustering results to those of the p-ED-XRF data. Increasing the spectral range and resolution of the image data would therefore clearly improve the identification of (sub)layers based on image data. This is consistent with the results of laboratory analyses of, e.g., Steffens et al. [62] or Hobley et al. [63].

Taking the characteristics of the examined profile into account, we consider its stratigraphy complex: While it consists only of a few major layers, the overall heterogeneity of the profile is quite high. This complexity renders sediment sampling rather complicated, as one has to decide which and how many samples to take. At this point, analyses based on image data could fill a gap. This would, however, require a device that offers an improved spectral range and quality. Spectral imaging devices are still in a crucial phase of development though. Imaging technology becomes more sophisticated: Systems become smaller and are more easy to use, as recent studies suggest, using either snapshot (e.g., [12,82]) or push broom (e.g., [83]) technology. However, the offered devices are still often limited to wavelengths below 1000 nm (cf. [84]), rendering the examination of many sediment properties problematic. Established hyperspectral scanners that capture wavelengths beyond 1000 nm are most often expensive and difficult to use under fieldwork conditions due to their dimensions, weight, and power consumption. While the limited capabilities of the presented spectral imaging devices render the extensive analysis of sediment data not yet applicable for most excavations, selective spectral measurements as performed in this study may constitute an easy-to-apply additional step towards a more transparent way of field documentation during archaeological excavations.

Keeping in mind the complex stratigraphy of the profile at hand, applicability of the proposed approach to profiles and plana that include more distinct stratigraphic features (e.g., post-holes, pits, trenches) appears likely. The good performance of RGB image analysis for the examination of high-contrast soil and sediment data was lately described by Haburaj et al. [12] and Zhang and Hartemink [28], indicating a high potential of image classification for archaeological excavations in general. Our results of the selectively measured colour and spectral data indicate that hyperspectral measurements (as we measured with a spectroradiometer) could offer supportive information when analysing more complex or low-contrast stratigraphies (e.g., paleosols).

The sedimentological record obtained in the laboratory is still necessary to describe and interpret the layers. However, the good clustering results of the image data and the general performance of the selective spectral data stresses the potential of more advanced spectral image sensors for future stratigraphic studies. By extrapolating sediment properties from samples to image data, one could combine the benefits of both worlds: A sedimentological record that is not limited to selected sediment samples. While several laboratory studies were already able to produce extensive parameter maps (e.g., [62]), transferability of this approach to on-site recordings still has to be examined.

Based on our results, future studies should either focus on the optimisation of an RGB-camera-based workflow or the in-depth review of more potent spectral sensors. While RGB images delineate layers in the presented study, our results show that image data that would involve spectral information of the same quality as our selective VIS-NIR measurements could prove to be as suitable for assisting stratigraphic delineation and interpretation as labour-intensive laboratory analyses.

5. Conclusions

The presented results indicate that quantitative colour measurements and spectral measurements during fieldwork can support stratigraphic delineation and interpretation of profiles in archaeological excavations. Depth-constrained hierarchical clustering of spectral data as well as of p-ED-XRF data should be considered a useful tool when analysing stratigraphic sequences quantitatively.

The discussed benefits of the multispectral image data suggest a huge potential of the spectral domain for automating stratigraphic delineation and interpretation and, likewise, render this process more traceable. Observed drawbacks show that we cannot offer a ready-to-use approach yet. In particular, the limited capabilities of the presented spectral imaging devices render the extensive analysis of sediment data not yet applicable for most excavations. Rather, additional on-site studies should be carried out to create standardised workflows. Image data that would involve spectral information of the same quality as our selective VIS-NIR measurements could prove to be as suitable for assisting stratigraphic interpretation as labour-intensive laboratory analyses. Quantitative colour measurements and spectral measurements, as performed in this study, may constitute an easy-to-apply, non-destructive additional step towards a fast and more traceable way of field documentation during archaeological excavations.

Supplementary Materials: The following are available online at <http://www.mdpi.com/2571-9408/3/2/31/s1>, **Online Resource 1** includes the image data used throughout this study along with the R-scripts that were used for image analyses. **Online Resource 2** covers the elemental concentrations of the sediment samples retrieved from a p-ED-XRF, as well as documentation of the processing workflow of these data. **Online Resource 3** comprises the VIS-NIR spectra of all sediment samples, recorded with a spectroradiometer (350–2500 nm). Additionally, the documentation of the pre-processing workflow is included.

Author Contributions: Concept and methodology devised by V.H. and B.S.; laboratory work and validation by V.H., P.H., M.N., B.S., and J.M.; formal analysis and software by V.H.; original draft of the manuscript prepared by V.H.; review and editing by B.S., M.N., P.H., J.M., and V.H.; supervision by B.S. All authors have read and agreed to the published version of the manuscript.

Funding: This research was funded by the Cluster of Excellence EXC264 Topoi (The Formation and Transformation of Space and Knowledge in Ancient Civilizations, Research Area A; Deutsche Forschungsgemeinschaft (DFG) project number 39235742.

Acknowledgments: We thank the Cluster of Excellence EXC264 Topoi (The Formation and Transformation of Space and Knowledge in Ancient Civilizations, Research Area A) for funding this research. The publication of this article was funded by Freie Universität Berlin. Additional thanks is expressed to the Geography Department of the Humboldt-Universität zu Berlin for the possibility to use their spectroradiometer. Furthermore, we would like to thank Fabian Becker, Sebastian van der Linden, Jacob Hardt, and Jan Krause for their support. We thank the four anonymous reviewers for their detailed and valuable reviews, which helped to improve the manuscript substantially.

Conflicts of Interest: The authors declare no conflict of interest.

Abbreviations

The following abbreviations are used in this manuscript:

VIS-NIR	visible and near-infrared
SOC	soil organic carbon
p-ED-XRF	portable energy-dispersive X-ray fluorescence spectrometer
CRM	certified reference material
SNV	standard normal variate
clr	centred log ratio
TPS	thin plate spline
FWHM	full width half maximum
PCA	principle component analysis

References

1. Harris, E.C. *Principles of Archaeological Stratigraphy*; Academic Press: London, UK, 1979.

2. Vincent, M.L.; Kuester, F.; Levy, T.E. Opendig: Contextualizing the past from the field to the web. *Mediterr. Archaeol. Archaeom.* **2014**, *14*, 109–116.
3. Simonson, R.W. Soil Color Standards and Terms for Field Use—History of Their Development. *Soil Color* **1993**, *31*, 1–20, [CrossRef]
4. Landa, E.R.; Fairchild, M.D. Charting Color from the Eye of the Beholder. *Am. Sci.* **2005**, *93*, 436–443. [CrossRef]
5. Hassan, F.A. Sediments in Archaeology: Methods and Implications for Palaeoenvironmental and Cultural Analysis. *J. Field Archaeol.* **1978**, *5*, 197–213, [CrossRef]
6. Goldberg, P.; Holliday, V.T.; Ferring, C.R. *Earth Sciences and Archaeology*; Springer Science & Business Media: New York, NY, USA, 2013.
7. Hoelzmann, P.; Klein, T.; Kutz, F.; Schütt, B. A new device to mount portable energy-dispersive X-ray fluorescence spectrometers (p-ED-XRF) for semi-continuous analyses of split (sediment) cores and solid samples. *Geosci. Instrum. Methods Data Syst.* **2017**, *6*, 93. [CrossRef]
8. French, C. *Geoarchaeology in Action: Studies in Soil Micromorphology and Landscape Evolution*; Routledge: London, UK, 2003.
9. Kooistra, M.J.; Kooistra, L.I. Integrated research in archaeology using soil micromorphology and palynology. *CATENA* **2003**, *54*, 603–617, [CrossRef]
10. Meister, J.; Krause, J.; Müller-Neuhof, B.; Portillo, M.; Reimann, T.; Schütt, B. Desert agricultural systems at EBA Jawa (Jordan): Integrating archaeological and paleoenvironmental records. *Quat. Int.* **2017**, *434*, 33–50, [CrossRef]
11. Zhang, Y.; Hartemink, A.E. A method for automated soil horizon delineation using digital images. *Geoderma* **2019**, *343*, 97–115, [CrossRef]
12. Haburaj, V.; Krause, J.; Pless, S.; Waske, B.; Schütt, B. Evaluating the Potential of Semi-Automated Image Analysis for Delimiting Soil and Sediment Layers. *J. Field Archaeol.* **2019**, *44*, [CrossRef]
13. Stenberg, B.; Viscarra Rossel, R.A. Diffuse Reflectance Spectroscopy for High-Resolution Soil Sensing. In *Proximal Soil Sensing*; Viscarra Rossel, R.A., McBratney, A.B., Minasny, B., Eds.; Progress in Soil Science; Springer: Dordrecht, The Netherlands, 2010; pp. 29–47, [CrossRef]
14. Debret, M.; Sebag, D.; Desmet, M.; Balsam, W.; Copard, Y.; Mourier, B.; Susperrigui, A.S.; Arnaud, F.; Bentaleb, I.; Chapron, E.; et al. Spectrocolorimetric interpretation of sedimentary dynamics: The new “Q7/4 diagram”. *Earth-Sci. Rev.* **2011**, *109*, 1–19, [CrossRef]
15. Zeeden, C.; Krauß, L.; Kels, H.; Lehmkuhl, F. Digital image analysis of outcropping sediments: Comparison to photospectrometric data from Quaternary loess deposits at Şanovița (Romania) and Achenheim (France). *Quat. Int.* **2017**, *429*, 100–107, [CrossRef]
16. Udelhoven, T.; Emmerling, C.; Jarmer, T. Quantitative analysis of soil chemical properties with diffuse reflectance spectrometry and partial least-square regression: A feasibility study. *Plant Soil* **2003**, *251*, 319–329, [CrossRef]
17. Mutuo, P.K.; Shepherd, K.D.; Albrecht, A.; Cadisch, G. Prediction of carbon mineralization rates from different soil physical fractions using diffuse reflectance spectroscopy. *Soil Biol. Biochem.* **2006**, *38*, 1658–1664, [CrossRef]
18. Brown, D.J.; Shepherd, K.D.; Walsh, M.G.; Dewayne Mays, M.; Reinsch, T.G. Global soil characterization with VNIR diffuse reflectance spectroscopy. *Geoderma* **2006**, *132*, 273–290, [CrossRef]
19. Sankey, J.B.; Brown, D.J.; Bernard, M.L.; Lawrence, R.L. Comparing local vs. global visible and near-infrared (VisNIR) diffuse reflectance spectroscopy (DRS) calibrations for the prediction of soil clay, organic C and inorganic C. *Geoderma* **2008**, *148*, 149–158, [CrossRef]
20. Volkan Bilgili, A.; van Es, H.M.; Akbas, F.; Durak, A.; Hively, W.D. Visible-near infrared reflectance spectroscopy for assessment of soil properties in a semi-arid area of Turkey. *J. Arid Environ.* **2010**, *74*, 229–238, [CrossRef]
21. Soriano-Disla, J.M.; Janik, L.J.; Viscarra Rossel, R.A.; Macdonald, L.M.; McLaughlin, M.J. The Performance of Visible, Near-, and Mid-Infrared Reflectance Spectroscopy for Prediction of Soil Physical, Chemical, and Biological Properties. *Appl. Spectrosc. Rev.* **2014**, *49*, 139–186, [CrossRef]
22. Melville, M.D.; Atkinson, G. Soil colour: Its measurement and its designation in models of uniform colour space. *J. Soil Sci.* **1985**, *36*, 495–512, [CrossRef]

23. Viscarra Rossel, R.A.; Walvoort, D.J.J.; McBratney, A.B.; Janik, L.J.; Skjemstad, J.O. Visible, near infrared, mid infrared or combined diffuse reflectance spectroscopy for simultaneous assessment of various soil properties. *Geoderma* **2006**, *131*, 59–75, [CrossRef]
24. Jarmer, T.; Lavée, H.; Hill, P.S.J. Using Reflectance Spectroscopy and Landsat Data to Assess Soil Inorganic Carbon in the Judean Desert (Israel). In *Recent Advances in Remote Sensing and Geoinformation Processing for Land Degradation Assessment*; Röder, A., Hill, J., Eds.; CRC Press: London, UK, 2009; pp. 227–243. [CrossRef]
25. Hill, J.; Udelhoven, T.; Vohland, M.; Stevens, A. The Use of Laboratory Spectroscopy and Optical Remote Sensing for Estimating Soil Properties. In *Precision Crop Protection—The Challenge and Use of Heterogeneity*; Oerke, E.C., Gerhards, R., Menz, G., Sikora, R.A., Eds.; Springer: Dordrecht, The Netherlands, 2010; pp. 67–85, [CrossRef]
26. Sprafke, T. *Löss in Niederösterreich—Archiv Quartärer Klima- und Landschaftsveränderungen*; Würzburg University Press: Würzburg, Germany, 2016.
27. Vodyanitskii, Y.N.; Kirillova, N.P. Application of the CIE-L*a*b* system to characterize soil color. *Eurasian Soil Sci.* **2016**, *49*, 1259–1268, [CrossRef]
28. Zhang, Y.; Hartemink, A.E. Digital mapping of a soil profile. *Eur. J. Soil Sci.* **2019**, *70*, 27–41, [CrossRef]
29. Kiekebusch, A. Das Königsgrab von Seddin. In *Führer zur Urgeschichte*; Number 1; Dt. Buchvertr. Ges.: Augsburg, Germany, 1928.
30. May, J. Der Fundplatz und die Umgebung des Grabhügels von Seddin als ortsfestes Bodendenkmal. In *Jürgen Kunow (Hrsg.), Das »Königsgrab« von Seddin in der Prignitz. Kolloquium Anlässlich des 100. Jahrestages Seiner Freilegung am 12. Oktober 1999*; Number 9 in Arbeitsberichte zur Bodendenkmalpflege in Brandenburg; Brandenburgisches Landesamt für Denkmalpflege und Archäologisches Landesmuseum: Zossen, Germany, 2003; pp. 7–11.
31. May, J.; Hauptmann, T. Das » Königsgrab « von Seddin und sein engeres Umfeld im Spiegel neuer Feldforschungen. In *Gräberlandschaften der Bronzezeit. Internationales Kolloquium zur Bronzezeit*; Bérenger, D., Bourgeois, J., Talon, M., St. Wirth (Hrsg.), Eds.; Number 51 in Bodenaltertümer Westfalens; LWL-Archäologie in Westfalen und Altertumskommission für Westfalen: Darmstadt, Germany, 2012.
32. Wüstemann, H. Zur Sozialstruktur im Seddiner Kulturgebiet. *Zeitschrift für Archäologie* **1974**, *8*, 67–107.
33. May, J. Neue Forschung am 'Königsgrab' von Seddin. In *Der Grabhügel von Seddin im Norddeutschen und Südsandinavischen Kontext*; Hansen, S., Schopper, F., Eds.; Number 33 in Arbeitsberichte zur Bodendenkmalpflege in Brandenburg; Brandenburgisches Landesamt für Denkmalpflege und Archäologisches Landesmuseum: Zossen, Germany, 2018.
34. Schenk, T.; Goldmann, T.; Kultfeuerreihe, D.S. Geomagnetische Prospektion am Königsgrab in der Prignitz. *Archäologie in Berl. und Brandenbg.* **2004**, 57–59.
35. May, J. Fokussieren, Positionieren, Schritthalten. Aspekte von Raum und Zeit am 'Königsgrab' von Seddin in der Prignitz. In *Das Ganze Ist Mehr als die Summe Seiner Teile. Festschrift für Jürgen Kunow*; Number 27 in Materialien zur Bodendenkmalpflege im Rheinland; LVR-Amt für Bodendenkmalpflege im Rheinland: Bonn, Germany, 2018.
36. Landesamt für Bergbau, G.U.R. Geologische Karte 1:25.000 (GK25) des Landes Brandenburg, Blatt Baek (2837). 1905. Available online: <https://lbgr.brandenburg.de/sixcms/detail.php/622447> (accessed on 15 June 2020).
37. Götze, A. Die vor- und frühgeschichtlichen Denkmäler des Kreises Westprignitz. *Kunstdenkmäler der Prov. Brandenbg.* **1912**, *1*, 1–54.
38. Brunke, H.; Bukowiecki, E.; Cancik-Kirschbaum, E.; Eichmann, R.; Ess, M.V.; Gass, A.; Gussone, M.; Hageneuer, S.; Hansen, S.; Kogge, W.; et al. Thinking Big. Research in Monumental Constructions in Antiquity. *Space Knowl.* **2016**, 250–305, [CrossRef]
39. Company, M.C. *Munsell Soil Color Charts, Revised Edition*; Munsell Color: Baltimore, Germany, 1994.
40. Ad-hoc-Arbeitsgruppe Boden. *Bodenkundliche Kartieranleitung (KA5)*, 5th ed.; Schweizerbart: Hannover, Germany, 2005.
41. Blume, H.P.; Stahr, K.; Leinweber, P. *Bodenkundliches Praktikum: Eine Einführung in Pedologisches Arbeiten für Ökologen, Land- und Forstwirte, Geo- und Umweltwissenschaftler*; Springer: Heidelberg, Germany, 2011.

42. Vogel, S.; Märker, M.; Rellini, I.; Hoelzmann, P.; Wulf, S.; Robinson, M.; Steinhübel, L.; Di Maio, G.; Imperatore, C.; Kastenmeier, P.; et al. From a stratigraphic sequence to a landscape evolution model: Late Pleistocene and Holocene volcanism, soil formation and land use in the shade of Mount Vesuvius (Italy). *Quat. Int.* **2016**, *394*, 155–179. [CrossRef]
43. Schmidt, M.; Leipe, C.; Becker, F.; Goslar, T.; Hoelzmann, P.; Mingram, J.; Müller, S.; Tjallingii, R.; Wagner, M.; Tarasov, P.E. A multi-proxy palaeolimnological record of the last 16,600 years from coastal Lake Kushu in northern Japan. *Palaeogeogr. Palaeoclimatol. Palaeoecol.* **2019**, *514*, 613–626. [CrossRef]
44. Aitchison, J. *The Statistical Analysis of Compositional Data*; Monographs on Statistics and Applied Probability; Chapman & Hall Ltd.: London, UK, 1986.
45. R Core Team. *R: A Language and Environment for Statistical Computing*; R Foundation for Statistical Computing: Vienna, Austria, 2018.
46. Boogaart, K.G.V.; Tolosana-Delgado, R.; Bren, M. *Compositions: Compositional Data Analysis*. 2018. Available online: <https://cran.r-project.org/package=compositions> (accessed on 15 June 2020).
47. Sánchez-Marañón, M.; Delgado, G.; Delgado, R.; Pérez, M.M.; Melgosa, M. Spectroradiometric and visual color measurements of disturbed and undisturbed soil samples. *Soil Sci.* **1995**, *160*, 291–303. [CrossRef]
48. Savitzky, A.; Golay, M.J.E. Smoothing and Differentiation of Data by Simplified Least Squares Procedures. *Anal. Chem.* **1964**, *36*, 1627–1639. [CrossRef]
49. Lehnert, L.W.; Meyer, H.; Bendix, J. *HSDAR: Manage, Analyse and Simulate Hyperspectral Data in R*; 2017. Available online: <https://cran.r-project.org/package=hsdar> (accessed on 15 June 2020).
50. Stenberg, B.; Viscarra Rossel, R.A.; Mouazen, A.M.; Wetterlind, J. Visible and Near Infrared Spectroscopy in Soil Science. In *Advances in Agronomy*; Sparks, D.L., Ed.; Academic Press: Burlington, MA, USA, 2010; Volume 107, pp. 163–215. [CrossRef]
51. Owen, A.J. Uses of derivative spectroscopy. *Agil. Technol.* **1995**, *8*.
52. Barnes, R.J.; Dhanoa, M.S.; Lister, S.J. Standard Normal Variate Transformation and De-trending of Near-Infrared Diffuse Reflectance Spectra. *Appl. Spectrosc.* **1989**, *43*, 772–777. [CrossRef]
53. Retzlaff, R. On the Potential of Small UAS for Multispectral Remote Sensing in Large-Scale Agricultural and Archaeological Applications. Ph.D. Thesis, Universität Trier, Trier, Germany, 2015.
54. Duchon, J. Splines minimizing rotation-invariant semi-norms in Sobolev spaces. In *Constructive Theory of Functions of Several Variables*; Lecture Notes in Mathematics; Springer: Berlin/Heidelberg, Germany, 1977; pp. 85–100. [CrossRef]
55. Hijmans, R.J. *Raster: Geographic Data Analysis and Modeling*. 2019. Available online: <https://cran.r-project.org/package=raster> (accessed on 15 June 2020).
56. Leutner, B.; Horning, N. *RStoolbox: Tools for Remote Sensing Data Analysis*. 2017. Available online: <https://cran.r-project.org/package=RStoolbox> (accessed on 15 June 2020).
57. Jarmer, T.; Schütt, B. Analysis of iron contents in carbonate bedrock by spectroradiometric detection based on experimentally designed substrates. In *1st EARSeL Workshop on Imaging Spectroscopy*; Remote Sensing Laboratories, University of Zurich: Zurich, Switzerland, 1998; pp. 375–382.
58. Schwertmann, U.; Cornell, R.M. *Iron Oxides in the Laboratory: Preparation and Characterization*; John Wiley & Sons: Weinheim, Germany, 2008.
59. Barron, V.; Torrent, J. Use of the Kubelka—Munk theory to study the influence of iron oxides on soil colour. *J. Soil Sci.* **1986**, *37*, 499–510. [CrossRef]
60. Baumgardner, M.; Silva, L.; Biehl, L.; Stoner, E. Reflectance properties of soils. *Adv. Agron.* **1985**, *38*, 1–44.
61. Hill, J.; Schütt, B. Mapping Complex Patterns of Erosion and Stability in Dry Mediterranean Ecosystems. *Remote Sens. Environ.* **2000**, *74*, 557–569. [CrossRef]
62. Steffens, M.; Kohlpaintner, M.; Buddenbaum, H. Fine spatial resolution mapping of soil organic matter quality in a Histosol profile. *Eur. J. Soil Sci.* **2014**, *65*, 827–839. [CrossRef]
63. Hopley, E.; Steffens, M.; Bauke, S.; Kögel-Knabner, I. Hotspots of soil organic carbon storage revealed by laboratory hyperspectral imaging. *Sci. Rep.* **2018**, *8*. [CrossRef] [PubMed]
64. Strauss, T.; Maltitz, M.J.v. Generalising Ward’s Method for Use with Manhattan Distances. *PLoS ONE* **2017**, *12*, e0168288. [CrossRef] [PubMed]
65. Gill, D.; Shomrony, A.; Fligelman, H. Numerical Zonation of Log Suites and Logfacies Recognition by Multivariate Clustering. *AAPG Bull.* **1993**, *77*, 1781–1791.

66. Grimm, E.C. CONISS: A FORTRAN 77 program for stratigraphically constrained cluster analysis by the method of incremental sum of squares. *Comput. Geosci.* **1987**, *13*, 13–35, [CrossRef]
67. Hartigan, J.A.; Wong, M.A. Algorithm AS 136: A k-means clustering algorithm. *J. R. Stat. Soc. Ser. C (Appl. Stat.)* **1979**, *28*, 100–108. [CrossRef]
68. Hornik, K. A CLUE for CLUster Ensembles. *J. Stat. Softw.* **2005**, *14*, [CrossRef]
69. Schoeneberger, P.; Wysocki, D.; Benham, E.; Staff, S.S. *Field Book for Describing and Sampling Soils*; Version 3.0.; Natural Resources Conservation Service, National Soil Survey Center: Lincoln, NE, USA, 2012.
70. Zhang, Y.; Hartemink, A.E. Soil horizon delineation using vis-NIR and pXRF data. *Catena* **2019**, *180*, 298–308, [CrossRef]
71. Daniel, K.W.; Tripathi, N.K.; Honda, K. Artificial neural network analysis of laboratory and in situ spectra for the estimation of macronutrients in soils of Lop Buri (Thailand). *Soil Res.* **2003**, *41*, 47–59, [CrossRef]
72. Viscarra Rossel, R.A.; Behrens, T. Using data mining to model and interpret soil diffuse reflectance spectra. *Geoderma* **2010**, *158*, 46–54, [CrossRef]
73. Morellos, A.; Pantazi, X.E.; Moshou, D.; Alexandridis, T.; Whetton, R.; Tziotziou, G.; Wiebenson, J.; Bill, R.; Mouazen, A.M. Machine learning based prediction of soil total nitrogen, organic carbon and moisture content by using VIS-NIR spectroscopy. *Biosyst. Eng.* **2016**, *152*, 104–116, [CrossRef]
74. Viscarra Rossel, R.A.; Cattle, S.R.; Ortega, A.; Fouad, Y. In situ measurements of soil colour, mineral composition and clay content by vis-NIR spectroscopy. *Geoderma* **2009**, *150*, 253–266, [CrossRef]
75. Post, J.L.; Noble, P.N. The Near-Infrared Combination Band Frequencies of Dioctahedral Smectites, Micas, and Illites. *Clays Clay Miner.* **1993**, *41*, 639–644, [CrossRef]
76. Bishop, J.L.; Pieters, C.M.; Edwards, J.O. Infrared Spectroscopic Analyses on the Nature of Water in Montmorillonite. *Clays Clay Miner.* **1994**, *42*, 702–716, [CrossRef]
77. Madejova, J.; Komadel, P. Baseline studies of the clay minerals society source clays: Infrared methods. *Clays Clay Miner.* **2001**, *49*, 410–432. [CrossRef]
78. Fairchild, M. *Color Appearance Models*; John Wiley & Sons: Chichester, UK, 2013.
79. Liu, H.; Huang, M.; Cui, G.; Luo, M.; Melgosa, M. Color-difference evaluation for digital images using a categorical judgment method. *J. Opt. Soc. Am. A* **2013**, *30*, 616–626, [CrossRef]
80. Sánchez-Marañón, M.; García, P.; Huertas, R.; Hernández-Andrés, J.; Melgosa, M. Influence of Natural Daylight on Soil Color Description: Assessment Using a Color-Appearance Model. *Soil Sci. Soc. Am. J.* **2011**, *75*, 984–993, [CrossRef]
81. Funt, B.; Bastani, P. Irradiance-independent camera color calibration. *Color Res. Appl.* **2014**, *39*, 540–548, [CrossRef]
82. Bareth, G.; Aasen, H.; Bendig, J.; Gnyp, M.L.; Bolten, A.; Jung, A.; Michels, R.; Soukkamäki, J. Low-weight and UAV-based Hyperspectral Full-frame Cameras for Monitoring Crops: Spectral Comparison with Portable Spectroradiometer Measurements. *Photogramm. Fernerkund. Geoinf.* **2015**, *2015*, 69–79, [CrossRef]
83. Behmann, J.; Acebron, K.; Emin, D.; Bennertz, S.; Matsubara, S.; Thomas, S.; Bohnenkamp, D.; Kuska, M.T.; Jussila, J.; Salo, H.; et al. Specim IQ: Evaluation of a New, Miniaturized Handheld Hyperspectral Camera and Its Application for Plant Phenotyping and Disease Detection. *Sensors* **2018**, *18*, 441, [CrossRef] [PubMed]
84. Lodhi, V.; Chakravarty, D.; Mitra, P. Hyperspectral Imaging for Earth Observation: Platforms and Instruments. *J. Indian Inst. Sci.* **2018**, *98*, 429–443, [CrossRef]



© 2020 by the authors. Licensee MDPI, Basel, Switzerland. This article is an open access article distributed under the terms and conditions of the Creative Commons Attribution (CC BY) license (<http://creativecommons.org/licenses/by/4.0/>).

Opinion

The Implication of Vision and Colour in Cultural Heritage

Ricardo Bernárdez-Vilaboa 

Professor in Optometría y Visión Department, Univeridad Complutense de Madrid, 28044 Madrid, Spain; ricardob@ucm.es; Tel.: +34-649-172-142

Received: 5 September 2020; Accepted: 23 September 2020; Published: 25 September 2020

Abstract: Colour is important in art, particularly in pictures. The eyes receive images with a particular condition after traversing the cornea, other surfaces and interior liquid of orbit. It is possible for changes in colour to be perceived when pictures are viewed by one eye that has defects in any surface. Cone defects are directly related to colour failure. Can the original colour be recovered by modifying the visual function? There are multiple colour tests, but there is no consensus on which colour test is best. After detecting a problem with colour, we found several techniques to enhance colour contrast for dichromats. Treatments considered were reversible and innocuous and combined with melanopsin-based blue light sensitivity for melatonin suppression, allowing visual acceptance and luminous perception. A light source of 4000 K with a Duv value of zero, a good observer and adequate illumination were necessary. Subjective assessment may be affected by visual functions such as accommodation, binocular vision and quality of the eye.

Keywords: colour; art; visual; accommodation; binocular vision

1. Introduction

The human eye detects light at wavelengths between 400 and 700 nm, the visible band. There are three kinds of colour-sensitive pigments for absorbing energy in this range, which allow the eyes to see [1]. There are different tests to evaluate colour fidelity indices (CIE-Ra, CQS-Qf, CRI2012, CRI-CAM02UCS, and IES-Rf). Prediction is better with CIE-Rf than with CIE-RaFew [2].

In this paper, the appearance of objects in a museum situation with different spectral power distributions was investigated [3,4]. Other studies have analysed relative attractiveness, naturalness and preference for exhibits in correlation with colourfulness. All differences were compared based on the realisation of different targets for light emitting diode (LED) blending and standard light sources [5–7].

It is easy to find different evaluations of perceptions of LED-based white-light sources in persons of different ethnicity with different objects (fresh food, packaging material or skin tone) [8–11]. The colour perception of an object is little influenced by the neutral interior of a light booth [12]. This usually involves judging brightness, colourfulness and pleasantness when lit with pre-set spectra with correlated colour temperatures (CCTs) via LED and fluorescent lights, in approximately 500 lx. The lighting choices did not differ based on individuals' selections, ranging (2850 to 14,000 K) and lying slightly below the blackbody curve [7,13]. Other attributes did, however, have an impact on perception: attraction, vividness and warmth [14].

The spectral region around 570–580 nm is deleterious to the perception of colour and brightness [15]. High-quality LEDs can improve observers' perceptions and can make the colour appearance more vivid and saturated [16]. With colour LEDs, the hue and the saturation of a target colour can be modified according to preference [17].

Smartphone and tablet use are associated with visual and ocular discomfort such as headaches, eyestrain and other symptoms; this is also reported with desktop computer use. Smartphones, tablets and similar devices differ from desktop computers in position and distance, screen size and luminance. It is important to know that accommodations decrease with handheld device use, lag increases and it induces changes in convergence [18,19]. These changes in accommodation and convergence for near items in inadequate lighting conditions are implicated in the evolution of myopia. There is greater accommodative lag in myopes than in emmetropes and in schoolchildren than in adults [20]. Longitudinal chromatic aberration is related to this accommodation and changes in the emmetropisation process and the change of the depth of field (DOFi). This state causes a dioptric change in the monochromatic accommodation response [21]

Intraocular lenses (IOLs) with more diopters are problematic in that their central thickness and aberrations reduce image quality [22]. In measuring the quality of a polychromatic image using IOLs, a model eye was constructed with diffractive optical elements. Image quality was evaluated for vergences, lengths and pupil modulation transfer functions and image quality. There was a significant modification in the near-distance balance [23].

It is possible that changes in colour are observed when pictures are viewed by one eye with any surface defects? These aberrations could be caused by opacity or trauma in any of the elements in front of the retina, although it can also be produced in the retina itself. Cone defects are directly related to colour failure. Can original colour be recovered by modifying the picture viewed by that eye? With another functional eye problem, would it be possible to visualise the original colour with adequate irradiation?

2. Materials and Methods

All of the observers had normal colour vision. A refractive correction lens was evaluated [3,24]. Currently, there is no consensus on which colour test is the most complete. It is recommended to use at least 2 tests to uncover more information about visual perception [25]; possible tests include Ishihara, Color Vision Testing Made Easy (CVTME), Farnsworth–Munsell 100-Hue and other similar tests [25]. In many experiments, multiple light sources were used, with a CCT different in K value at different Duv values. These represent the most common light sources used, for example, in Chinese museums [3]. The application of memory and preferred colours to colour rendition evaluation of white light sources is reviewed with Sanders, Judd's flattery index, Thornton's colour preference index and Smet's memory colour rendition index. Here, we evaluated the agreement of data on visual appreciation and perception of naturalness [26]. Referenced patient studies comply with the Helsinki statement.

The participants evaluated a room with objects chosen to cover a range of hue, saturation and lightness values to evaluate the subjective impressions of a light source's colour quality [27]. The interpretation of lighting conditions included naturalness, vividness or preference in two scenes illuminated with different SPDs (spectral power distributions) [28].

With any transformation, colours varied in many directions and there was with no guarantee that colours fell within in the desired range [29]. In other experiments, the observer matched the left eye standard square with the luminance and chromaticity of the right eye modified by a control after being previously dark adapted [30]. The values were noted after the observer expressed that they were satisfied with the match by pressing a key [31]. The CVTME test consists of 10 plates for demonstration containing a circle, star and square, visible to all colour-deficient and colour-normal subjects and other plates designed for young children and those with learning difficulties [32,33].

Accommodation and vergence, in conjunction with ocular surface and blink, were evaluated while the participants were reading a text on a smartphone for a large time and were measured during reading. Eye fatigue and other symptoms, fixation disparity and binocular accommodation were assessed, and the frequency and amplitude of the blink and viewing distance were measured [19].

Accommodative lag and accommodative fluctuations were evaluated with the Grand Seiko WAM-5500 open-field auto-refractor [20]. Subjective DOFi was measured using a motorised Badal system. The subject's eye was paralysed and different, previously measured accommodative states were simulated with a deformable mirror. Different colour conditions were tested [21]. Spherical IOLs with different diopters were implanted in a IOL eye model and measured with a modulation transfer function (MTF) [22].

3. Results

Criteria for Successful CVTME Testing

For the present purposes, a child was able to cooperate with and respond to each test plate in order and in demonstration was successful when a subject name each of the black and white figures [32]. OCTs provided information on surface depth and size as well as pigment distribution. This information also applied to surfaces with higher roughness [34].

Subjects preferred daylight for visual acceptance and glare. Photometric variables modulated changes in visual light perception, alertness and mood in the afternoon [35]. Red, green and blue light could affect the colour appearance of the objects illuminated, particularly when they were vivid and saturated by high gamut area index. There was a strong preference for colours with enhanced saturation [16].

Perceptions were measured for different combinations of LEDs and perceived quality and links were assessed [5]. There was a preference for naturalness and colourfulness, and naturalness was weakly related to colourfulness [6]. The judgments for colour preference and comfort were highly correlated, and the whiteness of the lighting influenced colour preference, comfort and discrimination [3]. The average colour difference between the original and the recovered colours was relatively high; when the high value was disregarded, the average colour difference was reduced to 4.2 [1]. For dark objects, chroma was overestimated to lightness [31]. In dichromatic persons, the number of discernible colours was about 7% of normal. Only modest improvements could be obtained for dichromats [33].

The ocular symptoms increased with the use of the smartphone, in comfort, fatigue and drowsiness ($p \leq 0.02$). Accommodation was also reduced ($p = 0.01$). There were no other changes except an increase in the number of incomplete blinks, associated with a general worsening of eye symptoms ($\rho = -0.65$, $p = 0.02$) and fatigue ($\rho = 0.70$, $p = 0.01$) [19]. The accommodative lag was significantly different between schoolchildren and adults [$F(1219, 35,354) = 11,857$, $p < 0.05$] and non-myopic and myopic [$F(3107, 31,431) = 12,187$, $p < 0.05$]. It was higher in myopic schoolchildren (0.655 ± 0.198 D) than in non-myopic patients (0.202 ± 0.141 D, $p < 0.05$) and myopic young adults (0.316 ± 0.172 D, $p < 0.05$). The accommodative delay was greater in the mesopic room (all $p < 0.05$) [20].

Blue measured 0.45 ± 0.09 D, green 0.07 ± 0.02 D, and red 0.49 ± 0.10 D. The monochromatic DOFi was 1.10 ± 0.10 D with 0 D, 1.20 ± 0.08 D with 2 D and 1.26 ± 0.40 D with 4 D. The polychromatic white DOFi was higher than the monochromatic one (19%, 9% and 14%) [21]. MTF values were significantly higher than the values measured at the low range of polychromatic light [22]. Chromatic aberration resulted from a bifocal change in the quality of the near image; objects viewed at a distance were better with the design [23].

4. Discussion

It is possible to enhance the colour moderately and with degradation [17]. Use of a 4000 K light source with a Duv value of zero is preferable to enhance and comfortably view colour [3]. OCT measures the volume of pigment in a layer, the thickness of varnish layers, the voids and the depth of microcracks; when applied to cultural heritage it generates spectacular images [34].

The dependence between intensity, duration, pattern, timing, light history and wavelength can change the response of the circadian system. The photopic visual system responds equally to non-visual responses with high intensities [36]. The colour quality (CQ) attributes (naturalness,

colour and preference) of light were assessed in immersive environments. Preference was related to naturalness and colour, however naturalness was weakly related to colour [6]. There was a high correlation of preference with perception. White light improved colour preference, comfort and discrimination [3,31]. Other behavioural variables decreased visual acceptance, including variations in subjective alertness, mood and inter-correlations of these dependent variables. Daylight availability was one of the indicators of individual satisfaction [35].

Protans and deutans have a preference for re-coloured images with enhanced contrast. This information makes it possible to design good visualisations in these cases [29]. WGR mixes produce more attractive colour images than do other types of lights [5].

Eyestrain symptoms and ocular surface symptoms increased tiredness and sleepiness. These visual functions represent a loss of image sharpness. Binocular accommodative facility decreased [19] and focus variation is less accurate.

Among myopics, there was a greater lag in schoolchildren than in young adults. This is therefore a problem of focus among schoolchildren, preventing unintentional maintenance of attention, especially in ametropia such as myopia; this was greater under mesopic room conditions for all ages. Good photopic lighting is necessary to avoid it. Accommodative lag and accommodative fluctuations at far distance (6 m) and near distance (25 cm) were measured using the Grand Seiko WAM-5500 open-field autorefractor [20].

For polychromatic white DOFi with colour versus monochromatisms, some visual aid is essential to relax the accommodative stimulus that colour variations require [21]. Increased effects related to the IOL diopter were observed, and MTF values were found to be increased with the increase in the IOL diopter [22]. This also affects populations of people with cataract surgery or with ametropia, where the lens is replaced by IOLs. Such people are mostly over 60 years of age. For bifocals, adding power produced changes in the near image quality in terms of wavelength and pupil size [23].

Finally, there is a large population with healthy eyes and those with different visual problems due to accommodation, binocular vision, intraocular lenses or pupils, that may not see a well-lit object well in any museum.

5. Conclusions

As a first conclusion, the changes in quality of lighting produce subjective alterations in the observers. It is preferable to use a light source with a Duv value of zero to enhance and comfortably view colour. The visual functions affected are accommodation, binocular vision and the quality of the eye, as well as artificial changes in the eye with variations of the pupil or age conditions. Any subjective evaluation procedure for a work of art can be affected by lighting and the living eye.

Funding: This was funded by Ministerio de Ciencia e innovación of Spain with grant number [RTI2018-097633-A-100] And The APC was funded by the project Restauración fotónica aplicada a patrimonio cultura: aplicación al cuadro de dali “dos figuras”.

Conflicts of Interest: The authors declare no conflict of interest.

References

1. Kim, A.; Oh, I.-H.; Kim, H.-S.; Park, Y. Recovering the Colors of Objects from Multiple Near-IR Images. *J. Opt. Soc. Korea* **2015**, *19*, 102–111.
2. Jost, S.; Cauwerts, C.; Avouac, P. CIE 2017 Color Fidelity Index Rf: A Better Index to Predict Perceived Color Difference? *J. Opt. Soc. Am. A* **2018**, *354*, 202–213. [CrossRef]
3. Huang, Z.; Liu, Q.; Pointer, M.R.; Chen, W.; Liu, Y.; Wang, Y. Color quality Evaluation of Chinese Bronzeware in Typical Museum Lighting. *J. Opt. Soc. Am. A* **2020**, *374*, 170–180. [CrossRef] [PubMed]
4. He, J.; Lin, Y.; Yano, T.; Noguchi, H.; Yamaguchi, S.; Matsubayashi, Y. Preference for Appearance of Chinese Complexion under Different Lighting. *Lighting Res. Technol.* **2015**, *492*, 228–242. [CrossRef]
5. Jost-Boissard, S.; Fontoynt, M.; Blanc-Gonnet, J. Perceived Lighting Quality of LED Sources for the Presentation of Fruit and Vegetables. *J. Mod. Opt.* **2009**, *5613*, 1420–1432. [CrossRef]

6. Zhang, F.; Xu, H.; Feng, H. Toward a Unified Model for Predicting Color Quality of Light Sources. *Appl. Opt.* **2017**, *5629*, 8186–8195. [CrossRef] [PubMed]
7. Smet, K.; Ryckaert, W.R.; Pointer, M.R.; Deconinck, G.; Hanselaer, P. Correlation Between Color Quality Metric Predictions and Visual Appreciation of Light Sources. *Opt. Express*. **2011**, *199*, 8151–8166. [CrossRef]
8. Tang, X.; Teunissen, C. The Appreciation of LED-based White Light Sources by Dutch and Chinese People in Three Application Areas. *Lighting Res. Technol.* **2018**, *513*, 353–372. [CrossRef]
9. Liu, Q.; Huang, Z.; Pointer, M.R.; Luo, M.R.; Xiao, K.; Westland, S. Evaluating Colour Preference of Lighting with an Empty Light Booth. *Lighting Res. Technol.* **2017**, *508*, 1249–1256. [CrossRef]
10. Islam, M.S.; Dangol, R.; Hyvärinen, M.; Bhusal, P.; Puolakka, M.; Halonen, L. User Preferences for LED lighting in Terms of Light Spectrum. *Lighting Res. Technol.* **2013**, *456*, 641–665.
11. Khanh, T.Q.; Bodrogi, P. Colour Preference, Naturalness, Vividness and Colour Quality Metrics, Part 3: Experiments with Makeup Products and Analysis of the Complete Warm White Dataset. *Lighting Res. Technol.* **2016**, *502*, 218–236. [CrossRef]
12. Chen, W.; Huang, Z.; Liu, Q.; Pointer, M.R.; Liu, Y.; Gong, H. Evaluating the Color Preference of Lighting: The Light Booth Matters. *Opt. Express* **2020**, *2810*, 14874–14883.
13. Dikel, E.E.; Burns, G.J.; Veitch, J.A.; Mancini, S.; Newsham, G.R. Preferred Chromaticity of Color-Tunable LED Lighting. *LEUKOS* **2014**, *102*, 101–115.
14. Liu, K.; Zhang, Y.; Liu, Q.; Cao, G.; Li, Q.; Huang, Z. Relationship of Different Scales for Evaluating the Quality of LED lighting. In *Applied Sciences in Graphic Communication and Packaging*; Springer: Berlin/Heidelberg, Germany, 2018; pp. 29–37.
15. Wei, M.; Houser, K.W.; Allen, G.R.; Beers, W.W. Color Preference under LEDs with Diminished Yellow Emission. *LEUKOS* **2014**, *103*, 119–131.
16. Feng, X.F.; Xu, W.; Han, Q.Y.; Zhang, S.D. Colour-enhanced Light Emitting Diode Light with High Gamut Area for Retail Lighting. *Lighting Res. Technol.* **2015**, *493*, 329–342.
17. Viénot, F.; Coron, G.; Lavédrine, B. LEDs as a Tool to Enhance Faded Colours of Museums Artefacts. *J. Cult. Herit.* **2011**, *124*, 431–440.
18. Jaiswal, S.; Asper, L.; Long, J.; Lee, A.; Harrison, K.; Golebiowski, B. Ocular and Visual Discomfort Associated with Smartphones, Tablets and Computers: What We Do and Do Not Know. *Clin. Exp. Optom.* **2019**, *1025*, 463–477.
19. Golebiowski, B.; Long, J.; Harrison, K.; Lee, A.; Chidi-Egboka, N.; Asper, L. Smartphone Use and Effects on Tear Film, Blinking and Binocular Vision. *Curr. Eye Res.* **2020**, *454*, 428–434.
20. Chen, A.H.; Ahmad, A.; Kearney, S.; Strang, N. The Influence of Age, Refractive Error, Visual Demand and Lighting Conditions on Accommodative Ability in Malay Children and Adults. *Graefes. Arch Clin. Exp. Ophthalmol.* **2019**, *2579*, 1997–2004.
21. Jaskulski, M.; Marín-Franch, I.; Bernal-Molina, P.; López-Gil, N. The Effect of Longitudinal Chromatic Aberration on the Lag of Accommodation and Depth of Field. *Ophthalmic Physiol. Opt.* **2016**, *366*, 657–663.
22. Song, H.; Yuan, X.; Tang, X. Effects of Intraocular Lenses with Different Diopters on Chromatic Aberrations in Human Eye Models. *BMC Ophthalmol.* **2016**, *16*, 9. [CrossRef] [PubMed]
23. Ravikumar, S.; Bradley, A.; Thibos, L.N. Chromatic Aberration and Polychromatic Image Quality with Diffractive Multifocal Intraocular Lenses. *J. Cataract. Refract Surg.* **2014**, *407*, 1192–1204. [CrossRef] [PubMed]
24. Cao, D.; Zele, A.J.; Pokorny, J. Chromatic Discrimination in the Presence of Incremental and Decremental Rod Pedestals. *Vis. Neurosci.* **2008**, *253*, 399–404. [CrossRef] [PubMed]
25. Fanlo Zarazaga, A.; Gutiérrez Vázquez, J.; Pueyo Royo, V. Review of the Main Colour Vision Clinical Assessment Tests. *Arch Soc. Esp. Oftalmol.* **2019**, *941*, 25–32. [CrossRef]
26. Smet, K.A.G.; Hanselaer, P. Memory and Preferred Colours and the Colour Rendition of White Light Sources. *Lighting Res. Technol.* **2015**, *484*, 393–411. [CrossRef]
27. Royer, M.P.; Wilkerson, A.; Wei, M.; Houser, K.; Davis, R. Human Perceptions of Colour Rendition Vary with average Fidelity, Average Gamut, and Gamut Shape. *Lighting Res. Technol.* **2016**, *498*, 966–991. [CrossRef]
28. David, A.; Smet, K.A.G.; Whitehead, L. Methods for Assessing Quantity and Quality of Illumination. *Annu. Rev. Vis. Sci.* **2019**, *5*, 479–502. [CrossRef]
29. Kuhn, G.R.; Oliveira, M.M.; Fernandes, L.A. An Efficient Naturalness-Preserving Image-Recoloring Method for Dichromats. *IEEE Trans. Vis. Comput. Graph.* **2008**, *146*, 1747–1754. [CrossRef]

30. Shepherd, A.J.; Wyatt, G. Changes in Induced Hues at Low Luminance and Following Dark Adaptation Suggest Rod-Cone Interactions May Differ for Luminance Increments and Decrements. *Vis. Neurosci.* **2008**, *253*, 387–394. [CrossRef]
31. Giesel, M.; Gegenfurtner, K.R. Color Appearance of Real Objects Varying in Material, Hue, and Shape. *J. Vis.* **2010**, *109*, 10. [CrossRef]
32. Richardson, P.; Saunders, K.; McClelland, J. Colour Vision Testing Made Easy: How Low Can You Go? *Optom. Pract.* **2008**, *91*, 17.
33. Linhares, J.M.; Pinto, P.D.; Nascimento, S.M. The Number of Discernible Colors Perceived by Dichromats in Natural Scenes and the Effects of Colored Lenses. *Vis. Neurosci.* **2008**, *253*, 493–499.
34. Elias, M.; Mas, N.; Cotte, P. Review of Several Optical Non-Destructive Analyses of an Easel Painting. Complementarity and Crosschecking of the Results. *J. Cult. Herit.* **2011**, *124*, 335–345.
35. Borisuit, A.; Linhart, F.; Scartezzini, J.L.; Münch, M. Effects of Realistic Office Daylighting and Electric Lighting Conditions on Visual Comfort, Alertness and Mood. *Lighting Res. Technol.* **2014**, *472*, 192–209. [CrossRef]
36. Andersen, M.; Mardaljevic, J.; Lockley, S.W. A framework for Predicting the Non-Visual Effects of Daylight—Part I: Photobiology-Based Model. *Lighting Res. Technol.* **2012**, *441*, 37–53.



© 2020 by the author. Licensee MDPI, Basel, Switzerland. This article is an open access article distributed under the terms and conditions of the Creative Commons Attribution (CC BY) license (<http://creativecommons.org/licenses/by/4.0/>).

MDPI
St. Alban-Anlage 66
4052 Basel
Switzerland
Tel. +41 61 683 77 34
Fax +41 61 302 89 18
www.mdpi.com

Heritage Editorial Office
E-mail: heritage@mdpi.com
www.mdpi.com/journal/heritage



MDPI
St. Alban-Anlage 66
4052 Basel
Switzerland
Tel: +41 61 683 77 34
www.mdpi.com



ISBN 978-3-0365-4635-3